Identification of Defect Locations in Forged Products using the Finite-Element Method.

by

Sally Elizabeth Clift

A thesis submitted in supplication for the degree of Ph.D.

Department of Mechanical Engineering,

Faculty of Engineering,

University of Birmingham.

April 1986.

CORRIGENDUM

The term generalised plastic work, as used in this thesis, refers to generalised plastic work per cubic metre.

1432088

Synopsis.

In recent years the development of the finite-element technique has brought with it many advances in metalforming analysis. Its use in the prediction of metal flow in three dimensional forging is now well established.

This thesis describes the use of the finite-element technique in a study of deformation and fracture initiation in a range of simple metalforming operations. These cover typical industrial processes and enable deformation and fracture initiation to be examined under several different loading conditions.

The background theory relating to both techniques of metalforming analysis and fracture in metalforming are first examined. Then, the theory of finite-elements in general and the finite-element technique used here are briefly described.

In the first of the metalforming operations considered, that of plane-strain side-pressing, the finite-element predicted deformation behaviour of 60-40 brass and 7075 aluminium alloy has been compared with experiment. Both visioplasticity and hardness studies have been performed. The macrohardness survey was found to be the most appropriate in validating the use of the finite-element technique.

The numerical calculations of the local stress and strain distributions are then used with a number of previously published continuum fracture criteria to predict the fracture initiation sites. For certain of the successful criteria the level of deformation at fracture has also been predicted using critical values at fracture found experimentally from an axisymmetric tensile test. For the operation of plane-strain side-pressing, very good agreement with both the experimental fracture initiation site, and the level of deformation at

fracture, is reported for the criterion of a critical value of generalised plastic strain at fracture, and the equivalent criterion of generalised plastic work.

The second metalforming operation considered is simple upsetting. The fracture initiation behaviour of 60-40 brass has been examined for specimens of the four initial aspect ratios of 0.5, 1.0, 1.5 and 2.0. Again, the generalised plastic strain/work criterion has successfully predicted the experimental fracture initiation sites in all cases. However, satisfactory level of deformation at fracture predictions have only been found for the two lower aspect ratio specimens.

A small range of strip compression and tension operations on 60-40 brass compose the third type of metalforming operation considered in this thesis. Yet again the generalised plastic strain/work criterion has successfully predicted the fracture initiation site found experimentally but not the level of deformation at fracture.

Finally, the axisymmetric extrusion of 60-40 brass and 7075 aluminium alloy is examined. For the brass using the generalised plastic strain/work criterion, good agreement with experiment has been found for both the fracture initiation site and level of deformation at fracture found experimentally. However, for the aluminium alloy only the correct fracture initiation site has been found.

In summary, it appears that the fracture criterion of a critical value of generalised plastic strain/work has successfully predicted the fracture initiation site found experimentally in all the operations considered in this thesis but has been unable to consistently predict the correct level of deformation at fracture. These differences in the predicted and experimental level of deformation at fracture cannot be explained with reference to the finite-element calculated levels of hydrostatic stress. Further work is necessary to explain this difference.

To my mom and dad, Jenny and Dennis,

and my brothers, Andrew and Robert.

Acknowledgements.

I should like to thank the Science and Engineering Research Council for funding this research, and Professor S.A. Tobias for the use of the facilities of the Department of Mechanical Engineering.

My thanks are also due to Mr B. Beighton for help with the experimental work; Alcan International and Alcan Plate for supplying some of the experimental material, and to the staff of the Centre for Computing and Computer Science at Birmingham, and the University of Manchester Regional Computer Centre for the use of computer facilities and help on computing matters.

I am grateful to Dr I. Pillinger who wrote the finite-element program used in this thesis and who has been a constant uncomplaining source of help; and to Dr B. Dodd for help in the understanding of fracture.

Finally, I should like to thank my supervisors, Dr P. Hartley, Dr C.E.N. Sturgess and Professor G.W. Rowe for their continual advice and encouragement.

Contents.

Table of nomenclature.

a	maximum radius of the necked region of an axisymmetric tensile test specimen.
a_{ps}	plane-strain fracture strain.
c	constant.
$\underline{d}_i$	displacement vector of node i.
$\underline{f}_i$	force vector for node i.
f	ratio of apparent density of the porous material to the density of its pore-free matrix in the model of Oyane(1980).
j	number of nodes per element.
k_f	material constant in the model of Ghosh (1976).
k_n	yield stress in shear.
l_x, l_y, l_z	void spacings in the model of McClintock (1968).
n	work hardening exponent.
p_1, p_2	yield stress values of cylinders of height h_1 and h_2.

r	initial void radius in McClintock (1968) model.
x,y,z	Cartesian coordinates.
A,G	material constants in the model of Oyane (1980).
$[B_n]$	strain-nodal displacement matrix.
C	right Cauchy-Green deformation tensor.
C1,C2,C3,W^*	material constants for given temperature and strain rate.
[D]	incremental stress-strain matrix.
D_L, D_T	hole growth damage parameters in the longitudinal and transverse directions respectively.
F	deformation gradient matrix.
[I]	unit matrix.
[K]	global stiffness matrix.
$[K_n]$	stiffness matrix for node n.
$[K]^{\epsilon}$	deformation stiffness matrix.
$[K]^{\sigma}$	rotation stiffness correction.
$[K]^{\varphi}$	constant volume stiffness correction.

L	strain ratio $d\epsilon_1/d\epsilon_2$
[L]	strain displacement operator matrix.
$[N_i]$	shape function for node i.
R	radius of curvature of the neck of an axisymmetric tensile test specimen.
$\underline{U}$	displacement vector.
U_x, U_y, U_z	displacement in x, y and z directions respectively.
X,Y,Z	local coordinates.
Y	yield stress.
$\underline{\epsilon}$	strain vector.
$\Delta\underline{\epsilon}$	strain increment vector.
$\bar{\epsilon}$	generalised plastic strain.
$d\bar{\epsilon}$	generalised plastic strain increment.
$\bar{\epsilon}_f$	generalised plastic strain at fracture.
$\epsilon_x, \epsilon_y, \epsilon_z$	Cartesian strain components.

$\epsilon'_x, \epsilon'_y, \epsilon'_z$ deviatoric Cartesian strain components.

$\epsilon_{\theta f}$ circumferential fracture strain.

ϵ_{zf} axial fracture strain.

ϵ_v volumetric strain.

ϵ_{vf} volumetric strain at fracture.

$\underline{\sigma}$ stress vector.

$(\sigma_x)_{av}$ mean axial stress.

$\bar{\sigma}$ generalised stress.

σ normal stress.

$\sigma_1, \sigma_2, \sigma_3$ principal stress components.

σ_H hydrostatic stress.

$\sigma_x, \sigma_y, \sigma_z$ Cartesian stress components.

σ_o yield stress.

μ coefficient of friction.

γ shear strain.

γ_L	Lagrangian strain tensor.
τ	shear stress.
Δ	symbol denoting incremental values.
F_L, F_T	Hole growth factors in the longitudinal and transverse directions respectively.
ρ	density.
σ^*	maximum principal tensile stress.

Introduction.

Until recently, metalworking theory was primarily concerned with the prediction of forces and to a lesser extent the metal flow within a workpiece. However, there has been more progress since the initial application of the finite-element method to metalforming analysis. Its use in the prediction of metal flow in three-dimensional forging is now well established. Detailed variations of strain with yield stress, strain rate and temperature may now be modelled.

This now opens the way to the study of the initiation of fracture in metalforming operations. This thesis reports the results of such a study of fracture initiation in cold forging which utilises the detailed stress and strain values produced by an elastic-plastic finite-element program. With these results it is then possible to use continuum fracture criteria in a predictive capacity, and subsequently to compare this with experimental results.

Chapter one is a brief summary of some of the literature relating to metalforming theory. The following chapter reviews the literature relating to continuum fracture criteria, and presents those selected to be used in conjunction with the finite-element results. Chapter three briefly examines the finite-element program used and describes the additional software written to determine the fracture criteria predictions. Chapters four to seven inclusive present the numerical and experimental results obtained for the four metalforming operations studied, that is plane-strain side-pressing, simple upsetting, strip compression and tension, and axisymmetric extrusion.

Finally, chapter eight provides an overall assessment of the results.

Chapter 1.

Analytical techniques in metalforming.

1.1 Introduction.

This chapter reviews the analytical and numerical methods that could in principle be useful in solving the specific metalforming problems in this thesis. The available methods are examined with respect to their ability to provide detailed stress and strain values throughout the deformation process. These are needed to examine the predictions of various continuum fracture criteria.

The capabilities of upper bound theory are briefly reviewed in section 1.3. This is accompanied by more detailed presentations of slip-line field theory, in section 1.2, and finite-element theory in section 1.4. Where they have been performed, the application of these theories to the geometries of interest in this study are also presented. Finally, section 1.5 presents the conclusions of this chapter.

1.2 Slip-line field theory.

Slip-line field theory was originally formulated by Hencky (1923) and has been widely used as a theoretical technique for analysing metal flow since its first application to metalforming by Hill, Lee and Tupper in 1946.

Slip-lines show the directions of maximum shear stress within a body during a small increment of deformation. This theory applies only to plane-stain deformation where the strain perpendicular to the plane is zero so that the only shear stresses which occur are in the plane. Once these shear stresses have reached the yield value for the material plastic flow will occur.

On the slip lines deformation of the material can be assumed to take

place intensely. The value of hydrostatic stress along the slip-line can vary and is shown by the curvature of the line, the more curved the slip-lines the greater the hydrostatic stress will be and the higher the forming load. The absolute magnitude of the hydrostatic stress may be found by starting any calculation at a boundary. The technique is also capable of calculating metal flow in bodies subject to a variety of interface friction conditions. However, the shear stress stays the same along a slip-line as the material response is usually modelled as rigid-perfectly plastic.

Strain hardening effects have been included in slip-line field theory by Farmer and Oxley (1971). However, experimentally determined velocity gradients are needed, so that the technique is no longer fully predictive. There is no unique net of slip-lines, so that some judgement is required as to a satisfactory deformation mode. In order to check the validity of any slip-line field a hodograph should be constructed. This diagram represents the velocity of each region of the deforming body as a vector and ensures that there is no discontinuity in the component of velocity in the direction normal to the slip-line, and thus that there is no metal pile up or holes left in the body.

The theory gives only an instantaneous picture of the directions of maximum shear stress, and therefore plastic flow within the deforming workpiece. It is not possible to trace the deformation pattern throughout the entire metalforming operation unless the slip-line field is determined at each level of deformation. Attempts have been made to computerise this approach (Collins, 1969 and Hartley, 1979).

In summary, it appears that slip-line field theory is not sophisticated enough to produce the detailed stress and strain values required for this study of fracture initiation. This is for two main reasons; firstly, due to its limitation to plane-strain deformation; and secondly to the simplicity of the rigid-perfectly plastic material

response model. However, for the two plane-strain metalforming operations which are considered in this thesis it may be of interest to examine the slip-line field solutions which have previously been reported in the literature.

1.2.1 Plane-strain side-pressing.

Plane-strain side-pressing, as illustrated in figure 1.1, refers to the transverse upsetting of a circular section rod in plane-strain. It has been the focus of research interest due to its relevance in the manufacture of turbine blades.

Jain and Kobayashi (1970) proposed three modes of deformation from slip-line field theory, depending on the ratio of the height of the workpiece to the width of material in contact with the die. Figure 1.2(a) illustrates the slip-line field solution for Type I deformation. This occurs in the very early part of the compression of an initially circular section specimen when the height to width ratio (H/W) of the deforming workpiece is high and flow is confined to the material close to the dies. Once this ratio decreases below a critical value, in this case approximately nine, plastic flow occurs in the central section of the workpiece and opposite sides of the specimen move apart as rigid masses. This type of deformation, termed type II, is illustrated in figure 1.2(b). For H/W ratios of unity or below the majority of the specimen becomes subject to plastic deformation and a third slip-line field becomes applicable (Figure 1.2(c)).

The experimental investigation included observation of the distortion of the grids on a plane-strain constrained surface throughout the deformation process for both initially circular section specimens and

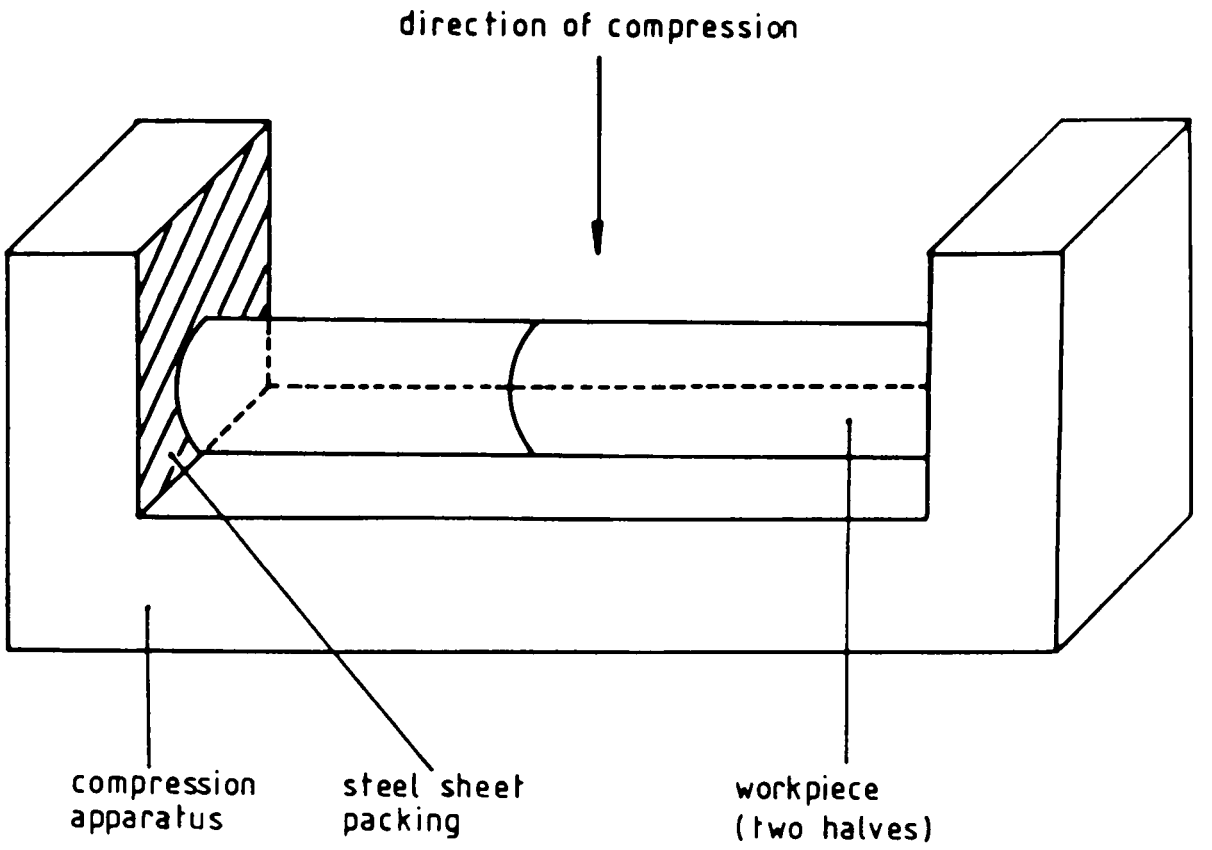

Figure 1.1

Schematic illustration of plane-strain side-pressing.

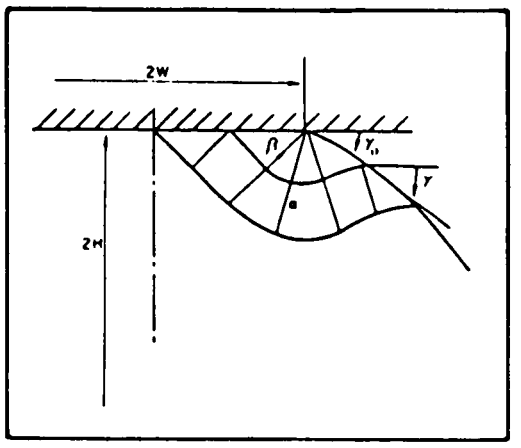

(a) Type I

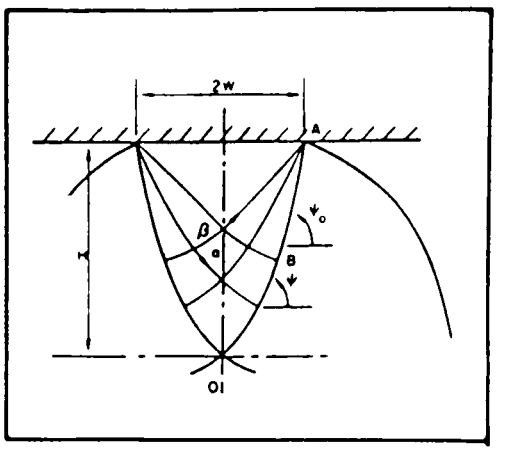

(b) Type II

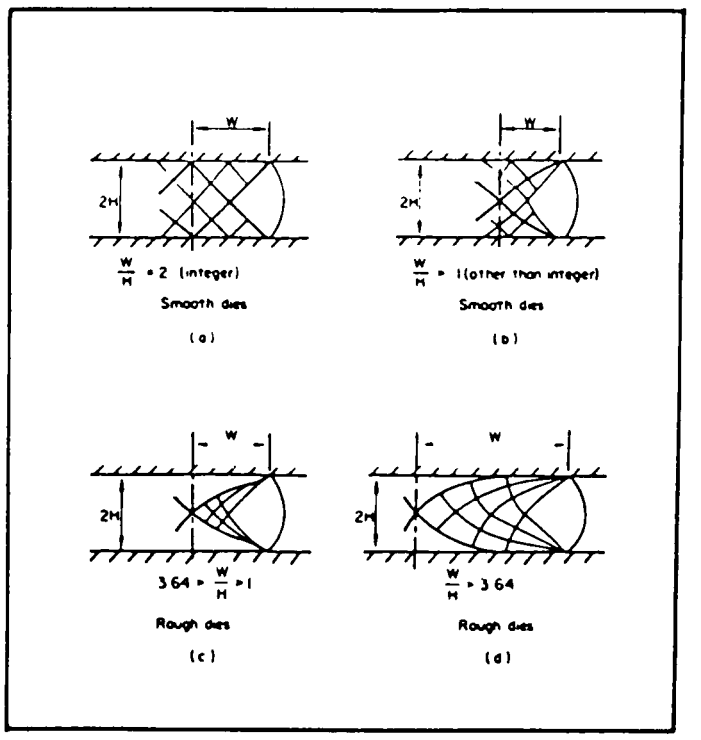

(c) Type III

Figure 1.2

Three types of deformation for plane-strain side pressing.

After Jain and Kobayashi (1970)

specimens with machined flats. These authors report the qualitative agreement between the theoretical and experimental grid deformation, but a quantitative comparison, for example of strain calculated from the displacement of grid intersection positions, was not presented. Comparisons were made between the experimental and slip-line field values of the variation of the H/W ratio of the workpiece as a function of height. As figure 1.3 shows, the slip-line field prediction generally overestimated the actual width of contact, but the same trends may be observed in both sets of results.

1.2.2 Strip compression.

Hill (1950) proposed a solution for the expansion of a semi-cylindrical cavity in a plane surface. This is analogous to the strip compression operation considered in this thesis. Hill's solution has been reproduced in figure 1.4. Figure 1.4(a) shows the slip-line field and deformation around the cavity. BEB is the surface of the cavity and ABC is the coronet. The impression is supposed to have been initiated at point O, and the pressure applied only over BEB and not on AB. Figure 1.4(c) shows the distortion of an initially square grid, obtained using the hodograph construction shown in figure 1.4(b).

1.3 Upper bound theory.

Accurate results may be obtained from slip-line field theory if the assumed conditions are satisfied. However, industrially it is very useful to have a load bounding tehnique. Upper bound theory will predict a load which is at least sufficient to perform a metalforming operation. It does this by considering only surfaces of intense shear,

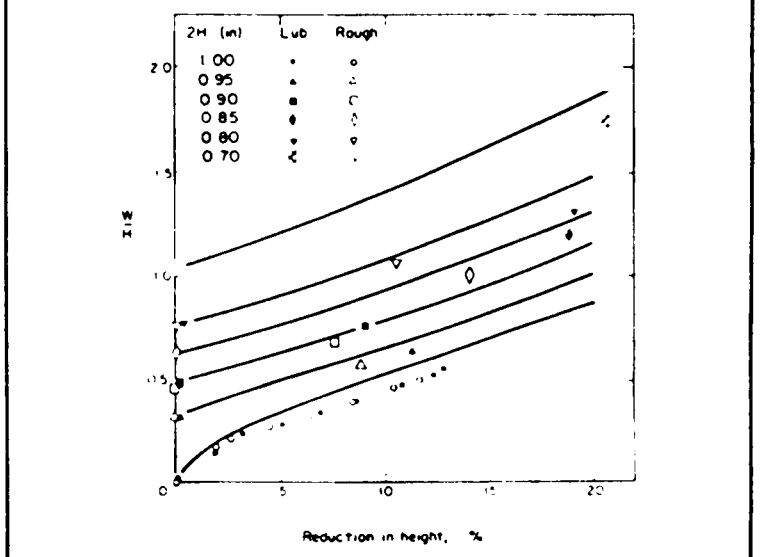

FIG. 9 Variation of the height-width ratios as a function of reduction in height.
(solid lines indicate slip-line field results)

Figure 1.3 Variation of the height to width ratio in plane-strain side-pressing as a function of reduction in height.

After Jain and Kobayashi (1970)

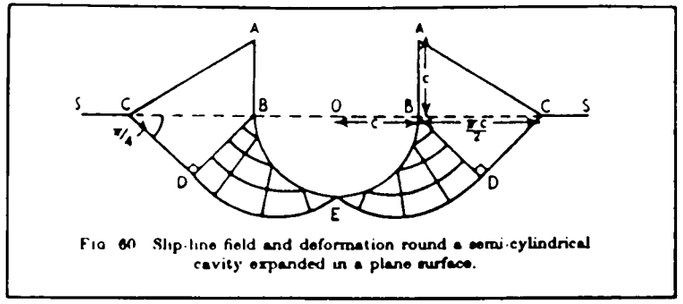

Fig. 60 Slip-line field and deformation round a semi-cylindrical cavity expanded in a plane surface.

(a)

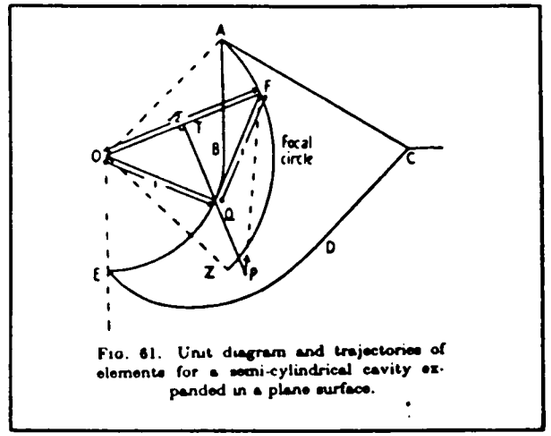

Fig. 61. Unit diagram and trajectories of elements for a semi-cylindrical cavity expanded in a plane surface.

(b)

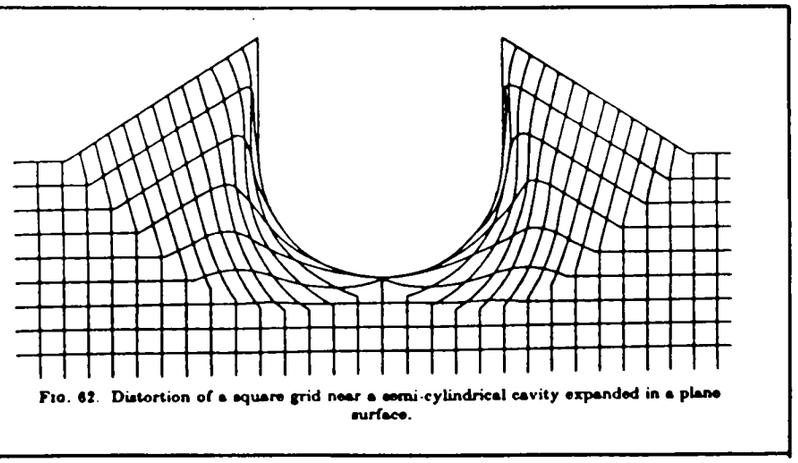

Fig. 62. Distortion of a square grid near a semi-cylindrical cavity expanded in a plane surface.

(c)

Figure 1.4

Slip-line field results for the formation of a semi-cylindrical cavity in a plane surface.

After Hill (1950)

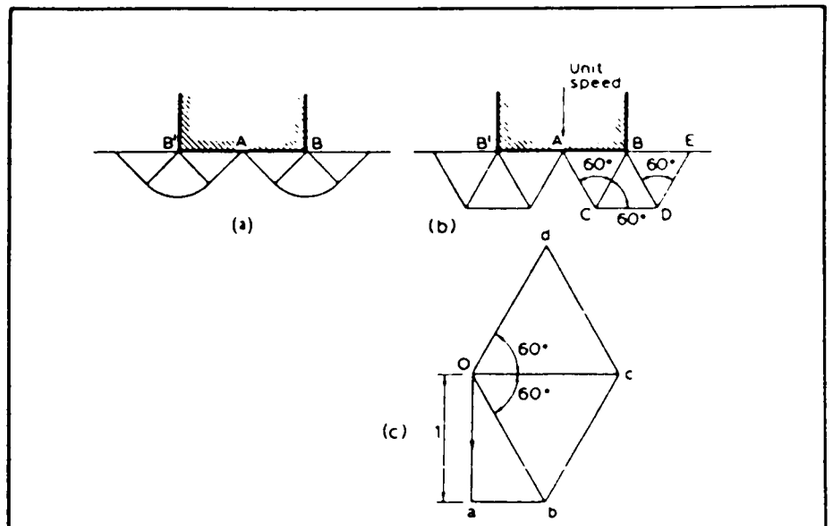

Figure 7.3 (*a*) A slip-line field for lubricated indentation of a large block (*b*) An approximate representation by straight lines to give an upper-bound solution consisting of equilateral triangles (c) The hodograph relating to (*b*)

Figure 1.5

Upper-bound and slip-line field solutions for indentation.

After Rowe (1979)

and equates the dissipation of energy on these surfaces to the rate of external work. The plastically deforming body is supposed to be divided into simple zones, usually triangular. These do not themselves deform but move with respect to each other along lines of tangential velocity discontinuity. Thus compatibility is satisfied as material is neither created or destroyed but equilibrium is not satisfied as no account is taken of the stress distribution.

The implied pattern of velocities must be consistent with the externally imposed conditions, as verified by drawing a hodograph. Figure 1.5 shows an upper bound solution and hodograph for the lubricated indentation of a large block. A slip-line field is also shown for comparison. In general the predictions from upper bound theory become more accurate as the fields themselves look more like slip-line fields.

Upper bound theory was originally developed for plane-strain deformation and is based on the work of many investigators including Hill (1950), Prager and Hodge (1951), Johnson, Mellor and Woo (1958) and Johnson (1959). Its capabilities were augmented by Kudo (1960a, 1960b) to apply to axial symmetry. However, Kudo's approach was restricted to rectangular units with two rigid boundaries. This was extended to elements with free flow across their boundaries by Cramphorn, Bramley and McDermott (1976). The technique has been most recently advanced by Osman and Bramley (1982) to follow the metal flow lines inside the deforming workpiece using their 'Upper bound elemental technique', UBET. This is an incremental upper bound solution, necessitating the use of a microcomputer.

Industrially, therefore, upper bound theory is very useful as it will predict a load at which a forming operation can be completed. However, due to its restriction to two dimensional geometries and its neglection of stress equilibrium it is not suitable for the analysis of fracture initiation proposed here.

1.4 Finite-element theory.

This stress analysis technique was originally utilised by the aircraft industry for dealing with structures, but has subsequently been extended to deal with non-linear material properties. Finite-element theory has been applied to continua, as is shown for the two dimensional model in figure 1.6, although three dimensional analyses are equally possible. The solid is split into a number of smaller regions, known as elements, which are usually of a fairly simple geometric form. The given example shows triangles. The points at which the corners of the elements meet are known as nodes and it is at these points that the equilibrium and compatibility conditions are satisfied.

Various different sized elements may be used within the same mesh, smaller elements being required where high strain gradients occur. With a high number of elements a more accurate solution may be obtained than with a smaller number of elements.

For a non-linear analysis, such as that required to model plastic flow, the behaviour of the material is approximated by a number of short linear steps, known as increments. These types of analyses are generally performed on large mainframe computers, due to the very large numbers of calculations that need to be performed. Each of these increments involves the solutions of the same number of equations as one simple elastic analysis. Smaller increments will lead to a more accurate solution, but it will take the computer a lot longer to perform the complete analysis.

Two types of material model are commonly used, although in principle it is possible to model any form of stress and strain variation. The elastic-plastic model, as the name suggests, models both elastic and plastic deformation. However, computational savings may result from the

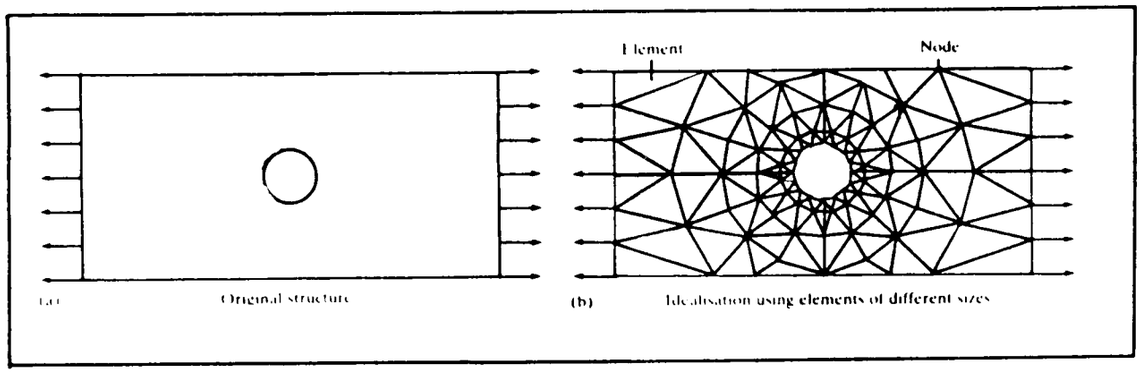

Figure 1.6

Two-dimensional finite-element mesh.

After Rao (1982).

use of the rigid-plastic material response model. Here, elastic deformation is neglected in the analysis of operations which undergo large plastic flow, due to its comparatively small effect on the stress system within a heavily deformed body. However, if the residual stresses left in the body after unloading are to be examined it is necessary to use an elastic-plastic formulation.

The finite-element technique has a number of advantages over the more established methods of forming analysis. These included the ability to give detailed stress and strain values throughout the deformation sequence and to follow the pattern of metal flow in three dimensions. However, its fundamental advantage is the ability to deal with complex geometries.

Although it is planned to study only simple metalforming operations in this thesis, the technique used should allow development to industrially relevant three dimensional geometries. Of those available the finite-element method therefore seems the most suitable for use in this study of fracture initiation in metalforming.

Applications of finite-element theory to the deformation of three out of the four geometries of interest in this thesis have been found. Section 1.4.1 refers to plane-strain side-pressing, section 1.4.2 to simple upsetting and section 1.4.3 to axisymmetric extrusion. No references to finite-element studies of strip compression or tension have been found.

1.4.1 Plane-strain side-pressing.

Using a two dimensional elastic-plastic finite-element formulation, Lee and Kobayashi (1971) performed an analysis of plane-strain side-pressing of an initially circular section rod. The stress-strain behaviour of 7075 aluminium alloy was modelled, and complete sticking was assumed at the tool-workpiece interface. The deformation of the

workpiece was modelled up to a reduction in height of 19%.

Results produced include the extent of the plastic zone at various stages during the side-pressing operation. These calculations revealed that some of the regions which had previously undergone plastic deformation could, at a later stage, deform in an elastic manner. Figure 1.7 provides more detailed information on the strain distribution within the deforming workpiece at approximately 10% reduction in height. Figure 1.7(a) shows the distortion of lines originally parallel to the x-axis and figure 1.7(b) gives the corresponding contours of effective strain. Unfortunately, it was not possible to ascertain any agreement with the slip-line field analysis of Jain and Kobayashi (1970) as finite-element predicted grid deformations at appropriate levels of deformation were not presented.

Oh, Lahoti and Altan (1982) used an isothermal rigid viscoplastic finte-element formulation, to analyse the plane-strain side-pressing of solid cylinders for two microstructures of 6242 titanium alloy. They found that the microstructure containing both alpha and beta phase is stable, whereas significant geometric strain localisation occurs when the beta microstructure is present alone. The extent of this strain localisation was successfully predicted by the finite-element solution as shown in figure 1.8. Very well defined shear bands are shown; strains as high as ten were calculated where the shear bands for the beta microstructure meet the die. The relevance of the strain localisation to fracture behaviour was not described.

1.4.2 Simple upsetting.

One of the first finite-element analyses of simple upsetting was published by Nagamatsu, Murota and Jimma (1971). They used a two dimensional elastic-plastic finite-element formulation to analyse the

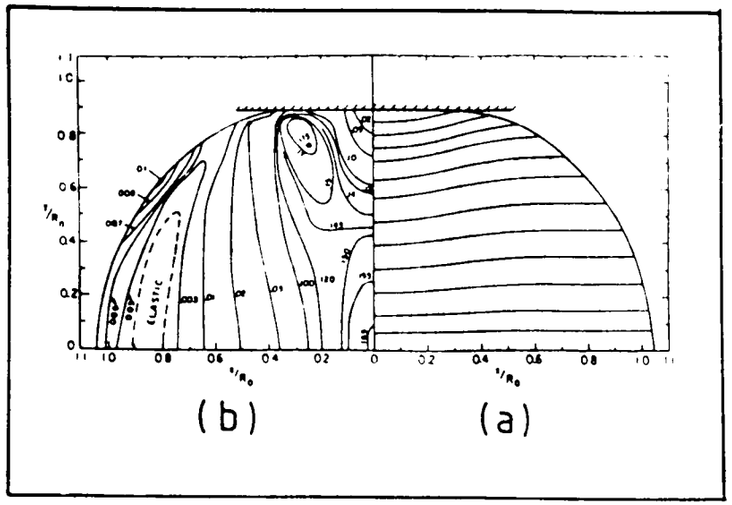

Figure 1.7. (a) Line distortions, and (b) contours of constant effective strain at 10% reduction in height in side pressing.

After Lee & Kobayashi (1971)

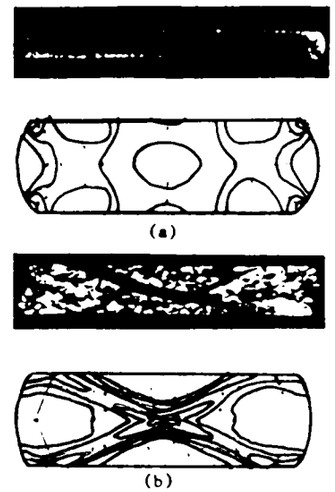

FIGURE 2. Results of Side Pressing of Ti-6242-0.1Si Compared with Experiments at 913 C.
(a) α+β Microstructure (b) β Microstructure

FIGURE 1.8 Finite element & experimental results for side pressing of titanium alloy.

After Oh et al (1982)

deformation of aluminium. A range of height to diameter ratios from 0.25 to 2.5 were examined. The analyses were only continued until the models had become fully plastic, that is up to about 4% reduction in original height. A much more comprehensive analysis of simple upsetting was produced in the same year by Lee and Kobayashi (1971). Experimental and finite-element results were obtained up to 33% reduction in height. Figure 1.9 shows the reasonable agreement found with experiment for load-displacement curves up to 20% reduction. Slight differences are accounted for in that the theoretical stress-strain relationship used is an idealised one typical of a group of aluminium alloys, and not precisely that of the alloy actually used. Figure 1.10 gives the theoretical and experimental bulge profiles at various reductions in height. Good agreement was obtained for low reductions, but this was not so good at higher levels of deformation. Experimentally, it is known that some of the originally free surface comes into contact with the die, but this was not predicted by the finite-element technique even at 33% reduction. The authors suggested that a much finer mesh is needed to model this behaviour, although an analysis was not presented.

Kudo and Matsubara (1978) collected and compared results for simple upsetting obtained by fourteen different research groups. This was presented as a comparative calibration test of various finite-element formulations for the analysis of large plastic deformation problems. The numerical method and computational procedure chosen to determine the upsetting load, equatorial stresses and side profile of the workpiece were left in the hands of the participators. Figure 1.11 presents a comparison of the predicted equatorial stresses against reduction in height. Considerable discrepancies are visible between the results of the various investigators. Other results, such as the bulge profiles presented in figure 1.12 do not show such considerable variation.

Differences in the number and shape of the elements was suggested to be

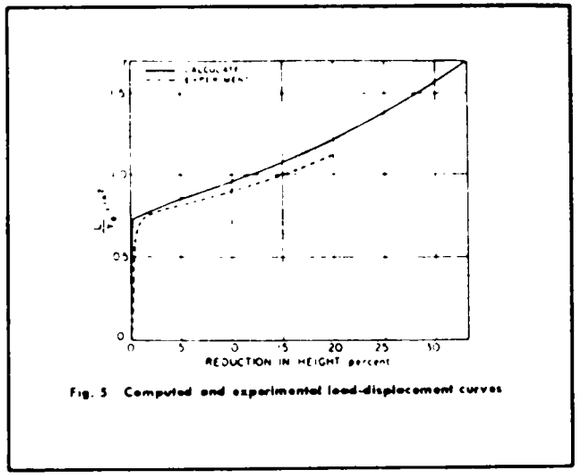

Fig. 5 Computed and experimental load-displacement curves

Figure 1.9

Slip-line field and experimental load-displacement curves.

After Lee and Kobayashi (1971).

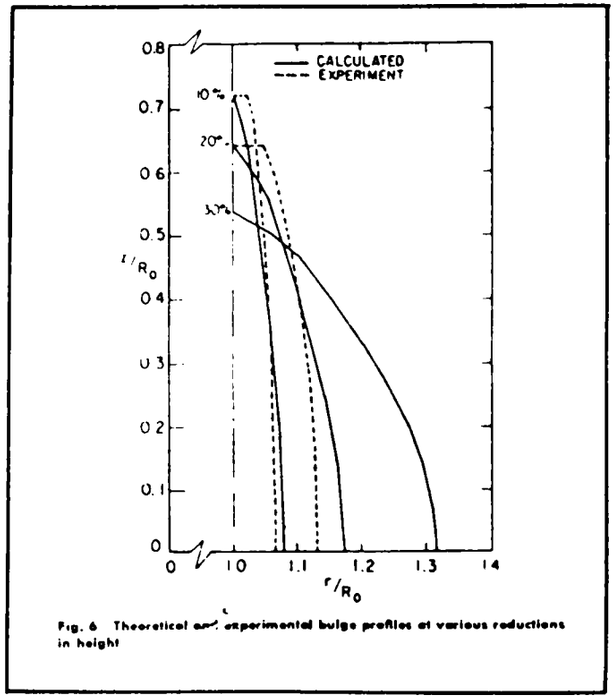

Fig. 6 Theoretical and experimental bulge profiles at various reductions in height

Figure 1.10

Slip-line field and experimental bulge profiles.

After Lee and Kobayashi (1971)

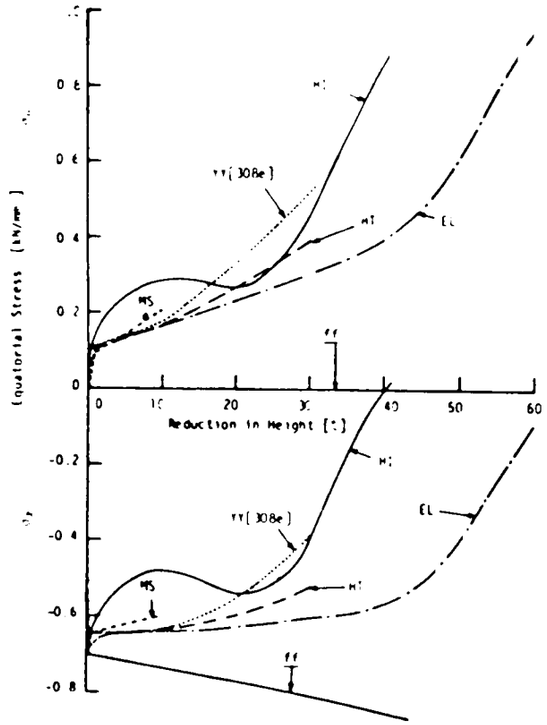

Figure 1.11

Comparison of predicted equatorial stresses.

After Kudo and Matsubara (1978)

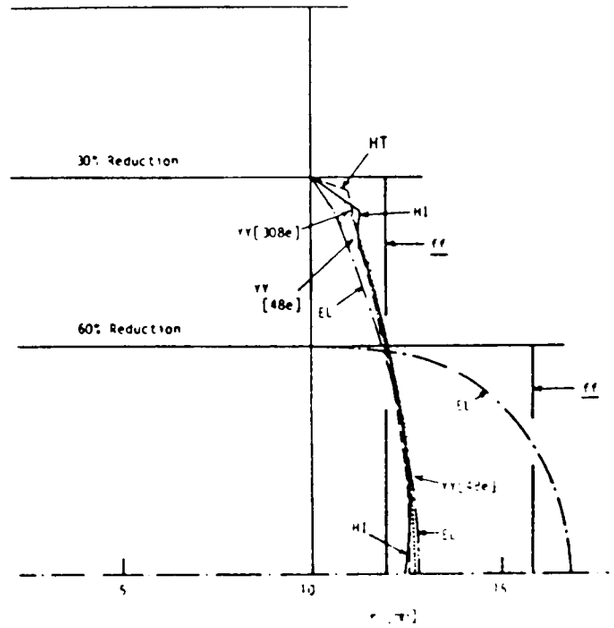

Figure 1.12

Comparison of predicted profiles in upsetting.

After Kudo and Matsubara (1978).

the major contributor to the dissimilarity of the results. Increment size was also thought to be significant. In agreement with Lee and Kobayashi (1971) it was thought that a finer mesh would have helped the originally free surface to roll into contact with the die. The differences obtained in this study emphasise the need for adequate comparison with experiment in order to validate any finite-element formulation. Such a comparison was not made here, it is therefore not possible to express the order of merit of the various approaches.

Hartley, Sturgess and Rowe (1980) considered the influence of friction on the finite-element predictions of simple upsetting. The technique used to model frictional restraint was based on the use of the interface shear factor, not relying on an experimental test to give the correct surface displacement for each individual operation. Figure 1.13 shows the predicted internal metal flow after 50% reduction in height for six different levels of the interface shear factor, m. Experimental and finite-element comparison for the hardness distribution were presented for low friction (m=0.1) and high friction (m=0.7). These results are reproduced in figure 1.14. This correlation demonstrates that, in two dimensions, it is possible to produce a fully predictive friction technique, not previously achieved by other investigators.

1.4.3 Axisymmetric extrusion.

Iwata, Osakada and Fujino (1972) performed an analysis of axisymmetric extrusion using an elastic-plastic finite-element formulation. This paper is a very good example of the range of output data possible in such an investigation. Figure 1.15 shows the effect of the coefficient of friction on the spread of the plastic zone in axisymmetric extrusion; figure 1.16 the distribution of stresses in the axial, tangential and radial directions; figure 1.17 the effective

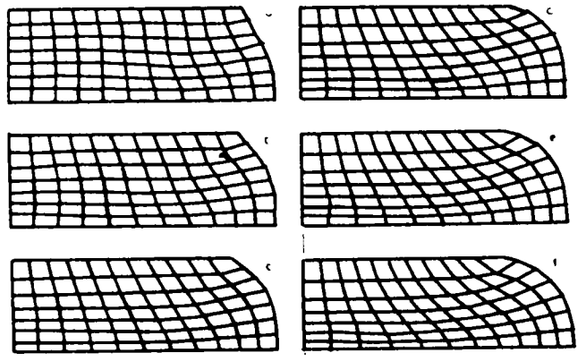

Fig. 3

FIG. 3. Predicted internal metal flow indicated by distortion of initial grid at 50% deformation. A number of grid lines are omitted for clarity. (a) Shows the deformation for an interface shear factor $m = 0.05$ (b) $m = 0.1$ (c) $m = 0.2$ (d) $m = 0.3$ (e) $m = 0.5$ (f) $m = 0.7$.

Figure 1.13

Effect of friction in upsetting.

After Hartley et al (1980).

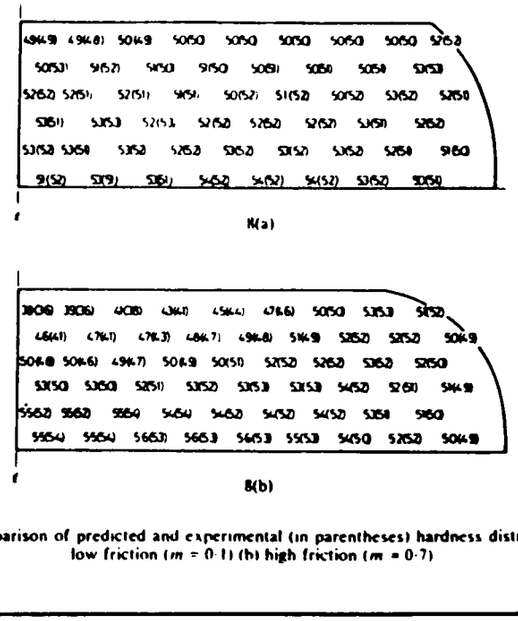

FIG. 8. Comparison of predicted and experimental (in parentheses) hardness distributions (a) low friction ($m = 0.1$) (b) high friction ($m = 0.7$)

Figure 1.14

Hardness distributions in upsetting.

After Hartley et al (1980).

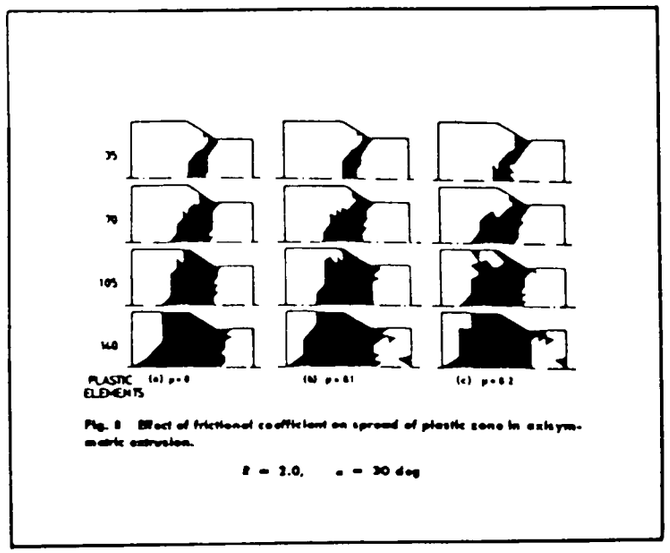

Fig. 8 Effect of frictional coefficient on spread of plastic zone in axisymmetric extrusion.

$R = 2.0, \quad \alpha = 30$ deg

Figure 1.15

Plastic zone development in extrusion.

After Iwata et al (1972)

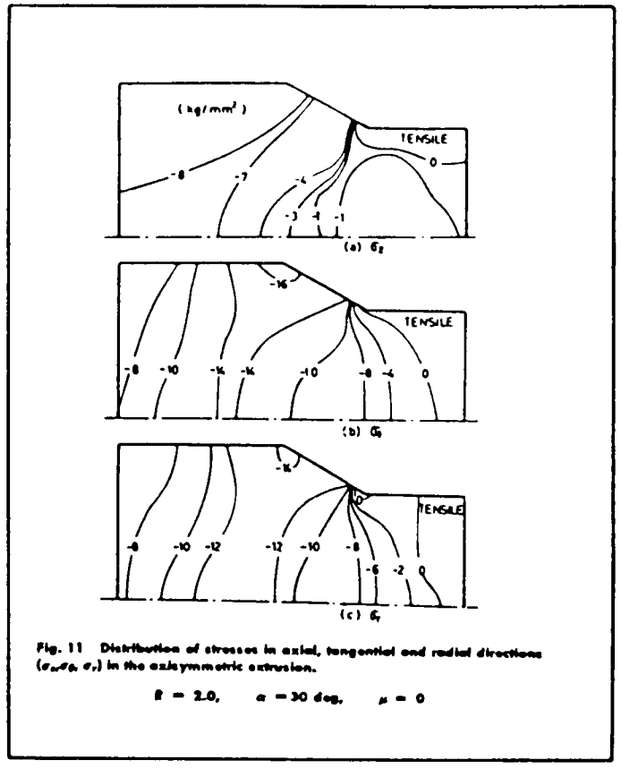

Fig. 11 Distribution of stresses in axial, tangential and radial directions ($\sigma_z, \sigma_\theta, \sigma_r$) in the axisymmetric extrusion.

$R = 2.0, \quad \alpha = 30$ deg, $\quad \mu = 0$

Figure 1.16

Stress distribution in extrusion.

After Iwata et al (1972)

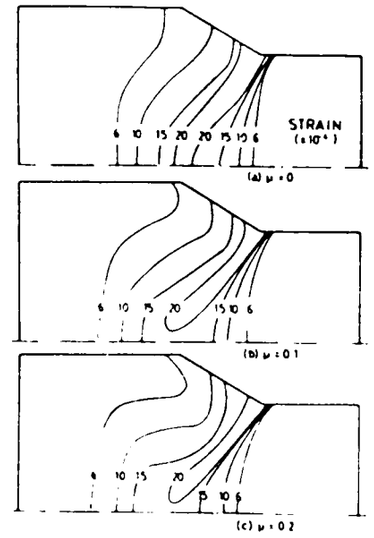

Fig. 10 Effective strain distribution of axisymmetric extrusion for three frictional conditions

R = 2.0, α = 30 deg, x/W ≃ 0.00013

Figure 1.17

Effective strain distribution in extrusion.

After Iwata et al (1972)

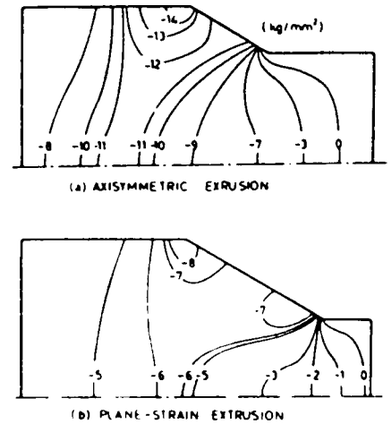

Fig. 13 Comparison of hydrostatic stress distribution between axisymmetric extrusion and plane-strain extrusion.

R = 2.0, α = 30 deg, μ = 0, ρ = 8.5 kg/mm³

Figure 1.18

Hydrostatic stress distribution in extrusion.

After Iwata et al (1972)

strain distribution for three frictional conditions, and figure 1.18 a comparison of the hydrostatic stress distribution between axisymmetric and plane-strain extrusion.

Figure 1.19 presents a comparison of the axial stress distribution in plane-strain extrusion from slip-line field theory and finite-element theory. Obviously this comparison cannot be made for axisymmetric extrusion where slip-line field theory does not apply. Quantitative agreement is apparent, although the slip-line field solution does not take work hardening into account. An important advantage of the finite-element method is that it can calculate stresses in the region that the slip-line technique assumes rigid. The finite-element solution reveals that a large tensile stress is situated behind the die exit and a smaller tensile stress near the centre of the specimen. Similarly placed tensile stresses have been found by Lee, Iwasaki and Kobayashi (1973) in their finite-element treatment of axisymmetric extrusion. These tensile stresses are very important in the determination of residual stresses, and may be important in the analysis of fracture initiation sites in extrusion.

Hartley, Sturgess and Rowe (1978) performed a finite-element analysis of backward extrusion using an elastic-plastic formulation. The plastic zone development shown in figure 1.20 was obtained. The internal metal flow was found to show good correlation with experimental results.

The finite-element analyses which have been mentioned so far in this section were formulated to allow the calculation of both elastic and plastic deformation. However, a second type of finite-element method, the rigid-plastic, or matrix, method neglects any elastic deformation. Shah and Kobayashi (1976) used this approach in the analysis of steady state axisymmetric extrusion. Figure 1.21 shows their

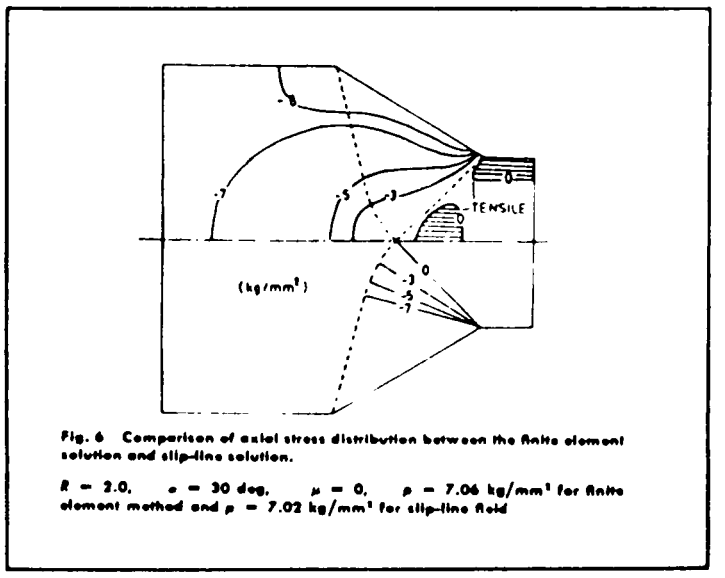

Fig. 6 Comparison of axial stress distribution between the finite element solution and slip-line solution.

R = 2.0, α = 30 deg, μ = 0, p = 7.06 kg/mm² for finite element method and p = 7.02 kg/mm² for slip-line field

Figure 1.19

Comparison of axial stress distribution.

After Iwata et al (1972)

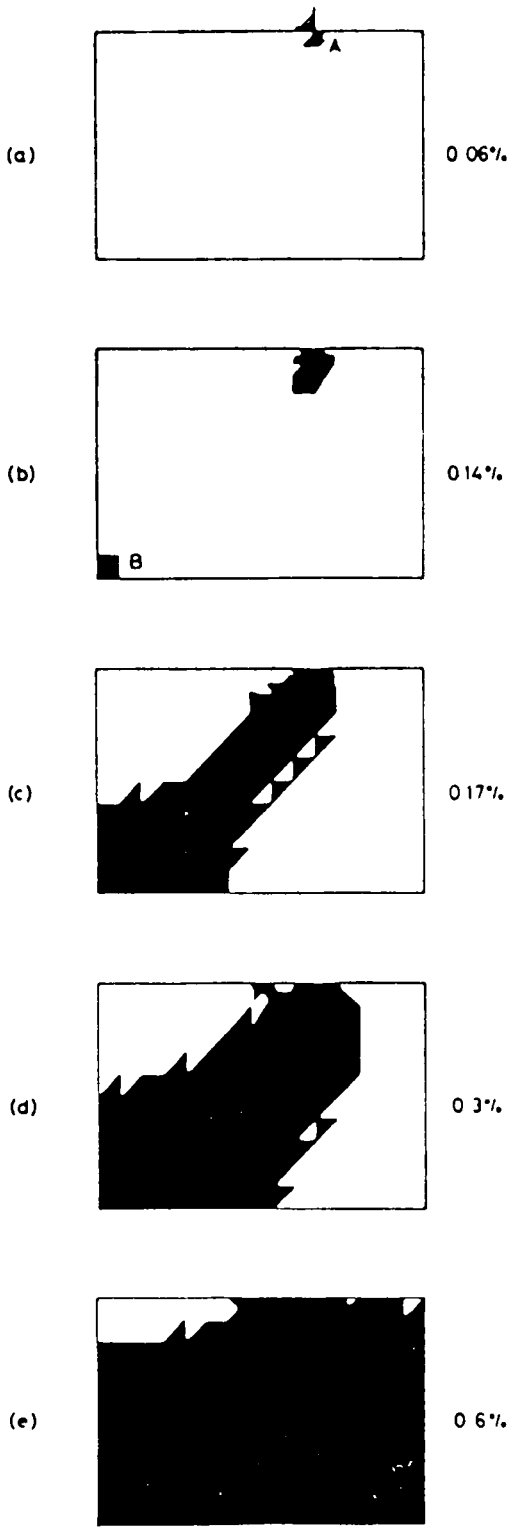

Figure 1.20

Plastic zones in extrusion.

After Hartley et al (1978).

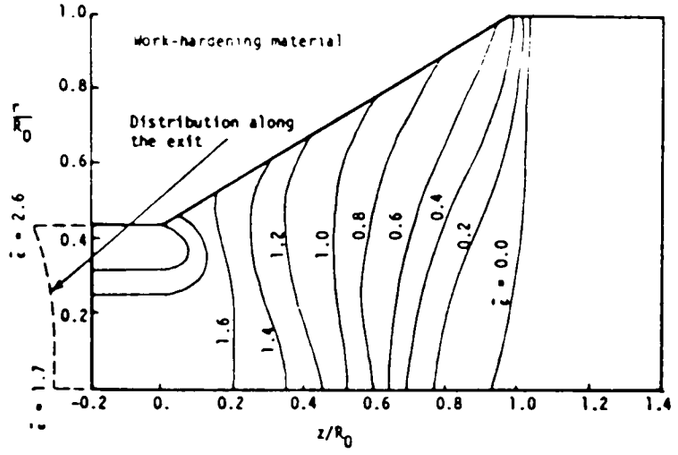

Figure 1.21

Effective strain distributions in steady-state axisymmetric extrusion.

After Shah and Kobayashi (1976).

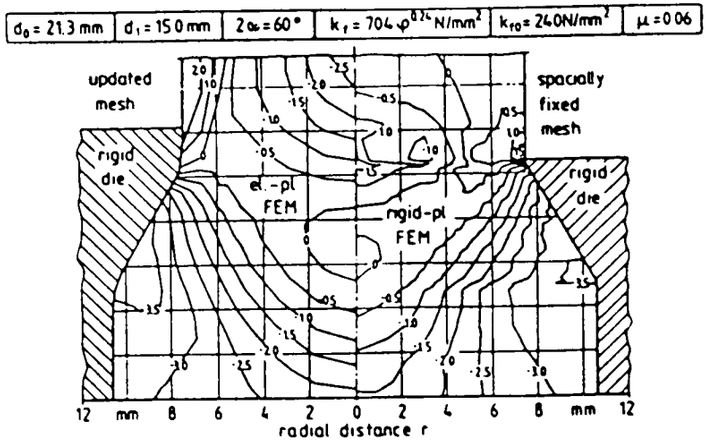

Normalized axial stresses for rod-extrusion with 50% area reduction.

Figure 1.22

Axial stress distribution in extrusion from elastic-plastic and rigid-plastic finite-element theory

After Tekkaya and Roll (1984).

calculated effective strain distributions.

Tekkaya and Roll (1984) recently examined axisymmetric extrusion using both elastic-plastic and rigid-plastic finite-element techniques. Figure 1.22 shows their normalised axial stress distributions plotted, on the left hand side of the diagram, for the elastic-plastic finite-element method, and, on the right hand side of the diagram, from rigid-plastic finite-element theory. Stresses below the conical portion of the die are in good agreement. However, at the exit region there is very poor agreement between the two solutions. This is because some elastic springback occurs in this region and hence the axial stress values computed by the rigid-plastic technique are therefore unreliable. As it is not known what contribution elastic springback makes to fracture initiation in extrusion it is important that the finite-element technique employed is an elastic-plastic formulation, as in the work presented in this thesis.

1.5 Conclusions.

This chapter has reviewed the analytical and numerical methods that could in principle be useful in solving the specific metalforming problems in this thesis. Upper bound theory was originally used for load determination but may be used, with limited accuracy, for flow field determination. Slip-line field theory finds the directions of maximum shear stress, and therefore the directions of instantaneous plastic flow, but is restricted to plane-strain deformation. In order to obtain a complete flow field the slip-line field has to be found at each level of deformation.

The capabilities of the finite-element method make it the most useful of those available for this study of fracture initiation in cold forging. Realistic material properties and their variation with processing

conditions can be incorporated. Detailed stress and strain values can be made available throughout the deformation process. However, its fundamental advantage over upper bound and slip-line field theory is in its applicability to three dimensional geometries.

Chapter 2.

Fracture in metalforming.

2.1 Introduction.

The aim of this part of the literature survey is to select ductile fracture criteria which are compatible with the output of a continuum finite-element analysis and which can be used to make fracture site predictions in the metalforming operations considered later in this thesis.

The group of ductile fracture criteria which are broadly suitable are those which do not contain variables of a highly metallurgical nature but are based on values of stress and strain and their variation.

Comparatively little work has been done on ductile fracture because of its complexity. The fracture criteria which have been developed are usually geometry and, sometimes additionally, material specific. Many problems are encountered in experimentally characterising the loading history to fracture. Surface cracks and tool-workpiece cracks may be identified by visual inspection, but it is obviously much more difficult to locate internal cracks before these have led to catastrophic failure of the workpiece.

There are, therefore, many possible advantages to be gained from using the output of a continuum finite-element analysis in attempting to formulate a ductile fracture criterion that can be applied to a wide variety of metalforming operations.

Section 2.2 of this chapter presents the previously published ductile fracture criteria which may be of interest. These are sub-divided into two categories: void growth models in section 2.2.1 and empirical and semi-empirical theories in section 2.2.2. Section 2.3 examines the published results from fracture experiments in the specific geometries to be considered later in this thesis. Section 2.3.1 refers to fracture in plane-strain side-pressing, section 2.3.2 to fracture in simple

upsetting and section 2.3.3 to fracture in extrusion. Finally, section 2.4 presents the conclusions of this chapter.

2.2.1 Void growth models.

Ductile fracture has been widely studied as a process of void nucleation, growth and subsequent coalescence. Voids may be created at inclusions and second phase particles (as shown by, for example, Argon (1975) and Goods and Brown (1979)) and may occur by cracking of the particles or debonding at the particle matrix interface. This process of void creation and growth leading to ductile fracture may be interpreted as one of progressive damage. A characteristic amount of damage may be accumulated over the plastic strain path until a critical value associated with fracture is reached. This critical value would be dependent upon the material, its heat treatment and such parameters at the hardness, quantity and distribution of inclusions and second phase particles. It would be independent of the geometry of the workpiece and its loading mode.

McClintock, Kaplan and Berg (1966) derived approximate equations for the deformation of holes in shear bands. In this two dimensional model large numbers of equi-spaced, equal sized cylindrical holes are assumed to be located uniformly throughout the material. The material is assumed to be divided into a number of regular elements, each containing a single centrally located hole. Since the spacings between the holes are usually considerably greater than the hole diameter over much of the strain to fracture, the motion of each hole is calculated as if the hole lay in an semi-infinite body. The calculations eventually predict that the holes meet the boundaries of their elements, at which point fracture is assumed to occur. From this two modes of fracture are predicted, depending on which boundary of the element (as shown in figure 2.1) the edge of the hole touches. This process of hole growth may be interpreted as one of progressive damage, where increasing plastic strain results in an increasingly disordered material.

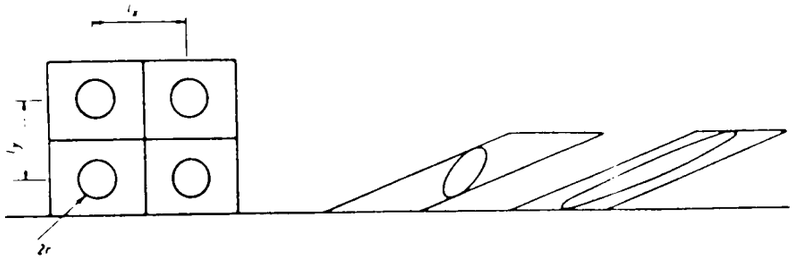

Figure 2.1

McClintock model of void growth in a shear stress field.

After Atkins and Mai (1985).

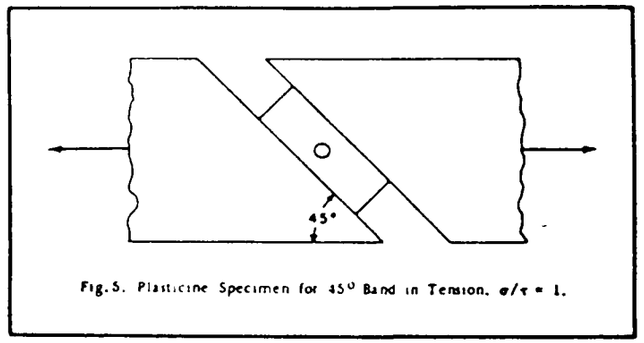

Fig. 5. Plasticine Specimen for 45° Band in Tension, $\sigma/\tau = 1$.

Figure 2.2

Grooved plasticine test specimen.

After McClintock et al (1966)

The following hole growth damage functions were derived to quantify this disorder:

(a) For hole growth in the longitudinal direction of the shear band:

$$D_L = \ln F_L = \ln\sqrt{(1+\gamma^2)} + \frac{\gamma}{2(1-n)} \sinh(1-n)\,\frac{\sigma_H}{\tau} \qquad (2.1)$$

and (b) For hole growth in the thickness direction of the shear band:

$$D_T = \ln F_T = \frac{\gamma}{2(1-n)} \sinh(1-n)\,\frac{\sigma_H}{\tau} \qquad (2.2)$$

where

D = hole growth damage parameter,

F = hole growth factor,

γ = shear strain,

n = work hardening exponent,

σ_H = induced hydrostatic stress.

The hole growth damage parameter is required to reach a critical value for fracture to occur. In this way, ductile fracture is treated as an accumulation of damage, and is dependent on the entire history of stress and strain.

Two simple experiments were performed to validate the theory, both using plasticine as the model material. As a test of hole growth in pure shear (σ/τ=0) a plasticine cylinder with a small transverse circular hole was twisted. The measured shear strain and orientation of the hole at closure of the only experimental result quoted agrees well with that predicted by theory.

The second test consisted of pulling a grooved plasticine bar, as shown

in figure 2.2. The results agree very well with theory except for very large holes which were found to grow more rapidly than predicted. This may be due to the breakdown of one of the assumptions on which the model is based. In the derivation of the hole growth functions it is assumed that the hole diameter is small when compared with the interhole spacing. However, it may be that the hole diameter becomes too large in this test for this assumption to remain valid.

This model of void growth under shear loading was extended by McClintock (1968) to apply to the growth and coalescence of preexisting holes in plastically deforming materials for various ratios of the principal components of stress. Referring to figure 2.3 the following hole growth damage functions were derived:

$$\ln(l_y/2r) = \int_0^{\epsilon_f} \left(\frac{\sqrt{3}}{2(1-n)} \sinh\left\{ \frac{\sqrt{3}(1-n)}{2} \frac{(\sigma_x - \sigma_y)}{\bar{\sigma}} \right\} + \frac{3}{4} \frac{(\sigma_x - \sigma_y)}{\bar{\sigma}} \right) d\bar{\epsilon} \qquad (2.3)$$

where

l_y is the original spacing of the holes along the y-axis, and n is the work hardening exponent.

There are two other equations for the coalescence of holes with their axes parallel to the y- and z- axes, obtained by swapping the suffices correspondingly.

A similar approach to void growth and coalescence has been taken by Rice and Tracey (1969). They considered the growth of a spherical void in a general remote stress field. The results suggest a rapidly decreasing fracture ductility with increasing hydrostatic tension.

Oyane and co-workers (1972,1980) formulated certain criteria for the ductile fracture of pore-free and pore-containing materials. Based on the principle that the volumetric strain (or density) decreases due to void growth, it is postulated that when a critical material-dependent

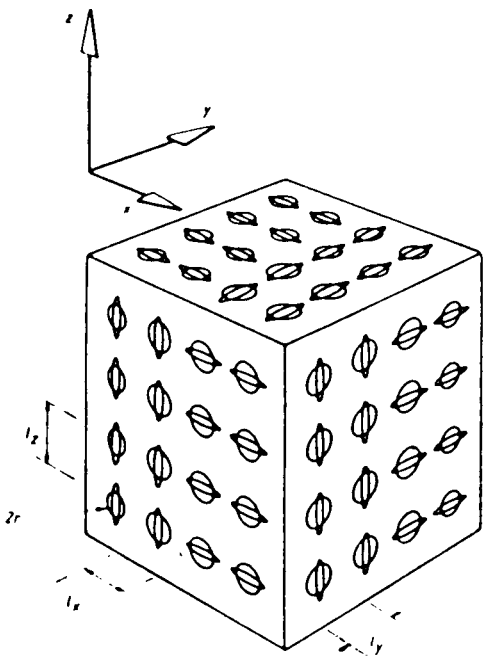

Figure 2.3

McClintock model of void growth in a normal stress field.

After Atkins and Mai (1985).

volumetric strain is reached the material fractures. This criterion may be written in the following form for initially pore-free materials:

$$\int_0^{\bar{\epsilon}_f} \left(1 + \frac{\sigma_H}{A\bar{\sigma}} \right) d\bar{\epsilon} = G \qquad (2.4)$$

where G is a material constant and is given by

$$G = \int_0^{\epsilon_{Vf}} f^2 \rho^{2n-1} \, d\epsilon_V \qquad (2.5)$$

where

f = a function of the relative density (defined by the ratio of the apparent density of the porous material to the density of its pore free matrix);

A = material constant;

ϵ_V = volumetric strain;

ϵ_{Vf} = volumetric strain at fracture.

ρ density

The density dependence of both these functions was slightly modified in the form of this fracture criterion relating to initially pore-containing materials. A method for estimating the values of the constants required using compression test results was provided.

In addition to many studies of bulk forming, the void growth and coalescence model has also been applied to the fracture of sheet materials. Ghosh (1976) proposed a fracture criterion based on the shear joining of voids in the stretch forming of sheet materials, as illustrated in figure 2.4.

This is given by:

$$k_f \left(1 + \frac{\sigma_2}{\sigma_1} \right) \sigma_1^2 \qquad (2.6)$$

where σ_1 and σ_2 are principal stresses and k_f is a material constant

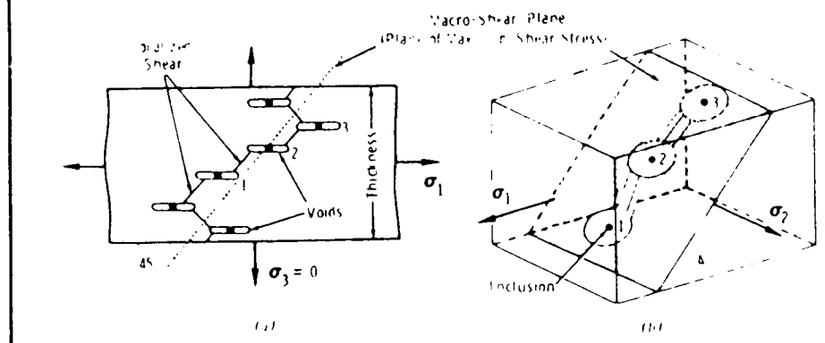

Fig. 2— Two schematic views of the process of shear-joining of growing voids in sheets, on the maximum shear stress plane normally occurring along the direction of greatest slope (*a*) between voids 2 and 3, and occasionally at small angles to it (voids 1 and 2).

Figure 2.4

Shear joining of voids.

After Ghosh (1976).

found from the results of a simple sheet tension test. (The expression for this constant is rather long and therefore has not been reproduced here.) This constant contains the information regarding the role of inclusions in the material, but without detailed metallographic analysis. Biaxial fracture limits produced using this criterion are in reasonable agreement for brass, aluminium and some steels.

The parameters required to calculate numerical values for the fracture criteria presented here are compatible with the output of a continuum finite-element analysis and can therefore be used to make fracture site predictions in the metalforming operations to be considered in this thesis.

2.2.2 Empirical and semi-empirical theories.

This section reviews some of the empirical and semi-empirical theories that have been developed to model ductile fracture. Like the void growth criteria, many of these criteria are accumulated over the plastic strain path until a critical value associated with fracture is reached. Most of the continuum models presented in this section may be useful in the type of study undertaken in this thesis as they can be evaluated without a highly detailed knowledge of the microstructure of the material.

In 1950 Freudenthal postulated that the energy to fracture is the critical parameter. This suggests that the work done reaches a critical value at fracture. Mathematically, this may be expressed as:

$$\int_0^{\bar{\epsilon}_f} \bar{\sigma}\, d\bar{\epsilon} = C1 \qquad (2.7)$$

where

$\bar{\sigma}$ = equivalent stress,

$d\bar{\epsilon}$ = equivalent strain increment,

$\bar{\epsilon}_f$ = equivalent strain at fracture,

C1 = constant for a given material, temperature and strain rate.

Gillemot (1976) used this criterion in an investigation of brittle fracture in 0.35% carbon steel. In tension, compression and low cycle fatigue tests a crack appeared after a characteristic amount of energy had been absorbed.

The validity of this generalised plastic work fracture criterion was also assessed by Cockroft and Latham (1966,1968). They used tensile test

specimens of EN2A mild steel (0.085%C,0.05%Si,0.03%S,0.013%P,0.45%Mn) which showed a well defined neck at fracture. However, at this stage, a correction, such as that proposed by Bridgman (1944) or Davidenkov and Spiridova (1946), was not made to the axial stress to allow for the triaxial nature of the stress system at fracture. The measured axial stress was assumed to be that which led to separation of the material under uniaxial conditions. Cockroft and Latham then chose to modify the work criterion explicitly for the effect of the peak tensile stress in the necked region, rather than implicitly by using the corrected value of axial stress. Thus, the modified equation now assumed the following form:

$$\int_0^{\bar{\epsilon}_f} \sigma^* \, d\bar{\epsilon} = C2 \qquad (2.8)$$

where

C2 is a constant for a given material, temperature and strain rate.

This criterion was validated using further experimental work in which the tensile test specimens were remachined after appropriate amounts of deformation to avoid the development of a significant neck. From these experiments Cockroft and Latham concluded that the integral of tensile plastic work per unit volume must reach a critical, material dependent, value for fracture to occur. Following the way in which this modified criterion has been developed, it would be expected to agree with the original plastic work criterion if, in this latter case, the axial stress had been corrected for the effects of necking. Thus it appears that the tensile plastic work criterion developed by Cockroft and Latham is a special case of the generalised plastic work to fracture relationship and would be expected to apply in operations where the stress system is predominantly tensile. For general applications the generalised plastic work to fracture criterion appears to be the more

suitable.

This generalised plastic work to fracture criterion may be interpreted as a critical value of generalised plastic strain at fracture as the level of generalised stress is dependent upon that of generalised plastic strain.

Brozzo, DeLuca and Rendina (1972) proposed an empirical modification to Cockroft and Latham's fracture criterion as it predicted generalised strains at fracture which were too low when compared with experimental results for sheet forming. This led to the following criterion:

$$\int_0^{\bar{\epsilon}_f} \frac{2\sigma_1}{3(\sigma_1 - \sigma_H)}\, d\bar{\epsilon} = W^* \qquad (2.9)$$

where

σ_H = hydrostatic stress and W^* is a constant for a given material, temperature and strain rate.

The integral must reach a critical value, in this case dimensionless, for fracture to occur. This critical value was estimated from the results of a tensile test on a notched specimen. This criterion was used to predict fracture strains in bulge tests on three low carbon deep drawing steels. Good correlation between theory and experiment was found if the material was equally ductile in all directions in the plane.

Oh and Kobayashi (1976) and Oh, Chen and Kobayashi (1979) used a modification to Cockroft and Latham's criterion of a form originally suggested by Latham and Cockroft (1966). They considered that the ratio of the maximum tensile stress with the generalised stress is the important parameter in ductile fracture, as expressed mathematically in the following way:

$$\int_0^{\bar{\epsilon}_f} \left(\frac{\sigma_1}{\bar{\sigma}}\right) d\bar{\epsilon} = \text{Constant} \qquad (2.10)$$

Although the authors report that their results were inconclusive, Kobayashi and co-workers were the first research group to use the output of a finite-element analysis in ductile fracture prediction and therefore demonstrate the potential of such an approach.

Norris, Reaugh, Moran and Quinones (1978) developed the following fracture criterion:

$$\int_0^{\bar{\epsilon}_f} \frac{1}{(1 - c\sigma_H)} \, d\bar{\epsilon} = c \qquad (2.11)$$

where c is a material constant.

This was arrived at using both experimental results and results of a finite-difference computer program for several tensile test geometries including a simple axisymmetric tensile test and a Charpy V-notch specimen.

Atkins (1981) modified the criterion of Norris et al (1978) to agree with experimental results obtained from sheet metal working. This led to the following criterion:

$$\int_0^{\bar{\epsilon}_f} \frac{(1 + 1/2L)}{(1 - c\sigma_H)} \, d\bar{\epsilon} = \text{Constant} \qquad (2.12)$$

where L is the strain ratio $d\epsilon_1 / d\epsilon_2$

This modification was made as it was found in some tests that at the instant of fracture the current hydrostatic stress state was most tensile for the greatest strains to fracture. This is in contradiction to the established inverse relationship between hydrostatic stress and strain to fracture (See, for example, Hancock and Mackenzie (1976) and Goods and Brown (1979)). Therefore, in order to produce a correct prediction a path dependency term was included in the damage integral.

As previously found for the void growth models presented in section

2.2.1 the parameters required to calculate numerical values for the fracture criteria presented here are compatible with the output of a continuum finite-element analysis and can therefore be used to make fracture site predictions in the metalforming operations to be considered in this thesis.

2.3 Fracture in specific geometries.

2.3.1 Fracture in plane-strain side-pressing.

Only one previous study of fracture in plane-strain side-pressing has been found in the literature, although several deformation studies have been previously reported in sections 1.2.1 and 1.4.1.

In this fracture study, Jain and Kobayashi (1970) examined the side-pressing of 7075 aluminium alloy. Using high speed photography, an attempt was made to record the initiation of fracture and subsequent crack growth.

Unfortunately, the camera speed of 120 frames per second proved inadequate to record the site of fracture initiation. The behaviour of specimens of initially circular cross section and specimens with machined flats of the initial geometry shown in figure 2.5 was studied. In all cases the fractures appear qualitatively to follow the lines of maximum shear stress calculated in the slip-line field analyses (see figure 1.2).

Figure 2.6 shows the grid patterns at various stages during the side-pressing of an initially circular section rod with rough dies. Localised deformation bands have formed diagonally across the specimen and the fracture pattern appears to follow this high shear zone. Fracture in plane-strain side-pressing is further examined in Chapter 4 of this thesis.

2.3.2 Fracture in simple upsetting.

The experimental observations examined in this section may help to build up an overall picture of the phenomenon of ductile fracture, not merely in the specific case of fracture on the free surface of an upset specimen.

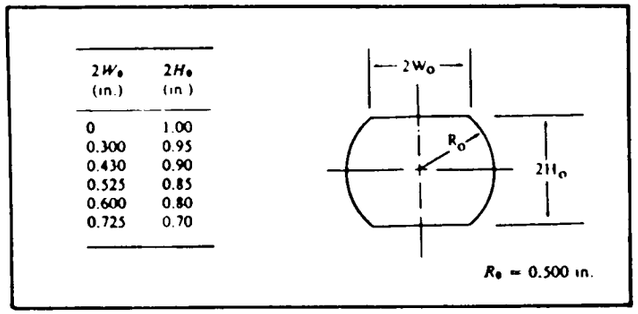

Figure 2.5 Initial geometry of plane strain side pressing specimens.

After Jain & Kobayashi (1970)

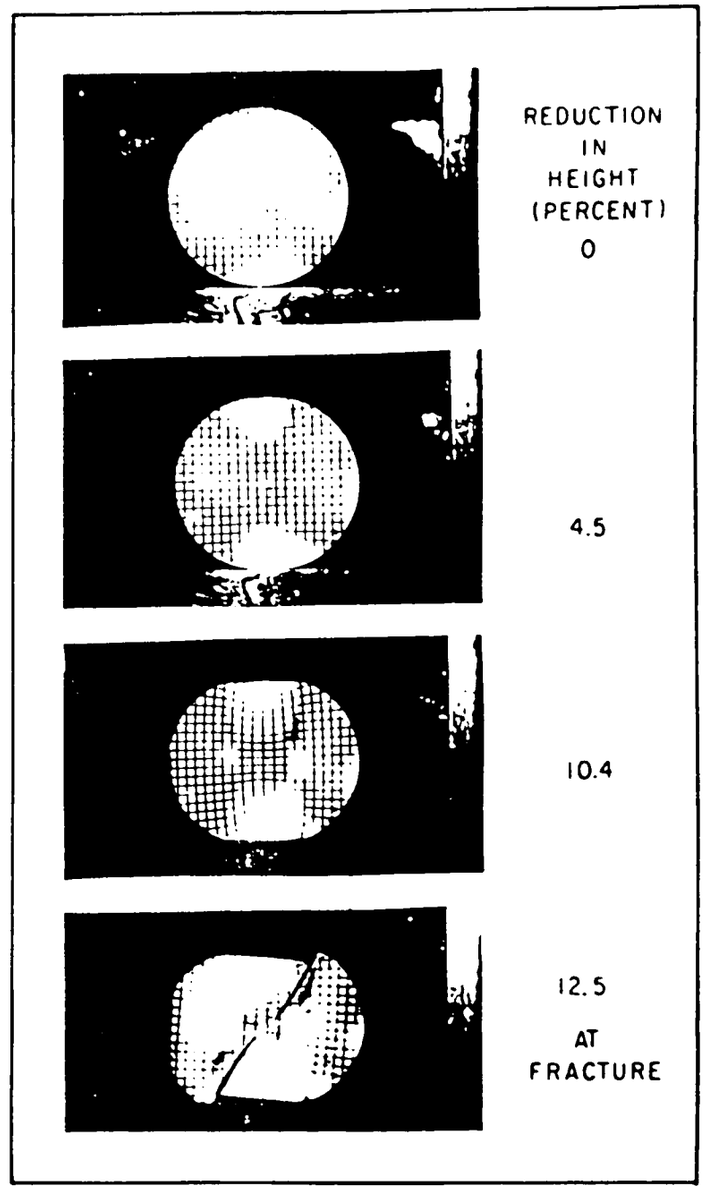

FIGURE 2.6 Grid patterns at various stages during side pressing of a circular cylindrical bar with rough dies.

After Jain & Kobayashi (1970)

In the absence of a technique capable of producing a full analytical solution, one approach to ductile fracture in simple upsetting has been to accumulate experimental data on the surface strain development leading up to fracture. Most notably this approach has been taken by Kudo and Aoi (1967). By varying the loading paths to fracture achieved using a range of height to diameter ratios and interface friction conditions, they found that an approximately linear relationship existed between the equatorial tensile and compressive surface strains at fracture.

This surface strain fracture locus was described by the following equation:-

$$\epsilon_{\theta f} = a_{ps} - \epsilon_{zf}/2 \qquad (2.13)$$

where

$\epsilon_{\theta f}$ = circumferential fracture strain

ϵ_{zf} = axial fracture strain

a_{ps} = plane strain fracture strain.

This gives an approximately linear locus of fracture strains with a slope of -1/2 and a material dependent intercept a_{ps}, as shown in figure 2.7. This relationship is described as approximately linear as some points fall above it and some fall below. However, the relationship does seem to hold, irrespective of the types of cracks which occur. Two types of cracks were identified by Kudo and Aoi, and are illustrated in figure 2.8. The first type is designated Mode I. Here, the stresses local to the fracture site are compressive in the axial direction and tensile in the circumferential direction. The plane of the crack directions appear to follow the maximum shear stress, which is located

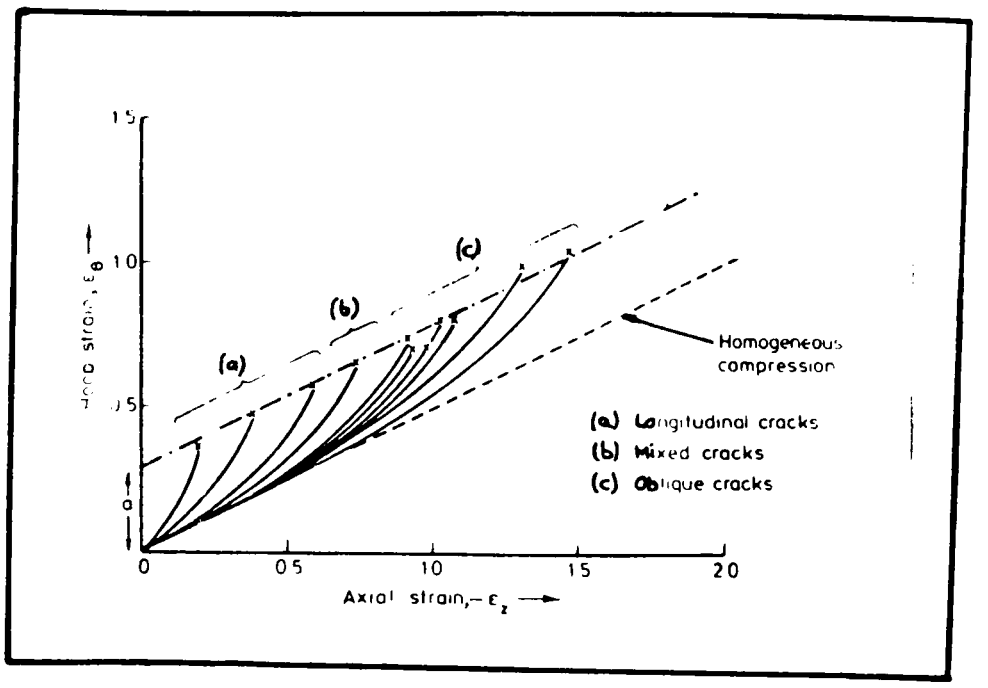

FIGURE 2.7 Straight line fracture condition observed by Kudo & Aoi (1967).

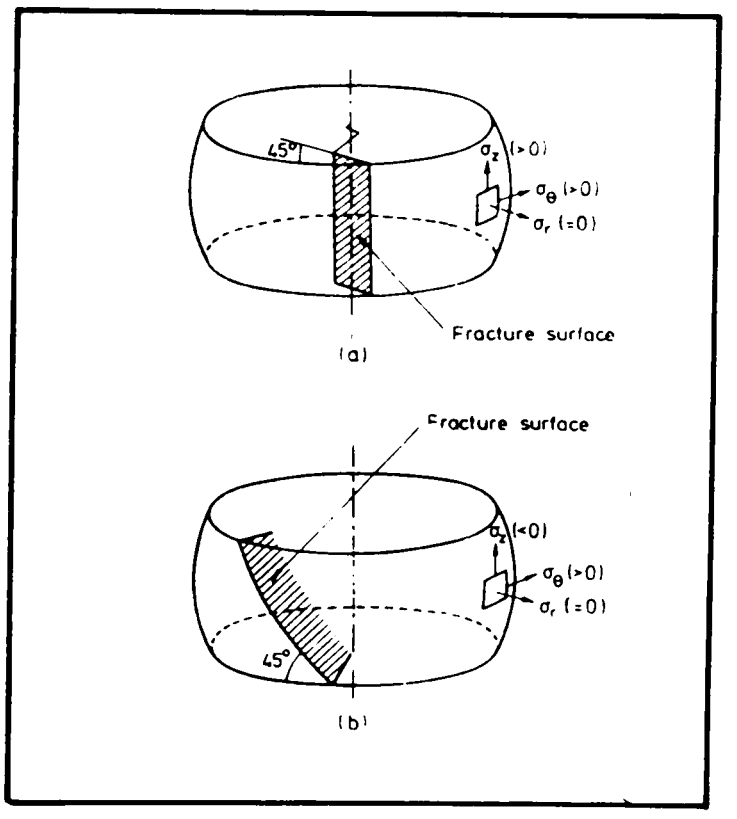

FIGURE 2.8 The two planes of fracture on the surface of an upset cylinder

After Kudo & Aoi (1967)

at 45^{o} in the z-theta plane, extending radially, in a zig-zag manner, into the cylinder. Mode I cracks occur when barrelling is slight, that is under conditions of good lubrication and low aspect ratio.

When barrelling is severe, Mode II cracking occurs. As illustrated in Figure 2.8(b), the axial stress local to the fracture site can become tensile. With tensile circumferential stress and zero radial stress, this gives vertical planes of maximum shear stress located at 45^{o} to the radial direction. Again, experimentally, cracks are found on these maximum shear stress planes. Both types of cracks appeared for specimens whose strain variations fell into the boundary region between the two modes of fracturing. Kivivuori and Sulonen (1978) observed experimentally a mode of cracking which is essentially a shear crack where the direction of propagation has been reversed several times. Korhonen (1980) proposed a slip-line field model which may lead to fracture on a shear plane.

Kuhn and Lee (1971) made experimental measurements of localised surface strains during simple upsetting. These revealed the presence of a pertubation in the strain path, as shown in figure 2.9. Subsurface void formation was observed in specimens deformed beyond the reduction in height at which the perturbation occurs. Lee and Kuhn (1973) found that these same results agreed with Kudo and Aoi's surface strain fracture locus. Other studies have also found agreement with this fracture locus. Kuhn, Lee and Erturk (1973) analysed the experimental results for upsetting, bending, rolling and plane-strain tests. Oh and Kobayashi (1976) studied upsetting and rolling. Kuhn and Dieter (1977) examined upsetting and cold heading.

Using the same type of approach to the prediction of fracture initiation in cold forging as used in this thesis, Sowerby,

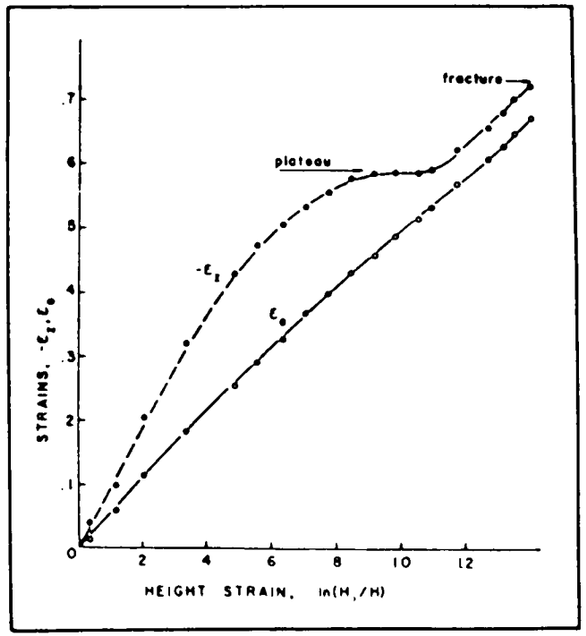

Figure 2.9 Perturbation in the strain path on the free surface of upset cylinders.

After Kuhn & Lee (1971)

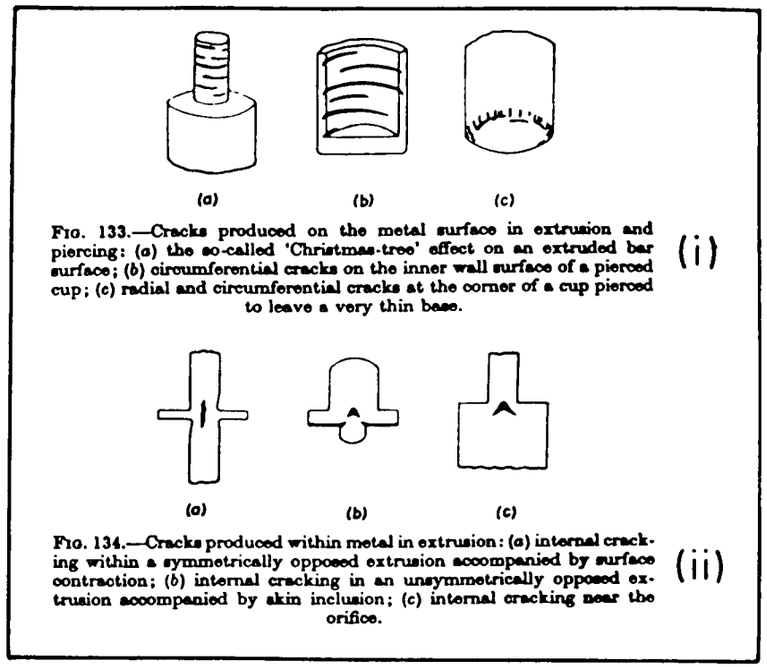

FIG. 133.—Cracks produced on the metal surface in extrusion and piercing: (*a*) the so-called 'Christmas-tree' effect on an extruded bar surface; (*b*) circumferential cracks on the inner wall surface of a pierced cup; (*c*) radial and circumferential cracks at the corner of a cup pierced to leave a very thin base. (i)

FIG. 134.—Cracks produced within metal in extrusion: (*a*) internal cracking within a symmetrically opposed extrusion accompanied by surface contraction; (*b*) internal cracking in an unsymmetrically opposed extrusion accompanied by skin inclusion; (*c*) internal cracking near the orifice. (ii)

Figure 2.10

Types of fracture in extrusion

(i) 'fir tree' or 'Christmas tree' effect

(ii) central bursting or chevron cracking.

After Johnson and Kudo (1962)

Chandrasekaran, Dung and Mahrenholtz (1985) investigated the prediction of damage accumulation during upsetting tests based on McClintock's model. A finite-element program was used to examine the stress and strain behavour of preselected elements. The accumulated damage as formulated by McClintock was found to be greatest near the surface of the model. The experimental fracture sites were not explicitly stated but would be expected to be surface fractures and therefore agree with the predicted site. No predictions of the level of the deformation at fracture were reported.

2.3.3 Fracture in extrusion.

Fracture in extrusion may be broadly classified into two categories; the so called 'fir tree' or 'christmas tree' effect where cracks are initiated on the surface of the extruded billet, and the chevron crack or central burst which is produced within the metal during extrusion. Figure 2.10 from Johnson and Kudo (1962) gives examples of these two general types of effect.

Avitzur (1968a,1968b) used upper bound theory to reach a criterion of fracture in extrusion based on the postulate that the flow pattern will always be that which minimizes the required energy. For a certain range of the main independent variables, that is reduction, die cone angle, friction and properties of the material, flow with a central burst requires the least amount of energy. As shown in figure 2.11 when zone III moves faster than zone I a central burst will appear. The upper bound theory used in this analysis assumes zero strain hardening and Avitzur (1968b) reports that a more precise accounting for material properties is required. Dodd and Kudo (1980) pointed out that an extra energy term needed to be included in the slip-line field to account for the new surfaces produced.

Iwata, Osakada and Fujino (1972) performed an analysis of hydrostatic extrusion by the finite-element method. Using the stress distribution given in figure 2.12 they suggested that surface cracks are caused by secondary tensile stresses behind the die exit and are affected by tensile residual stress on the surface of the extrudate.

Secondary tensile stresses at the site of fracture initiation have also been identified in upsetting (Kudo and Aoi (1967)).

Oh, Chen and Kobayashi (1979) also examined fracture in extrusion using

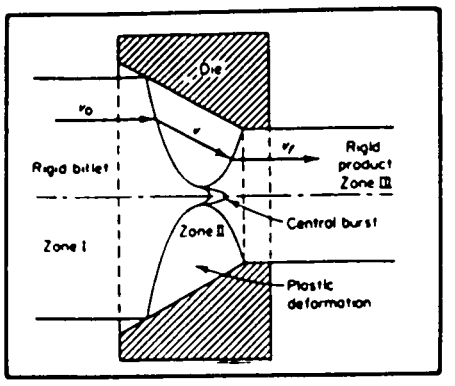

Figure 2.11

Postulated velocity field associated with central burst formation in extrusion.

After Avitzur (1968a)

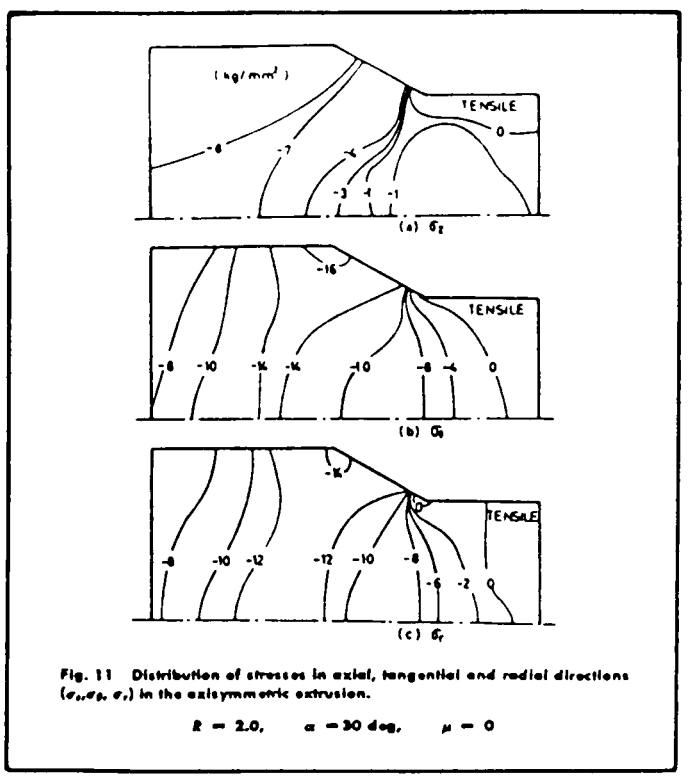

Figure 2.12

FE predicted stress distributions in hydrostatic extrusion.

After Iwata et al (1972)

finite-element generated stress and strain values. Unfortunately, they reported that their results were inconclusive.

In their finite-element treatment of axisymmetric extrusion for the calculation of residual stresses Lee, Iwasaki and Kobayashi (1973) found two zones where the axial stress is tensile. The first was along the free surface extended from the die exit, and the second in the central region of the workpiece near the die exit. However, no attempt was made by these authors to link these findings with possible fracture initiation sites although the importance of tensile stresses in fracture has been widely reported in the literature, for example by Alexander and Lengyel (1964) and Rogers and Coffin (1967).

Garner and Rice (1974) experimentally examined central burst formation during hydrostatic extrusion using a model wax to simulate metal flow. Grids were scribed on the specimen and viewed through an acrylic die. These authors report that the results obtained support Avitzur's contention that, in central burst formation, the extent of the plastic zone diminishes periodically so that it surrounds an inner rigid core, and thus the product will consist in part of material which has not been plastically deformed.

Shah and Kobayashi (1976) used rigid-plastic finite-element theory to examine frictionless axisymmetric extrusion. Stress and strain distributions were plotted to help in the understanding of central bursting. Lee and McMeeking (1978) re-examined Avitzur's theory that chevron cracking occurs when the force required to maintain the extrusion operation falls. By using lower bound theory (where a statically admissible stress field is constructed so that the stresses at each point in the material lie inside or on the yield surface) these authors calculated the flow field for a cracked workpiece. They suggested that the energy required to initiate and extend the crack must be included for a correct analysis.

2.4 Conclusions.

Based on the literature survey presented in this chapter ductile fracture criteria due to the following investigators have been found to be compatible with the output of a continuum finite-element analysis:

1. McClintock, Kaplan and Berg (1966);
2. McClintock (1968);
3. Oyane, Sato, Okimoto and Shima (1980);
4. Ghosh (1976);
5. Generalised plastic work;
6. Generalised plastic strain;
7. Cockroft and Latham (1968);
8. Brozzo, DeLuca and Rendina (1972);
9. Norris, Reaugh, Moran and Quinones (1978);
10. Atkins (1981).

These criteria will therefore be used in the investigation of fracture initiation in cold forging presented in this thesis.

Chapter 3.

Numerical analysis of forming and fracture initiation.

3.1 Introduction

This chapter provides the theoretical background and details of the approach used for the numerical analysis of forming and fracture as presented in this thesis. It is divided into two main parts. The first part, section 3.2, introduces the finite-element technique (section 3.2.1) and describes the use of finite-elements in plasticity (section 3.2.2), and the elastic-plastic finite-element program used and developed for large-deformation analysis, (section 3.2.3). The next subsection of this first part of the chapter, section 3.2.4, examines some of the computational techniques used to improve the accuracy of the solutions.

One of the basic aims of the work presented in this thesis, as has already been stated, is to use the stress and strain values, calculated for a particular deformation using the finite-element program in a continuum analysis of fracture initiation. This required the development of a post processing package for the assessment of various fracture criteria and this is described in section 3.3.

Section 3.3.1 describes the modifications which were made to the original finite-element program in order to output the data required in the correct format to be processed by the programs described in section 3.3.2. These programs calculate the numerical values of a variety of fracture criteria.

3.2 Metalforming analysis

3.2.1 The Finite-element method.

The finite-element method is a technique which breaks down a

large complicated stress analysis problem into a series of smaller less complicated problems to which an approximate solution may be more easily found.

Within this method the following procedure is adopted. First, the continuum is broken down into a number of discrete elements, appropriately shaped for the problem at hand. This choice is usually made with particular reference to the boundary shape. These elements may be of several types, such as triangles or quadrilaterals for two dimensional analysis or tetrahedra or 'bricks' for three dimensional analysis. The number of nodes and their arrangement in an element determines the order of the interpolating function used to approximate the unknown displacements within any element. Figure 3.1 illustrates three families of finite-elements and their nodal locations for linear, quadratic and cubic interpolating functions. This interpolating, or shape function, N_i, is defined such that it has the property of attaining the value of unity at node i, zero at all other nodes, and varies linearly (with respect to local coordinates) between any two adjacent nodes.

The assumed function for displacement takes the form

$$\underline{U} = [N_i]\ \underline{d}_i \qquad (3.1)$$

where

$$[N_i] = (N_1[I]\ N_2[I]\ \ldots.\ N_j[I]) \qquad (3.2)$$

and

$\underline{U}$ is the displacement vector;

j is the number of nodes per element;

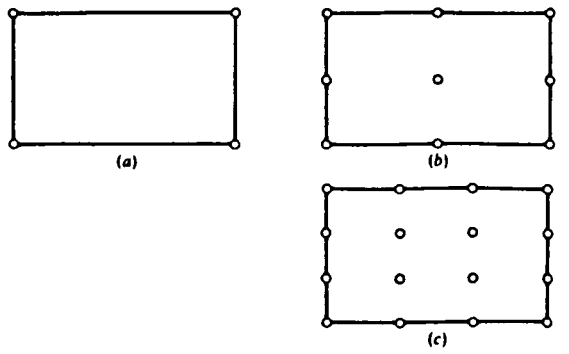

Fig. 7.6 Three elements of the Lagrange family (*a*) linear, (*b*) quadratic, and (*c*) cubic

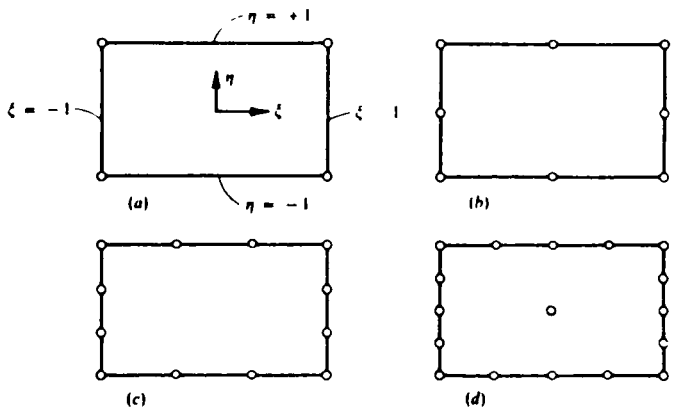

Fig. 7.8 Rectangles of boundary node (serendipity) family (*a*) linear, (*b*) Quadratic, (*c*) cubic, (*d*) quartic

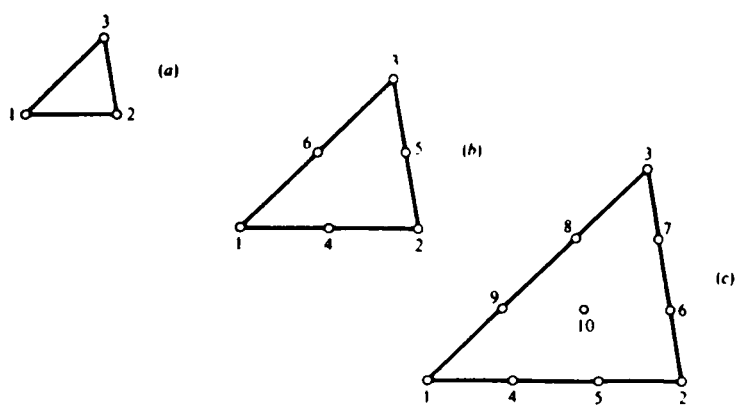

Fig. 7.15 Triangular element family (*a*) linear, (*b*) quadratic, and (*c*) cubic

Figure 3.1 A variety of finite elements.

After Zienkiewicz (1977)

[I] is the unit matrix;

$\underline{d}_i$ is the displacement vector of node i.

The remaining expressions in this chapter are written in terms of incremental values since this form is essential for non-linear forming analyses. An elastic analysis would normally be completed in one increment and for such cases the incremental symbol Δ could be omitted. Strain increments are defined by the equation

$$\Delta \underline{\epsilon} = [L] \ \underline{U} \tag{3.3}$$

where

$\Delta \underline{\epsilon}$ is the strain increment vector

[L] is the strain-displacement operator matrix.

Substituting the incremental form of equation (3.1) into equation (3.3) gives

$$\Delta \underline{\epsilon} = [\underline{B}_i] \ \underline{d}_i \tag{3.4}$$

where

$$[\underline{B}_i] = [L][N_i] \tag{3.5}$$

$[\underline{B}_i]$ is the strain-nodal displacement matrix for the ith element and is a function of position.

Using the principle of virtual work the external work done during an increment can be equated to the change in internal work.

i.e. $$\Delta \underline{d}_i \; \underline{f}_i = \int \Delta \underline{\epsilon}^T \; \underline{\sigma} \; \text{dvol} \qquad (3.6)$$

where $\underline{\sigma}$ is the stress vector

Substituting equation (3.4) into equation (3.6) gives

$$\underline{f}_i = \int [\underline{B}_i]^T \; \underline{\sigma} \; \text{dvol} \qquad (3.7)$$

and if $[\underline{B}_i]$ is taken to be constant during an increment of deformation then

$$\Delta \underline{f}_i = \int [\underline{B}_i]^T \Delta \underline{\sigma} \; \text{dvol} \qquad (3.8)$$

Let $[D_i]$ be the incremental stress-strain relationship appropriate to the deformation of this element, so that

$$\Delta \underline{\sigma} = [D_i] \; \Delta \underline{\epsilon} \qquad (3.9)$$

The form of the [D] matrix is dependent on the type of model used to represent the material behaviour. This will be discussed further in section 3.2.2.

Substituting equation (3.9) into (3.8) and then using equation (3.4) gives:

$$\underline{f}_i = \Delta \underline{d}_i \int [\underline{B}_i]^T [D_i \;] [\underline{B}_i] \; \text{dvol} \qquad (3.10)$$

As an analytical solution to this integral is not possible a numerical technique such as Gaussian quadrature must be used. (For a general description of this technique see, for example, Stark (1970).)

This integral is known as the stiffness matrix $[\underline{K}_i]$ such that

$$[\underline{K}_i] = \int [\underline{B}_i]^T [D_i] [\underline{B}_i] \, dvol \qquad (3.11)$$

and $$\Delta \underline{f}_i = [\underline{K}_i] \Delta \underline{d}_i \qquad (3.12)$$

This refers to a single element, but to simulate the behaviour of the whole body the effects for all the elements need to be superposed to find the global stiffness matrix.

The assembled equations take the form

$$\Delta \underline{f} = [K] \Delta \underline{d} \qquad (3.13)$$

where $\Delta \underline{f}$ and $\Delta \underline{d}$ are the vectors of nodal increment in force and displacement respectively and [K] is the global stiffness matrix. In linear elastic problems the load vector and stiffness matrix need only be derived once for the complete analysis. Consequently the calculation of the displacement vector is easy to perform in the equivalent of one increment. However, for non-linear problems the solution has to be obtained in a series of small steps, each of which may involve the recalculation of the stiffness matrix, or the load vector, or both. Thus the computational time required to obtain the solution is very considerably increased, so that care must be taken to ensure the use of efficient and accurate computational techniques.

3.2.2 Finite-elements in plasticity.

Due to the highly non-linear relationship between stress and plastic strain an incremental approach to the solution of the finite-element equations has to be adopted, as previously suggested in

section 3.2.1.

These material property non-linearities can be included in the finite-element technique in a number of ways. Three types of material property model are commonly in use. These are usually referred to as the rigid-plastic, visco-plastic and elastic-plastic models.

The rigid-plastic model, sometimes referred to as the matrix method, considers only the effect of plastic deformation and neglects the elastic response (as does slip-line field theory and upper bound theory). This response is ignored on the grounds that the strains associated with elastic deformation are orders of magnitude smaller than plastic strains when large flow has occurred. This rigid-plastic approach has some advantage when the amount of computer time required to obtain a solution is considered, as the basic matrices used in the analysis are reduced in size when compared with the elastic-plastic material model. As many increments of deformation are required to perform a satisfactory analysis of flow in metalforming this simplification can result in very large savings.

This model has been used by many investigators, including Lee and Kobayashi (1973) for the expansion and contraction of a hole in a circular plate, Chen and Kobayashi (1980) for ring compression, and Price and Alexander (1979) and Dung, Klie and Mahrenholtz (1980) for backward extrusion and the upsetting of a solid cylinder.

The second material model is that which simulates visco-plastic deformation. In this model yielded material is assumed to behave like a non-Newtonian fluid (where the relationship between stress and strain rate is non-linear) so that this method is particularly suitable for steady state processes. Typical applications include steady state forward extrusion (Zienkiewicz and Godbole, 1974), drawing (Price and Alexander, 1976) and rolling (Zienkiewicz, Jain and Onate, 1978).

The main disadvantage of the rigid-plastic and visco-plastic techniques is that they are unable to model elastic recovery once load has been removed. The residual stresses that may remain may well be important in further metalworking operations or under service conditions. Both these material property models are capable of simulating deformations where there is a large plastic flow in all regions of the body, but where there is a possibility of small strain deformation it may be necessary to invoke the third type of material property model, the elastic-plastic technique. This takes into account, as the name suggests, both elastic and plastic material response and the interaction between the two. This method has been used by such investigators as Marcal and King (1967) and Zienkiewicz, Valliappan and King (1969) for the plane stress deformation of a perforated plate and the plane strain deformation of a notched tensile specimen, Lee, Mallet and Yang (1977) for axisymmetric extrusion, Nagtegaal and deJong (1980) for the axisymmetric upsetting of a disc and Pillinger, Hartley, Sturgess and Rowe (1982) for the radial expansion of a thick walled hollow cylinder.

For the prediction of fracture initiation in metalforming Lee (1976) pointed out that criteria governing the initiation of cracks are commonly based on the stress history of an element and that elastic stress increments, particularly on initial loading and unloading, play an essential role in determining the stress distribution, especially with respect to hydrostatic stress. Therefore, although no quantitative data are available to support this, it appears desirable to use a finite-element solution technique which incorporates both elastic and plastic material response where the predictions of continuum fracture criteria are to be examined, as in the work presented in this thesis.

3.2.3 Description of the elastic-plastic finite-element program.

A computer program for three dimensional elastic-plastic finite-element analysis was partially developed at the start of this work (Pillinger, 1984). This has proved to be an excellent basis but could not be used without several modifications. These will be described, together with additional software necessary, in section 3.3. The sections following provide a summary of the important features of the elastic-plastic finite-element method. Further details are recorded by Pillinger (1984).

3.2.3.1 Constitutive relationship.

For the elastic-plastic treatment used here, yield is based on the von Mises' yield criterion and the flow of the material by the Prandtl-Reuss equations (see for example Ford and Alexander (1977)). The use of these relationships determines the form of the incremental stress-strain matrix used in equation 3.9 and subsequently used to determine the global stiffness matrix. Additional terms also need to be included in the formulation of the global stiffness matrix for the accurate modelling of metalforming processes (Pillinger, 1984). These are outlined in the following sections.

3.2.3.2 Global stiffness matrix.

The stiffness matrix given in equation 3.11, while suitable for one-step analyses as in elasticity, requires for plasticity the addition of terms to account for the effects of material rotation during an increment and for the effects of overconstraint caused by enforcing

incompressibility.

The modified global stiffness matrix may be written as

$$[K] = [K]^{\epsilon} + [K]^{\sigma} + [K]^{\varphi} \qquad (3.14)$$

$[K]^{\epsilon}$ is the deformation stiffness matrix as defined earlier in equation 3.11, although for plasticity the strain measure to use in calculating this matrix is linear co-rotational strain (Pillinger, 1984) which allows for the effect of rigid body rotation on strain (section 3.2.4.5 describes the use of this strain measure in more detail).

$[K]^{\sigma}$ contains terms to correct the resulting stress increments if deformation is combined with rotation. Plasticity theory conventionally defines stress and increments of strain in terms of Cartesian components in the current configuration without rotations occurring. However, as the theory used here must apply in the presence of rotation, a spin-invariant stress rate is needed. The Jaumann stress rate, as described by Lee (1976), was chosen by Pillinger for inclusion in the finite-element program to fulfill this requirement. (Section 3.2.4.4 describes the Jaumann stress rate in more detail.)

$[K]^{\varphi}$ includes corrections to reduce the constraint caused by enforcing constant volume when using a Poisson's ratio close to 0.5. This method was originally proposed by Nagtegaal, Parks and Rice (1974) to overcome the excessive restraint associated with the enforcement of volume constancy at every point of the material. Their solution is to relax the requirement that the bulk strain is zero at every sample point of an element and only require that the total volume of an element is kept approximately constant. This technique is referred to as 'Constant Dilatation' since the dilatation, or average bulk strain, for an element is the same for all points of the element. Section 3.2.4.2 briefly examines some of the effects of the inclusion of this method.

3.2.3.3 Finite-element solution.

The global stiffness matrix, once assembled with the various corrections, is inverted and solved using Gaussian elimination and back substitution to obtain the nodal displacements. Due to the non-linear nature of the relationship between stress and strain during plastic flow it is necessary to recalculate the stiffness matrix at the end of each increment of deformation. Instead of using the tangent modulus method where the stiffness matrix is evaluated using the stress and plastic strain at the start of the increment, this formulation recalculates the various matrices based on mid-increment values of stress and strain. This improves the accuracy of the solution and allows the use of larger increment sizes (this is discussed in more detail in section 3.2.4.3). Irrespective of this increment size it is important to ensure that the yield criterion is not violated at the end of the increment. This is done using a mean normal method based on work by Nagtegaal and De Jong (1980) and Santiago and Wisnieski (1982) and extended by Pillinger (1984) for non-linearly work hardening materials. For these work hardening materials, as considered in this thesis, a relatively simple iteration is required to ensure that the changes in deviatoric stress result in a generalised stress vector which remains on the yield surface.

Hydrostatic stress is calculated based on a method suggested by Alexander and Price (1977). Here hydrostatic stress may be calculated indirectly using the spatial derivatives of deviatoric stress provided that the hydrostatic stress is known at one point in the body. This one required value may be calculated using an element which has a free surface face. Since the component of total stress perpendicular to a free surface is equal to zero then at this point the deviatoric normal

stress is equal but opposite in sign to the value of hydrostatic stress.

For accurate predictions during the early stages of deformation when areas of the body may still be elastic, the size of the yield-transition increments are reduced using the technique suggested by Yamada, Yoshimura and Sakurai (1968).

3.2.3.4 Inclusion of boundary conditions.

The current finite-element program uses three dimensional 'brick' type elements each defined with respect to eight nodes. Movement of the dies during the forming operation can be modelled in one of two ways. In the first, individual external nodal forces may be specified. In the second method a specified displacement may be applied to a group of nodes on the boundary of the mesh to simulate the effect of die movement. As the forces are initially unknown for the analyses presented in this thesis the method of prescribed displacements has been used.

Boundary frictional conditions are modelled by defining an extra layer of elements, referred to as the friction layer, on the required surfaces. By altering the stiffness of the friction layer elements the tangential movement of the surface nodes of the mesh may be varied, thereby simulating the frictional response. In the version of the program used here the stiffness matrices of the friction layer elements have been multiplied by the function m/(1-m), where m is the interface shear factor, as previously used in the axisymmetric finite-element analysis of Hartley, Sturgess and Rowe (1979).

The importance of several of the features described here, being linear co-rotational strain, the Jaumann stress rate, constant dilatation and the mid-increment and mean normal techniques are discussed in the following section. The effects of increment size, integration order and element aspect ratio are also to be examined.

3.2.4 Assessment of the elastic-plastic finite-element program.

3.2.4.1 Introduction.

In order to assess the importance of including many of the features described in section 3.2.3, plane-strain compression with zero and also with sticking friction has been analysed. For compression with zero friction the deformation is homogeneous and the solution is known. This is used here to assess the effect of variations on the increment size, integration order and element aspect ratio in section 3.2.4.7.

But first, attention is focussed on the constant dilatation and mid-increment methods and the Jaumann stress rate, assessed in comparison to experimental results using plasticine as a model material (Chanda, 1985). Linearised co-rotational strain and the mean normal method are demonstrated to be important with reference to results published elsewhere.

3.2.4.2 Inclusion of the constant dilatation method.

The finite-element results presented in this section and the one following have been compared with experimental distortion of lines scribed on a plasticine specimen as obtained by Chanda (1985) and reproduced in figure 3.2. The finite-element mesh used for the simulation of this deformation is given in figure 3.3.

Finite-element results obtained to assess the effect of the various different methods are presented in figure 3.4. Figure 3.4(a) illustrates the basic tangent modulus solution and figure 3.4(b) the tangent modulus solution which incorporates the constant dilatation method.

In the solution incorporating constant dilatation some of the originally

Figure 3.2

Plane-strain compression of an initially square block of plasticine: sticking friction, 50% deformation. After Chanda (1982).

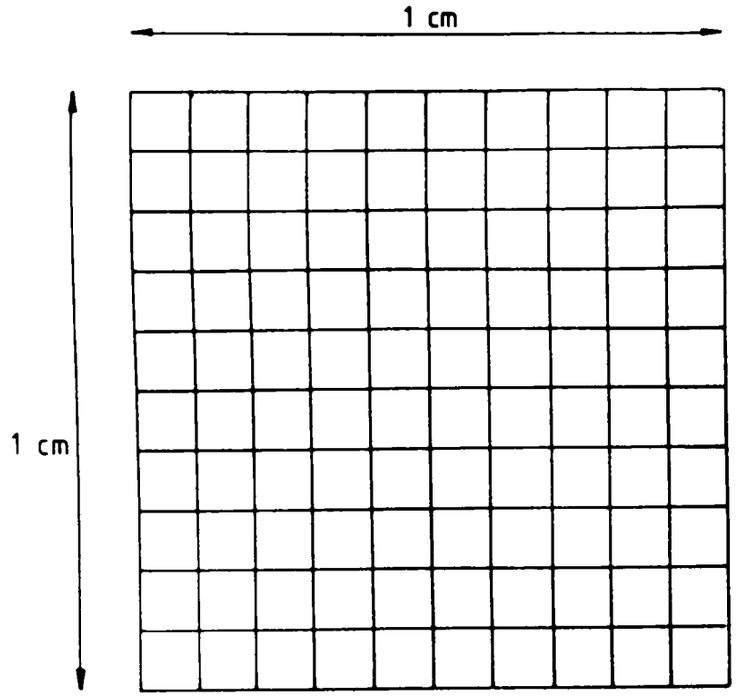

FE mesh:

100 elements

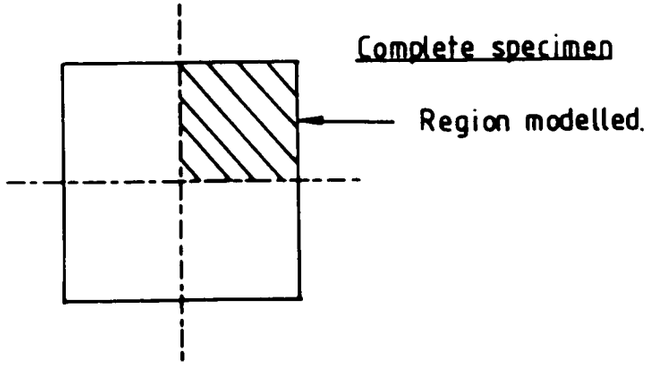

Figure 3.3 Undeformed mesh used in assessment of option choices in finite element program.

(a) TM

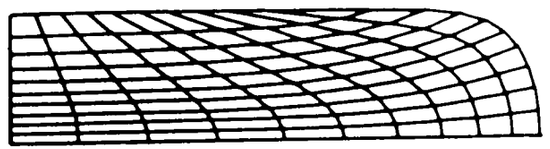

(b) TM + CD

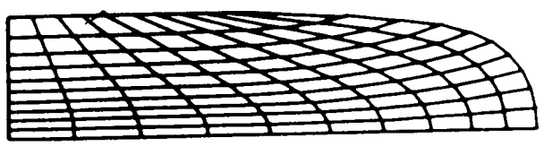

(c) TM + CD + MI

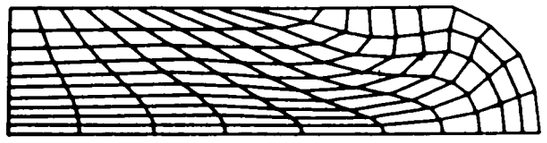

(d) TM + CD + MI + J

Figure 3.4

Finite-element solutions.

TM - Tangent modulus
CD - Constant dilatation
MI - Mid-increment
J - Jaumann correction

LCR strain and mean normal techniques included in all solutions.

free surface comes into contact with the die due to the relaxed volume constraint, although not as much as the experimental results indicate occurs in the compression of plasticine.

Therefore, although constant dilatation does have a very large effect, the comparison with experimental results suggests that the theoretical solution may still be improved.

3.2.4.3 Inclusion of the mid-increment method.

Figure 3.4(b) shows the results obtained for the tangent modulus solution incorporating constant dilatation, as selected in the previous section and figure 3.4(c) results from a solution containing both the mid-increment technique and constant dilatation.

In this case there is very little difference between the two solutions. In comparison with the experimental results the solution without the mid-increment technique actually appears to produce slightly better results. However, this plasticine test can only be used as a general guide to the deformation pattern as it refers to a non-work hardening material. The results of Pillinger (1984) show that the mid-increment method results in general produce better correlation and theoretically, a predictor-corrector technique of this type must produce more accurate results. On this basis the mid-increment technique has been included in the analyses presented in this thesis.

3.2.4.4 Jaumann stress rate formulation.

In a finite-element analysis of a metalworking operation some elements will undergo a combination of deformation and large rotation. This occurs early in the plane-strain compression of an initially square block when those elements originally on the free surface of the

workpiece move into contact with the dies. In order to accurately calculate stress in such situations a spin invariant stress measure is obviously required and is provided in the computer program used here by the use of the Jaumann stress increment. Qualitative results to support this are provided in figure 3.4(d). Comparison with the experimental results of Chanda show better agreement than for figure 3.4(c) which does not incorporate the spin invariant stress measure. Quantitative results to support the use of the Jaumann stress increment are provided in the work of Pillinger (1984) and reproduced in figure 3.5.

Here, a single element cube of 1cm edge length was rotated about the z axis by one degree per increment, the axis system (x',y',z') rotating with the element. At the same time the element was extended by approximately 0.00002mm in the current x' direction. The element has an initial tensile stress in the x direction of 100 MN/m^2 and was assumed to remain elastic throughout the deformation so that the stress acting at any stage could be calculated by classical elasticity theory. As the graphs show, excellent agreement has been found between the theoretical and finite-element solution with Jaumann correction, and very poor agreement with the finite-element solution which does not incorporate the Jaumann correction.

3.2.4.5 Linearised co-rotational strain.

In the finite-element analysis of metalforming the material displacements are small but finite. The infinitesimal formulation is therefore not an accurate strain measure, particularly when the material is rotating. For example, rigid-body rotation will not give zero strain. However, the true relationship between a finite-strain increment and incremental displacement gradients is not linear and would therefore be computationally demanding to solve. In the finite-element formulation

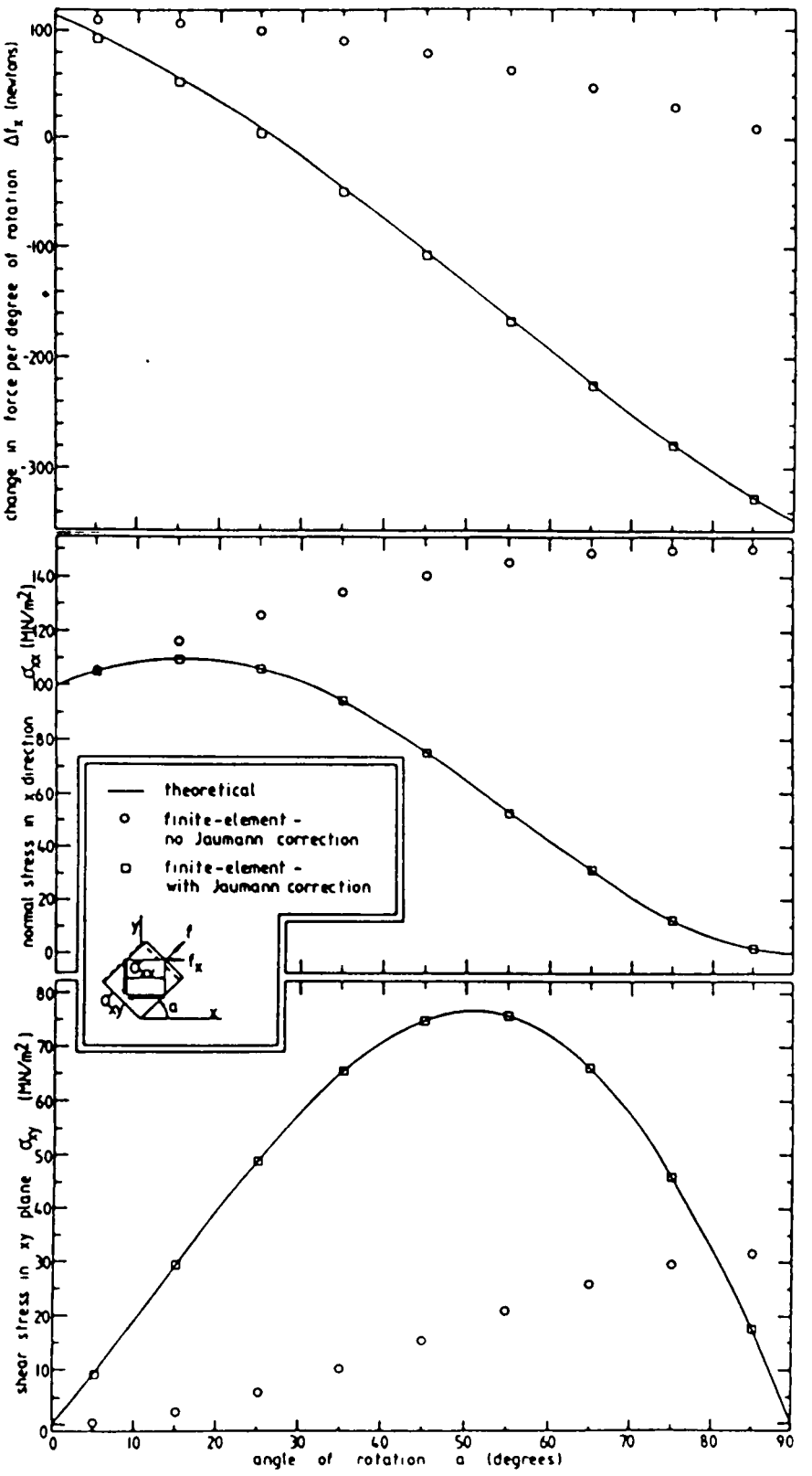

Figure 3.5. Effect of Jaumann correction on combined extension and rotation of a pre-stressed body. After Pillinger (1984).

a rotation invariant measure of strain has been derived, and is referred to as linearised co-rotational strain (LCR). The effect of this co-rotational strain on combined extension and rotation of a pre-stressed body is shown in figure 3.6. According to Pillinger (1984), this form of strain measure is acceptable providing the incremental rotation is one of the order of ten degrees or less and the incremental strain is of the order of one or two percent. As the finite-element analysis is carried out in small steps this is a fairly reasonable assumption.

3.2.4.6 Mean normal method.

In the mean normal method the plastic incremental strain vector is taken to be proportional to the deviatoric stress at the middle of the increment, instead of at the beginning. This technique was first suggested by Rice and Tracey (1973) and later studied analytically by Nagtegaal and De Jong (1980) to overcome the instability problem which can occur due to the presence of small errors in the calculated increment of strain. Pillinger (1984) generalised this technique to include strain hardening and an example of its use is given in figure 3.7.

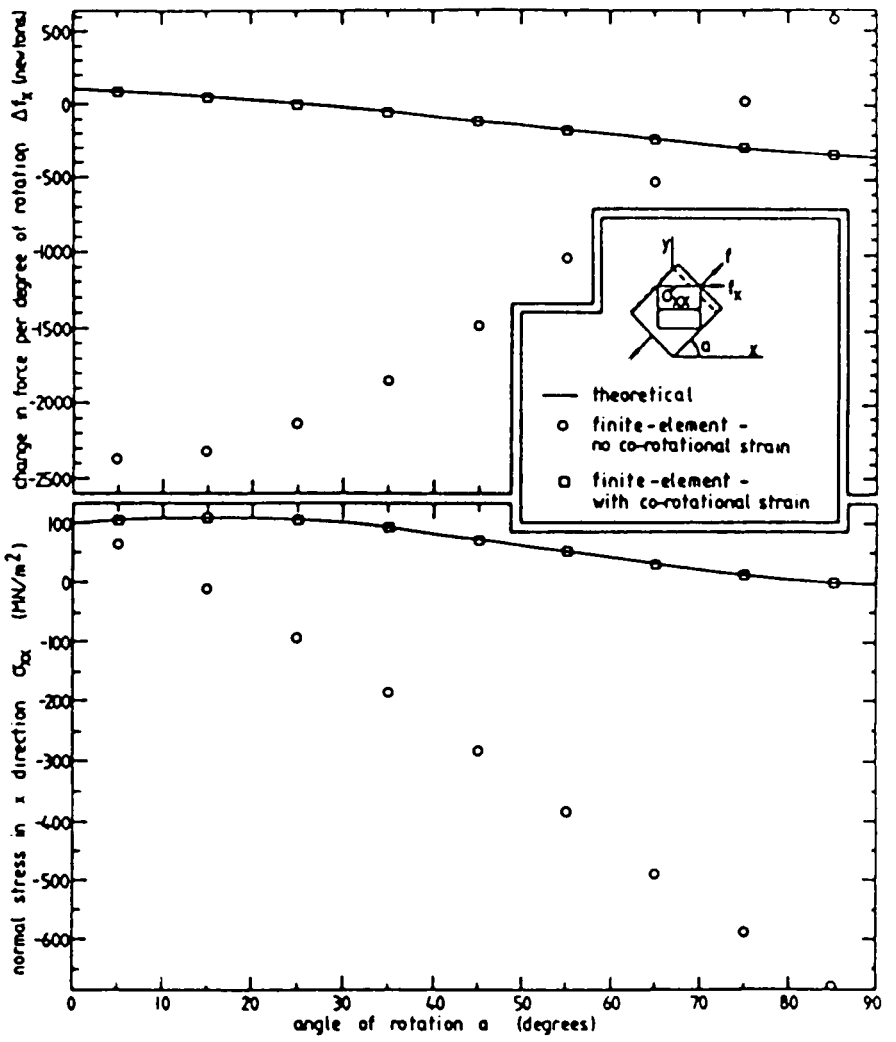

Figure 3.6

Effect of co-rotational strain on combined extension and rotation of a pre-stressed body.

After Pillinger (1984)

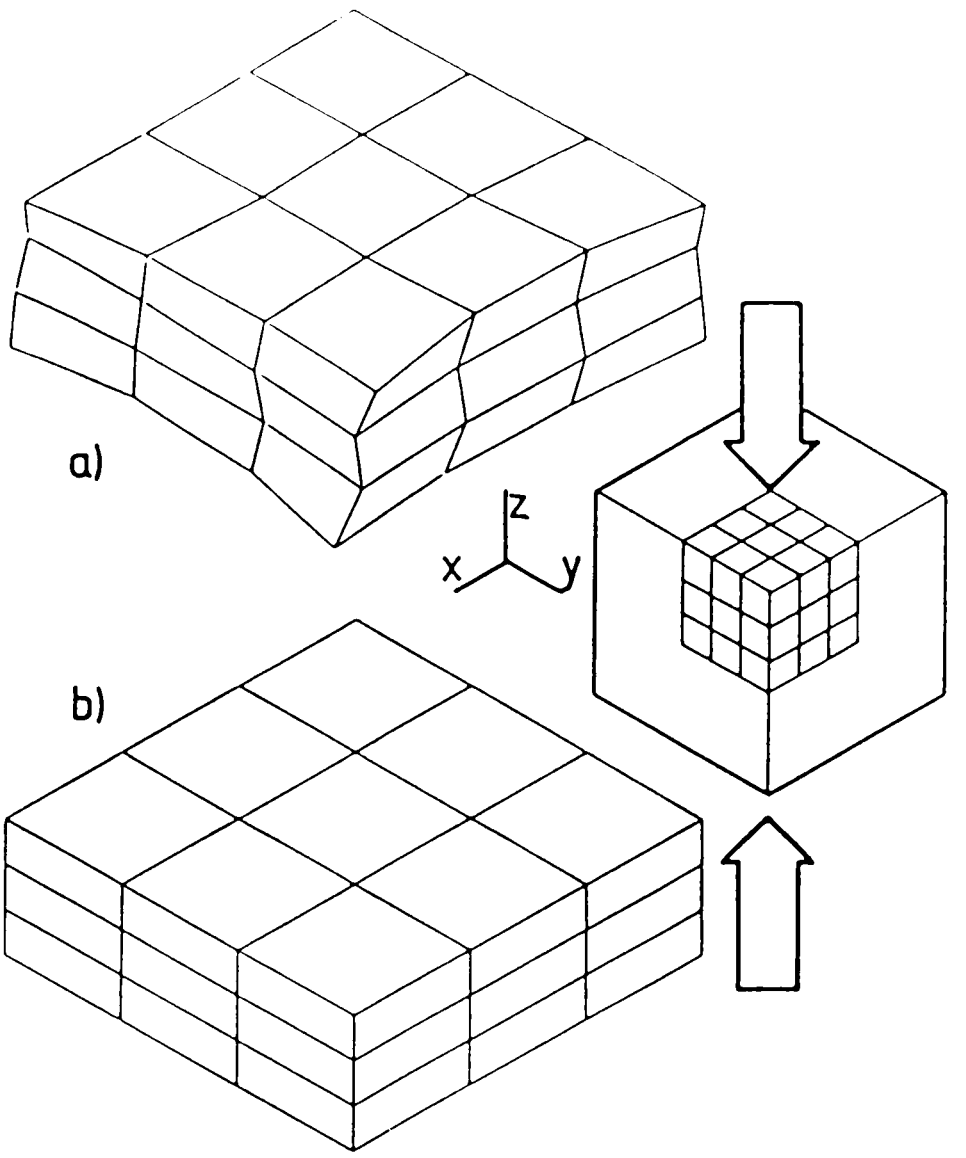

Figure 3.7

FINITE-ELEMENT PREDICTIONS OF SIMPLE UPSETTING OF A CUBE OF ECI AL WITH ZERO INTERFACIAL FRICTION.
(1/8 CUBE MODELLED; 50.075% DEFORMATION)
a) STRESS FROM TANGENT D-MATRIX & CORRECTION
b) STRESS FROM MEAN-NORMAL METHOD

After Pillinger (1984).

3.2.4.7 Assessment of some computational features.

In order to make an assessment of some of the features of the finite-element program which are suitable for use in this particular study involving large plastic flow the mesh previously shown in figure 3.3 was again used but this time zero interface friction was assumed. Again the mesh was constrained to deform in plane-strain. Under these circumstances it is possible to obtain a very simple theoretical solution with which the finite-element results may be compared.
Now,

$$\epsilon = \ln(1+e)$$

where

ϵ = natural strain

e = engineering strain

Therefore, for 50% deformation

$$\epsilon_x = \ln(1+1) = 0.693$$

$$\epsilon_z = \ln(1-0.5) = -0.693$$

($\epsilon_y = 0$ for plane-strain)

Generalised plastic strain may then be obtained using the equation:

$$\bar{\epsilon} = \sqrt{(2[(\epsilon_x-\epsilon_y)^2 + (\epsilon_y-\epsilon_z)^2 + (\epsilon_z-\epsilon_x)^2])/3}$$

which gives

Increment size	Generalised plastic strain
0·5%	0·797
1·0%	0·794
2·0%	0·788
5·0%	0·772
10·0%	0·745

Table 3.1

Finite-element calculated generalised plastic strain values for a range of increment sizes.

$\bar{\epsilon}$ = 0.80

This simple analysis provides a basis for comparison of results obtained using a variation in increment size (section 3.2.4.7.1) and integration order and element aspect ratio (section 3.2.4.7.2).

3.2.4.7.1 Increment size

The zero friction mesh described in the previous section was reduced in height by approximately 50% using a number of finite-element program executions. In each example a different increment size was used. The generalised plastic strain values determined from these analyses were examined with the aim of selecting that increment size most suitable for subsequent analyses.

Table 3.1 contains the generalised plastic strain values for the five increment sizes studied. Metal flow in all five solutions was homogeneous, with the calculated generalised plastic strain values approaching the theoretical solution as the increment size is reduced. A reduction of the increment size by a factor of one half approximately doubles the computational time required to obtain the solution. Thus it becomes important to achieve a balance between solution accuracy and the time taken to obtain that solution. On this basis it was decided to select a deformation increment of 1.00% as the standard size for the work reported in this thesis. This solution differs by 0.75% when compared with the simple theoretical solution. By halving this increment size the difference may be reduced to 0.38%, but this does not justify a two-fold increase in the computation time which, for a typical metalforming analysis, may be of the order of hours. Larger increment sizes may be of use in preliminary analyses when an approximate calculation of the expected metal flow may be obtained

fairly quickly, before a full analysis is performed; although the use of large steps may be restricted by sudden geometric changes in the analysis of complex shapes.

3.2.4.7.2 Variation of integration order and element aspect ratio

In the paper by Hampton et al (1980) dealing with elastic finite-element analysis, a correlation in deformation behaviour was found between the ratio of height to width of an element, referred to as the element aspect ratio, and the integration order used in the calculation of the stiffness matrix. It was therefore proposed to investigate whether any similar relationship exists within the results of a finite-element analysis dealing with large plastic flow. To this end the six meshes shown in figure 3.8 were set up, and were deformed to half the original height in each case using integration orders 2 to 6 inclusive, a total of 30 examples. The aspect ratios chosen represent typical values and also the extremes of aspect ratio which are likely to be necessary in forming analysis.

However, the results obtained did not reveal any differences between the calculated stress and strain values for any of the combinations tested. It was therefore concluded that an integration order of 2 is sufficient for analyses involving large plastic flow, with no loss in accuracy resulting from the smaller computational time.

The problem concerned with using large aspect ratio elements is more complicated. For a zero or low friction analysis all the aspect ratios tested were found to perform in a satisfactory manner. However, for an analysis which has a relatively high value of interface friction, deformation is inhomogeneous, and a large stress and strain gradient may exist over an element with a high aspect ratio resulting in an inaccurate average stress or strain value.

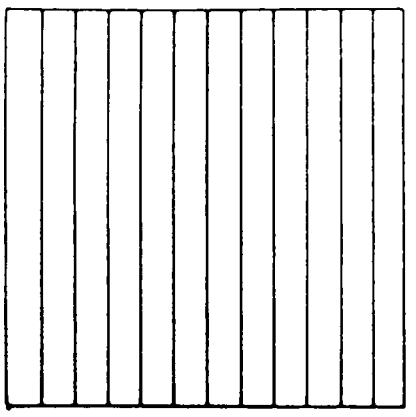

ARIO1 H/W = 12

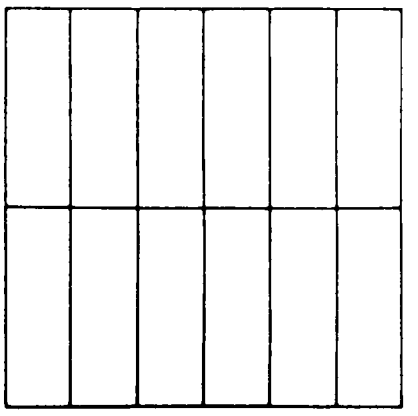

ARIO2 H/W = 3

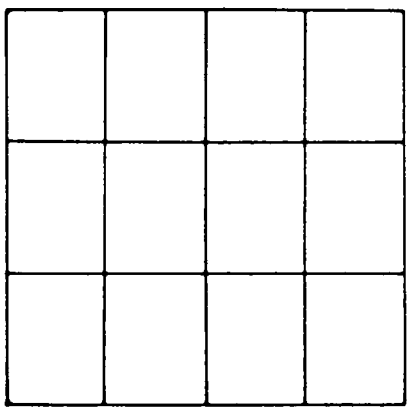

ARIO3 H/W = 1·33

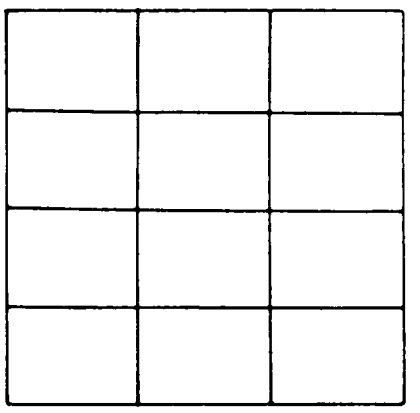

ARIO4 H/W = 0·75

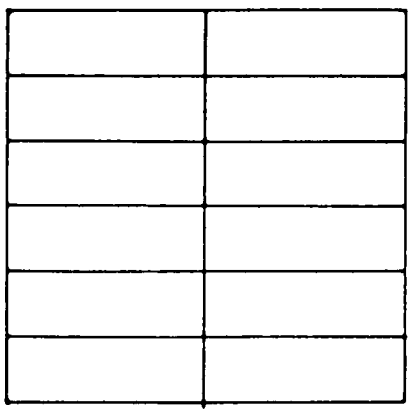

ARIO5 H/W = 0·33

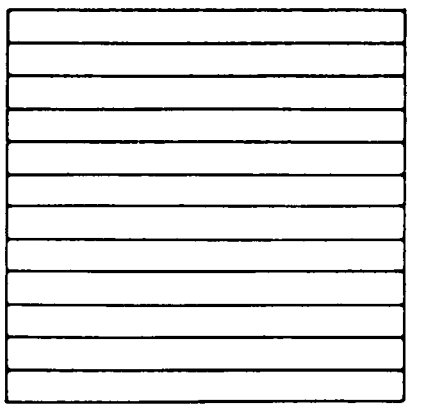

ARIO6 H/W = 0·08

FIGURE 3.8 Undeformed finite element meshes for aspect ratio / integration order tests.

It is therefore proposed, wherever possible, to use elements with an aspect ratio less than or equal to two in the work presented in this thesis.

3.2.4.7.3 Summary

The preceding sections have demonstrated the importance of incorporating certain features into the finite-element model for metalforming. Various computational options were also examined and the following chosen as suitable for use in subsequent analyses:

1. 1% deformation increments;
2. Integration order of 2;
3. Elements of aspect ratio in the range 2 to 0.5 if possible.

3.3 Computer analysis of fracture initiation.

3.3.1 Post processing of the stress and strain results.

The original finite-element program developed by Pillinger (1984) was not in a form entirely suitable for the analysis of fracture. Therefore, two modifications were made to this basic program in order to enhance its suitability to provide data for this investigation of fracture initiation sites in metalforming.

The first modification concerned the specification of the variation in yield stress with plastic strain in the initial data file. In the original formulation this was specified using a complicated function containing five material dependent coefficients. It proved very time consuming to obtain the required coefficients to fit each set of experimental data. Therefore, in order to reduce the time required in

preparing each new set of material property data to be used in the finite-element analysis the computer program was modified so that the actual recorded set of data points could be specified and through which the program could calculate a cubic spline fit. The NAG library routines E02BAF and E02BCF were required for this purpose. Linear strain hardening from a generalised plastic strain of 0.01 less than the final data point was assumed to extend the range of the experimentally determined stress values if the finite-element routines required a plastic strain outside the data specified.

The second modification to the basic program concerned the output of data in a format suitable for the subsequent post processing to assess various fracture criteria. After the finite-element program has completed the calculations relating to an increment of deformation the data indicated in appendix A is output to a data file. This operation, although very simple in principle involved time consuming practical problems, principally due to the limited availability of computer main memory. For example, strain components were not previously stored for each increment but were only calculated as an intermediate stage to determine stress components for each sample point. Therefore, only the strains calculated for the last sample point considered were previously available and changes were necessary to other areas of the program in order to accommodate these extra data.

The post processing file for a complete finite-element analysis of a metalforming operation might contain, for example, sixty sets of eleven records, one set for each increment of deformation.

3.3.2 Programs for the assessment of various fracture criteria.

This section describes the suite of computer programs written to find the numerical values of a number of fracture criteria using the

results produced from a finite-element analysis.

Program number 1: Data selection and general purpose calculation program

This program reads the finite-element incremental post-processing file and selects the data required for the subsequent numerical calculation of fracture criterion values. Total values of nodal generalised stress and strain were calculated from the incremental values supplied. Hydrostatic stress and principal stress components were also calculated from the supplied total stress components and written to the output file.

Program Number 2: Fracture data accumulation and plotting program

This program retrieves the data output from the data selection program and uses it to accumulate the values of various fracture criterion functions. It has been written in modules to make it flexible. The system flow chart is given in figure 3.9. The main module, module 1, controls and processes all the calls to the other modules. The fracture criterion calculation routines may be selected individually, or the results relating to a group of criteria may be obtained from one run. The values of each fracture criterion function are calculated at the nodes of the finite-element mesh. If no node number is specified to the main module from the input selection request data file then the program calculates the values of the selected fracture criterion functions for all the nodes in the mesh and then prints out or plots the details relating to the node at which the accumulated function value is the largest. This allows the location of this node in the finite-element mesh to be compared with the

experimental fracture initiation site for any metalforming operation. The variation in the value of the selected fracture criterion function for this, or any node, during the complete deformation can also be plotted out.

Nodes may also be specified to any of the accumulation routines by number, in which case the code which obtains the maximum value is not invoked.

This computer program also has the capability to plot out the variation in hydrostatic stress relating to the complete deformation for a requested node, and also the variation in principal strain path (ϵ_1 plotted against ϵ_2). In figure 3.9 modules 3 to 12 are those which calculate the values of the various fracture criteria from the finite-element post processing data, while modules 13 to 15 inclusive plot various values of stress and strain.

Modules 16 to 20 inclusive are service routines commonly used by many of the fracture accumulation modules.

Table 3.2 gives brief details of the function of each individual routine.

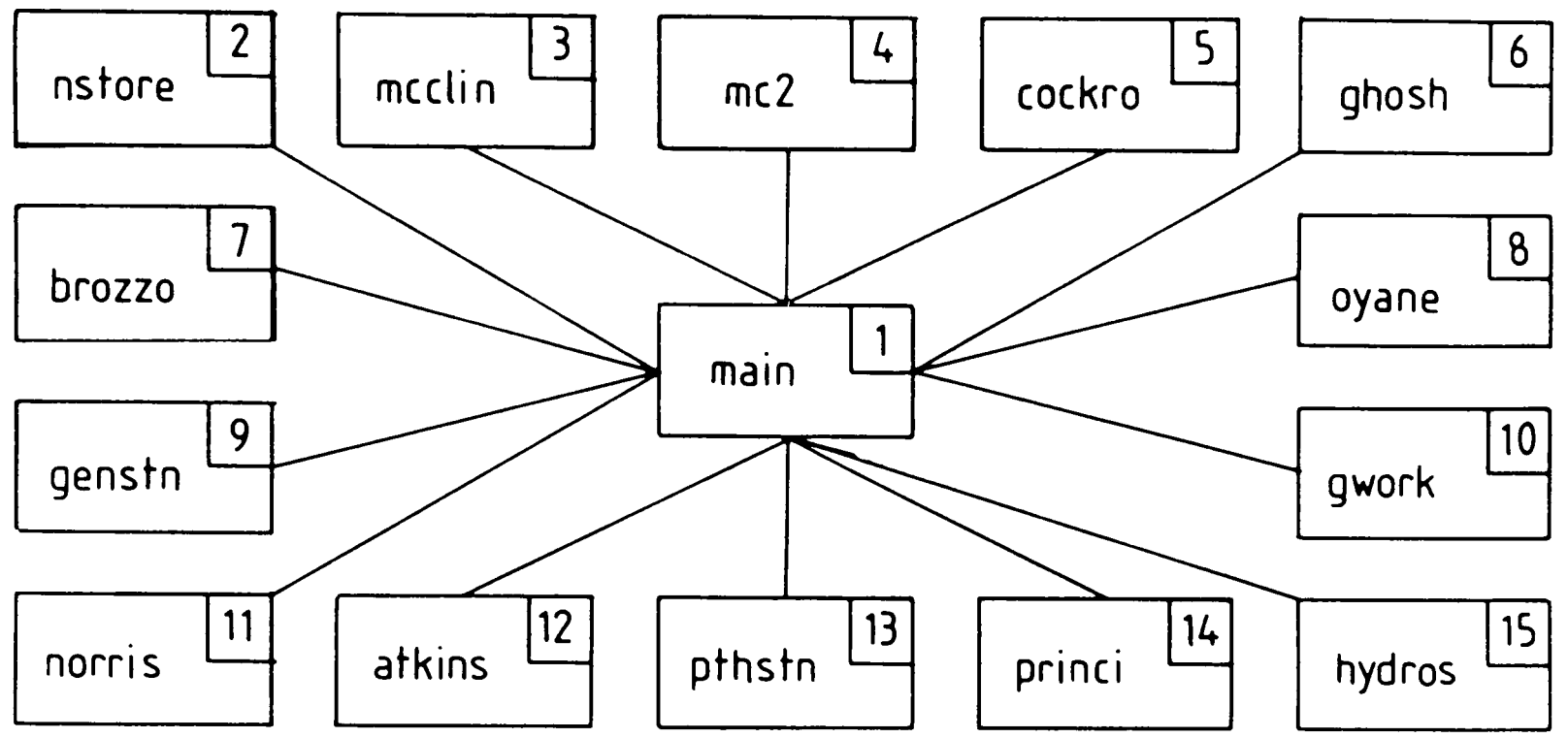

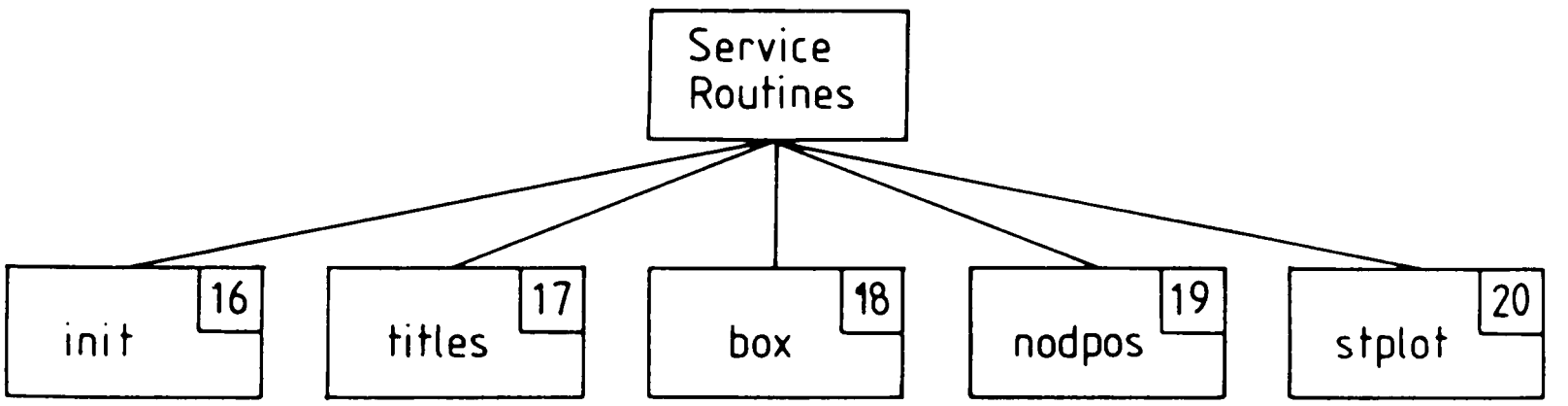

Figure 3.9

System flowchart for the fracture accumulation program.

Table 3.2

Details of modules in the fracture accumulation computer program.

Module Number	Module Name	Description
1	main	Reads in the selection request data, and calls the appropriate modules to process these requests.
2	nstore	Reads through the finite-element post processing data file and stores the nodal number order.
3	mcclin	Calculates and plots the hole growth functions derived by McClintock, Kaplan & Berg (1966) against overall level of deformation.
4	mc2	Calculates and plots the hole growth functions derived by McClintock (1968) against overall level of deformation.
5	cockro	Calculates and plots the accumulated tensile plastic work, according to the fracture criterion formulated by Cockroft and Latham (1968), against overall level of deformation.
6	ghosh	Calculates and plots the functional values associated with the fracture criterion of Ghosh (1976) based on the statistical process of the shear joining of voids, against overall level of deformation.
7	brozzo	Calculates and plots the functional values associated with the fracture criterion formulated by Brozzo et al (1972) against overall level of deformation.
8	oyane	Calculates and plots the functional values associated with the fracture criterion formulated by Oyane et al (1980) against overall level of deformation.
9	genstn	Plots values of generalised plastic strain against overall level of deformation.

Module Number	Module Name	Description
10	gwork	Calculates and plots values of generalised plastic work against overall level of deformation.
11	norris	Calculates and plots values of the fracture criterion of Norris et al (1978) against overall level of deformation.
12	atkins	Calculates and plots values of the fracture criterion of Atkins (1981) against overall level of deformation.
13	pthstn	Plots values of Cartesian stress components against overall level of deformation.
14	princi	Plots principal strain paths.
15	hydros	Plots values of hydrostatic stress against overall level of deformation.
16	init	Initialises data areas.
17	titles	Writes graph titles.
18	box	Draws the box in which graphs are plotted.
19	nodpos	Searches through the nodal number array to find the subscript of the supplied node.
20	stplot	Uses ginograf routines to plot supplied co-ordinates.

Chapter Four.

Plane-strain side-pressing.

4.1 Introduction.

This chapter presents, compares and discusses the finite-element and experimental results for the plane-strain side-pressing of a circular section rod, both with and without machined flats. The deformation behaviour and occurrence of fracture are reported for two materials: 60-40 brass and 7075 aluminium alloy.

Experimentally, the brass was tested in its 'as received' condition, having the microstructure shown in figure 4.1.

The composition of the second alloy used, 7075 aluminium alloy, is shown in table 4.1. This material has the microstructure shown in figure 4.2.

In addition to the initially circular section samples, as used in the testing of brass, the deformation behaviour of aluminium alloy was further studied for two additional shapes. These specimens were made from a circular section rod with machined flats of the type previously investigated by Jain and Kobayashi (1970). Each specimen was made in two halves and constrained to deform under the condition of plane-strain using the apparatus described in section 4.2.1. A photographic technique was used to form a grid which was positioned on one of the inside surfaces of the split specimen. Figure 4.3 shows the typical appearance of a gridded specimen in its deformed state. This technique, details of which are given in section 4.2.2, is preferred to inscribing lines as the latter may act as stress concentrators during the deformation process and initiate fracture prematurely. The experimental distortion of a grid on the specimen has distinct advantages for the purposes of comparison with finite-element calculations which may also produce predictions in this same visual form.

The Cartesian coordinates of the grid intersections were measured both before deformation and after selected reductions using a Zeiss MP320 measuring projector. The data obtained were input to a computer program, written to calculate the strain distribution of the deformed workpiece.

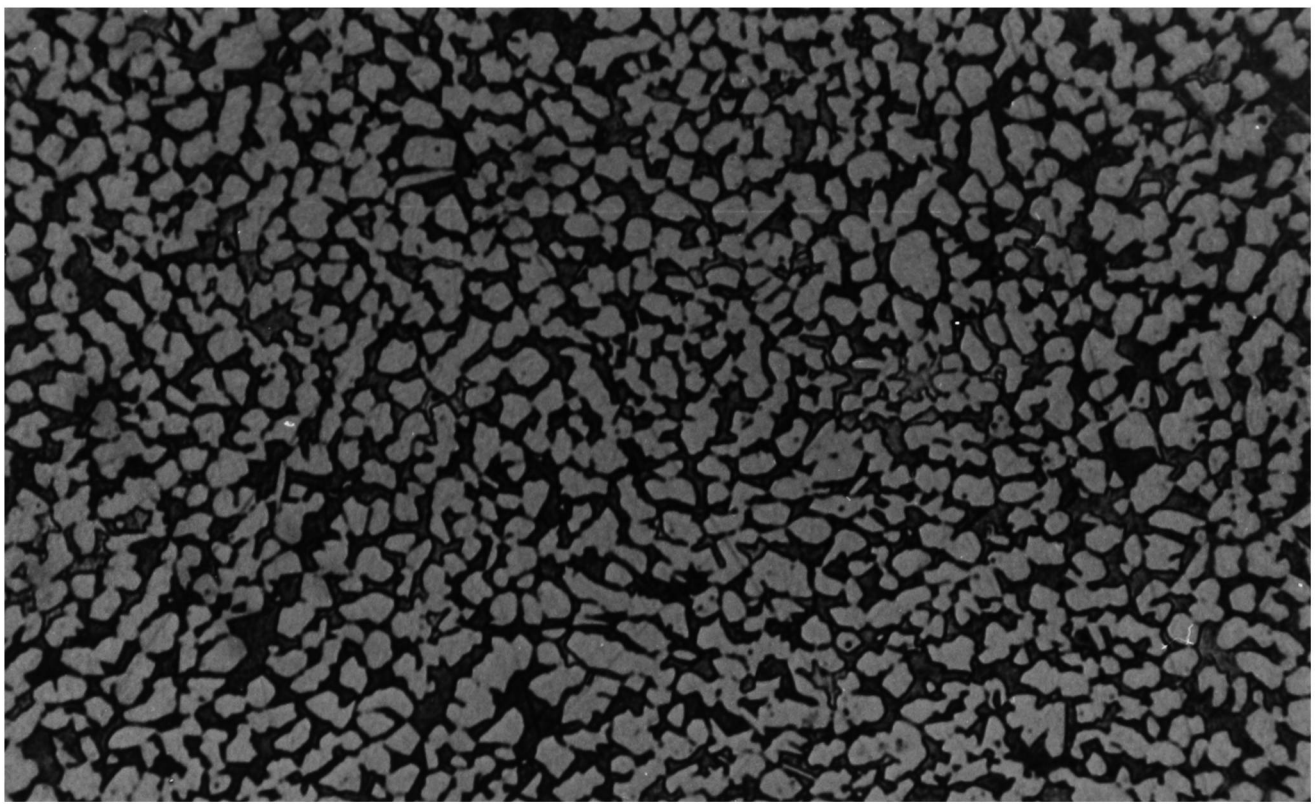

Figure 4.1

60-40 brass microstructure. (x240)

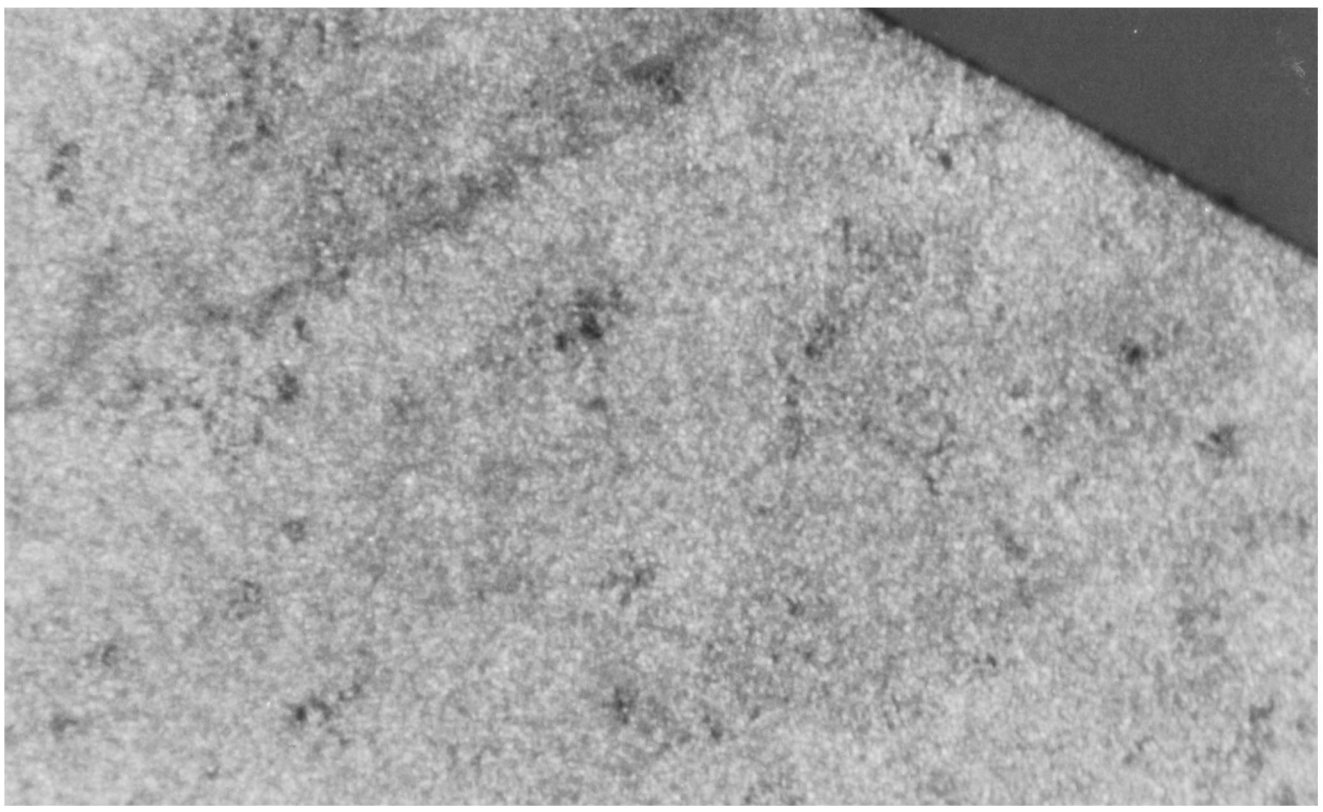

Figure 4.2

7075 aluminium alloy microstructure. (x80, continuous cast)

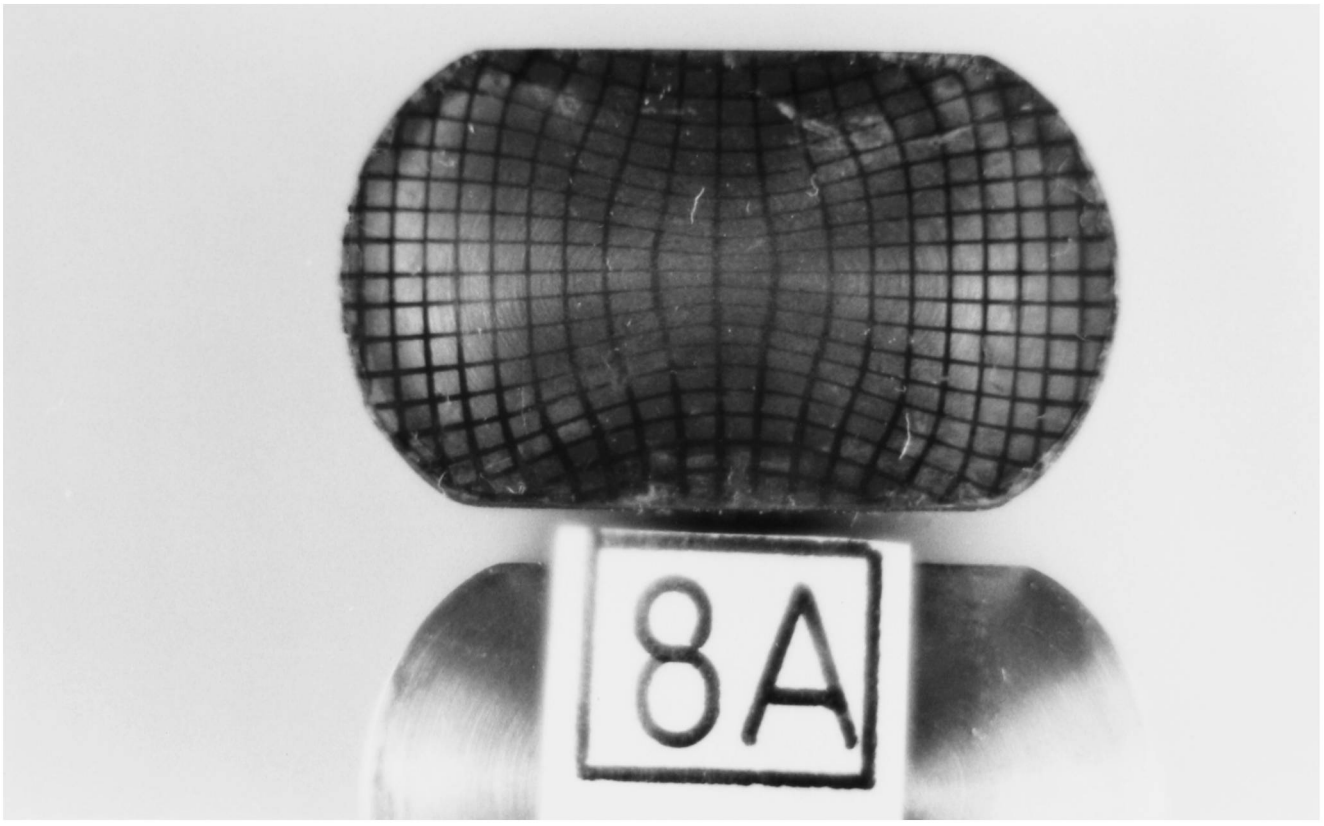

Figure 4.3

Typical photographic grid. (Initially circular section brass specimen, 29% deformation, x4)

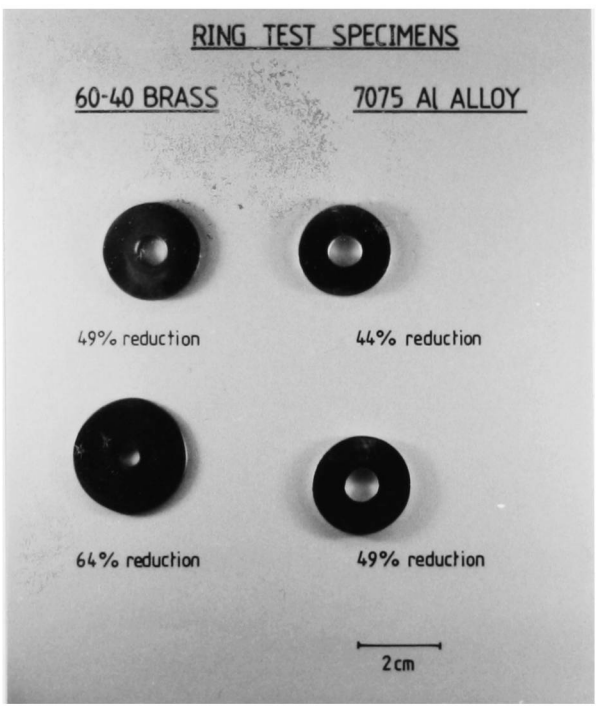

Figure 4.12

Typical ring test specimens.

Element	% Composition
Zn	5·5
Mg	2·5
Cu	1·5
Cr	0·3
Al	remainder

Table 4·1 Chemical Composition of 7075 Aluminium Alloy.

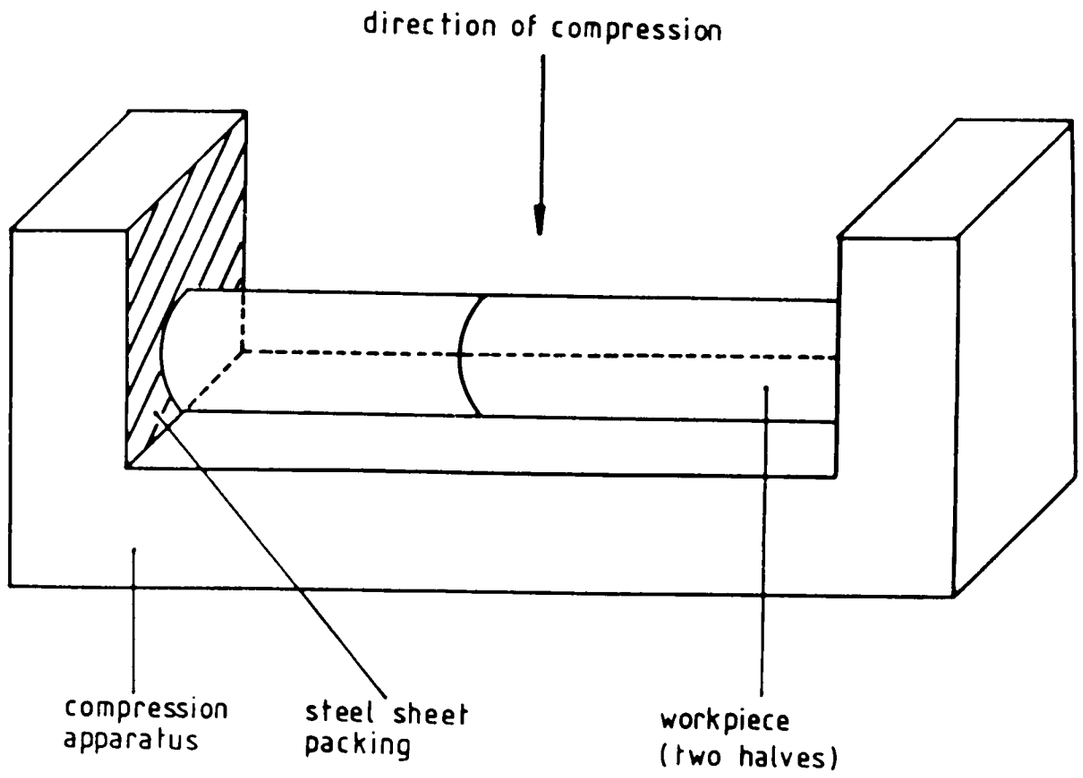

Figure 4·4 Experimental Apparatus for Plane-Strain Side-Pressing.

The formulation of this program is described in section 4.2.3, with the results of the deformation analyses presented in the following sections. Hardness measurements were also employed to validate the finite-element flow patterns and a brief background to the technique of hardness testing is given in section 4.2.4.

Section 4.3 contains the details of the information supplied to the finite-element computer program to enable it to model the forming problem of plane-strain side-pressing. Within section 4.3.1 are presented the finite-element meshes for all three shapes to be modelled. Sections 4.3.2 and 4.3.3 respectively contain details of the experimental determination of the stress-strain properties and frictional conditions of the two materials to be modelled.

Section 4.4 marks the beginning of the results and discussion section of this chapter. Section 4.4.1 presents the results of some numerical studies on the effect of a variation of the level of interface friction included in the model. The following two sections (4.4.2 and 4.4.3) compare the finite-element results with experimental results using the visioplasticity and the hardness assessment techniques respectively. Section 4.4.4 presents the results obtained from the finite-element technique for which there exists no direct experimental comparison, that is the plastic zone development and displacement vectors.

Section 4.5 presents and discusses results obtained relating to fracture initiation in plane-strain side-pressing, particularly the influence of initial cross-sectional geometry. Section 4.5.1 contains the experimental results, while section 4.5.2 compares them with the theoretical predictions obtained using the stress and strain values produced by the finite-element model in conjunction with a range of published fracture criteria. Finally, section 4.6 presents the conclusions.

4.2 Experimental Procedure.

4.2.1 Experimental Apparatus and Testing Procedure.

The apparatus used to constrain the circular section workpiece to deform under the condition of plane-strain is illustrated in figure 4.4. The specimen, manufactured in two halves, was packed to fit closely in the compression apparatus, using steel shims. These were needed to ensure that no significant lateral movement took place during compression of the specimen. Both the punch and the compression apparatus were manufactured from steel hardened to Rockwell B 45-50. A number of specimens of each geometry was tested in either an Avery 600kN or a Dennison 3000kN press, and a photographic record of each gridded specimen both before and after compression was kept, so that the complete experimental strain history to fracture could be calculated.

4.2.2 Sample Preparation.

As previously mentioned, each sample is made in two halves and constrained during deformation so that no plastic flow occurs in the plane parallel to its axis using the experimental apparatus previously shown in figure 4.4. The two surfaces to be located in the centre of this apparatus were prepared in different manners, to provide complementary information on the conditions within the deformed body. The first face had a good turned surface finish. This was sufficient for bands of high shear localisation to be visible to the naked eye. This half of the specimen was also available for hardness testing.
More detailed measurements of deformation were calculated from grids which were printed on the second half of the specimen. This was done

using the following procedure; first, the surface was prepared using fine emery paper and degreased using acetone. Then it was dusted with ground pummice to aid adhesion of the photographic emulsion. By dipping the end of the specimen into a very shallow dish the photographic emulsion 'Silver Magic' (manufactured by Barfen Photochemicals Ltd) was applied, in dark room conditions. In order to ensure an even coating, the emulsion occasionally required redistribution with a small artists paint brush. Ideally, this coating should be allowed to dry at room temperature for several hours before exposure. However, this drying time could be cut down by using a hot air blower. Care was required when using this technique because the force with which the hot air is expelled sometimes produced an uneven coating of emulsion.

When completely dry each specimen had a photographic negative of small square grids placed over it. This was weighted down by a small glass sheet to prevent buckling and thus ensure even contact of the negative with the photographic emulsion. Using a Durst M301 enlarging lamp a standard exposure time of 5 seconds was selected and used in all tests. The exposed emulsion required developing using normal black and white photographic processing chemicals. The specimen was covered in developing solution (Kodak D163) for one minute and washed in water, then immersed in a acid hardening fixing solution (Ilford Ilfofix) for one and a half minutes before a final rinse in water. Grids were then visible and secured for use.

4.2.3. Calculation of Strain Distributions.

By comparison of the grid pattern on a specimen both before and after deformation, the displacement of each grid intersection (node) may be calculated. These displacement details may then be used to calculate the strain distribution within the deformed specimen. Using

the infinitesimal strain formulation described by Spencer (1980), the following relationships between strain and displacement need to be evaluated in plane-strain deformation analysis:

$$\varepsilon_{xx} = \partial U_x / \partial x \qquad (4\text{-}1)$$

$$\varepsilon_{zz} = \partial U_z / \partial z \qquad (4\text{-}2)$$

$$\varepsilon_{zx} = \frac{1}{2}\left(\frac{\partial U_x}{\partial z} + \frac{\partial U_z}{\partial x} \right) \qquad (4\text{-}3)$$

A computer program was written to perform the necessary calculations using the resources of a DEC-20 computer. Each deformed element (square bounded by grid lines) as measured in global coordinates (x,z) was mapped onto a square in local coordinates (X,Z) as shown in figure 4.5. For each node the displacement gradients, with respect to local coordinates, were calculated. For example, at node 1 these are given by:

$$\left(\frac{\partial U_x}{\partial x}\right)_1 = \frac{U_x(2) - U_x(1)}{X(2) - X(1)} \qquad (4\text{-}4)$$

$$\left(\frac{\partial U_x}{\partial Z}\right)_1 = \frac{U_x(3) - U_x(1)}{Z(2) - Z(1)} \qquad (4\text{-}5)$$

$$\left(\frac{\partial U_z}{\partial X}\right)_1 = \frac{U_z(2) - U_z(1)}{X(3) - X(1)} \qquad (4\text{-}6)$$

$$\left(\frac{\partial U_z}{\partial Z}\right)_1 = \frac{U_z(3) - U_z(1)}{Z(3) - Z(1)} \qquad (4\text{-}7)$$

These displacement gradients were transformed back into global coordinates using the Jacobian formulation:-

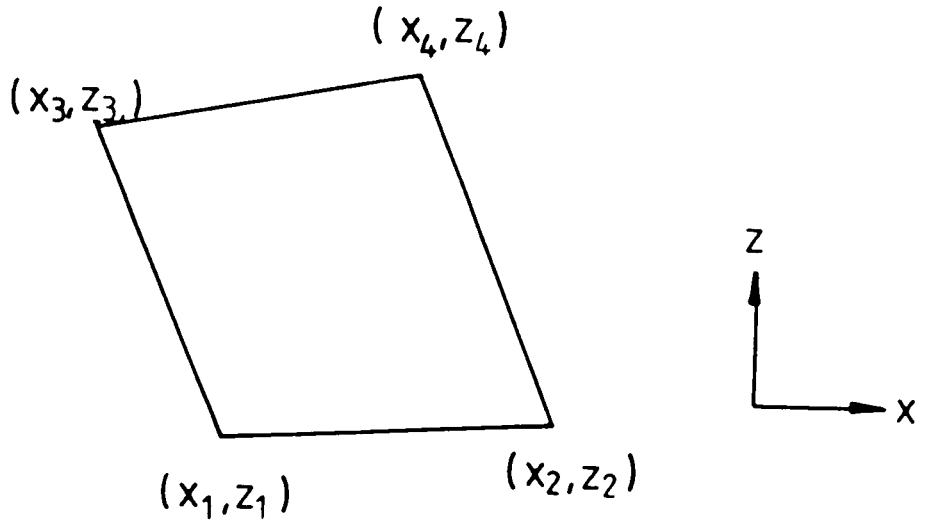

(a) Deformed element in Cartesian coordinates

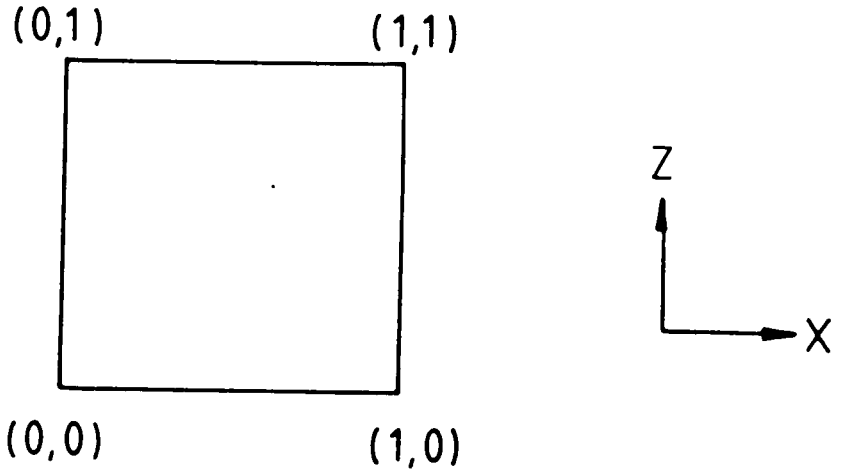

(b) Deformed element in local coordinates

Figure 4.5 Deformed element mapped onto local coordinates.

$$J = \begin{pmatrix} \frac{\partial x}{\partial X} & \frac{\partial z}{\partial X} \\ \\ \frac{\partial x}{\partial Z} & \frac{\partial z}{\partial Z} \end{pmatrix}$$

$$= \begin{pmatrix} \frac{x(2) - x(1)}{X(2) - X(1)} & \frac{z(2) - z(1)}{X(2) - X(1)} \\ \\ \frac{x(3) - x(1)}{Z(3) - Z(1)} & \frac{z(3) - z(1)}{Z(3) - Z(1)} \end{pmatrix} \qquad (4\text{-}8)$$

(evaluated for undeformed coordinates).

$$J^{-1} = \begin{pmatrix} \frac{\partial X}{\partial x} & \frac{\partial Z}{\partial x} \\ \\ \frac{\partial X}{\partial z} & \frac{\partial Z}{\partial z} \end{pmatrix} \qquad (4\text{-}9)$$

Therefore, it is now possible to evaluate the displacement gradients in the global coordinates in the following way:-

$$\left(\frac{dU_x}{\partial x}\right)_1 = \frac{\partial X}{\partial x}\ \frac{\partial U_x}{\partial X} + \frac{\partial Z}{\partial x}\ \frac{\partial U_x}{\partial Z} \qquad (4\text{-}10)$$

$$\left(\frac{\partial U_x}{\partial z}\right)_1 = \frac{\partial X}{\partial z}\ \frac{\partial U_x}{\partial X} + \frac{\partial Z}{\partial z}\ \frac{\partial U_x}{\partial Z} \qquad (4\text{-}11)$$

$$\left(\frac{\partial U_z}{\partial x}\right)_1 = \frac{\partial X}{\partial x}\ \frac{\partial U_z}{\partial X} + \frac{\partial Z}{\partial x}\ \frac{\partial U_z}{\partial Z} \qquad (4\text{-}12)$$

$$\left(\frac{\partial U_z}{\partial z}\right)_1 = \frac{\partial Z}{\partial z}\ \frac{\partial U_z}{\partial Z} + \frac{\partial X}{\partial z}\ \frac{\partial U_z}{\partial X} \qquad (4\text{-}13)$$

Using the results of these calculations and the fact that there is no displacement in the y-direction, it is possible to construct the

displacement gradient tensor for deformation at any specified node of the grid element. This tensor is important in the analysis of deformation, but does not itself provide a suitable measure of deformation as all its components are not zero for a rigid-body rotation. The Lagrangian strain tensor, γ_L , is one suitable measure of deformation which may be obtained with a knowledge of the value of the deformation gradient tensor. This is defined by:

$$\gamma_L = \frac{1}{2}(C-I) \qquad (4\text{-}14)$$

where C is the right Cauchy-Green deformation tensor, given by:

$$C = F^T . F \qquad (4\text{-}15)$$

and F is the deformation gradient matrix given by:-

$$F = \begin{bmatrix} \left(\frac{\partial U_x}{\partial x} + 1\right) & \partial U_z / \partial x \\ \partial U_x / \partial z & \left(\frac{\partial U_z}{\partial z} + 1\right) \end{bmatrix} \qquad (4\text{-}16)$$

Now the strain components relating to deformation at any specified node may be calculated using equations 4.1 to 4.3. Generalised plastic strain, as given by the following equation, may also be calculated:-

$$\bar{\varepsilon} = \sqrt{(2\{(\varepsilon'_x - \varepsilon'_y)^2 + (\varepsilon'_y - \varepsilon'_z)^2 + (\varepsilon'_z - \varepsilon'_x)^2\})/3} \qquad (4\text{-}17)$$

where ε'_x etc indicate deviatoric strain components.

This complete calculation process was repeated for each node within each element, and each element within the complete grid, to provide a strain map of the deformed specimen. The strain distributions obtained from this approach are presented in section 4.4.2.

4.2.4 Hardness Measurements.

The hardness test gives a measure of the stress required to cause plastic flow of a metal from its resistance to penetration of an indenter. This resistance may be calculated from the diameter of the impression remaining in a specimen after a known load has been applied to an indenter. The hardness measurements in this thesis were obtained using a Vickers pyramid indenter where the hardness number (Vickers Pyramid Number, or VPN) is defined as the load divided by the area of the indentation in kgf/mm^2 and bears the following relationship to the yield stress (Tabor, 1951)

$$VPN\ (kgf/mm^2) = 0.3\ Y\ (MN/m^2) \qquad (4.18)$$

Two different loads were used for testing purposes, 100g and 20kg. In the remainder of this work results obtained from using only 100g load will be referred to as microhardness values and those obtained using the heavier load as macrohardness values. The results are presented in section 4.4.3. The theoretical background to this test is dealt with in detail in the work of Tabor (1951) and Bowden and Tabor (1964).

4.3 Finite-element analyses.

4.3.1. Finite-element idealisation.

Three basic finite-element meshes were used for the work presented in this chapter. The first, used in the deformation modelling of an initially circular section specimen of both materials, is illustrated in figure 4.6. One quarter of the complete specimen cross section is modelled, because deformation in the remaining quadrants follows from arguments of symmetry. The elements are shown in section, with the complete mesh one layer thick as may be seen from the axonometric projection in figure 4.6. As is necessary when modelling a

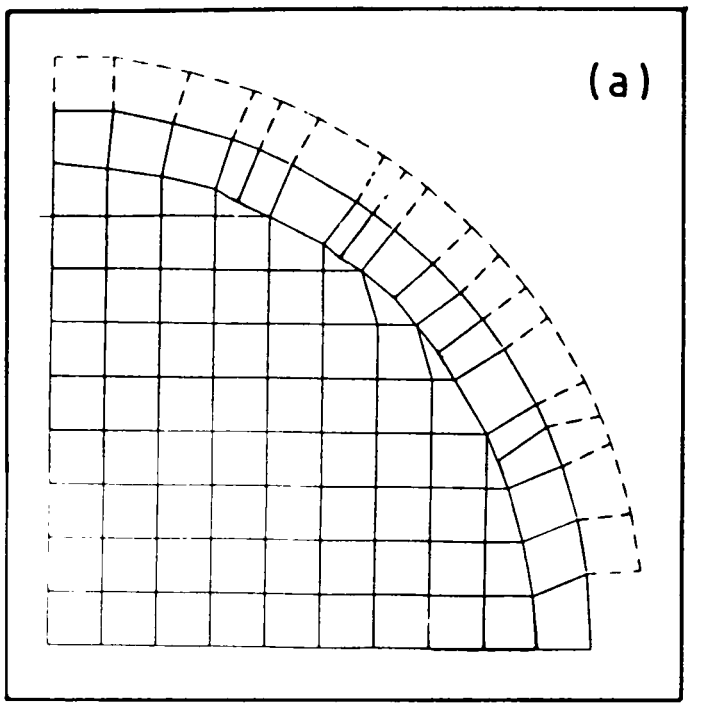

Figure 4·6 Finite-Element Mesh : Circular Section

(a) Cross-sectional view

(b) Axonometric projection

Friction layer elements are shown by the dashed lines in (a)

specimen of this shape with only eight-noded brick type elements, certain irregular nodal arrangements need to be introduced. Rather than locate these at the edge of the model, previous tests have shown that fewer computational problems arise if regular elements line the free surface. So the irregular elements are located within the body of the mesh. Eighty-seven elements are included, with an additional seventeen elements attached to its free surface. These extra elements are used in the finite-element formulation for the purpose of simulating interface friction. These friction layer elements are distinguished in the sectional illustration by broken line boundaries and are fictitious in the sense of not contributing to the dimensions of the workpiece being modelled. In this theoretical construction the specimen has a radius of 1 cm, which is equal to that used in the experimental investigation.

The first geometry to be examined, with machined flats, is shown in figure 4.7. This is very similar in construction to the circular section mesh, but contains slightly fewer elements because of the smaller volume of the specimen. The model conatins 82 elements for the workpiece and 16 friction layer elements. It has an initial height H = 0.9cm, and an initial contact width W = 0.443cm, so in this case H/W is 2.03. The second geometry with machined flats, illustrated in figure 4.8, had an initial height H = 0.8cm and H/W of 1.33. The model contained 90 elements of which 15 were used for the friction layer.

4.3.2. Determination of Constitutive Relationships.

As part of the input data which enables the finite-element technique to model metal flow, material properties in the form of a stress-strain curve are required.

A detailed set of axisymmetric compression tests was performed on 60-40 brass in order to determine the stress-strain relationship. First, a

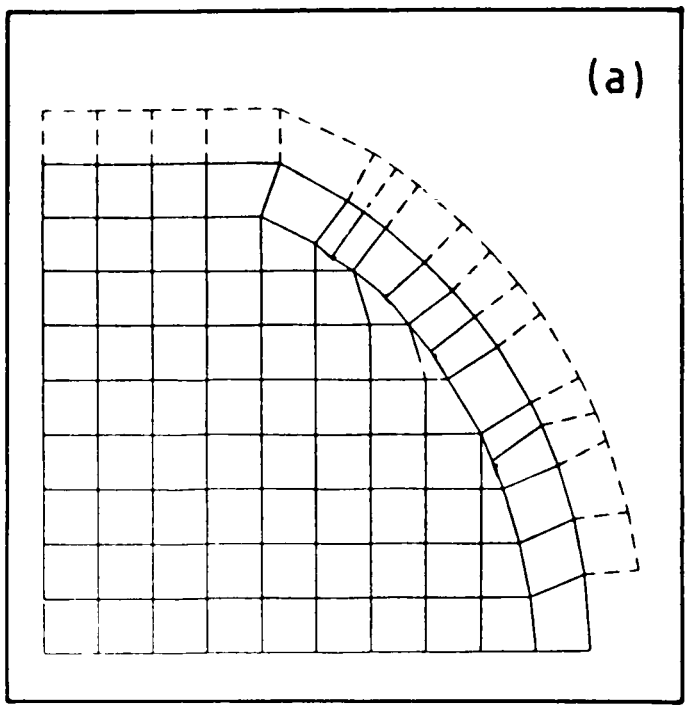

Figure 4·7 Finite-Element Mesh : H/W = 2·03

(a) Cross-sectional view

(b) Axonometric projection

Friction layer elements are shown by the dashed lines in (a)

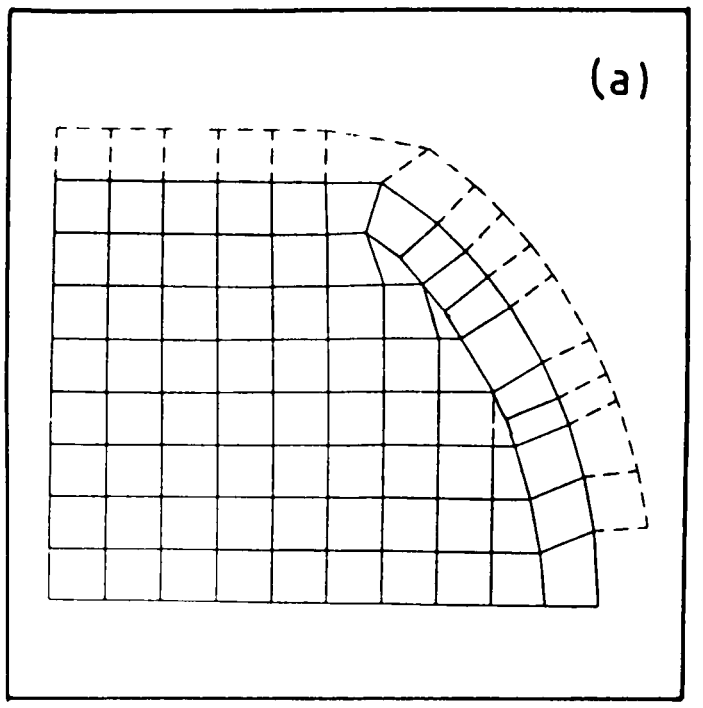

Figure 4·8 Finite-Element Mesh: H/W = 1·33

(a) Cross-sectional view

(b) Axonometric projection

Friction layer elements are shown by the dashed lines in (a)

specimen having an initial height to diameter ratio of unity and tested under well lubricated conditions (0.002" thick PTFE sheet) was used to produce the results shown in figure 4.9. An attempt was made to correct this compression test curve for the effects of friction using the method of Cook and Larke (1945). This method proposes that there will be no frictional contribution to the yield stress of an infinitely tall billet. Therefore, the extrapolation of the line connecting experimental values for known diameter to height values to zero diameter to height ratio should give a value of the yield stress independent of friction. Results obtained from cylindrical specimens of four aspect ratios at three different levels of strain have been plotted in figure 4.10. Unfortunately, these results do not support the model of Cook and Larke. Tests by Hartley (1979) also found that for very well lubricated specimens the trend to zero friction could not be identified.

One possible reason for the yield stress values for low diameter to height ratio departing from the expected trend is that there is a much larger contribution from redundant work for tall specimens. An alternative method of determining the coefficient of friction may be taken from the work of Rowe (1979), using the analogy of the strip compression test applied to cylindrical specimens of high height to diameter ratio. To this end the following equations are used:-

$$\frac{p_1}{2k_n} = 1 + \frac{1}{2}\mu\frac{D}{h_1} \qquad (4.19)$$

$$\frac{p_2}{2k_n} = 1 + \frac{1}{2}\mu\frac{D}{h_2} \qquad (4.20)$$

p_1 and p_2 are the yield stress values of cylinders of height h_1 and h_2

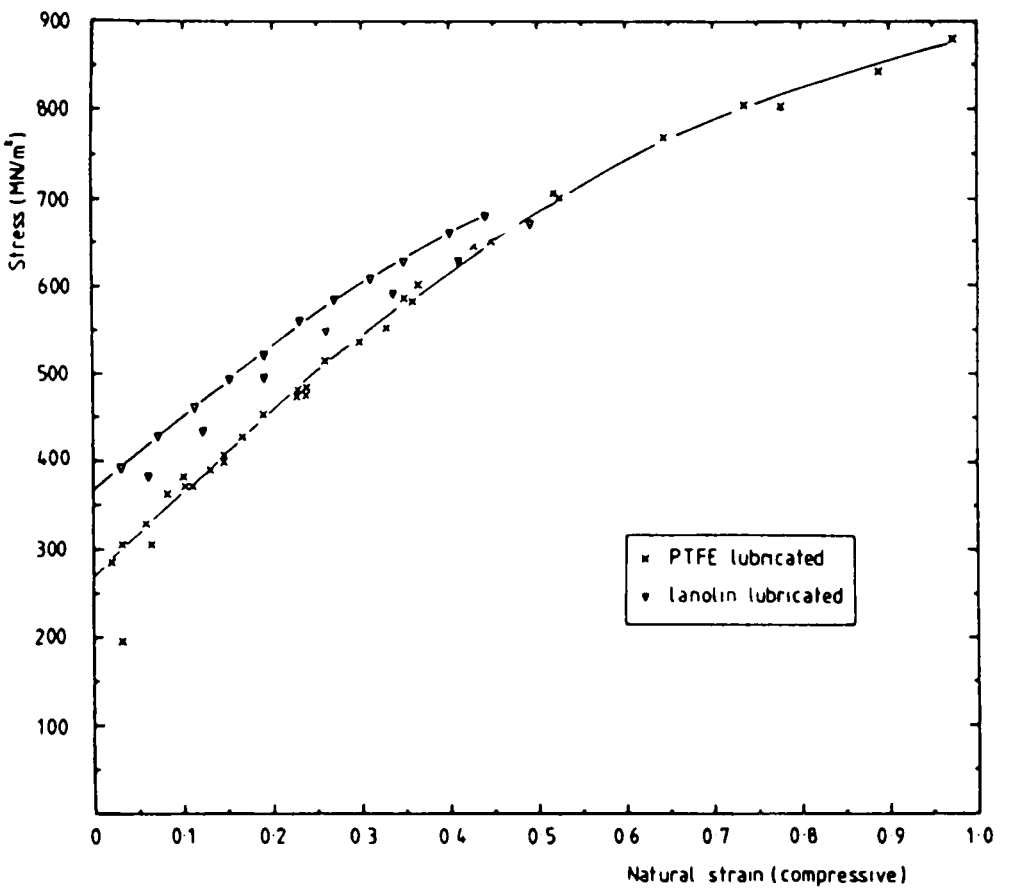

Figure 4·9

Compression test stress-strain curve for 60-40 brass.

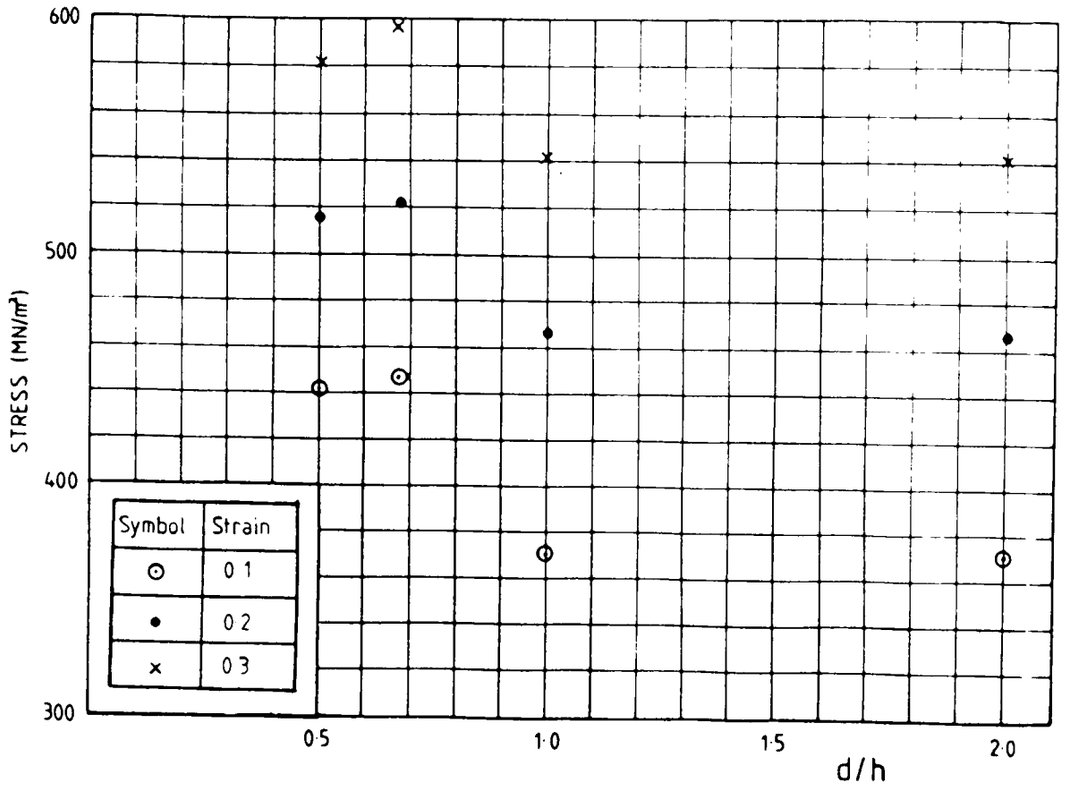

Figure 4·10 Results from the application of the Cook and Larke (1945) friction correction method to 60-40 brass

respectively. μ is the coefficient of friction. The true yield stress Y, is the same for both cylinders. As $p_1 = p_2$ for D/h = 1.0 and D/h = 2.0, μ must be equal to zero for these equations to hold. As a very effective lubricant was used (0.002" PTFE sheet) and no barreling of the specimen was observable it is quite possible that the level of friction is zero within the accuracy of this experiment. The compression test curve obtained using PTFE as a lubricant will therefore be supplied uncorrected to the finite-element modelling program. Figure 4.9 also contains, for comparison, the compression test curve obtained from brass specimens, with an initial height to diameter ratio of unity, lubricated with lanolin. As expected, these results are generally higher than those obtained using PTFE.

On the basis of the results presented for 60-40 brass a similar compression test with PTFE lubrication was performed on 7075 aluminium alloy. These stress-strain results are presented in figure 4.11.

4.3.3 Determination of interface friction conditions.

In order to model material deformation the finite-element program also requires a value for the interface shear factor, m, applicable to the material and lubrication conditions. This was determined experimentally using the 'Ring test' technique as used by Male and Cockroft (1964). This technique involves the forging of a flat ring shaped specimen. The coefficient of friction is related to the change in diameter produced by a given amount of compression. Specimens of aluminium and brass of outside diameter 1.905 cm, and geometric ratio 6:3:2 (outer diameter:inner diameter:height) were used in an unlubricated condition. The dies and specimen were cleaned with acetone before deformation, and the dies were reground for each material so that the results were not affected by a deposit on the dies of the previous

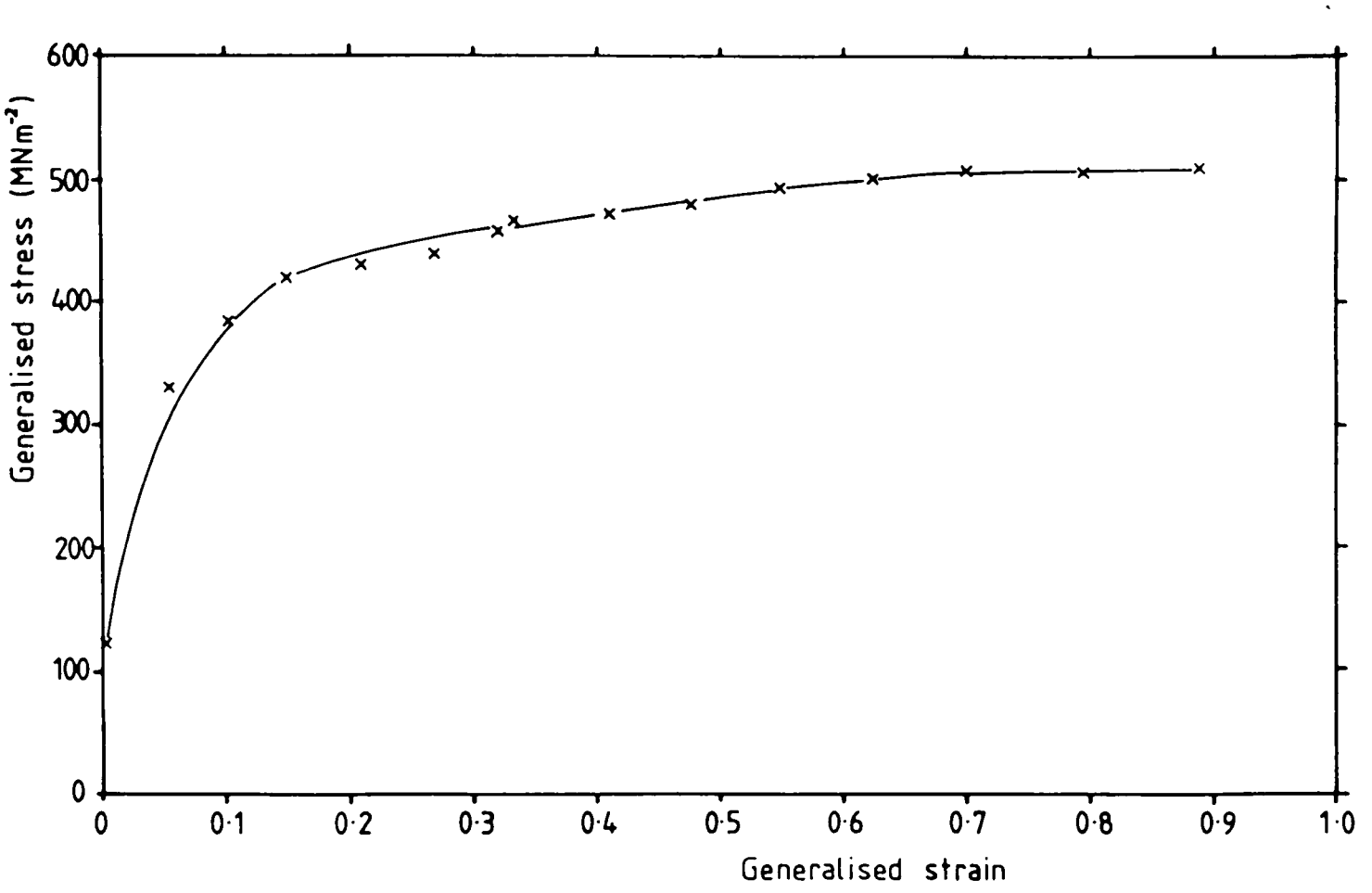

Figure 4·11.

Compression test stress-strain curve for 7075 aluminium alloy (continuous cast)

material tested. The tests were performed at room temperature, with a slow strain rate, on either an Avery 600 kN or a Dennison 3000 kN compression testing machine. All tests were performed with the specimen in its 'as turned' condition, as tests by Hartley (1979) indicated that surface finish had little effect.

Symmetric deformation of the material around the central hole was not observed throughout a sequence of tests, the asymmetry becoming more pronounced for increasing reduction in height. For this reason the maximum internal diameter was used.

(page 99)

A selection of the deformed specimens is shown in figure 4.12. Variation of the internal diameter with reduction in height is shown in figure 4.13, together with calibration curves calculated from data determined by Pillinger (1984) for the finite-element program EPFEP3.

Comparison of the experimental results with the calibration curves suggested a value for m of 0.25 for both materials. Further comment on the suitability of this choice follows in section 4.4.1.

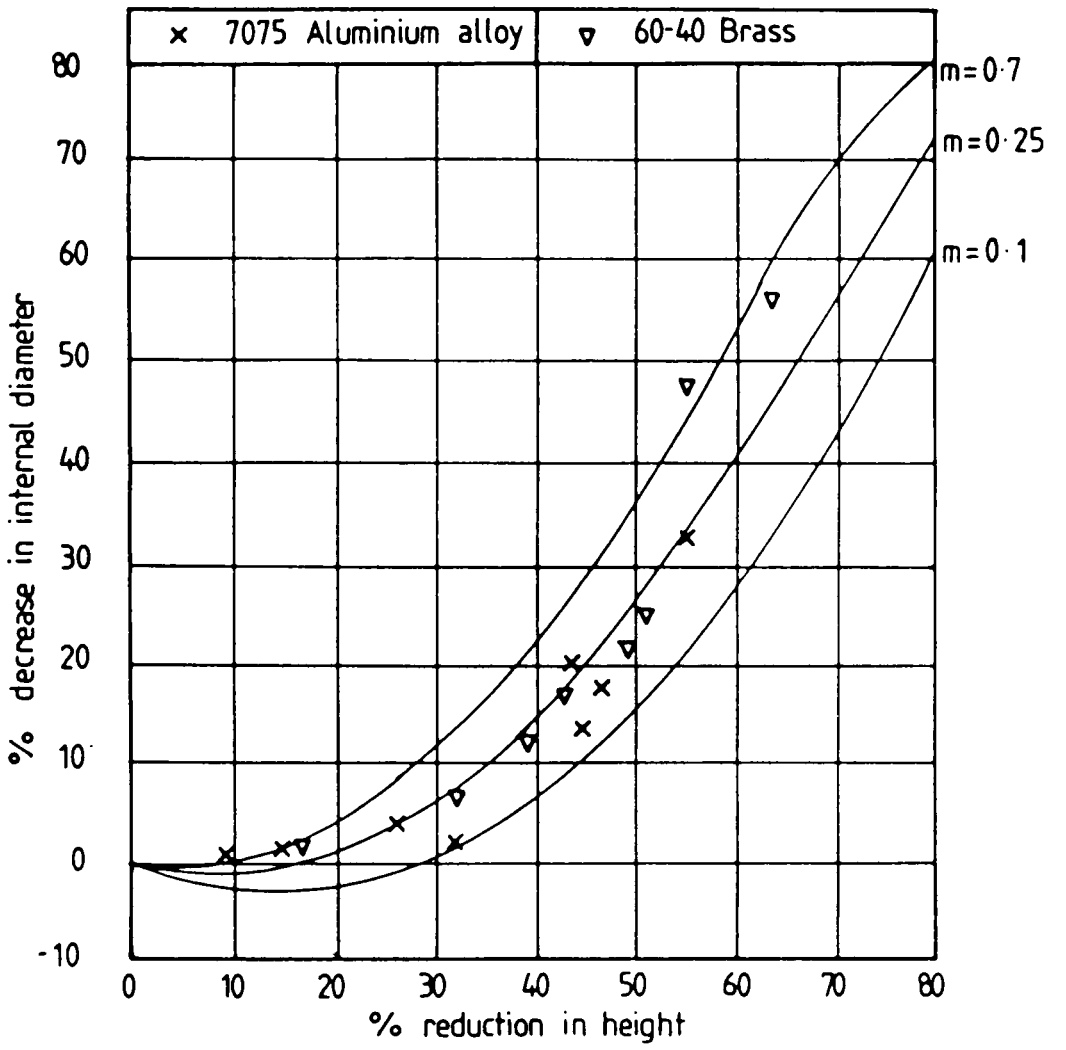

Figure 4.13

Ring test results and finite-element calibration curves.

4.4 Results and discussion.

4.4.1 Friction Sensitivity Tests.

In view of the experimental scatter shown in figure 4.13 the choice of friction factor needs to be explored further to ascertain the sensitivity of the finite-element model of side-pressing to different levels of friction. In order to investigate this effect the finite-element predicted deformation patterns were found for 60-40 brass with firstly a low value of interface friction (m = 0.01), as shown in figure 4.14(a), and secondly a high value of interface friction (m = 0.99) as shown in figure 4.14(b).

There is little observable difference between the two sets of results up to about 20% deformation. After this point the difference in flow patterns becomes more obvious and in the final illustration of each set, obtained after 60 increments of deformation, the difference is very clear, particularly with respect to the originally vertical lines which bulge much more for the high friction case. However, the difference in width of contact with the die is not very large.

Later results (see section 4.5.1) will show that the side-pressing operations are limited by the initiation of shear cracks, which occurred at about 16% reduction for aluminium and about 55% reduction for brass. For aluminium then, the choice of friction factor is not critical and the ring test results up to about 25% deformation lie close to the m=0.25 curve. In the case of brass the correct choice of friction factor is more important, but up to 55% deformation the choice of m=0.25 is the most reasonable.

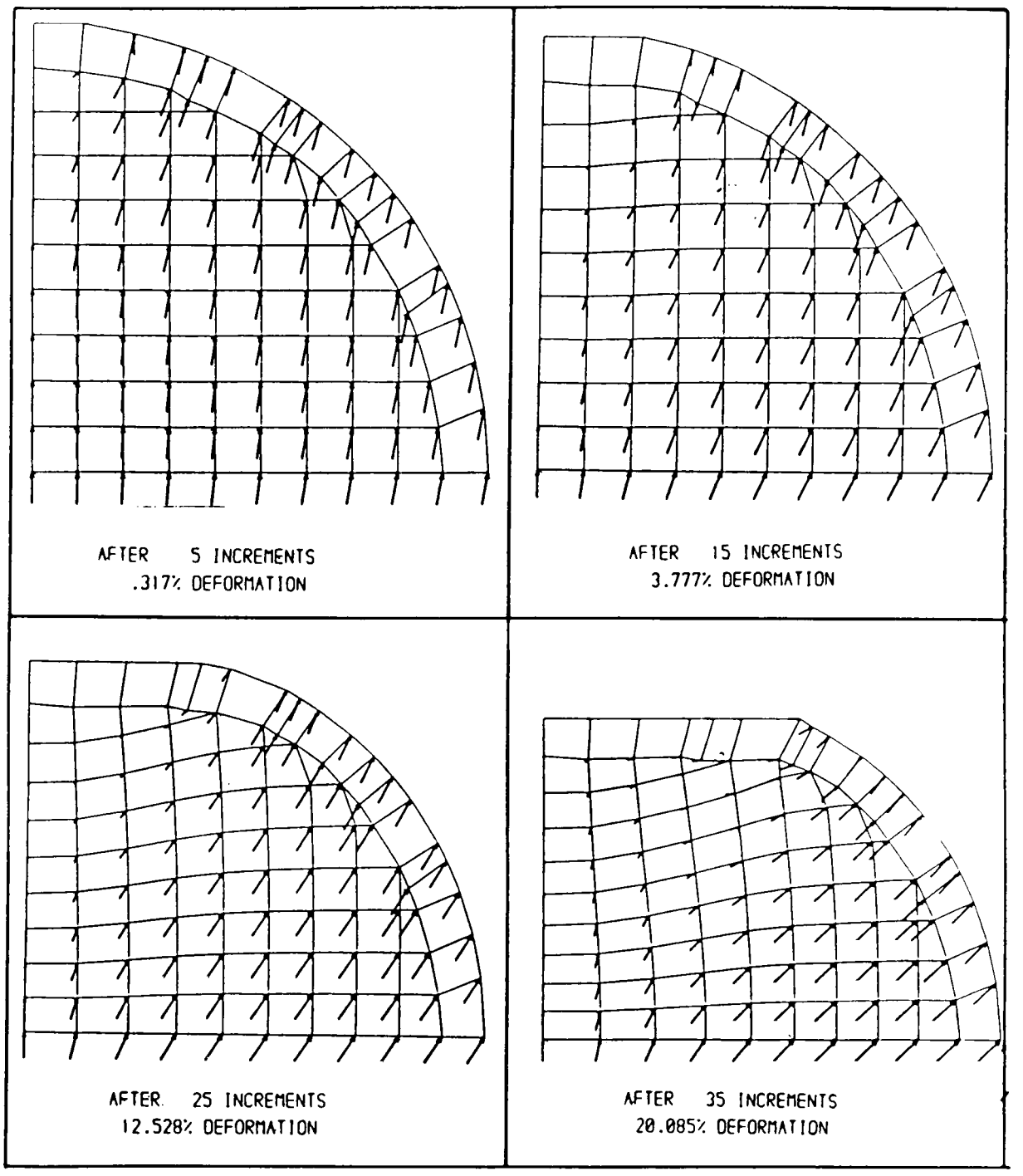

Figure 4·14(a) Incremental Displacement Vectors Calculated for Plane-Strain Side-Pressing of 60-40 Brass with Low Interface Friction (m = 0·01)

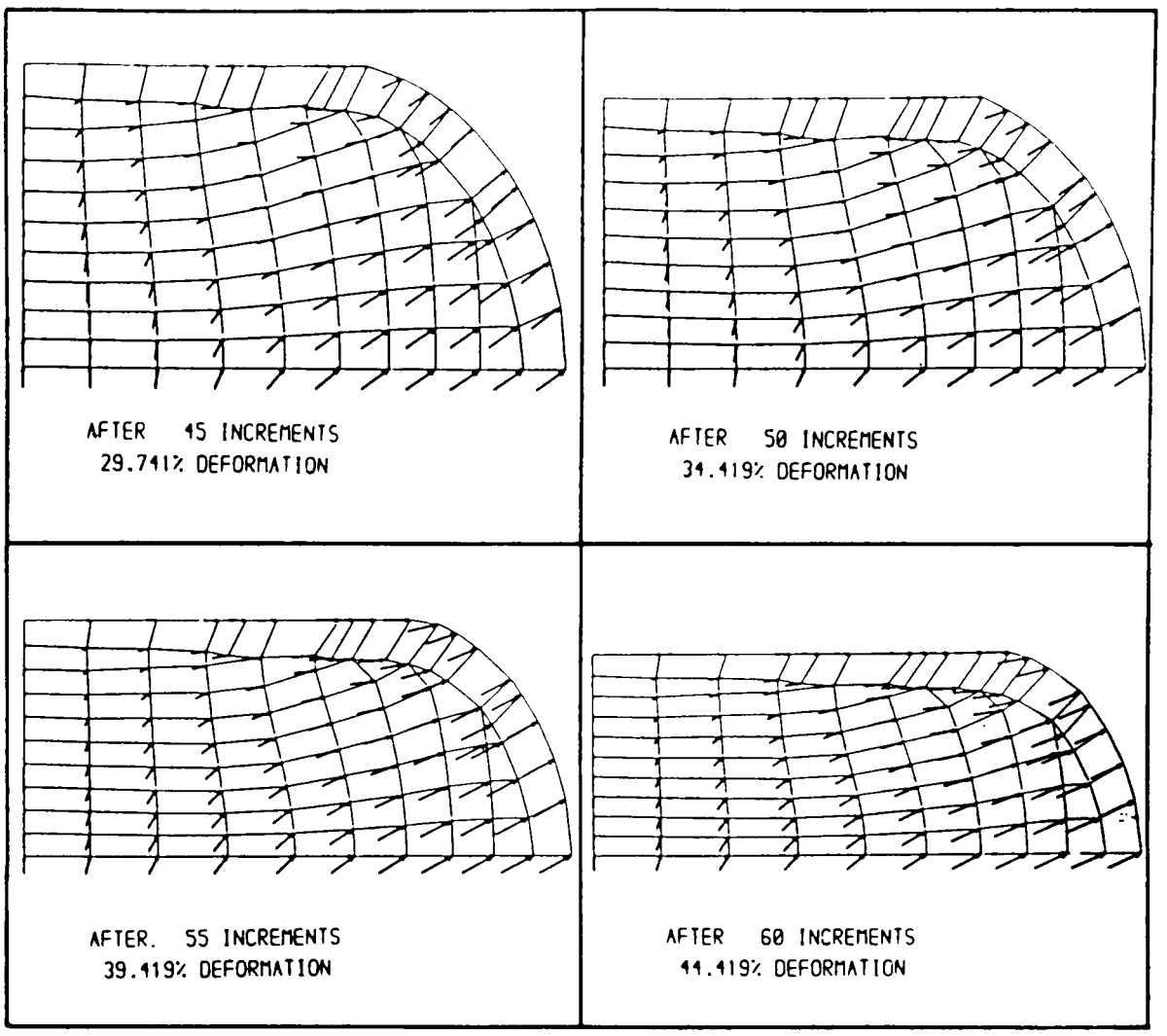

Figure 4·14(a) (cont) Incremental Displacement Vectors Calculated for Plane-Strain Side-Pressing of 60-40 Brass with Low Interface Friction (m = 0·01)

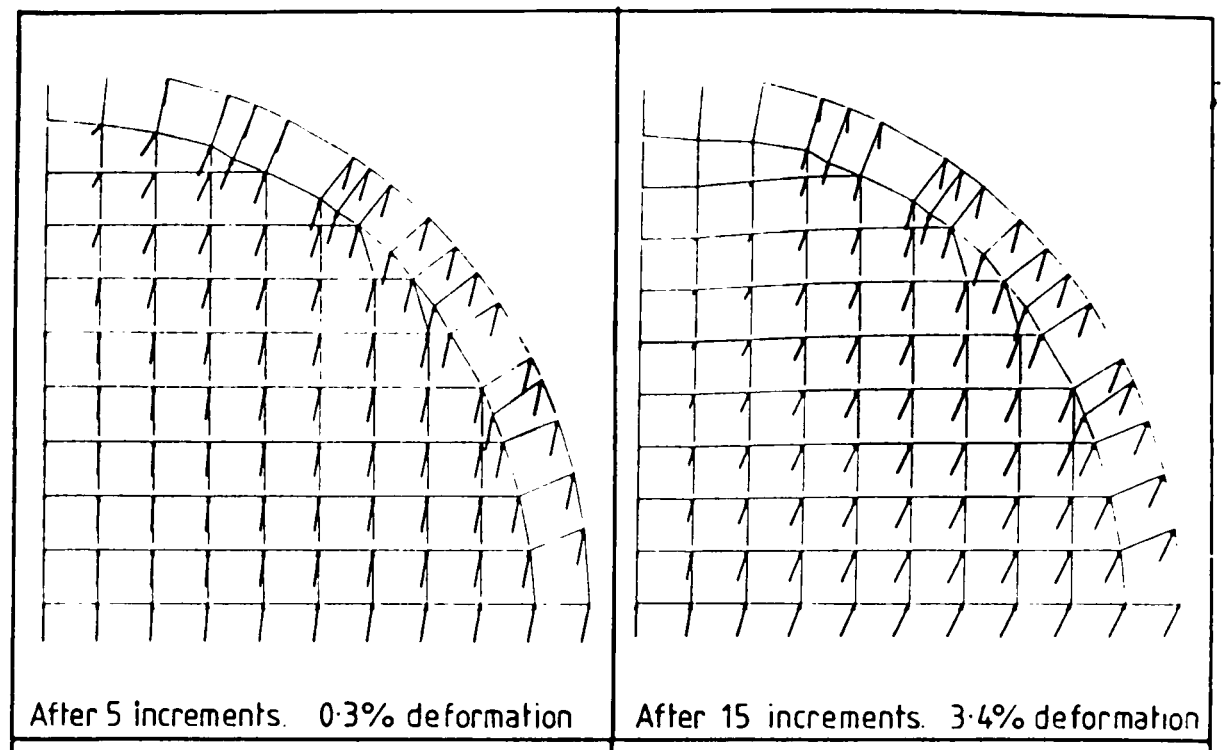

Figure 4·14(b) Incremental Displacement Vectors Calculated for Plane-Strain Side-Pressing of 60-40 Brass with high Interface Friction (m = 0·99)

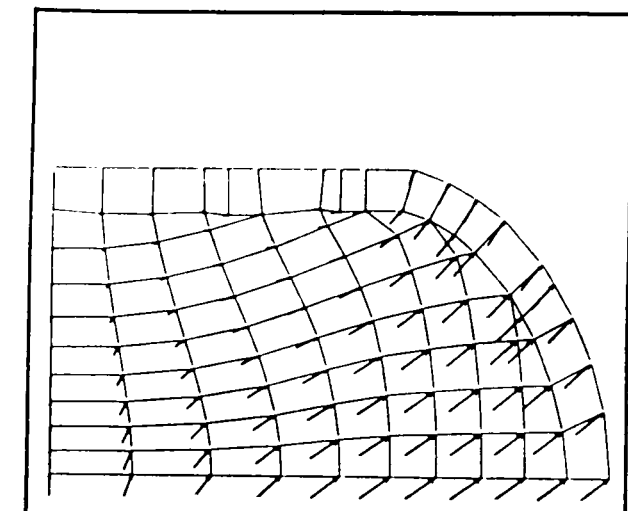

After 45 increments. 31·1% deformation

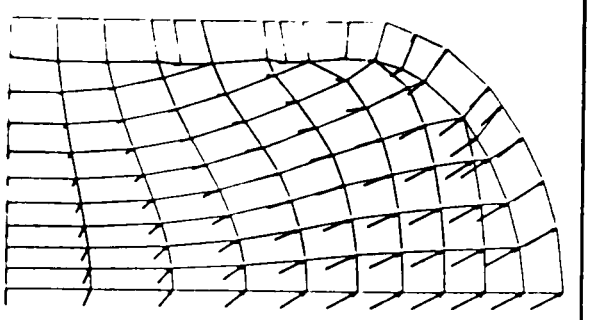

After 50 increments. 35·7% deformation

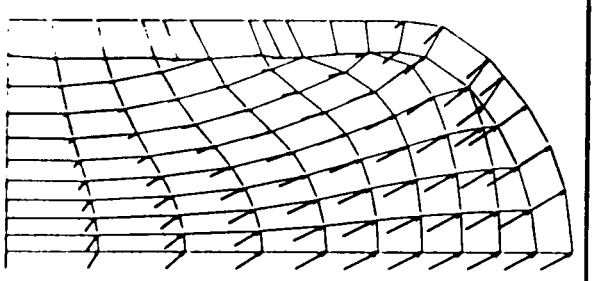

After 55 increments. 40·7% deformation

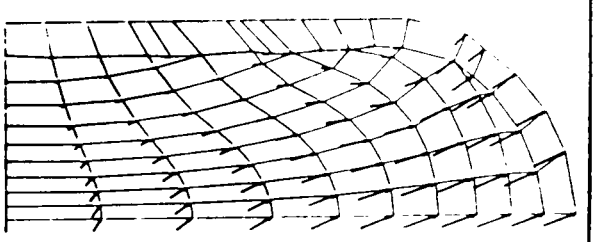

After 60 increments. 45% deformation

Figure 4·14(b) (cont) Incremental Displacement Vectors Calculated for Plane-Strain Side-Pressing of 60-40 Brass with high Interface Friction (m = 0·99).

4.4.2 Comparison of FE and visioplasticity results.

This section presents and compares the finite-element and visioplasticity results. Figure 4.15 shows the finite-element and experimental grid deformation patterns for the plane-strain side-pressing of the initially circular cross-sectional 60-40 brass. Here, the actual patterns of deformation appear to agree very well. However, the values of generalised strain calculated from the movements of the grid intersections are not in such good agreement; the peak strain in the experimental study, as indicated by the m zone in figure 4.15(d), is approximately double that obtained from the finite-element program as shown by the k zone in figure 4.15(c).
The regions of low strain agree much better but this is clearly an unsatisfactory comparison.

Results obtained from the visioplasticity study of 7075 aluminium alloy, and presented in figures 4.16, 4.17 and 4.18, also show rather poor agreement. General trends of metal flow may be picked out but quantitative comparisons of plastic strain prove unsatisfactory. For the example presented of the deformation of originally circular section 7075 aluminium alloy, peak strains for the visioplasticity solution are lower than those produced by the finite-element program.
The visioplasticity solutions obtained for the geometries with machined flats give values in excess of those obtained from the finite-element program.
In the case of the solution for 7075 aluminium alloy with an initial height to width ratio of 1.33 (figure 4.18) the shear band strains calculated from the visioplasticity grid are much higher than from the finite-element solution. This comparison has been made at a deformation of only 1/2 % less than that at which fracture initiation was observed experimentally and so the difference in strain may be due to a

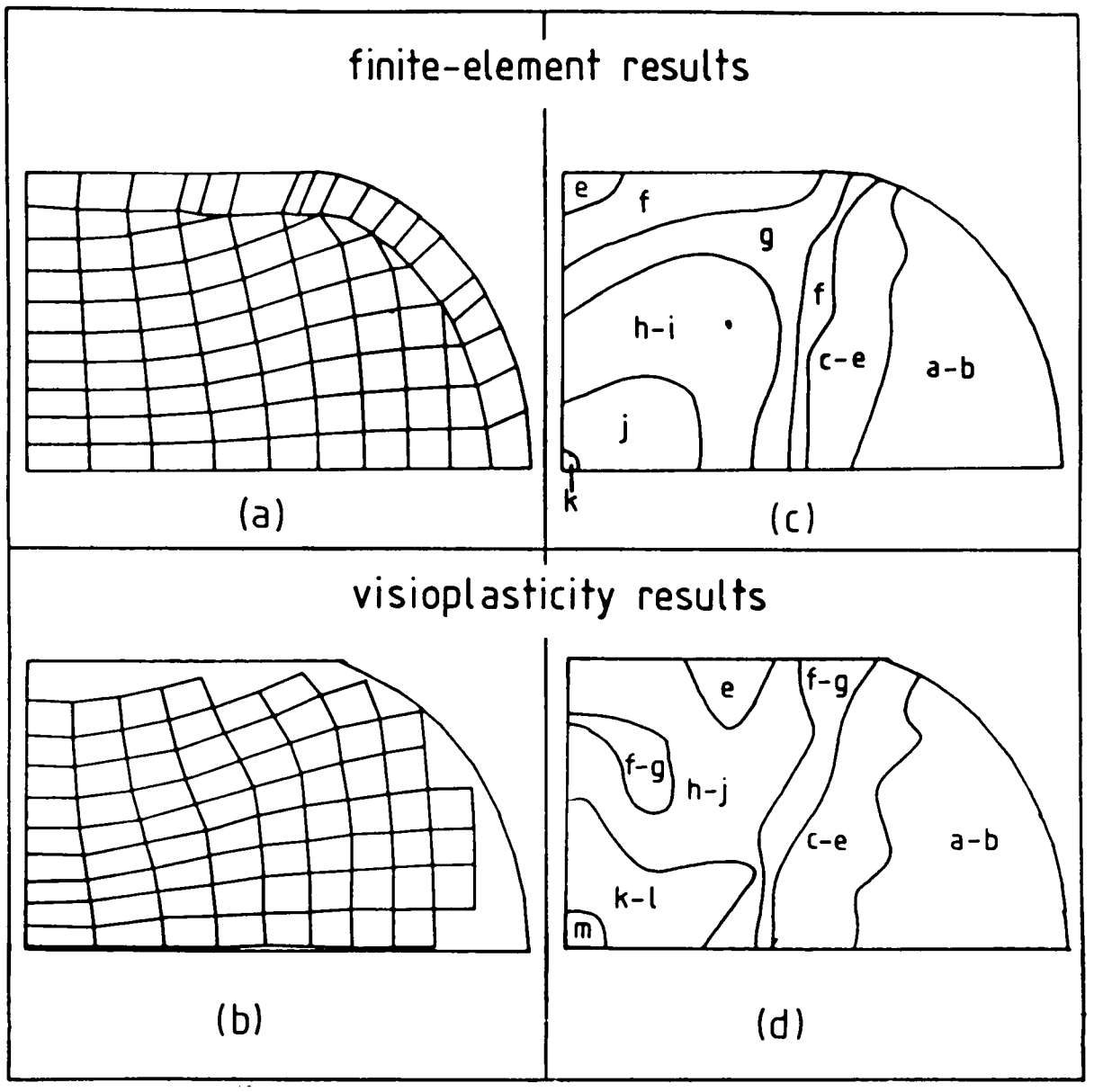

Key to contour values:

Region	G.P.S.
a	0·0 - 0·05
b	0·05-0·10
c	0·10-0·15
d	0·15-0·20
e	0·20-0·25
f	0·25-0·30
g	0·30-0·35
h	0·35-0·40
i	0·40-0·45
j	0·45-0·50
k	0·50-0·55
l	0·55-1·0
m	above 1·0

Figure 4·15.

Comparison of FE and visioplasticity results for initially circular section 60-40 brass at 28% deformation

(a),(b) grid deformation patterns

(c),(d) generalised plastic strain distributions.

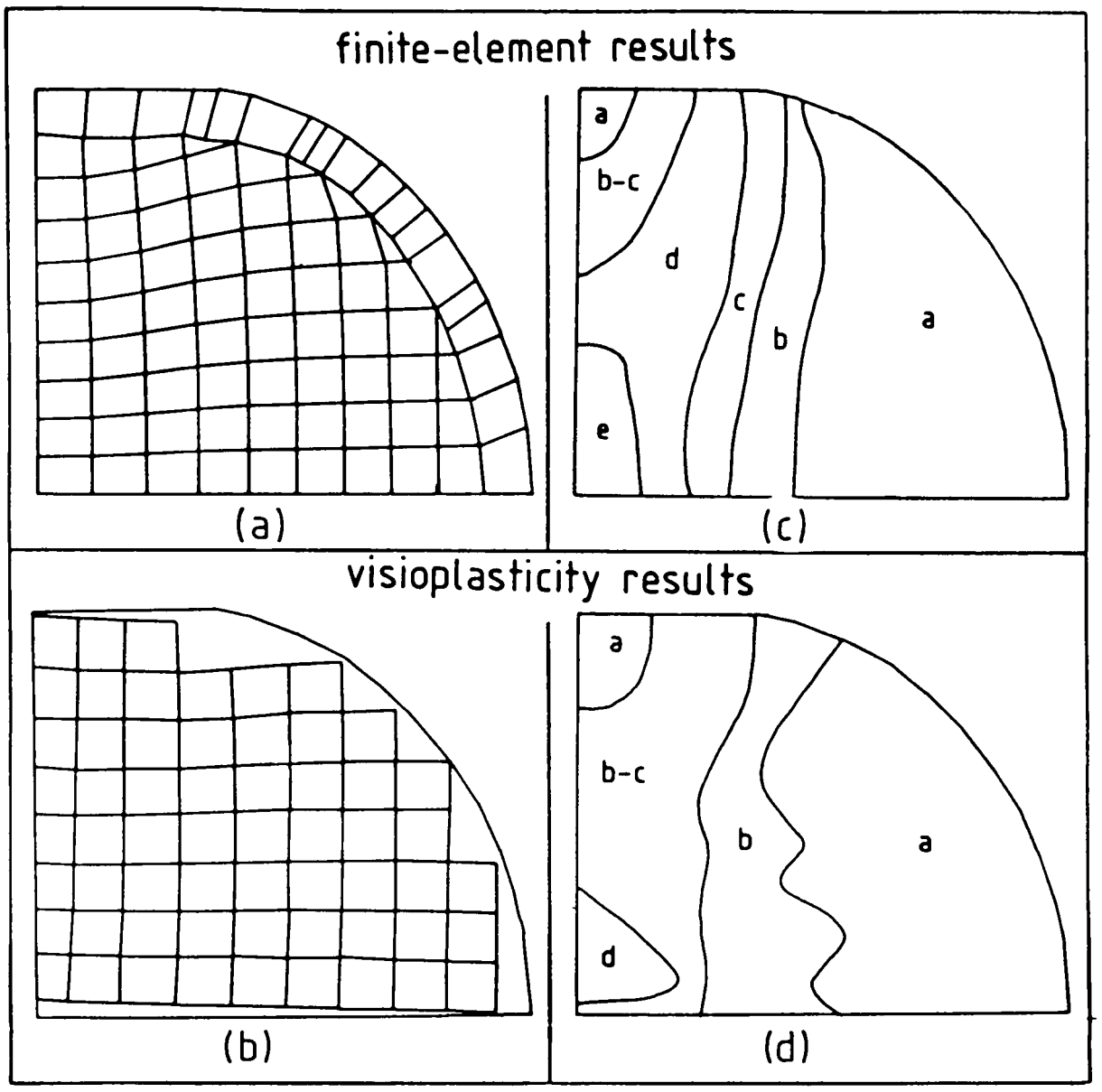

Key to contour values:

Region	G.P.S.
a	0·0 - 0·05
b	0·05-0·10
c	0·10-0·15
d	0·15-0·20
e	0·20-0·25
f	0·25-0·30
g	0·30-0·35
h	0·35-0·40
i	0·40-0·45
j	0·45-0·50
k	0·50-0·55
l	0·55-1·0
m	above 1·0

Figure 4·16.

Comparison of FE and visioplasticity results for initially circular section 7075 aluminium alloy at 12·7% deformation:

(a),(b) grid deformation patterns

(c),(d) generalised plastic strain distributions.

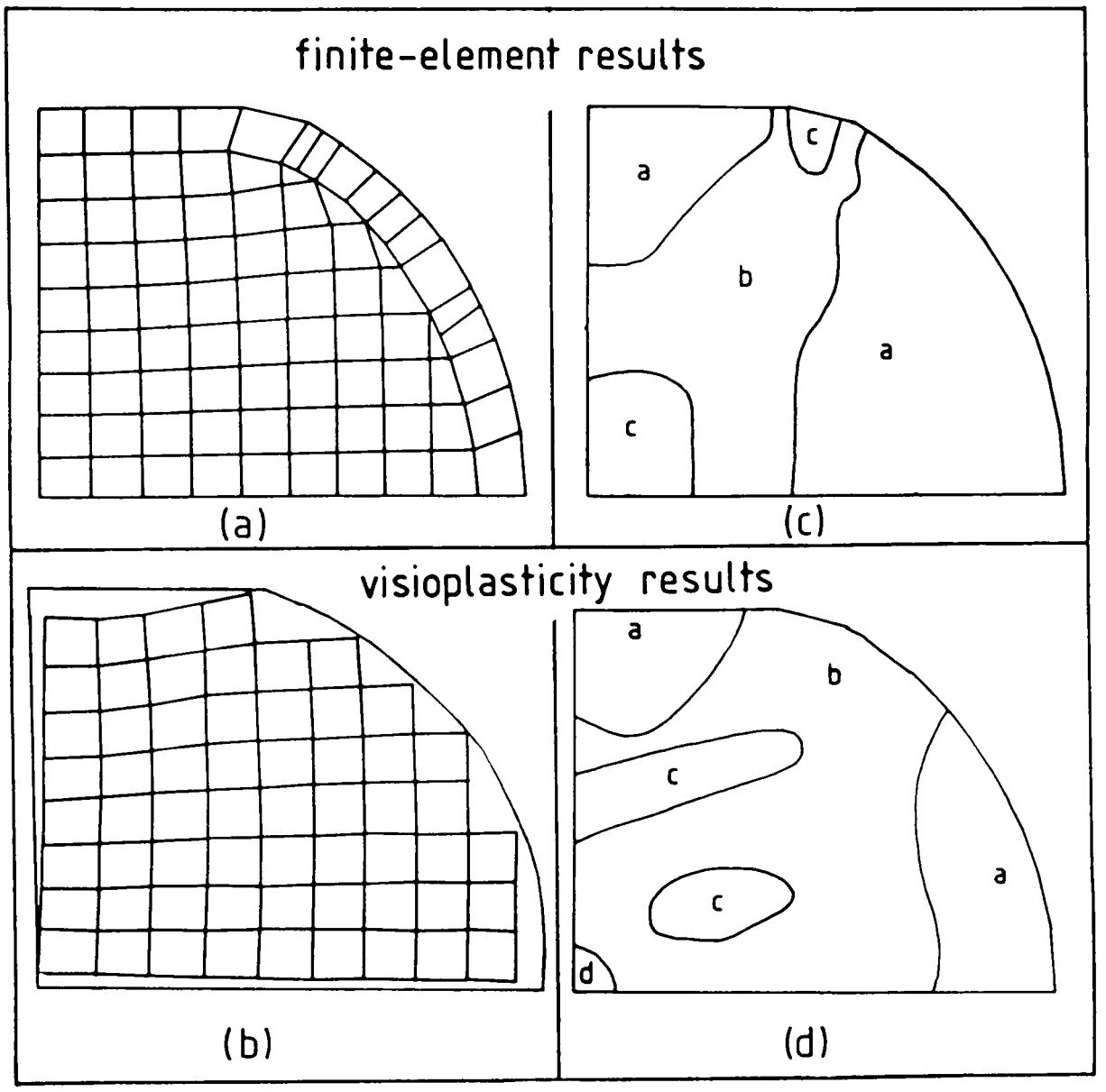

Key to contour values:

Region	G.P.S.
a	0·0 - 0·05
b	0·05-0·10
c	0·10-0·15
d	0·15-0·20
e	0·20-0·25
f	0·25-0·30
g	0·30-0·35
h	0·35-0·40
i	0·40-0·45
j	0·45-0·50
k	0·50-0·55
l	0·55-1·0
m	above 1·0

Figure 4·17.

Comparison of FE and visioplasticity results for 7075 aluminium alloy with initial H/W = 2·03 at 6·3% deformation:

(a),(b) grid deformation patterns

(c),(d) generalised plastic strain distributions

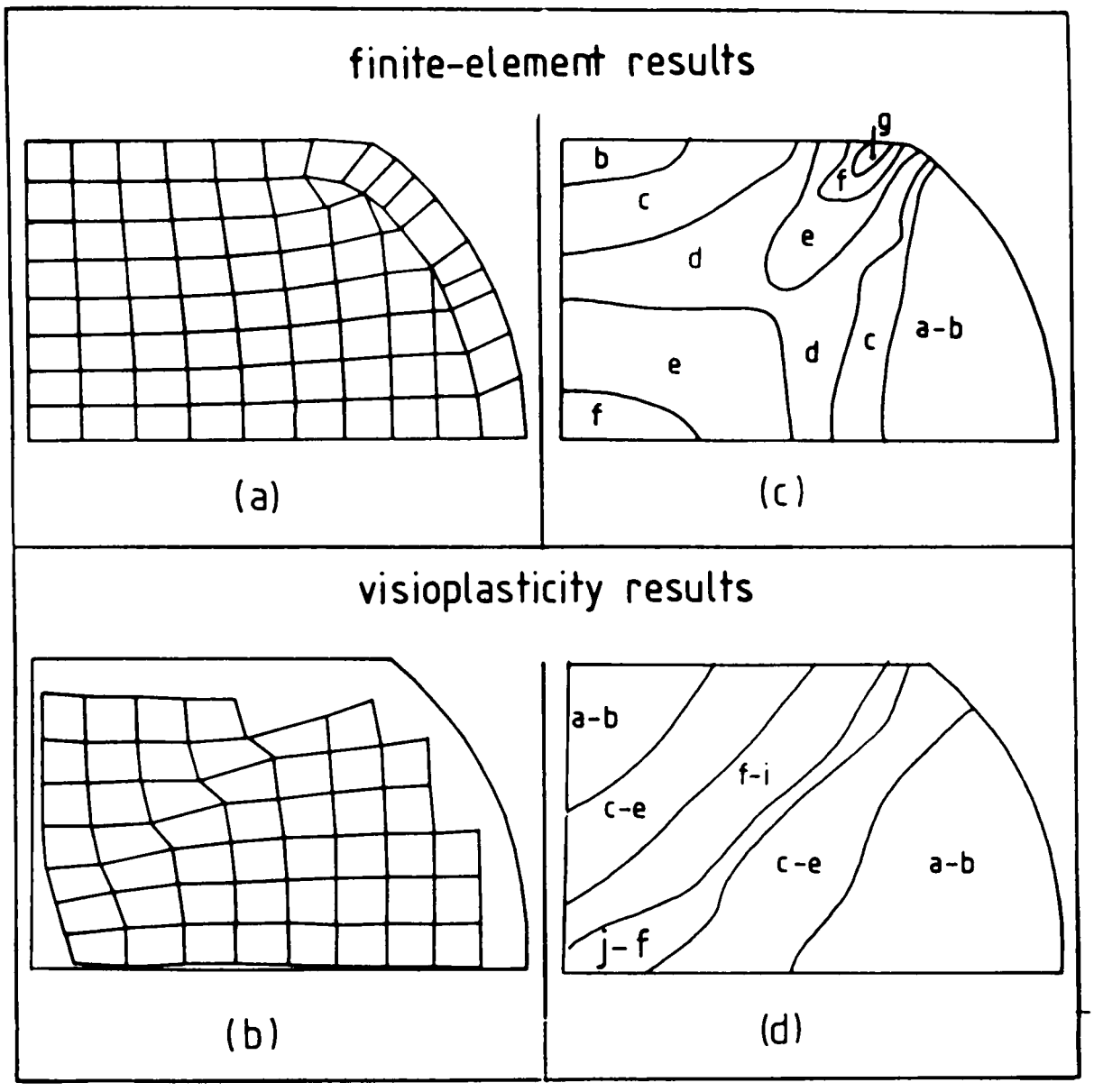

Key to contour values:

Region	G.P.S.
a	0·0 - 0·05
b	0·05-0·10
c	0·10-0·15
d	0·15-0·20
e	0·20-0·25
f	0·25-0·30
g	0·30-0·35
h	0·35-0·40
i	0·40-0·45
j	0·45-0·50
k	0·50-0·55
l	0·55-1·0
m	above 1·0

Figure 4·18.

Comparison of FE and visioplasticity results for 7075 aluminium alloy with initial H/W = 1·33 at 15·4% deformation:

(a),(b) grid deformation patterns

(c),(d) generalised plastic strain distributions.

localisation in plastic flow along the shear band prior to fracture initiation.

In the light of this generally unsatisfactory comparison of strain a series of accuracy tests were proposed. The first task set for both the FE and visioplasticity programs required the calculation of generalised plastic strain for the homogeneous plane-strain compression of a one-element slab to 50% deformation. The FE program calculated the theoretically correct value of 0.797 which is slightly lower than the 0.812 calculated using the visioplasticity analysis program. However, this strain difference is not large enough to account for the differences observed in practice. A more detailed series of tests was therefore performed to calculate the effect on the generalised plastic strain obtained from the visioplasticity technique of possible errors in the measurement of the photographic grid intersection positions as reported in the following section.

4.4.2.1 Possible effect of experimental errors on the visioplasticity strain calculation.

An undeformed grid square of the same size as defined experimentally was used (Figure 4.19(a)). Each deformed grid square had a corner, or combination of corners, moved out by a distance corresponding to:

(a) half a line width (0.00008m) or

(b) a full line width (0.00016m)

as measured for an originally vertical line in a heavily deformed grid. Part (b) corresponds to half a line width error in measurement of both the undeformed and the deformed grid. The four different cases studied are illustrated in figures 4.19(b) to 4.19(e).

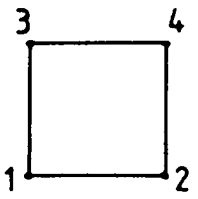

(a) An undeformed grid square of the same size as used experimentally.

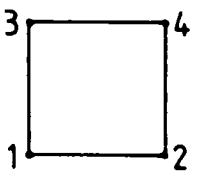

(b) Case 1.
Corner 4 moved out.

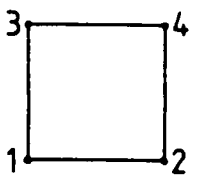

(c) Case 2.
Corners 2 and 4 moved out.

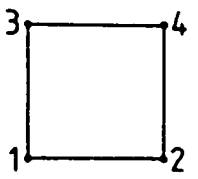

(d) Case 3.
Corners 2, 3 and 4 moved out.

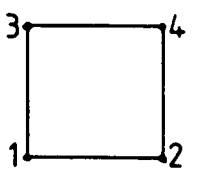

(e) Case 4.
All corners moved out.

Case	Line width		G.P. Strain
	half	full	
1	√		0·043
1		√	0·081
2	√		0·053
2		√	0·100
3	√		0·057
3		√	0·105
4	√		0·044
4		√	0·083

(f)
Table of generalised plastic strain values.

Figure 4·19.
Visioplasticity error studies.

This table shows that quite large generalised plastic strain values can result from typical errors in the measurement of the grid intersections in the visioplasticity mesh. The errors are large enough to account for the differences between most of the finite-element and experimental results previously presented.

Due to the high level of errors found here, it was considered necessary to produce an alternative experimental comparison and to this end the hardness results in section 4.4.3 were obtained.

4.4.3 Comparison of FE and hardness results.

As a result of the shortcomings of the visioplasticity strain calculation technique, as described in section 4.4.2, a series of hardness tests were performed on the experimentally deformed specimens. Initially, a microhardness survey was performed on a plane-strain side-pressed specimen of 60-40 brass at 55% deformation. The values obtained were converted to give an experimental value of yield stress using the equation previously given in section 4.2.4.

Comparison of these microhardness results with hardness calculated from FE predicted generalised plastic strain distribution showed that the experimental results were very much lower than the numerical calculations. This discrepancy prompted a further investigation to check the conversion factor used to obtain yield stress from Vickers Pyramid Number. This involved a microhardness survey of the upset cylindrical specimens used to obtain the compression test curve for 'as received' 60-40 brass (section 4.3.2). Six specimens were deformed, using PTFE as the lubricant, and eight hardness measurements were made on each

specimen. The plastic strain for each specimen was calculated using the reduction in height value and assuming uniform deformation. The levels of natural strain for these specimens were plotted against Vickers Pyramid Number as shown in figure 4.20. As may be seen from this graph there is so much scatter in these results that it was not possible to identify a relationship between true strain and microhardness.

One possible explanation for this is that in the microhardness test, such a small region of the metal is sampled that it may be substantially influenced by local changes in microstructure or by the quality of the surface finish of the prepared specimen as suggested by the wide range of microhardness values obtained for an undeformed specimen. In order to test this a Vickers macrohardness survey using an indenting load of 20kg (HV20) was performed on the other halves of the brass compression test specimens. Figure 4.21 shows the relationship that was obtained between true plastic strain, calculated using the reduction in height of the cylindrical specimens and assuming uniform deformation, and VPN after a correction had been made for an indentation associated strain of 8% as suggested by Tabor (1951). Much less experimental scatter was found and a curve could be easily fitted to these values, thus indicating that the macrohardness test is more suitable for this particular application than the microhardness test.

This experimental strain-macrohardness relationship was converted to the yield stress-macrohardness relationship and plotted in figure 4.22 using the compressive stress-strain curve previously illustrated in figure 4.9. This graph also contains Tabor's empirical stress-macrohardness line plotted for the same range of data. This latter line is a reasonable linear approximation to the experimental data for low stress, and if data had not been specifically calculated for 60-40 brass then it would have been a usable relationship for fairly low deformation.

The experimental curve based on macrohardness (HV20) does not show the

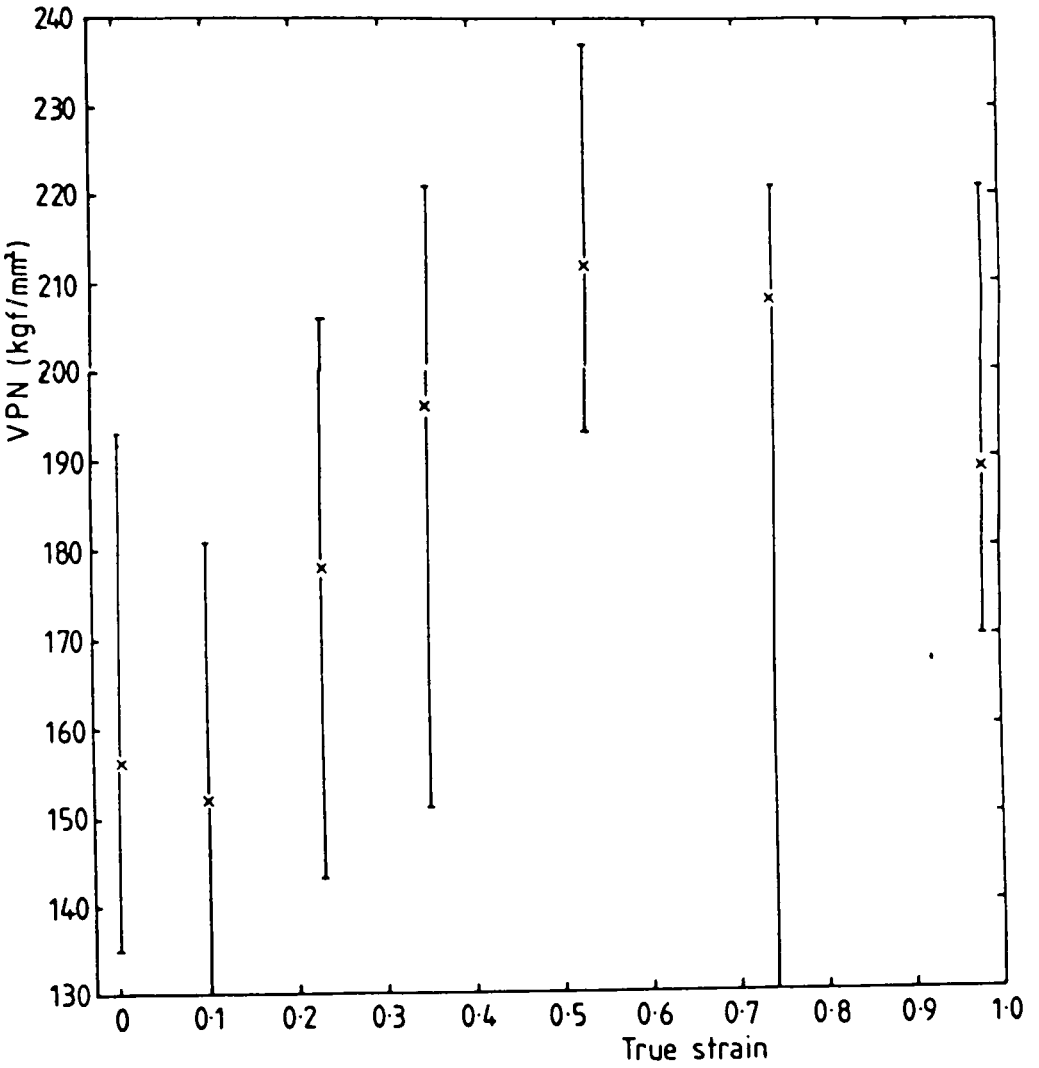

Figure 4·20.

Strain-microhardness relationship for 60-40 brass from compression test specimens (H/D=1).

x indicates average value.

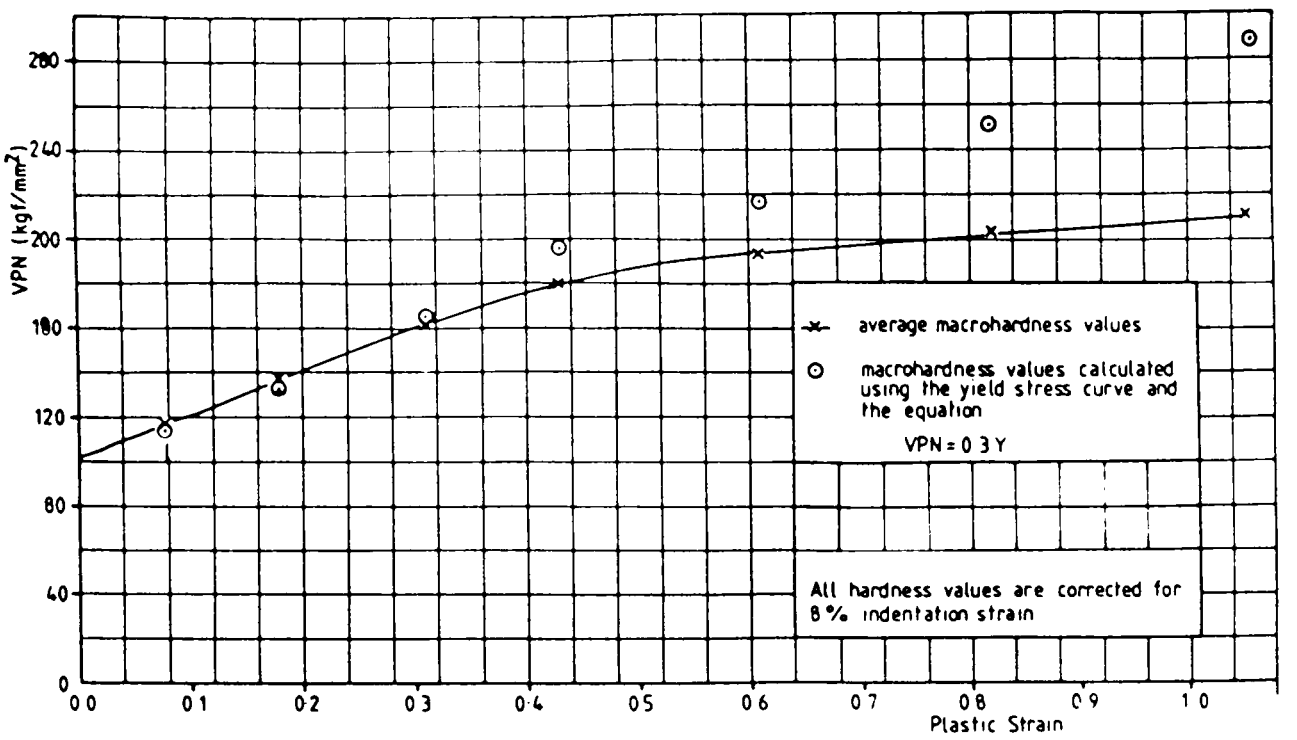

Figure 4·21 Strain-macrohardness relationship for 60-40 brass.

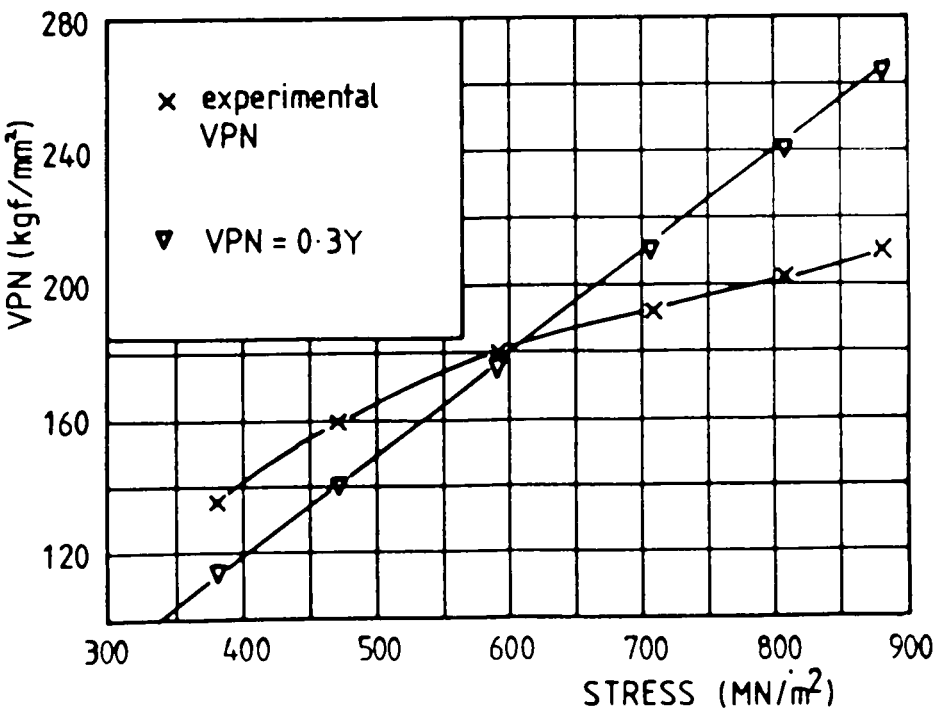

Figure 4·22. Stress-macrohardness relationship from Brass compression test specimens (H/D = 1·0).

scattering problems of microhardness testing, and will therefore be used in this investigation.

Pairs of corresponding FE and macrohardness results for the operation of plane-strain side-pressing of 60–40 brass, calculated using this relationship, are shown in figure 4.23. Very good correlation is shown here, with an overall average difference of 6 %. This gives confidence in the finite-element predictions.

Figure 4.24 illustrates pairs of FE and macrohardness results for the side-pressing of the three geometries of 7075 aluminium alloy. Good agreement has been found here, with an average difference between the experimental and finite-element values of only 6%. This material is much less ductile than 60–40 brass and lower strains are developed prior to fracture. Tabor's stress to hardness relationship is therefore satisfactory in this case.

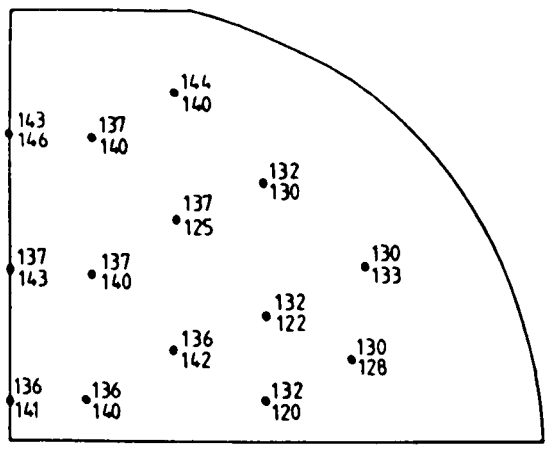

2% reduction

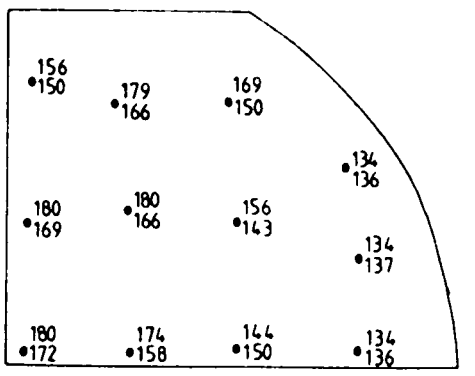

19% reduction

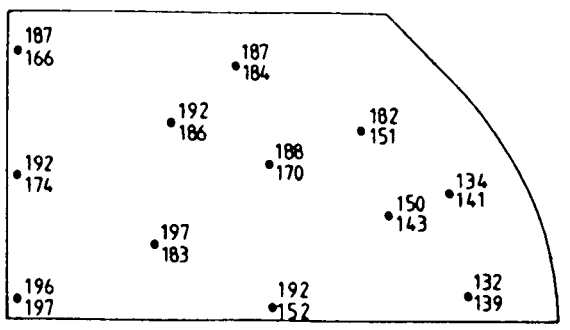

31% reduction

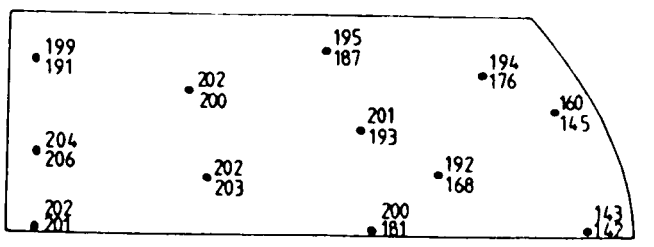

48% reduction

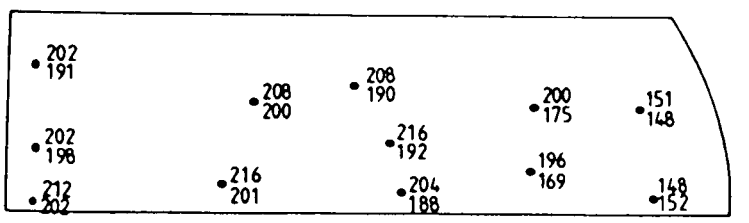

52% reduction

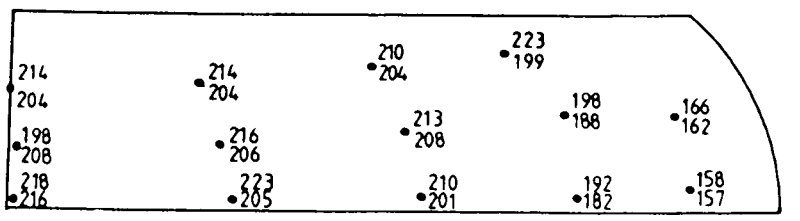

55% reduction

Figure 4·23. Hardness distributions at various reductions for initially circular section 60-40 brass. At each location the finite-element prediction appears above the experimental value

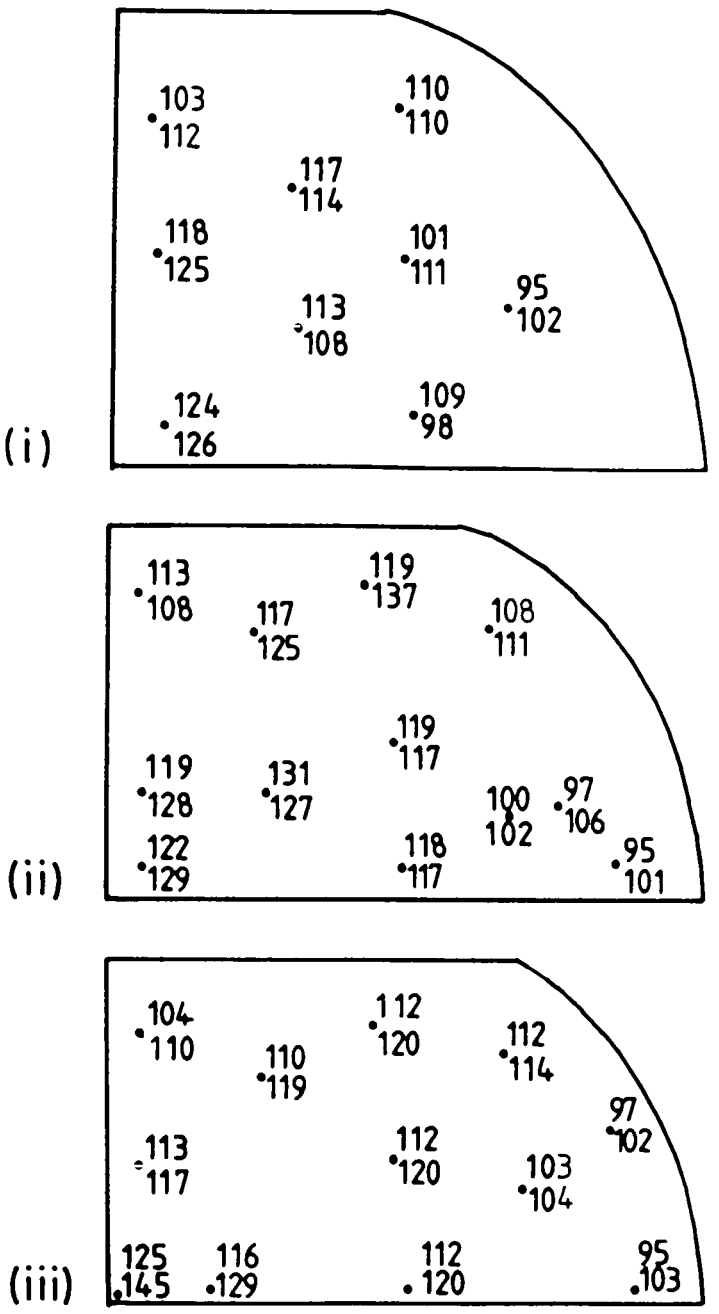

Figure 4·24.

Hardness distributions (VPN) at the experimental level of fracture for 7075 aluminium alloy

(i) initially circular section

(ii) initial H/W = 2·03

(iii) initial H/W = 1·33

At each location the finite-element prediction appears above the experimental value.

4.4.4 Plastic zone development and displacement vectors.

Finite-element analysis can also give detailed information about the way in which the plastic zone is initiated and develops as deformation proceeds.

Results obtained for the plane-strain side-pressing of initially circular section models of both 60-40 brass and 7075 aluminium alloy are presented in figure 4.25. The plastic zone development patterns for both materials are very similar. Corresponding illustrations in these two diagrams are at comparable levels of deformation. Yield is calculated to occur first in the region of the model near the die surface. This region then extends slightly outwards but mainly towards the centre of the billet. The centre is reached by the time that the original specimen height has been reduced by only 1%. At a little over 3% deformation both sets of finite-element results predict that several of the elements in contact with the die surface which have previously behaved in a plastic manner are now not doing so. The generalised stress in these elements has fallen below the required value for yield and their behaviour may now be considered to be elastic. Thus the load carrying regions have spread slightly further into the body of the specimen. As mentioned earlier, no direct experimental comparison is available. However, the analysis of this shape of specimen has also been examined by Lee and Kobayashi (1971) who encountered the same phenomenon. They suggested that this unloading could be attributed to the manner in which the die-workpiece contact width increased, as soon as a nodal point along the free surface touched the die the contact width suddenly increased and unloading was predicted. This argument is certainly consistent with the results obtained here; the surface area in contact with the die effectively being doubled over the increment in which unloading is

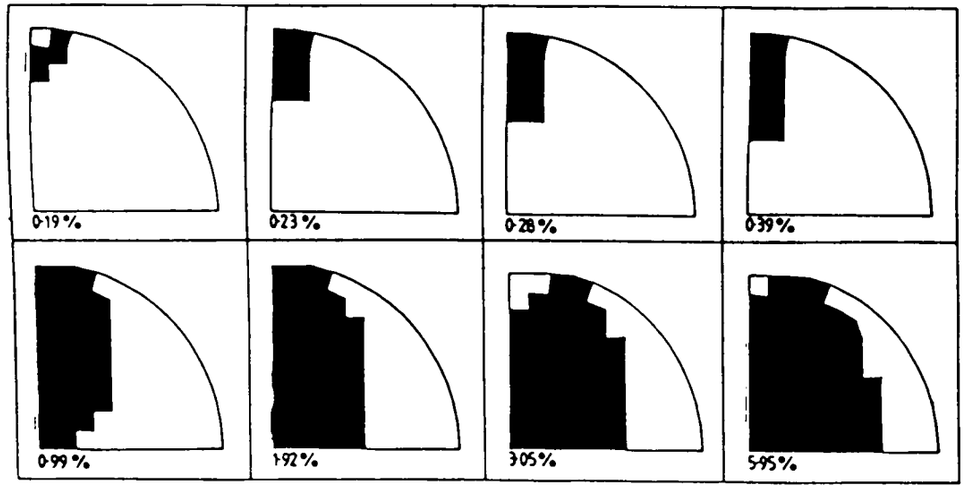

(a) 60-40 brass

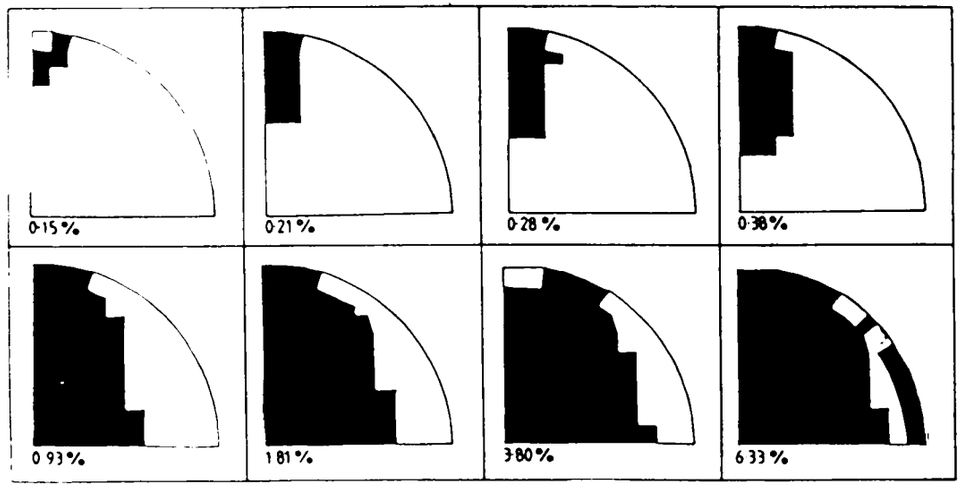

(b) 7075 aluminium alloy

Figure 4·25.

Plastic zone development in the plane-strain side-pressing of circular section rod.

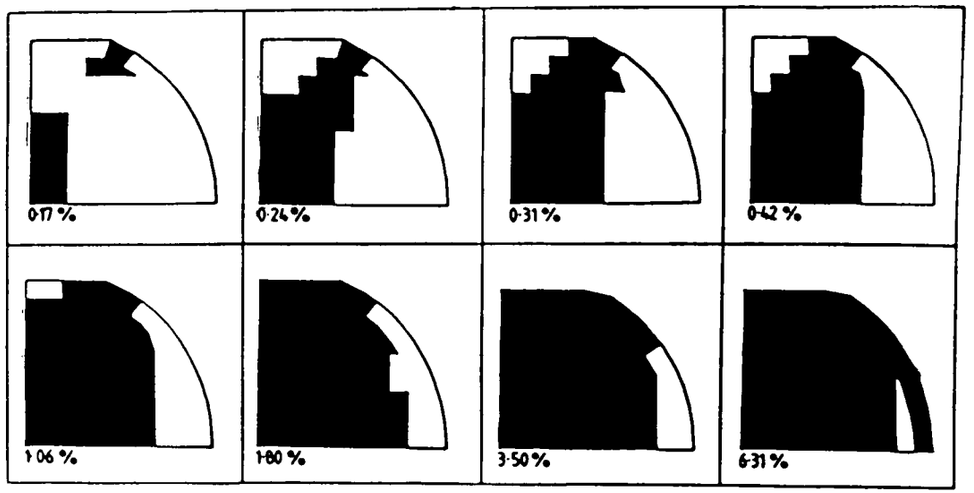

(a) initial H/W = 2·03

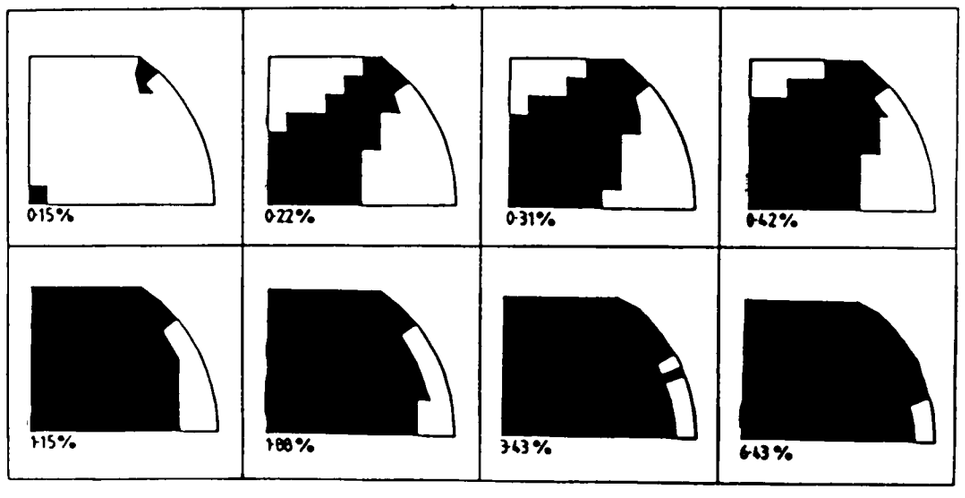

(b) initial H/W = 1·33

Figure 4·26.

Plastic zone development in the plane-strain side-pressing of 7075 aluminium alloy.

predicted. It is also consistent with the results obtained for the plastic zone development of 7075 aluminium alloy with machined flats. Here, there is a comparatively large area initially in contact with the dies so that the rolling round of an additional node into contact with the die has a very small effect. Unloading does not therefore occur as shown by the results in figure 4.26.

The pattern of plastic zone development for these models with machined flats is different from those with an initially circular cross-section. Yielding starts simultaneously in both the centre of the complete specimen and in the free surface material next to the die surface. These two regions then grow diagonally across the specimen until it is all deforming in a plastic manner after slightly more than 6% reduction in the original height.

On the basis of the very limited study of shapes presented here it would appear that plastic zone development in plane-strain side-pressing is geometry rather than material dependent.

Finite-element analysis is also capable of predicting the incremental displacement vectors in detail. This is also possible for slip-line field theory but only for plane-strain conditions and rather simple shapes. These illustrate the direction and magnitude of the movement of a node during the latest increment of deformation. Figures 4.27 to 4.30 present these displacement vectors for the operation of plane-strain side-pressing. Compression was simulated within the finite-element program by applying a specified displacement in the vertical direction to the mid-height layer of nodes. All of these vectors have a relative magnification of five when compared with the overall specimen dimensions. As figures 4.27 and 4.28 show, the displacement patterns of the initially circular section specimens of brass and aluminium alloy appear very similar. The comparison can be continued only to 18% reduction, at which the 7075 aluminium alloy fractures. Although the

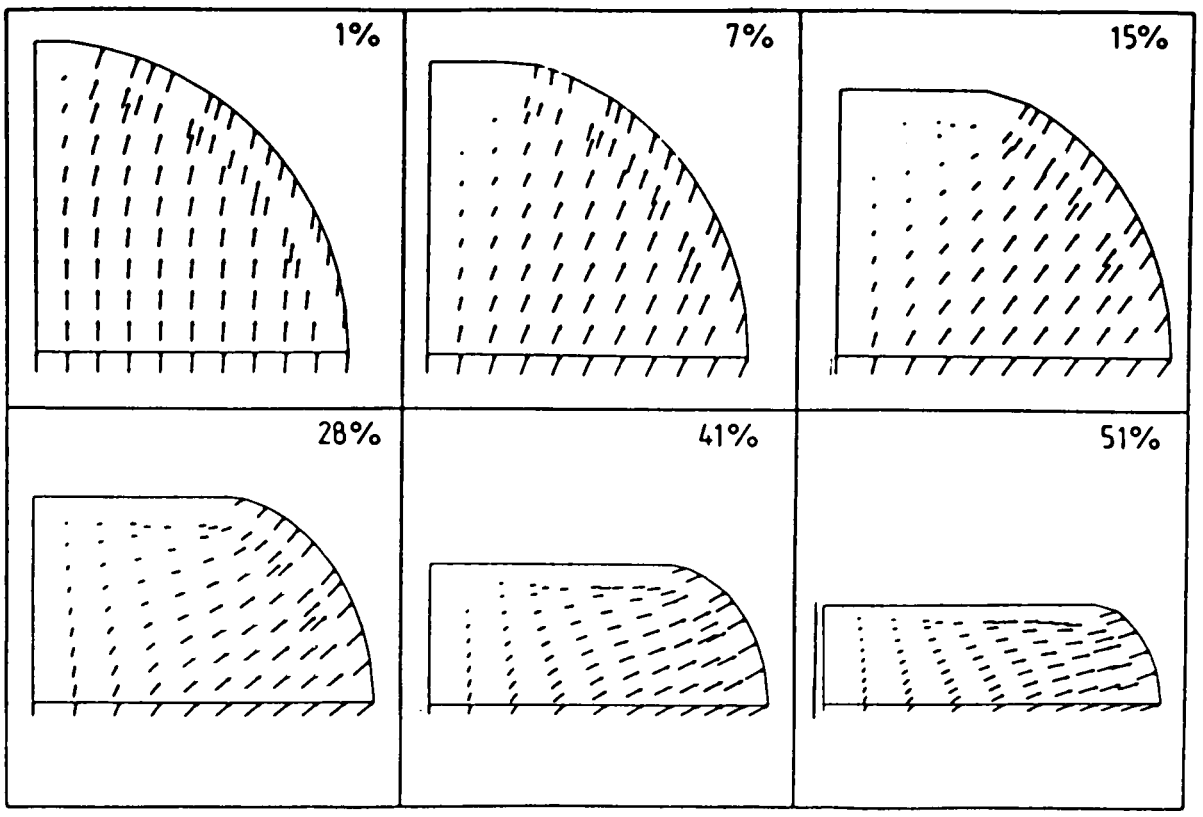

Figure 4·27.

Incremental displacement vectors for circular section 60-40 brass.

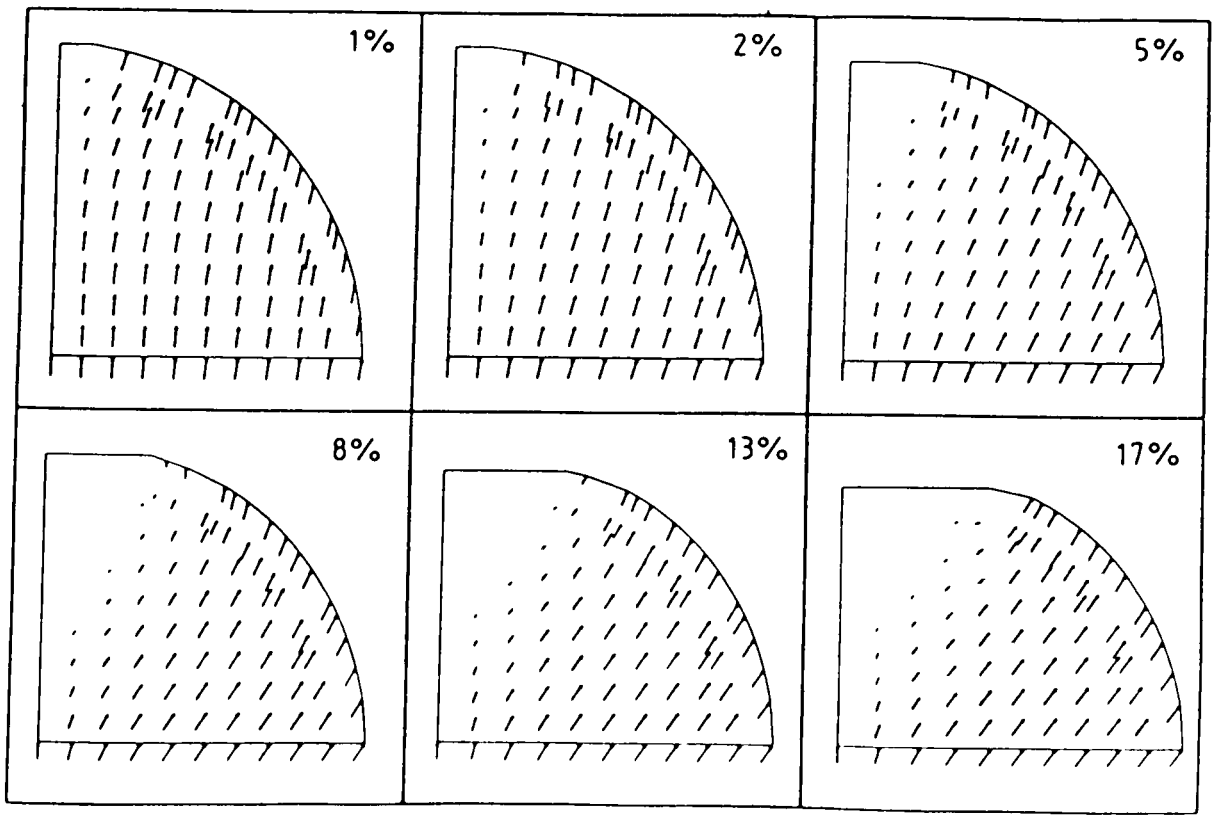

Figure 4·28.

Incremental displacement vectors for circular section 7075 aluminium alloy.

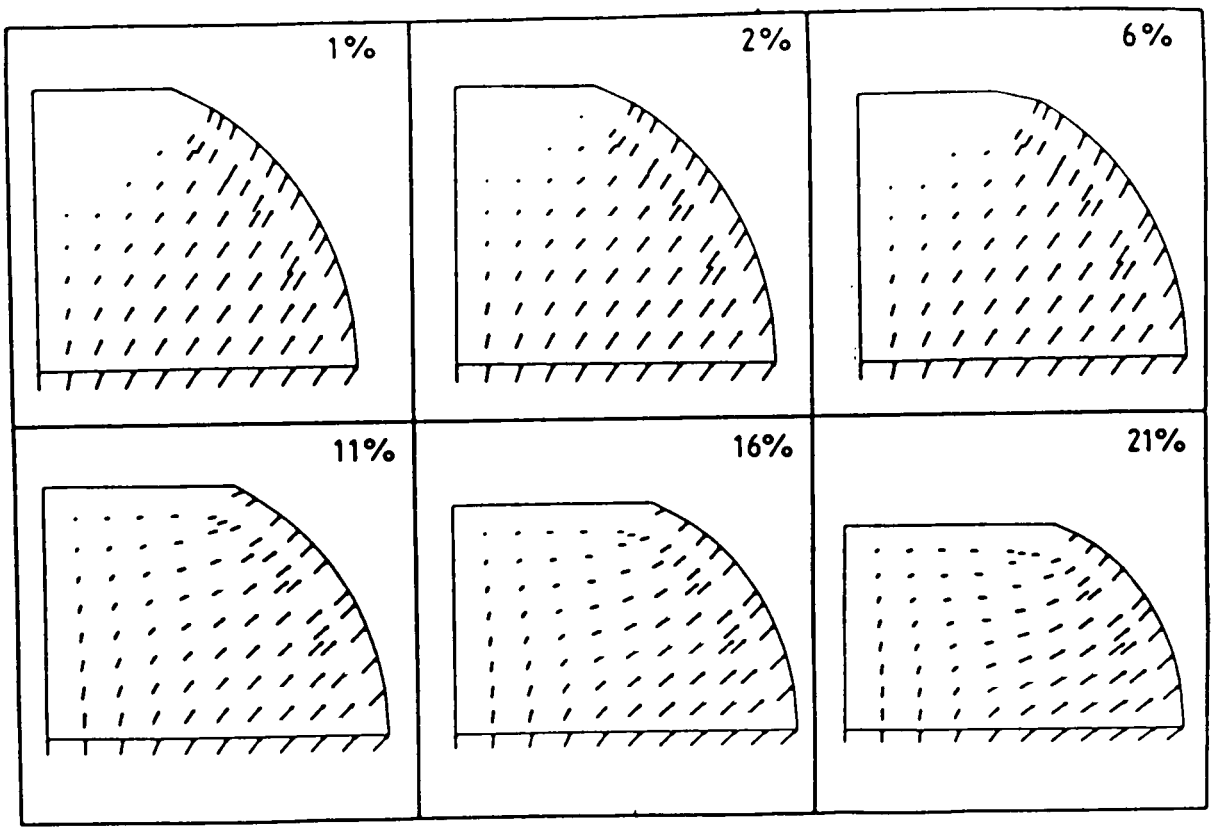

Figure 4·29.

Incremental displacement vectors of 7075 aluminium alloy with machined flats of initial H/W = 2·03.

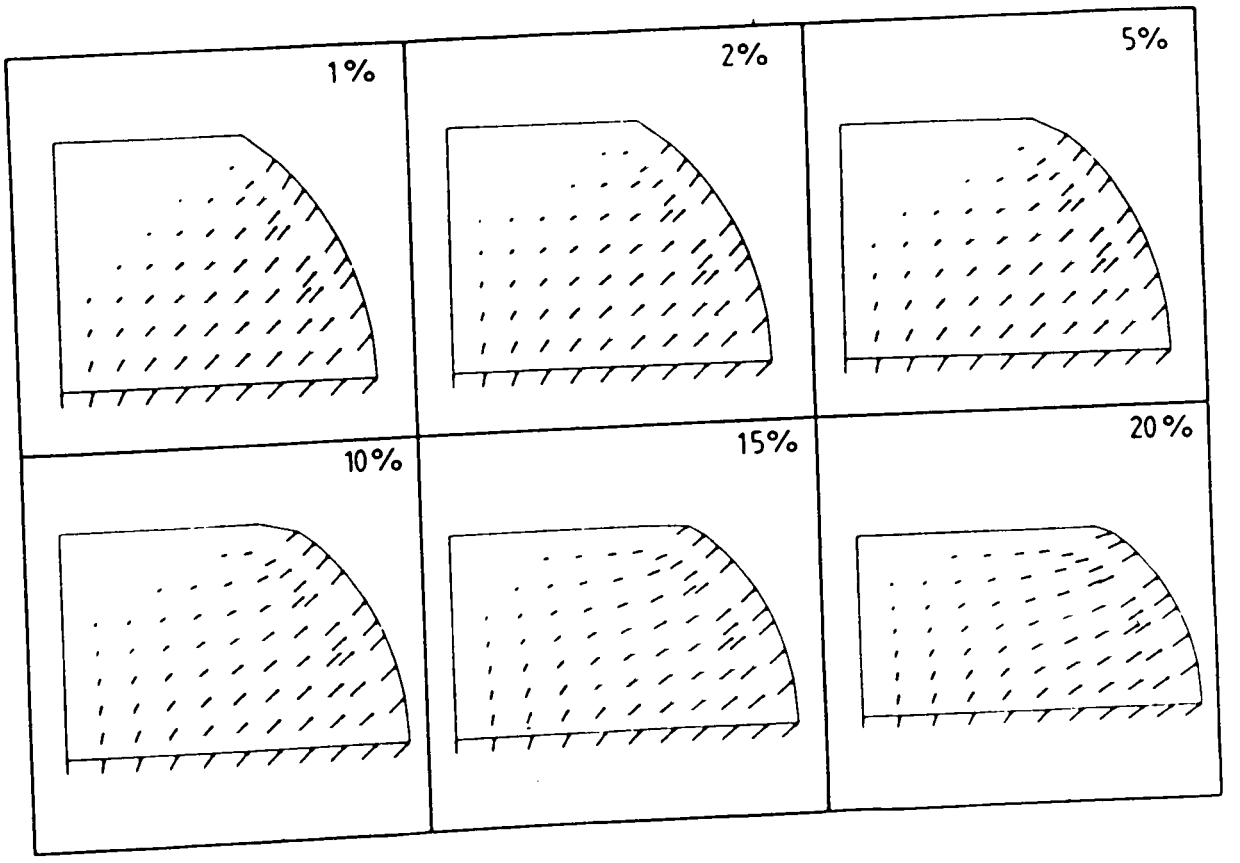

Figure 4·30.

Incremental displacement vectors for 7075 aluminium alloy with machined flats of initial H/W = 1·33.

patterns of deformation are so similar, the 60-40 brass continues to deform up to 55%. At very low levels of deformation, such as 1-2% reduction in the original height, metal deformation is concentrated around the material in contact with the die and the vectors are nearly vertical. The direction of flow of the displacement vectors steadily becomes more oblique as more of the originally free surface comes into contact with the die. This also results in the formation of a dead zone, most clearly defined around 7-8% reduction of the original height. For the 7075 aluminium alloy there remains very little flow in this dead zone material up to the point of experimental fracture.

For the 60-40 brass the material under the die subsequently starts to flow again in a direction approximately parallel to the die surface.

Flow for the two specimens with machined flats differs from those circular section models only in the initial stages. With machined flats a dead zone is present from the very start of the deformation, but otherwise the flow patterns are very similar.

4.5 Fracture results and discussion.

4.5.1 Experimental results.

Figure 4.31 shows the deformed grid and experimental fracture initiation site for the plane-strain side-pressing of initially circular cross sectional 7075 aluminium alloy. Fracture has initiated in the central region of the specimen and may be seen approximately to follow the lines of maximum shear stress as given in the slip-line field solution of Jain and Kobayashi (1970). Figure 4.32 shows a more highly magnified view of the initiated crack where the discontiniuity in the originally continuous photographic grids is clearly visible, thus indicating a shear crack.

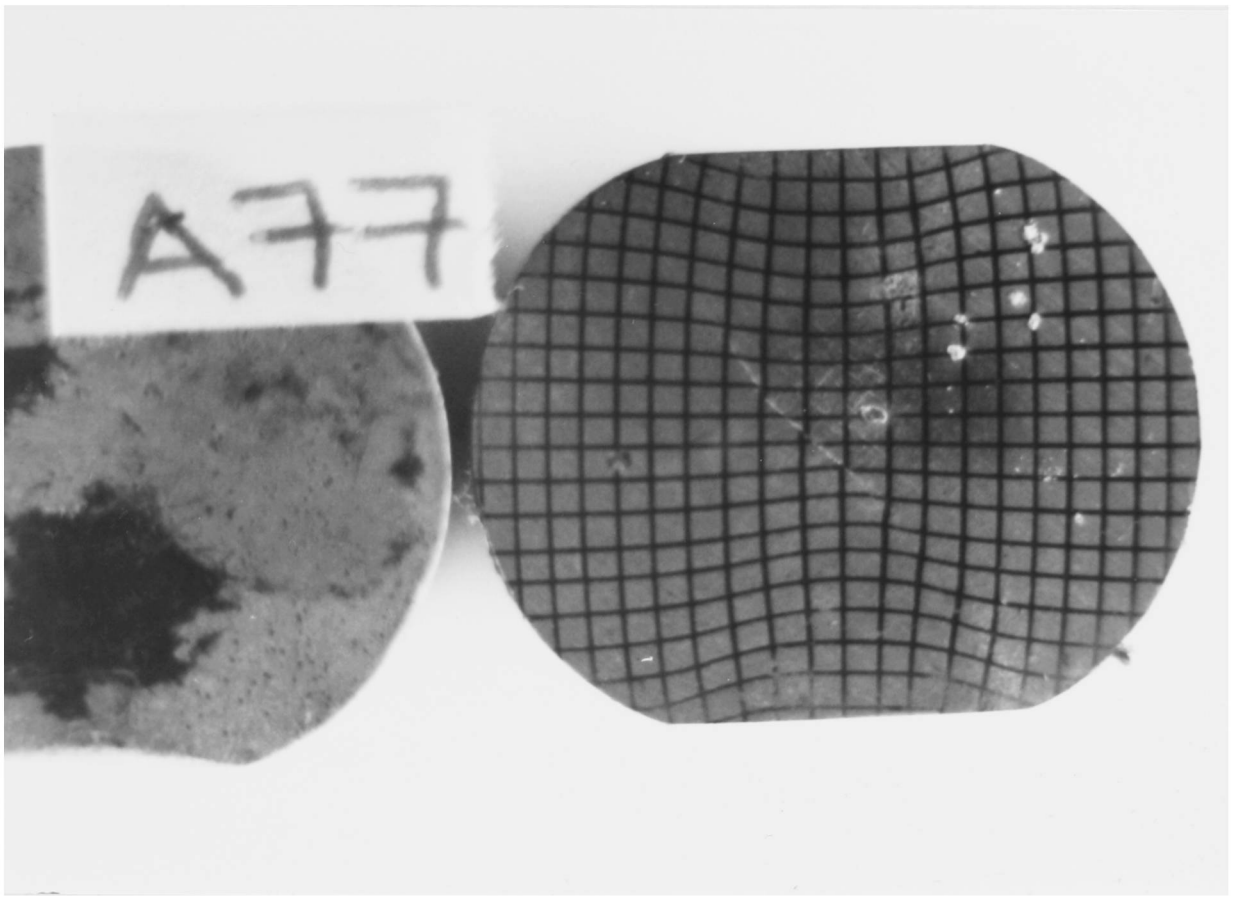

Figure 4.31

Fractured circular section 7075 aluminium alloy.

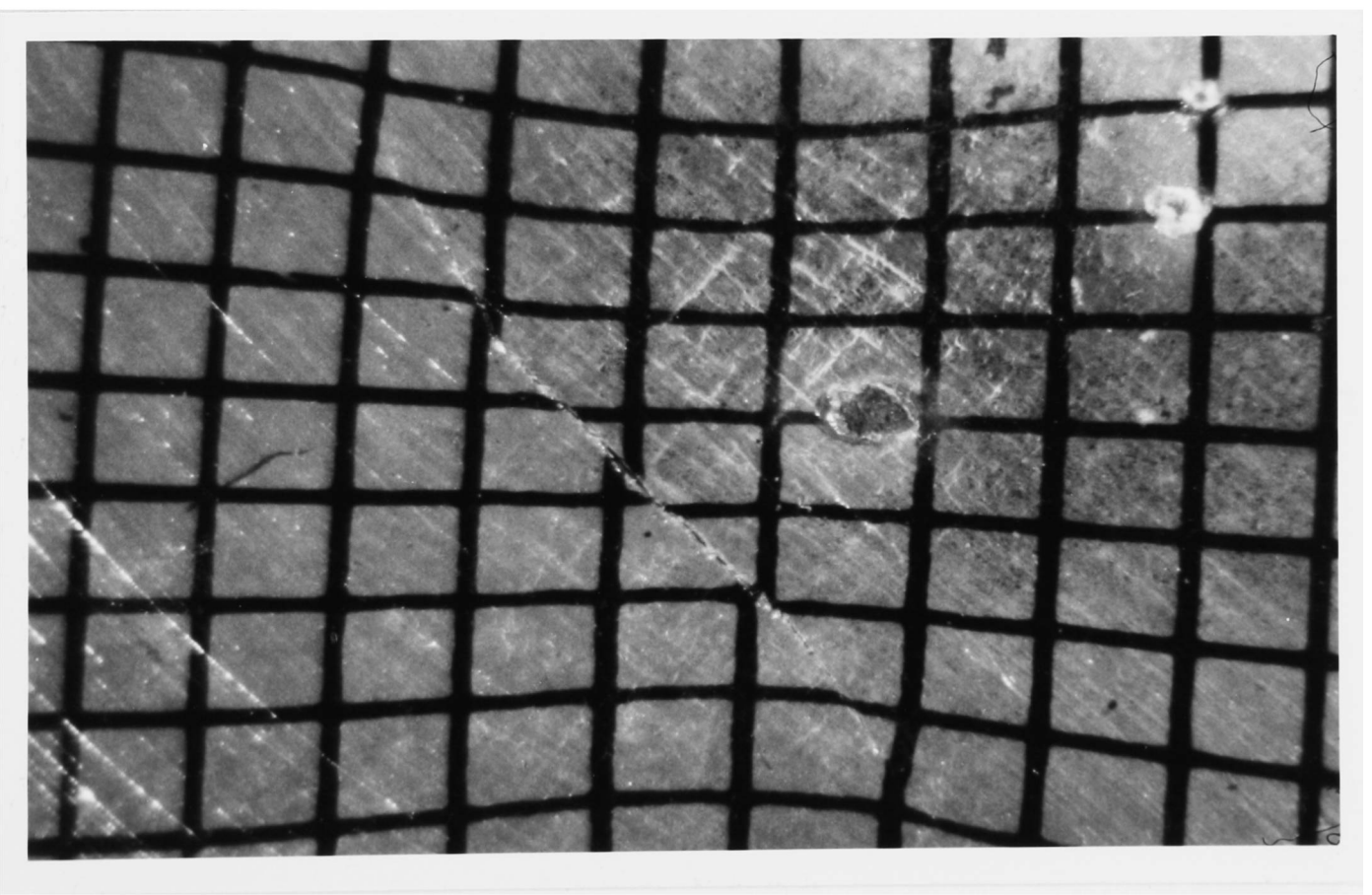

Figure 4.32

Magnified central region of the crack shown in figure 4.31.

For both 7075 aluminium alloy specimens with machined flats fracture was found to initiate from one of the surfaces in contact with the die, from a point approximately coincident with the position of the original corner, again indicating a shear crack. For the specimen with initial height to width ratio of 1.33 (Figure 4.33) fracture occurred at an overall level of deformation of 16% (see Table 4.2), and for the second specimen, that with a initial height to width ratio of 2.03 (Figure 4.34), fracture was found to occur at 18% reduction of the original height.

For initially circular section 60-40 brass, as with circular section 7075 aluminium alloy, fracture was found to be initiated in the central region of the deformed specimen, but this occurred in the brass only after an overall level of deformation of 55%. Figure 4.35 shows the initiated crack at a magnification of 100, while figure 4.36 shows a very well developed crack. Finally, figure 4.37 contains a scanning electron microscope photograph of one of the fracture surfaces obtained in the plane-strain side-pressing of initially circular cross sectional 60-40 brass. This photograph appears to be fairly typical of a ductile fracture shear surface, with parallel ridges observable perpendicular to the direction of shearing.

4.5.2 Assessment of various fracture criteria.

By using the finite-element program in conjunction with the fracture criterion accumulation program, as previously described in chapter 3 of this thesis, numerical predictions of the fracture initiation site in plane-strain side-pressing were obtained by finding the node in the mesh at which the cumulative value of each fracture criterion was a maximum at the level of deformation at fracture found experimentally. These predicted sites were then compared with the crack

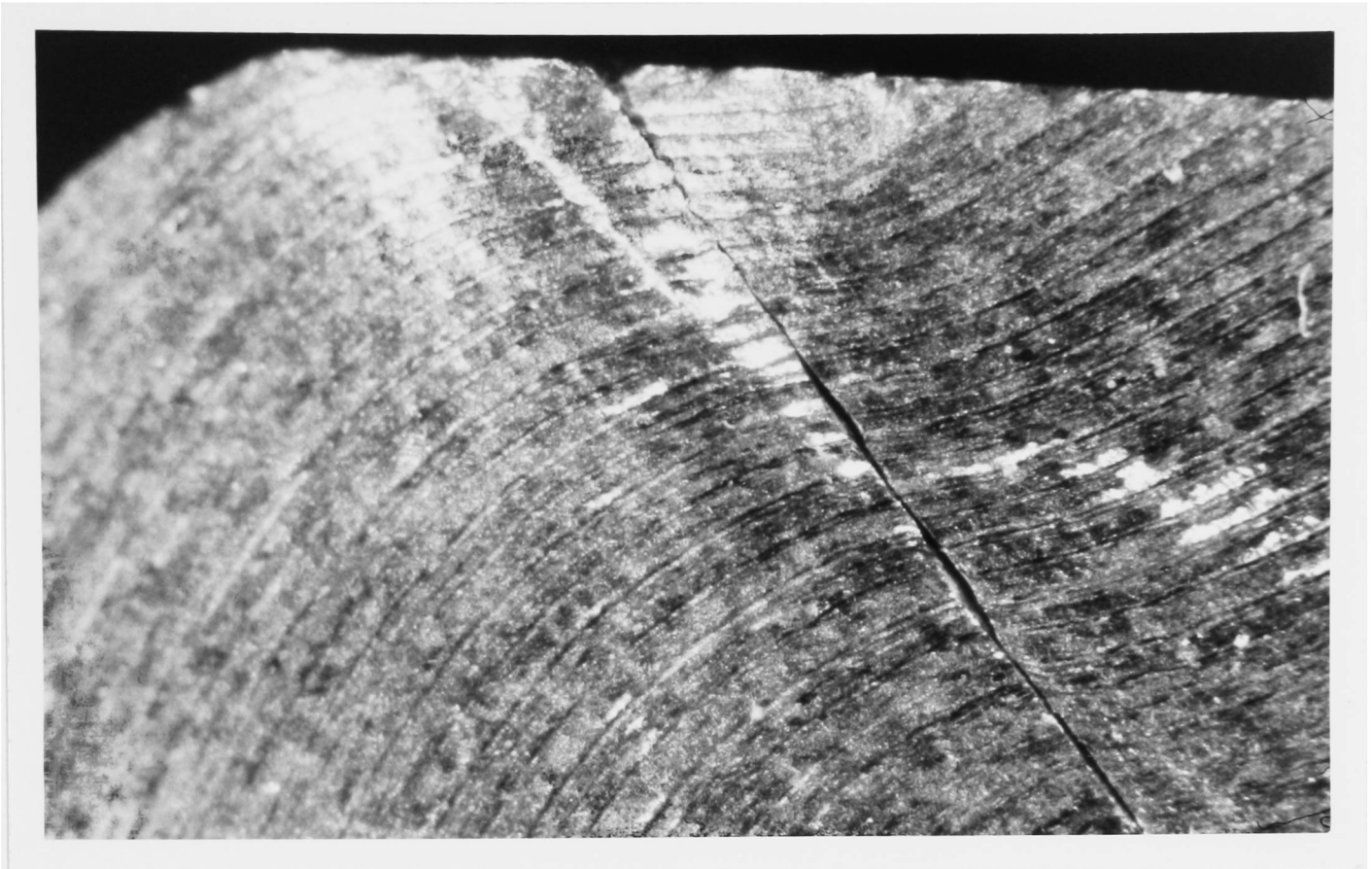

Figure 4.33

Fracture in 7075 aluminium alloy with initial H/W=1.33. (x48)

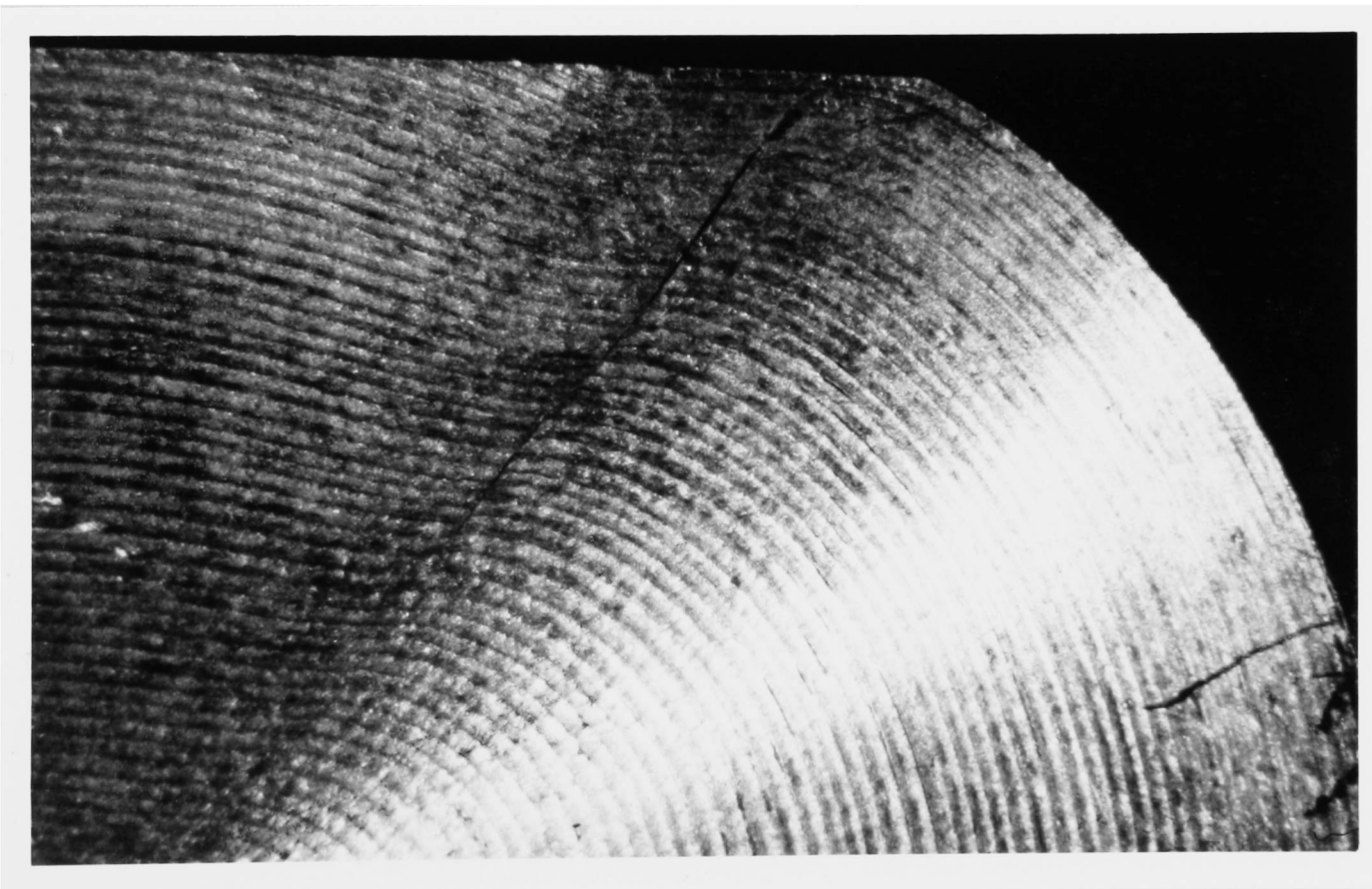

Figure 4.34

Fracture in 7075 aluminium alloy with initial H/W=2.03. (x24)

Material	Initial geometry	% Deformation at fracture
60-40 brass	circular	55
7075 Al	"	16
"	H/W = 2·03	18
"	H/W = 1·33	16

Table 4·2

Levels of deformation at fracture in plane-strain side-pressing.

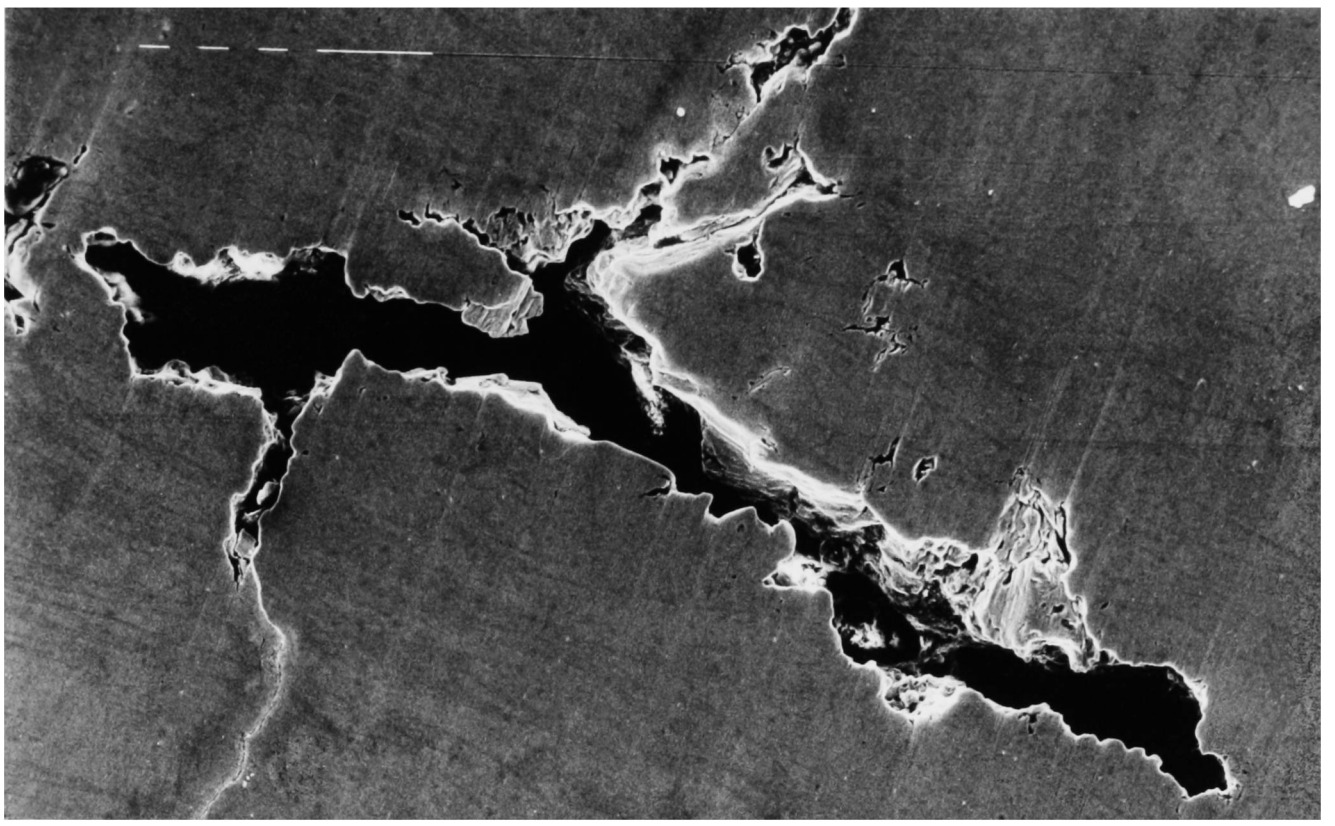

Figure 4.35

Central crack in initially circular section 60-40 brass. (x100)

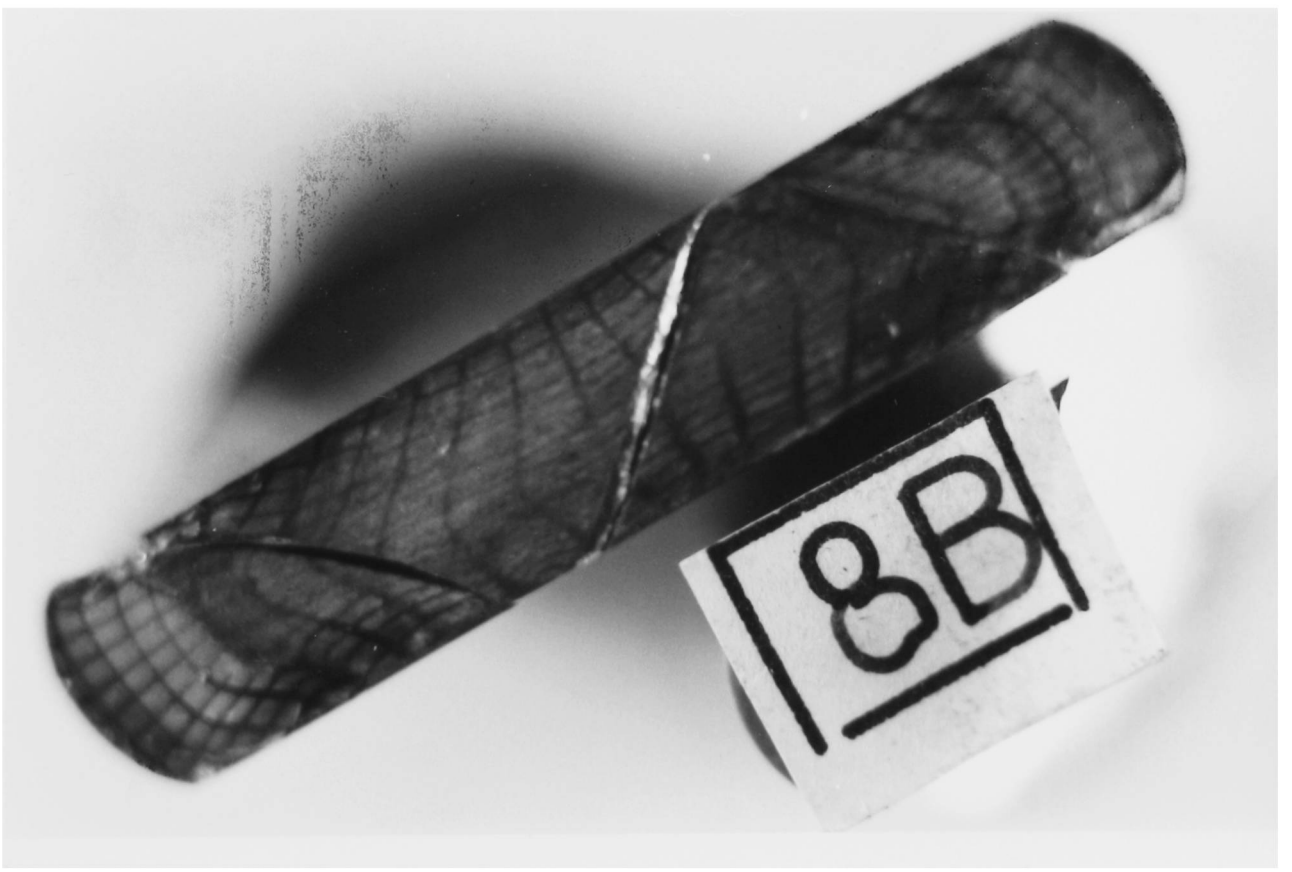

Figure 4.36

Well developed crack in 60-40 brass.

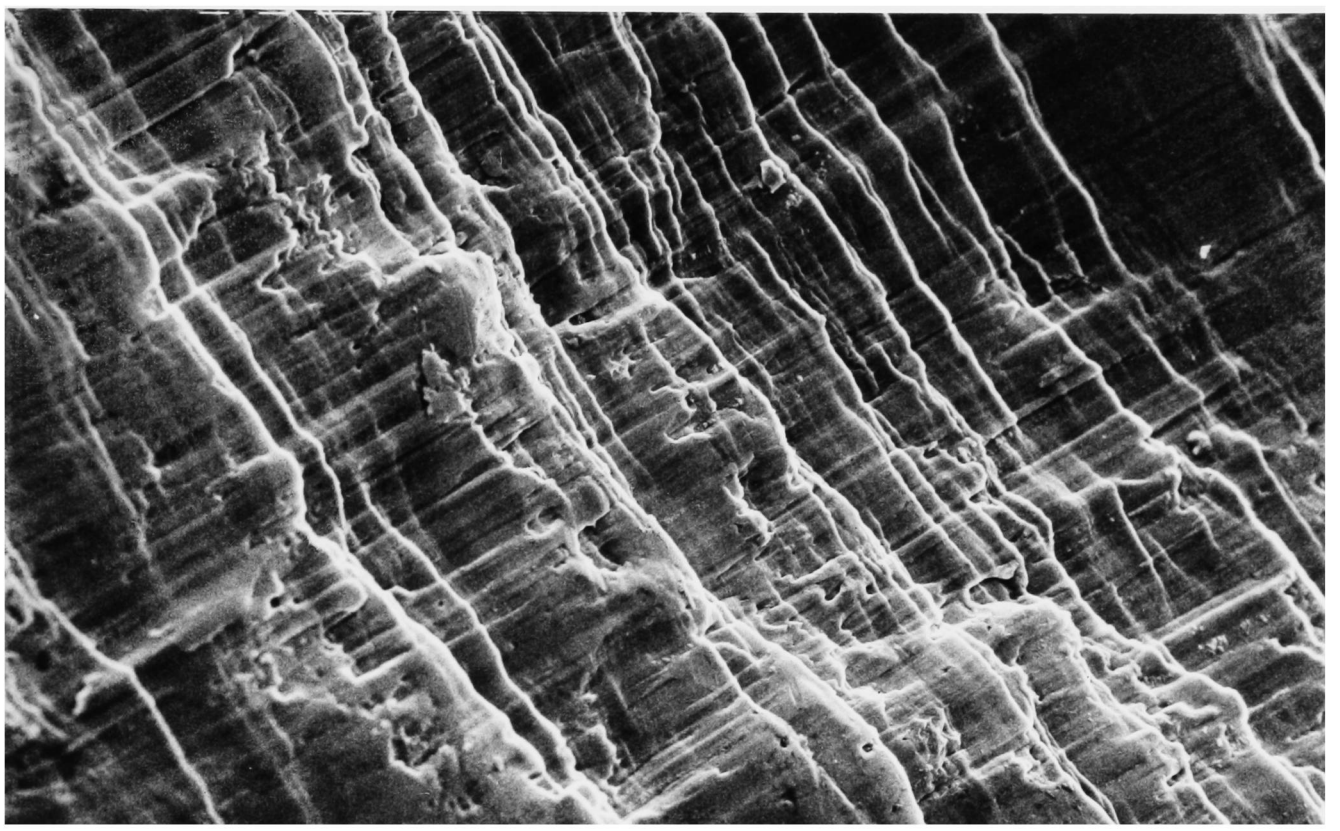

Figure 4.37

Scanning electron microscope photograph for the fracture surface in 60-40 brass. (x430)

initiation site found experimentally (as mentioned in section 4.5.1) and the comparisons presented in table 4.3 were made. A tick indicates that the experimental and numerically predicted sites of fracture initiation agree; a cross indicates that they disagree.

The numbers displayed in the bottom right hand corner of each table element refer to the node at which fracture initiation was predicted to occur. The location of these nodes is given in the deformed mesh diagrams in figure 4.38.

For the McClintock and Atkins criteria predictions can also be made of the plane of fracture. These are displayed in the top left hand corner of the appropriate table elements.

From this table it may be seen that the only two fracture criteria to successfully predict the experimental fracture initiation site for all four material/geometry combinations are those of generalised plastic strain and generalised plastic work. No agreement at all has been found for four of the fracture criteria examined: those of McClintock et al (1966), McClintock (1968), Ghosh (1976) and Norris et al (1978). Although both of the McClintock criteria do predict the zx fracture plane which was found to occur experimentally.

The criteria of Cockroft and Latham (1968), Brozzo et al (1972), Oyane et al (1980) and Atkins (1981) show partial agreement; that is they are capable of correctly predicting the experimental fracture initiation site in some but not all of the specimen geometries examined.

For the Cockroft and Latham, Brozzo et al and Oyane et al fracture criteria some agreement has been found for the initially circular section geometries.

This agreement may be expected from a situation where there is a large principal tensile stress acting at the experimental site of fracture initiation. Thus for the initially circular section specimens, the Cockroft and Latham criterion produces the correct numerical

criterion / specimen	McClintock (1968)	McClintock et al (1966) (shear)	Ghosh	Oyane	Cockroft and Latham	Brozzo	Gen. plastic strain	Gen plastic work	Norris	Atkins
60-40 Brass (circular)	zx × 209	zx × 203	× 192	× 144	√ 5	√ 5	√ 5	√ 5	× 11	zx × 201
7075 Al (circular)	yz × 210	xy × 203	× 83	√ 1	√ 1	√ 1	√ 1	√ 1	× 27	zx × 151
7075 Al (H/D = 2·03)	yz × 63	zx × 142	× 58	× 7	× 6	× 6	√ 192	√ 192	× 29	zx √ 192
7075 Al (H/D=1·33)	zx × 183	xy × 142	× 182	4	× 6	× 2	√ 170	√ 170	× 106	zx √ 170

Table 4·3

Comparison of FE predictions of fracture initiation site and experimental results for the plane-strain side pressing of 60-40 brass and 7075 aluminium alloy.

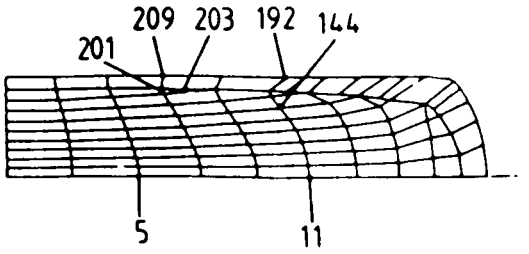

(a) Initially circular cross section
60-40 brass at 55% reduction.

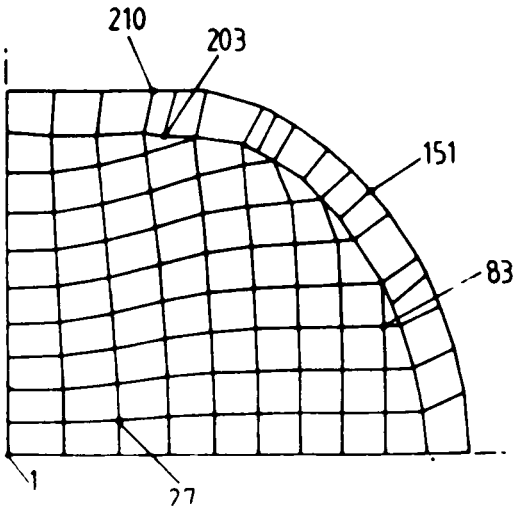

(b) Initially circular cross section
7075 aluminium alloy
16% reduction

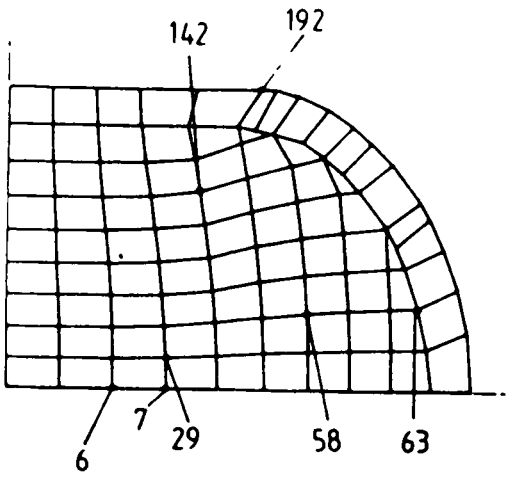

(c) Initial H/W = 2·03
7075 aluminium alloy
18% reduction

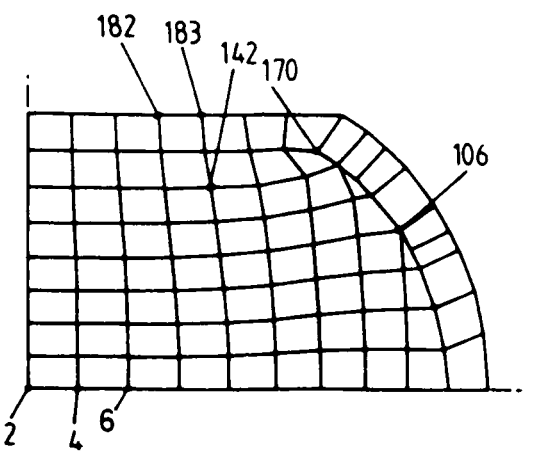

(d) Initial H/W = 1·33
7075 aluminium alloy
16% reduction

Node numbers refer to graphs in figures 4.39 and 4.40

Figure 4·38

Deformed FE grids at the experimental level of deformation at fracture.

predictions. Cockroft and Latham arrived at this criterion after pulling a number of axisymmetric tensile specimens to fracture. The generalised plastic work per unit volume at fracture was found not to give valid predictions over the range of specimens. The generalised plastic work to fracture criterion was dismissed because of the inconsistencies in this set of results and the modified work criterion based on the effect of the largest tensile principal stress was suggested. It was found that the results were unreliable because of the triaxial stress state induced in the neck. Axisymmetric tensile tests were again used but this time, as soon as a significant neck developed, the specimen was machined to remove the neck radius. In this manner the development of a triaxial stress state in the neck was avoided. Unfortunately, the generalised plastic work concept had already been abandoned and was not examined again.

The tensile plastic work criterion agreed with experiment in this special case of predominantly tensile deformation.

Thus it is possible that the tensile plastic work criterion of Cockroft and Latham is a special case of the generalised plastic work to fracture relationship and would be expected to apply in situations where the stress system is predominantly tensile.

This is the case in the centre of the initially circular cross sectional plane-strain side-pressing specimens, so the Cockroft and Latham criterion would be expected to apply as indeed it does as borne out by the results presented in table 4.3.

The criterion of Brozzo et al (1972) was developed in response to a need to predict the formability limits of metal sheets. These authors modified the Cockroft and Latham criterion to include the effects of hydrostatic stress. As the results presented in table 4.3 show, this criterion has successfully predicted the fracture initiation sites in the initially circular cross sectional specimens, as did the original

unmodified Cockroft and Latham criterion. This indicates that the failure of the Cockroft and Latham criterion explicitly to take into account the effect of hydrostatic stress on fracture, as described by Bridgman (1952), is not responsible for its failure to correctly predict the fracture initiation sites in plane-strain side-pressing specimens with machined flats.

From table 4.3 it may also be seen that the criterion of Oyane et al (1980), which is based on a critical volumetric strain at fracture, is only capable of predicting the fracture initiation site for initially circular section specimens.

This suggests that the criterion successfully takes into account the effects of tensile stress but cannot deal satisfactorily with situations where the stress system is not predominantly tensile.

The opposite problem has been encountered with the predictions of the Atkins fracture criterion. This is capable of predicting the correct fracture initiation site for the specimens which initially had machined flats, but not for the specimens with an initially circular cross section. All four of the Atkins fracture plane predictions agree with experiment.

An experimental determination of the critical value of generalised plastic work at fracture and of the critical value of the Cockroft and Latham tensile plastic work at fracture was made using a simple axisymmetric tensile test without machining off the neck surround. Two Hounsfield size 12 specimens of both materials were tested, and average results calculated. The method of Bridgman (1944) was employed to correct the final true yield stess for triaxial stress development in the necked region of the test specimen. These radial and transverse stresses raise the value of the axial stress required to cause plastic flow. According to this analysis, the ratio of the true axial stress, σ_{χ}, to the average axial stress, $(\sigma_{\chi})_{av}$, is:

$$\sigma_x = \frac{(\sigma_x)_{av}}{(1 + 2R/a)\left[\ln(1 + a/2R)\right]} \qquad (4.21)$$

where

a is the maximum radius of the necked region and

R is the radius of curvature of the neck.

These geometric parameters were measured using a Zeiss MP320 measuring projector. A correction factor of 0.83 was calculated for the 60-40 brass, and a factor of 0.91 for 7075 aluminium alloy. Using the stress and strain history to fracture determined from this tensile test the critical values of generalised plastic work and tensile plastic work at fracture were calculated for both materials.

These predicted values of tensile plastic work for both materials have been compared with the finite-element results as presented in figure 4.39. Figure 4.39(b) shows the variation in tensile plastic work with level of deformation for the brass for three nodes with the locations in the deformed mesh shown in figure 4.38. The maximum value of finite-element predicted tensile plastic work at the level of deformation at fracture found experimentally occurs at node 5 which, as explained previously is consistent with the experimental fracture initiation site. However, the value of tensile plastic work calculated from the tensile test of 540 MN/m^2 does not correlate at all well with the finite-element predictions. For the initially circular section 7075 aluminium alloy (Figure 4.39(a)) the maximum finite-element accumulated value occurs at node 1. Here the tensile test predicts 11% reduction at fracture compared with 16% found experimentally. This is a much better comparison than for brass but is still in error. Comparisons of the level of deformation at fracture have not been made for the geometries of 7075 aluminium alloy with machined flats as the Cockroft and Latham criterion

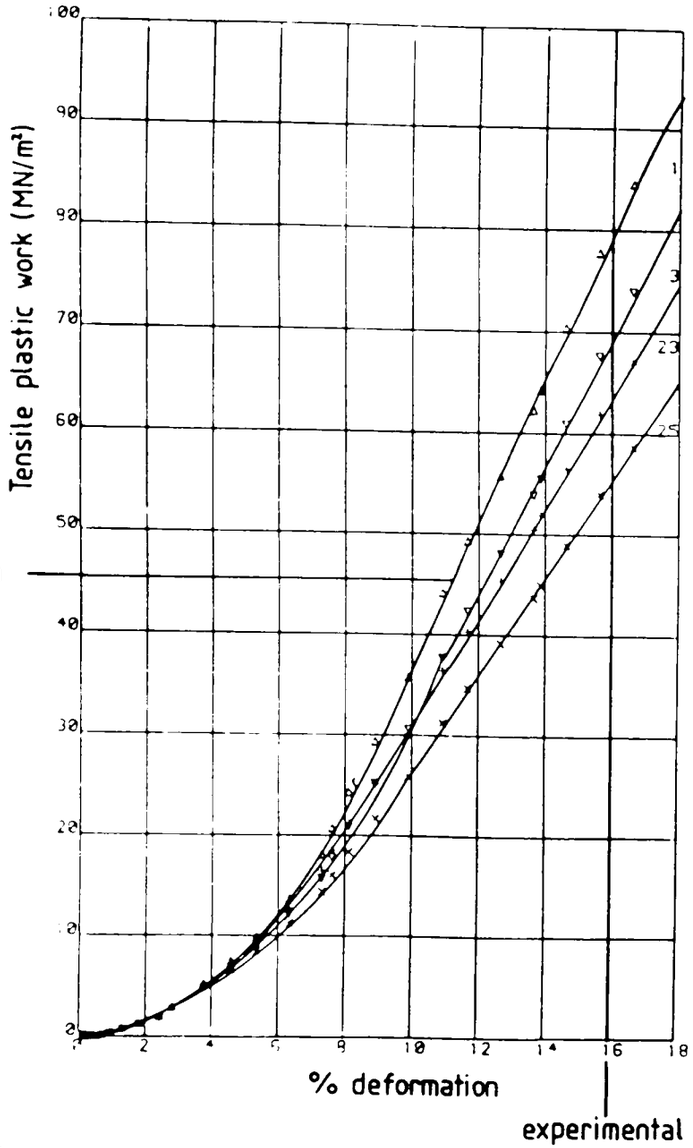

Figure 4·39(a).

Numerical calculation of the Cockroft and Latham fracture criterion for initially circular section 7075 aluminium alloy from FE results for nodes 1,3,23 and 25.

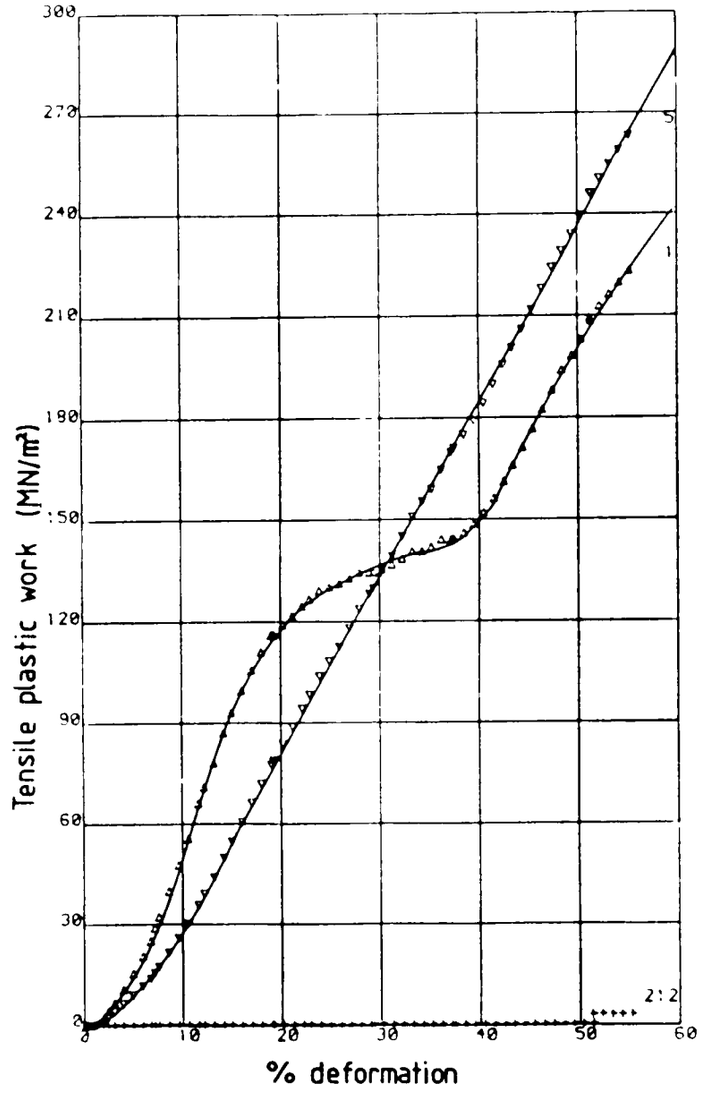

Figure 4·39(b).

Numerical calculation of the Cockroft and Latham fracture criterion for initially circular section 60-40 brass from FE results for nodes 1,5 and 212.

did not make a satisfactory prediction of the fracture initiation site.

Comparisons of the predicted and experimental levels of deformation at fracture for the generalised plastic work fracture criterion are presented in figure 4.40. Figure 4.40(a) shows the results obtained for the initially circular section 7075 aluminium alloy. Here, a predicted level of deformation at fracture of 15.5% agrees very well with the value of 16% obtained experimentally. Figure 4.40(b) refers to the initially circular section 60-40 brass. A predicted level of 48% reduction at node 5 obtained using the tensile test results has been found to compare very favourably with the 55% reduction at fracture found experimentally. For 7075 aluminium alloy with an initial height to width ratio of 2.03 (Figure 4.40(c)) the predicted value of generalised plastic work at the relevant node (192) is approximately 10% greater than that found experimentally, but this is still a satisfactory comparison. Good agreement has also been found for an initial height to width ratio of 1.33 (Figure 4.40(d)).

Exactly the same fracture site and level of deformation at fracture predictions have been obtained for the the fracture criterion of a critical value of generalised plastic strain. These predictions are presented in figure 4.41.

It therefore appears that the criterion of a critical value of generalised plastic work, or generalised plastic strain, at fracture are not only capable of predicting the correct fracture initiation site, as reported previously in this section, but when compared with the value of work at fracture calculated using a simple tensile test provide a reasonable prediction of the level of deformation at fracture for the range of materials and geometries studied here.

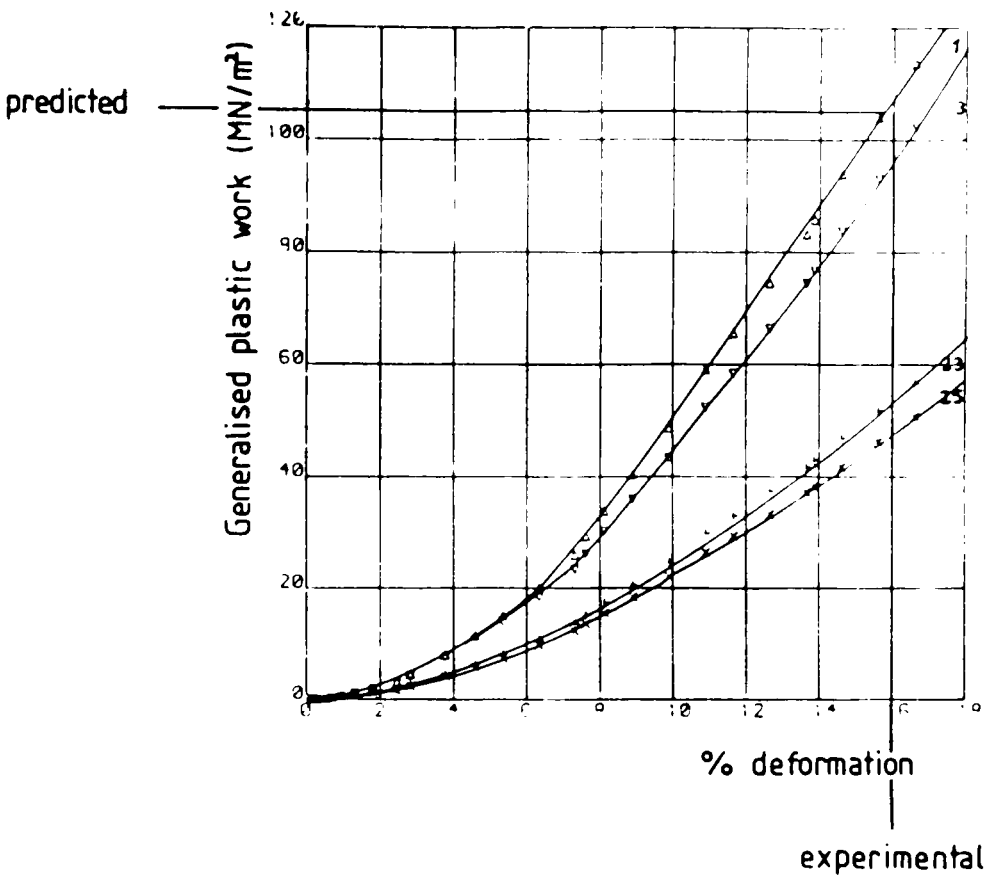

Figure 4·40 (a).

Numerical calculation of the generalised plastic work fracture criterion for initially circular section 7075 aluminium alloy from FE results for nodes 1, 3, 23 and 25.

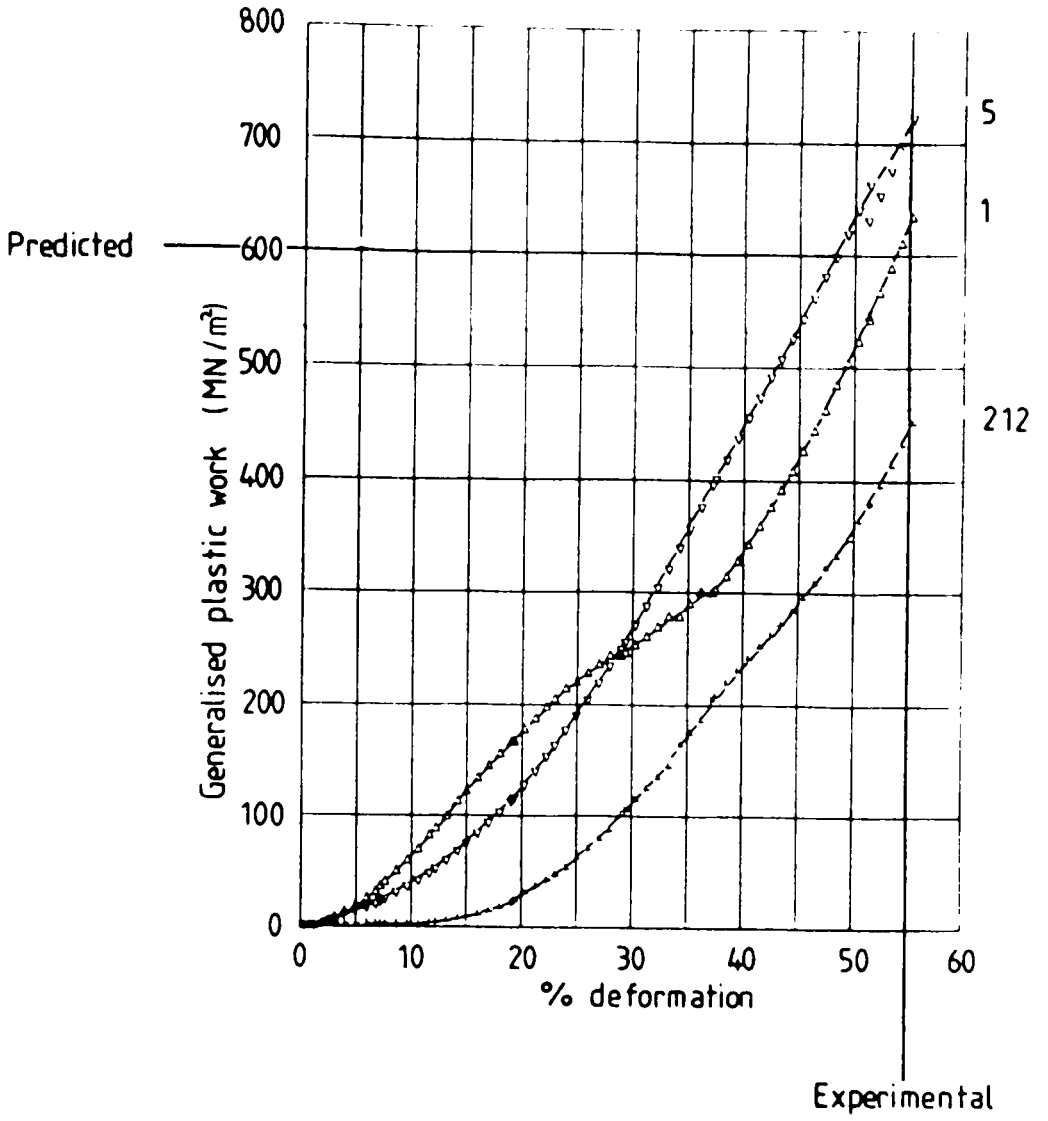

Figure 4·40 (b).

Numerical calculation of the generalised plastic work fracture criterion for initially circular section 60-40 brass from FE results for nodes 1, 5 and 212.

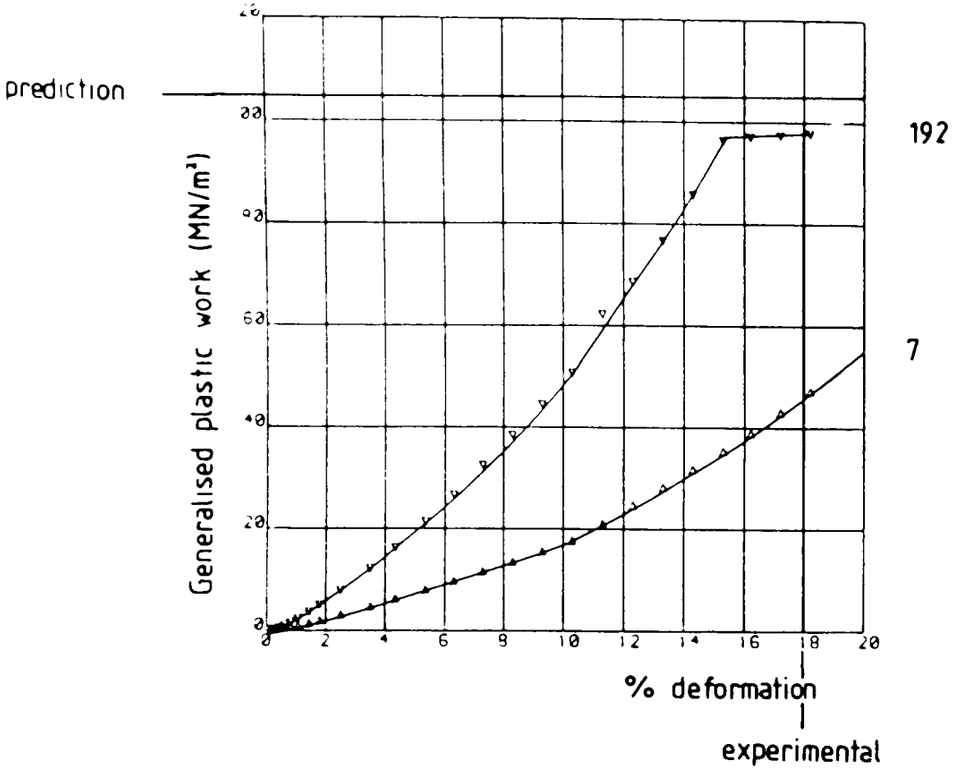

Figure 4·40(c).

Numerical calculation of the generalised plastic work fracture criterion for 7075 aluminium alloy with initial H/W = 2·03 from FE results for nodes 7 and 192

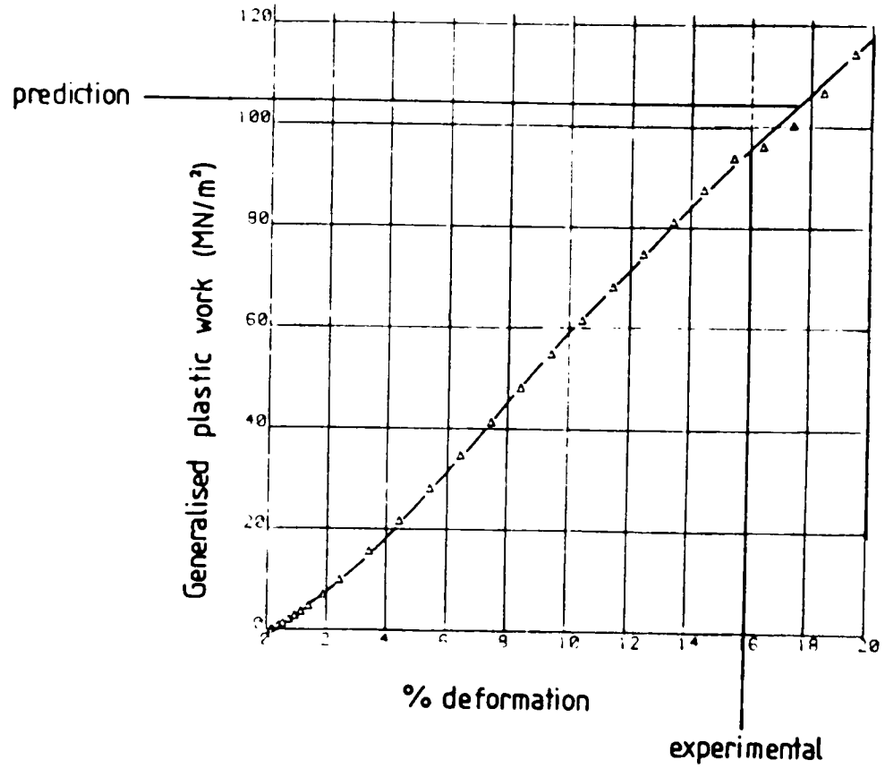

Figure 4·40(d)

Numerical calculation of the generalised plastic work fracture criterion for 7075 aluminium alloy with initial H/W = 1·33 from FE results for node 169.

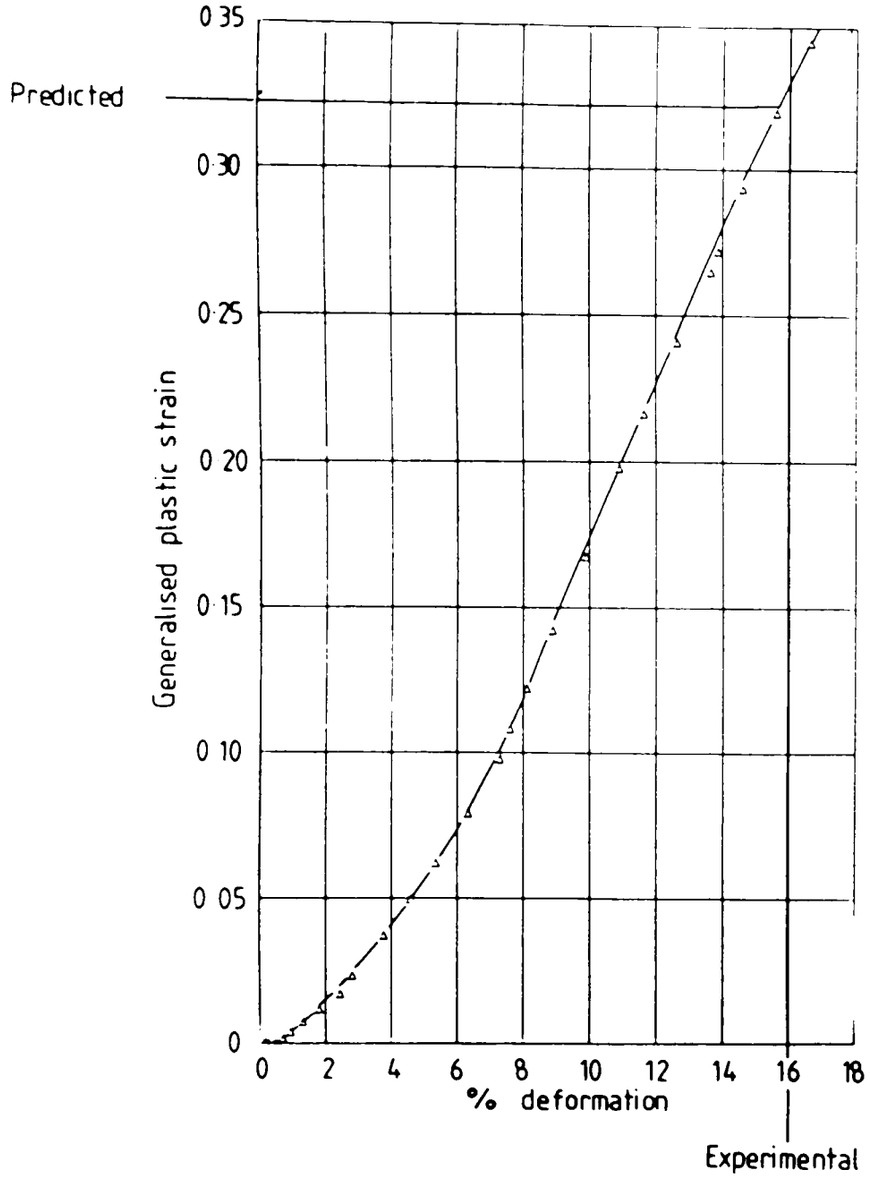

Figure 4.41(a)

Variation of FE generalised plastic strain for the plane-strain side-pressing of initially circular section 7075 aluminium alloy for node 1.

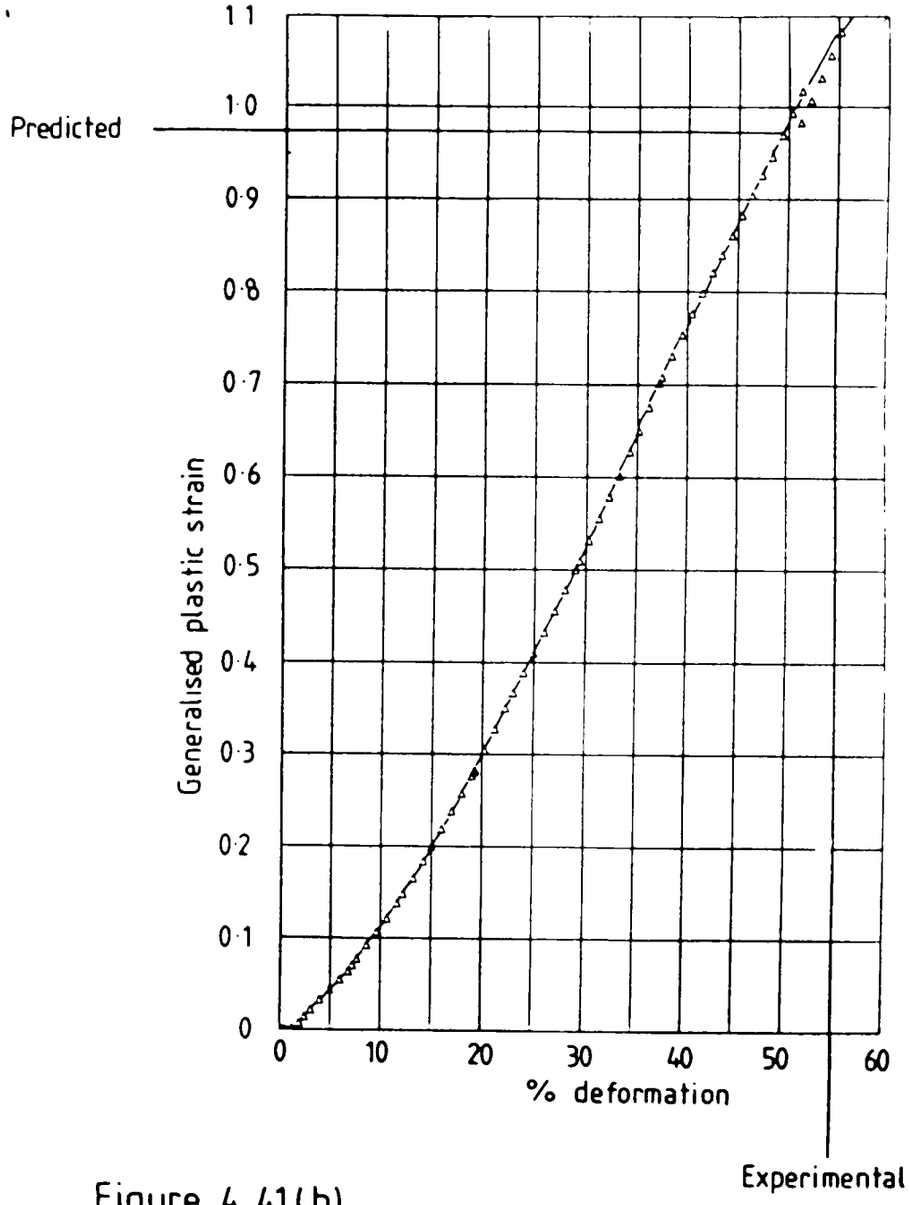

Figure 4.41(b)

Variation of FE generalised plastic strain for the plane-strain side-pressing of initially circular section 60-40 brass for node 5.

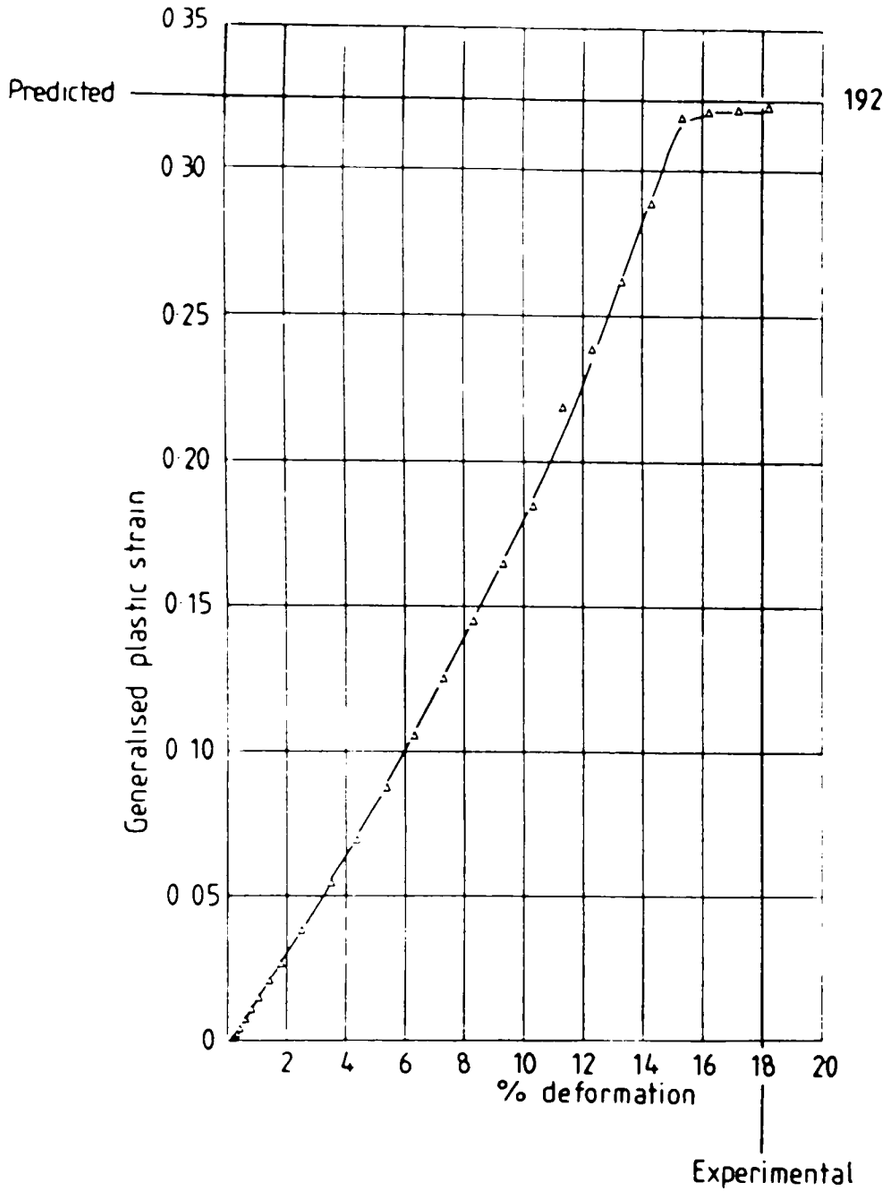

Figure 4.41(c)

Variation of FE generalised plastic strain for the plane-strain side-pressing of 7075 aluminium alloy with initial H/W = 2·03 for node 192.

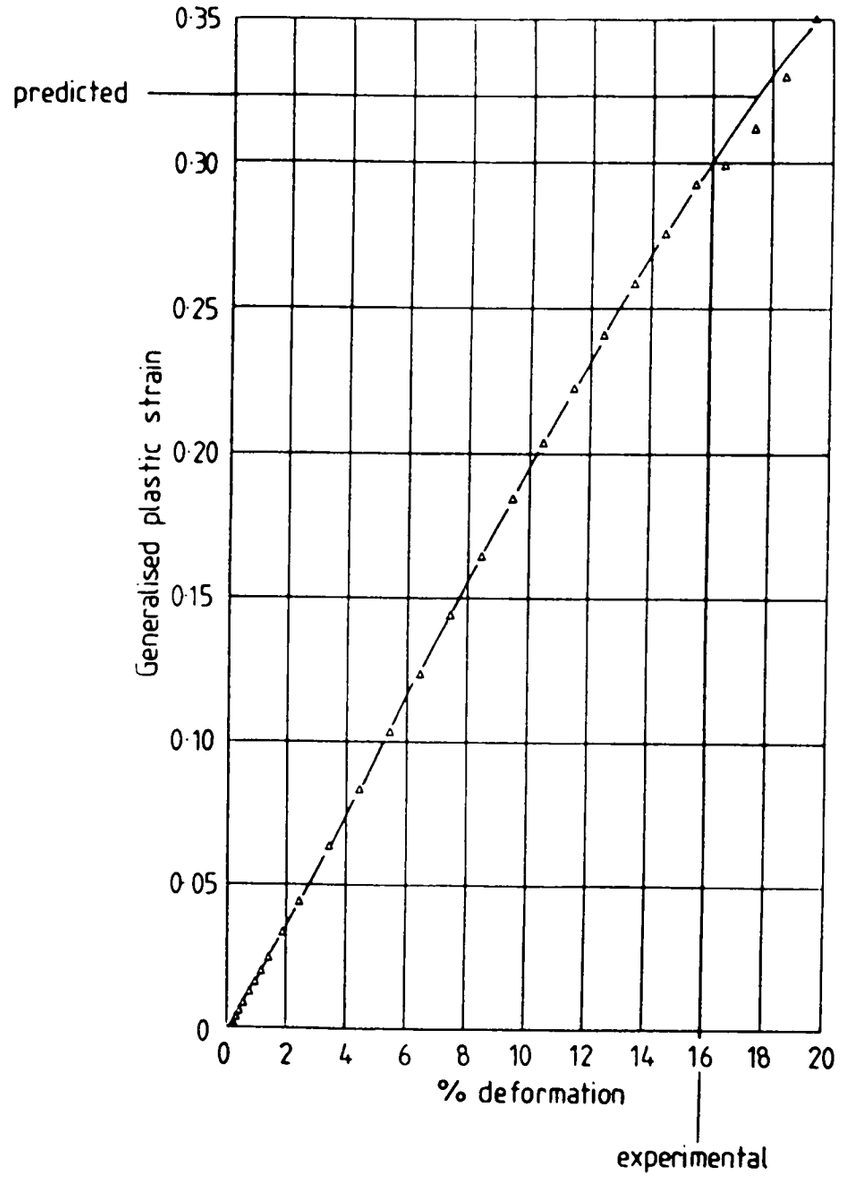

Figure 4.41(d)

Variation of FE generalised plastic strain for the plane-strain side-pressing of 7075 aluminium alloy with initial H/W = 1·33 for node 170.

4.6 Conclusions.

The plane-strain side-pressing of 60-40 brass and 7075 aluminium alloy has been examined experimentally and analysed theoretically using the elastic-plastic finite-element technique. The deformation patterns of one 60-40 brass shape (cylindrical) and three 7075 aluminium alloy shapes (cylindrical and two flat ratios) were analysed. In each case the agreement between the experimental and finite-element macrohardness distributions confirmed the reliability of the finite-element predictions of deformation.

The finite-element results were further used in conjunction with various continuum fracture criteria to predict the site of fracture observed experimentally. These had occurred in the centre of the originally cylindrical workpiece of both materials and at the corner of the workpiece near the platen for 7075 aluminium alloy with machined flats. Several of the fracture criteria examined only predict the correct site for the circular section specimens, others were not successful in any of the cases examined here. However, it was found that both the criteria of a critical value of generalised plastic work and strain were successful in predicting both the site of fracture and the level of deformation at fracture for all the shapes studied.

Chapter 5.

Simple Upsetting.

5.1 Introduction.

This chapter describes the experimental results and finite-element predictions obtained for the simple upsetting of 60-40 brass. Four specimens of differing initial height-to-diameter ratio were tested experimentally under three different frictional conditions. These are described in detail in section 5.2. Section 5.3 describes the finite-element analyses performed to model metal flow in one of the conditions examined experimentally. Section 5.4 presents and discusses both the finite-element and experimental results, both with regard to metal deformation and fracture initiation. Finally, section 5.5 presents the conclusions of the chapter.

5.2 Specimen preparation and experimental procedure.

Cylinders of lead-free 60-40 brass were machined out of a supplied rod of 1cm initial diameter. This rod had the microstructure previously shown in figure 4.1 of chapter 4. The four initial height-to-diameter ratios of 0.5, 1.0, 1.5 and 2.0 were compressed until fracture occurred, using the sub-press illustrated in figure 5.1, on an Avery 600 kN press. All tests were performed at room temperature and slow strain rate. The fracture initiation site and level of deformation at fracture were recorded for each aspect ratio specimen under each of the following three frictional conditions:

1. The specimens and platens were degreased with acetone and then lubricated with lanolin. The lubricant was reapplied after each 5% reduction in the original specimen height (Series L);

2. The specimens and platens were degreased with acetone, no lubricant was added (Series X);

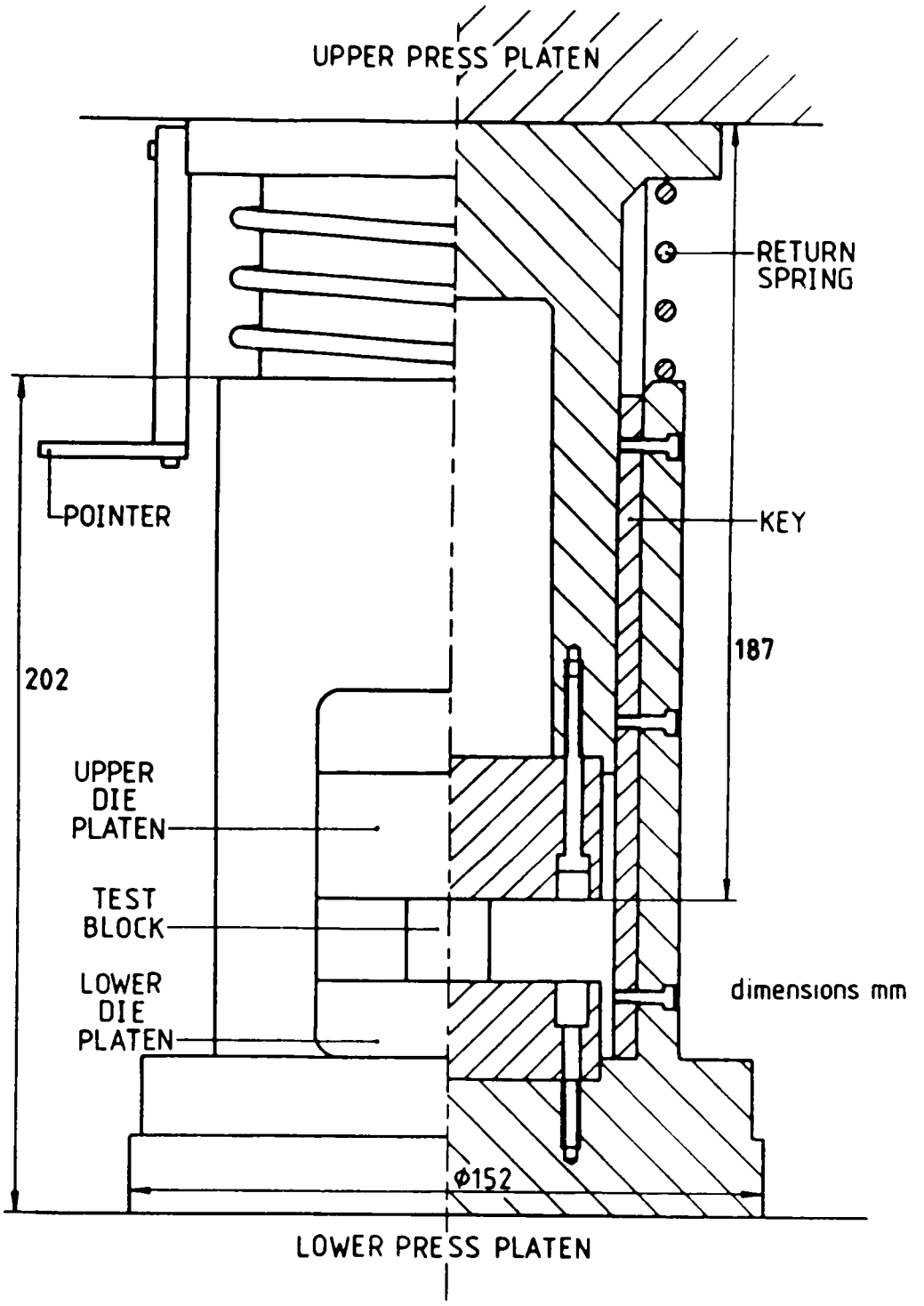

Figure 5.1

Die set used in the simple upsetting experiments.

After Pillinger (1984)

3. The specimens and platens were degreased with acetone, the platens were additionally rubbed with 400 micron grit paper (Series U).

5.3 Finite-element model.

Four finite-element meshes were used in this numerical analysis of the simple upsetting of 60-40 brass. The undeformed meshes are presented in figure 5.2. Each mesh corresponds to one quarter of the complete specimen cross section. Deformation in the other quadrants follows from arguments of symmetry. An eighteen degree segment has been modelled for all aspect ratios. The initial radius of each mesh is 0.5 cm and this has been divided up into ten equal-length regions. The number of regions in the axial direction depends upon the aspect ratio of the specimen. The specimens with initial aspect ratios of 0.5, 1.0, 1.5 and 2.0 contain 95, 190, 285 and 380 elements respectively. In addition there are friction layer elements as indicated by the dashed lines. Only eight node 'brick' type elements are available within the finite-element program used here. Due to this it was necessary to use a double row of elements after the one nearest the centre of the billet. The constitutive relationship is as previously presented in section 4.3.2 of chapter 4.

5.4 Results and Discussion.

5.4.1 Experimental results.

Table 5.1 shows the fracture sites and levels of deformation at fracture for each combination of aspect ratio and frictional condition considered. In each case surface cracks were found, but the precise initiation site could not be identified. For all three sets of results, as the table shows, no particular trend in the level of deformation at

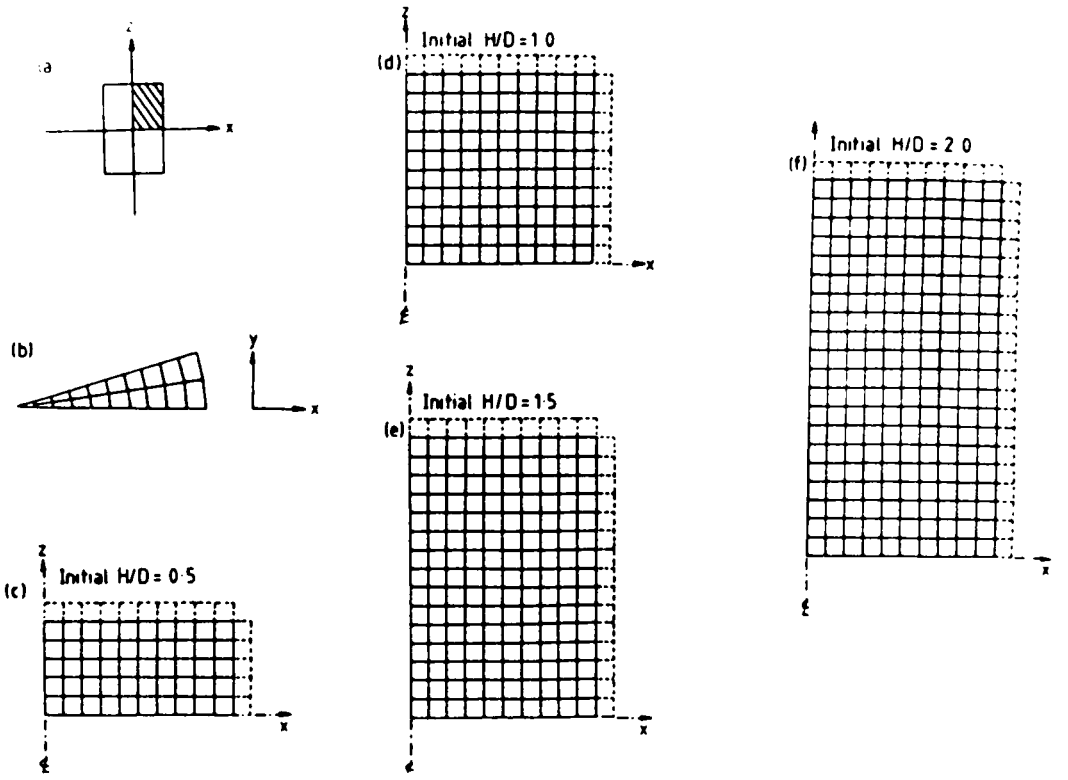

Figure 5.2

Finite-element meshes used in the analysis of simple upsetting.

(a) One quarter of the specimen cross section is modelled.
(b) 18° segment, xy plane.
(c)-(e) xz sections for different aspect ratio models.

H/D	LUBRICATION		
	Lanolin (Series L)	Platens cleaned with acetone (Series X)	Platens cleaned with 400μm grit and acetone (Series U)
0·5	69% 	74% 	70% 
1·0	67% 	72% 	58% 
1·5	70% 	71% 	68% 
2·0	59% 	72% 	72% 

Table 5.1

Type of crack and level of deformation at fracture in the simple upsetting of 60-40 brass under different frictional conditions.

(not to scale)

fracture could be identified for the range of aspect ratio specimens. With lanolin lubrication (Series L) all four aspect ratio specimens fractured by the same type of oblique surface crack. These appear to be the Mode II cracks as described by Kudo and Aoi (1967). (Two planes of fracture on the surface of an upset cylinder were described by these investigators and have previously been illustrated in figure 2.8). Longitudinal, or Mode I cracking, occurs when the mid-height surface axial stress at fracture is tensile. Oblique, or Mode II cracking, occurs when the mid-height surface axial stress is compressive.

Oblique cracks were also found in the experimental tests where the platens and the brass specimens were cleaned with acetone (Series X). For the specimens with an initial aspect ratio of 0.5 three parallel oblique cracks were found. In the next tallest specimen (H/D=1) several oblique cracks were also visible but these were arranged in a zig-zag pattern. For the higher two aspect ratio specimens (H/D = 1.5 and 2.0) single oblique surface cracks were found, as for the series of tests with lanolin lubrication.

For series U, where the platens had been rubbed with 400 micron grit paper and cleaned with acetone, both longitudinal (Kudo and Aoi's Mode I) and oblique (Mode II) cracks were produced.

For the two low-aspect ratio specimens, longitudinal cracking was found. In the specimens with initial aspect ratios of 1.5 and 2.0 mixed-mode cracking occurred: vertical cracks were present in the middle of the free surfaces of the specimens, with oblique cracks linking these to the top and bottom surfaces. For the highest aspect ratio specimen (2.0) both Mode II and mixed-mode cracking was visible.

In the specimens tested by Kudo and Aoi which developed mixed-mode cracking the vertical cracks were observed to occur before the oblique cracks. Unfortunately, it was not possible to identify where the crack initiated in any of the experimental tests reported here.

Figure 5.3 shows the corresponding 'Ring Test' results, as required for the numerical modelling of interface friction (see section 4.3.3), together with the calibration curves described by Pillinger (1984) for the finite-element program EPFEP3.

The set of experimental results corresponding to the highest level of experimental friction, that is series U, was selected for numerical modelling as it contains both modes of cracking. Comparison with the finite-element calibration curves shows that corresponding to m = 0.25 provides a reasonable approximation over the range of reductions for this series of tests. However, this line underestimates the deformation for low reduction in height and overestimates for high reductions. The effect of this discrepancy in form between the finite-element and experimental results on the fracture predictions is examined in section 5.4.3.

Photographs of the cracks in these specimens are given in figure 5.4. Figure 5.4(a) contains a photograph of the full width of the free surface of the brass specimen with an initial height-to-diameter ratio of 0.5. Here, the longitudinal crack has a variable width. The crack does not quite extend along the complete height of the specimen. (The white mark on a dark background visible to the left of the crack in this photograph is an artefact and may be ignored).

Figure 5.4(b) shows the longitudinal crack obtained for the specimen with an initial aspect ratio of 1.0. This crack is much straighter than that reported for the previous specimen, but it also does not extend across the complete height of the specimen.

Figure 5.4(c) and 5.4(d) show the mixed mode cracking found for the two higher aspect ratio specimens. In both cases the central longitudinal portion of the crack is much wider than the Mode II arms to either side.

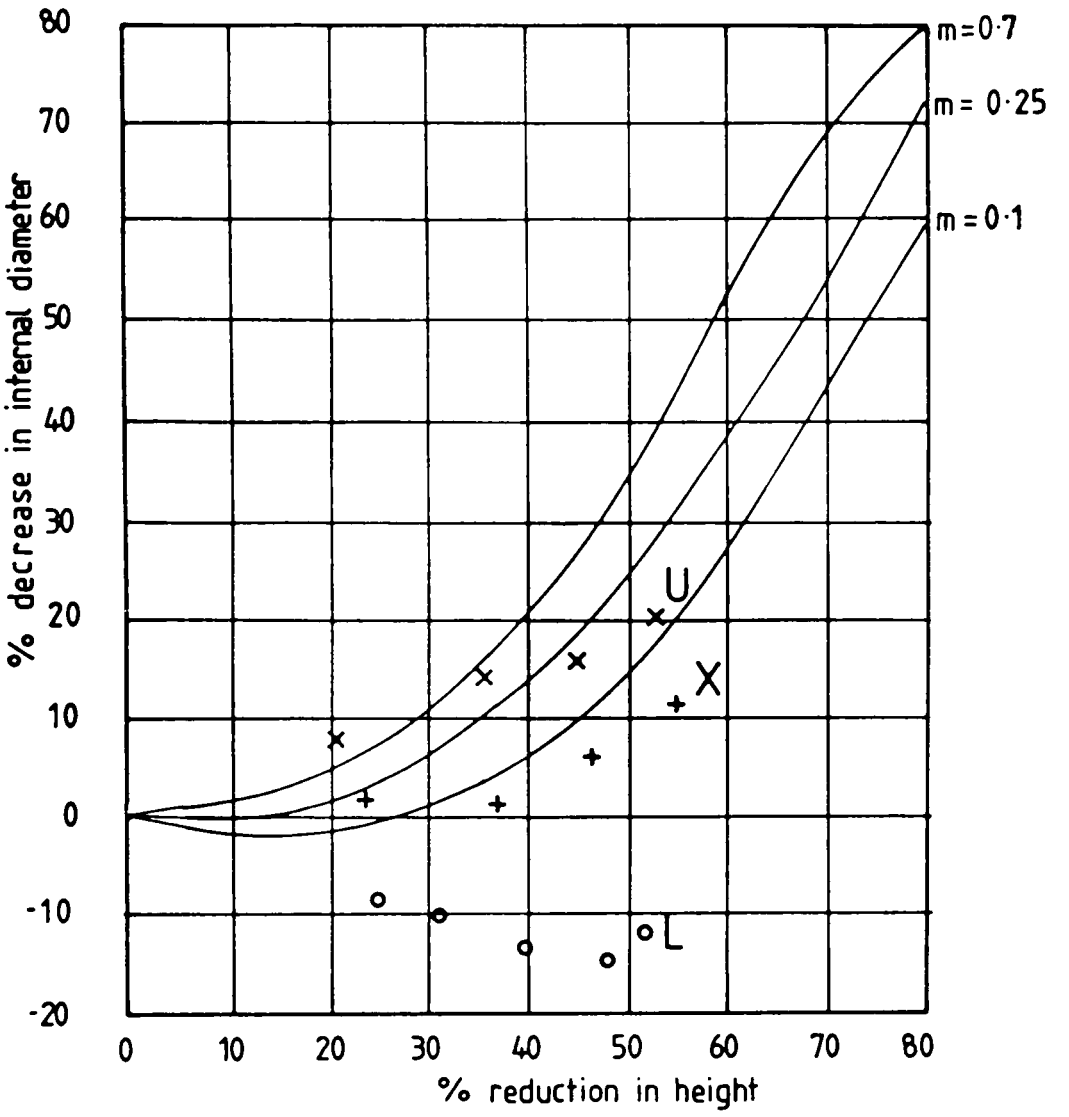

Figure 5.3

Ring test results and finite-element calibration curves for 60-40 brass.

Series X : Platens degreased with acetone.
Series U : Platens rubbed with 400 grit paper and degreased with acetone.
Series L : Lanolin lubrication.

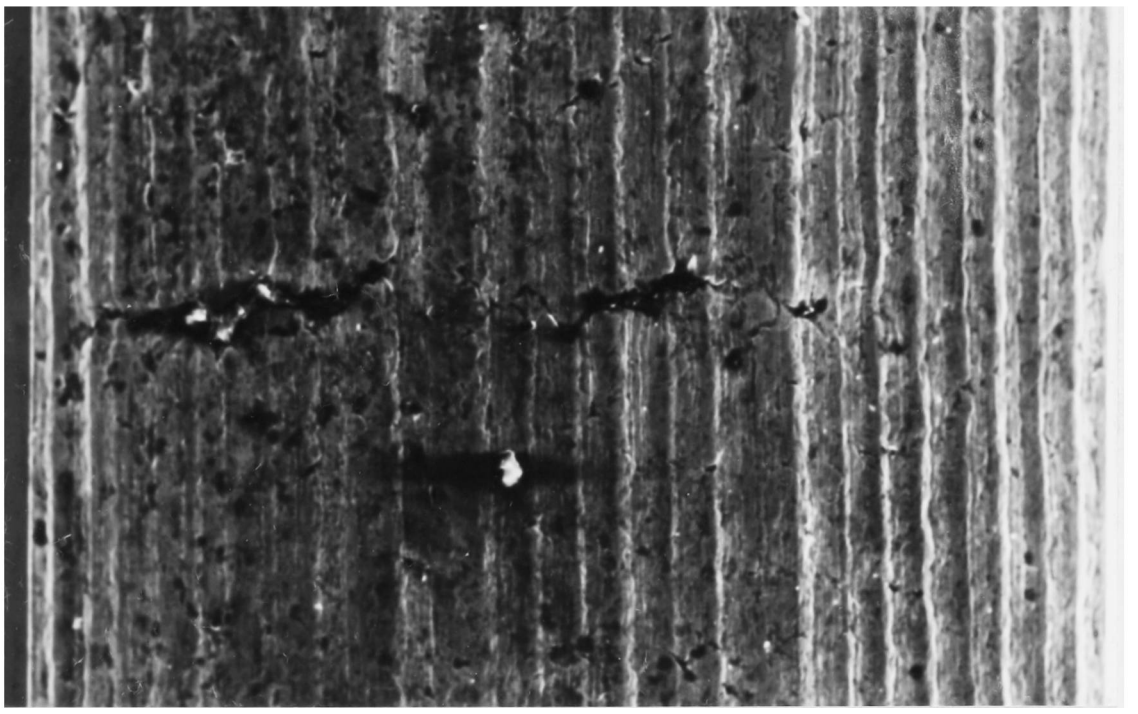

Figure 5.4(a)

Scanning electron microscope photograph of the fracture site in a brass specimen with initial H/D=0.5. (x65)

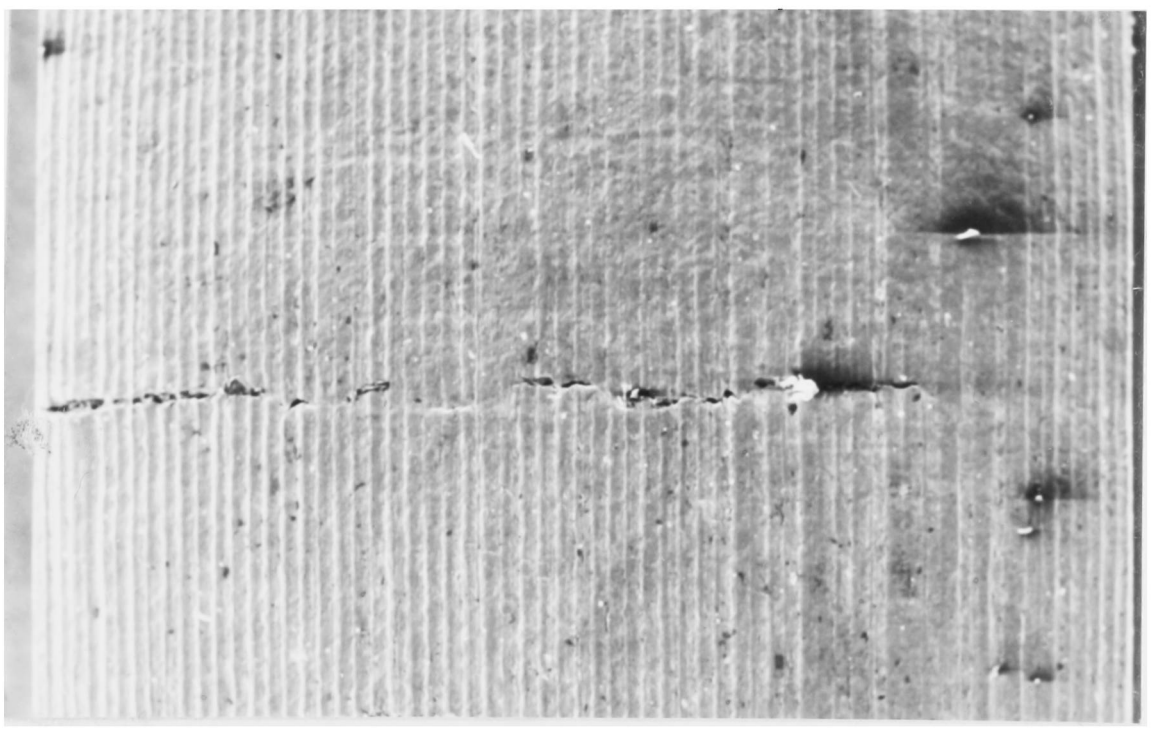

Figure 5.4(b)

Scanning electron microscope photograph of the fracture site in a brass specimen with initial H/D=1.0. (x27)

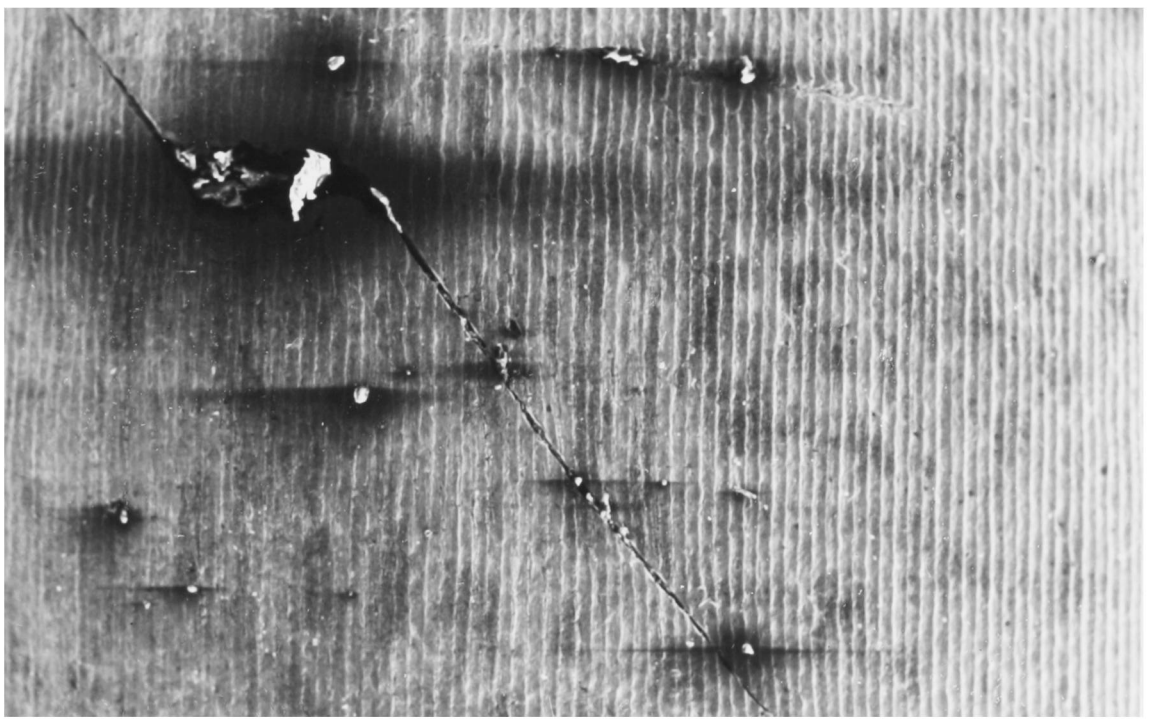

Figure 5.4(c)

Scanning electron microscope photograph of the fracture site in a brass specimen with initial H/D=1.5. (x27)

Figure 5.4(d)

Scanning electron microscope photograph of the fracture site in a brass specimen with initial H/D=2.0. (x24)

5.4.2 Finite-element results.

Several sets of data available from the finite-element technique which are not readily available from any other approach are described in this section. The first of these gives the incremental displacement vectors. These vectors illustrate the direction and magnitude of the movement of a node during the most recent increment of deformation. Figure 5.5 presents these displacement vectors for the operation of simple upsetting. These illustrations represent the top right hand quadrant of a specimen located between a stationary upper platen and a moving lower platen. All of these vectors have a relative magnification of five when compared with the overall specimen dimensions. The final illustration in each sequence is at the level of deformation at fracture found experimentally. The diagrams are not all drawn to the same scale (due to the automatic scaling of the graphics program), but the changes in the flow patterns which occur as the deformation proceeds may be identified. The metal flow for all four aspect ratio specimens follows the same pattern. Material along the central axis of the specimen is predicted to flow vertically, while that in contact with the die flows horizontally. Material in the body of the specimen flows in an oblique manner. The angle of the flow vector to the vertical is smallest in the central region of the specimen, then increases out towards the circumference of the specimen and then further increases up towards the top surface of the specimen in contact with the die. For the taller specimens the difference in the angle of the displacement vectors for adjacent nodes is less as there is more material present in which to accomodate the change from vertical to horizontal flow. The formation of a dead zone in the centre of the cross section of the specimen under the die surface is also apparent for the highly deformed specimens.

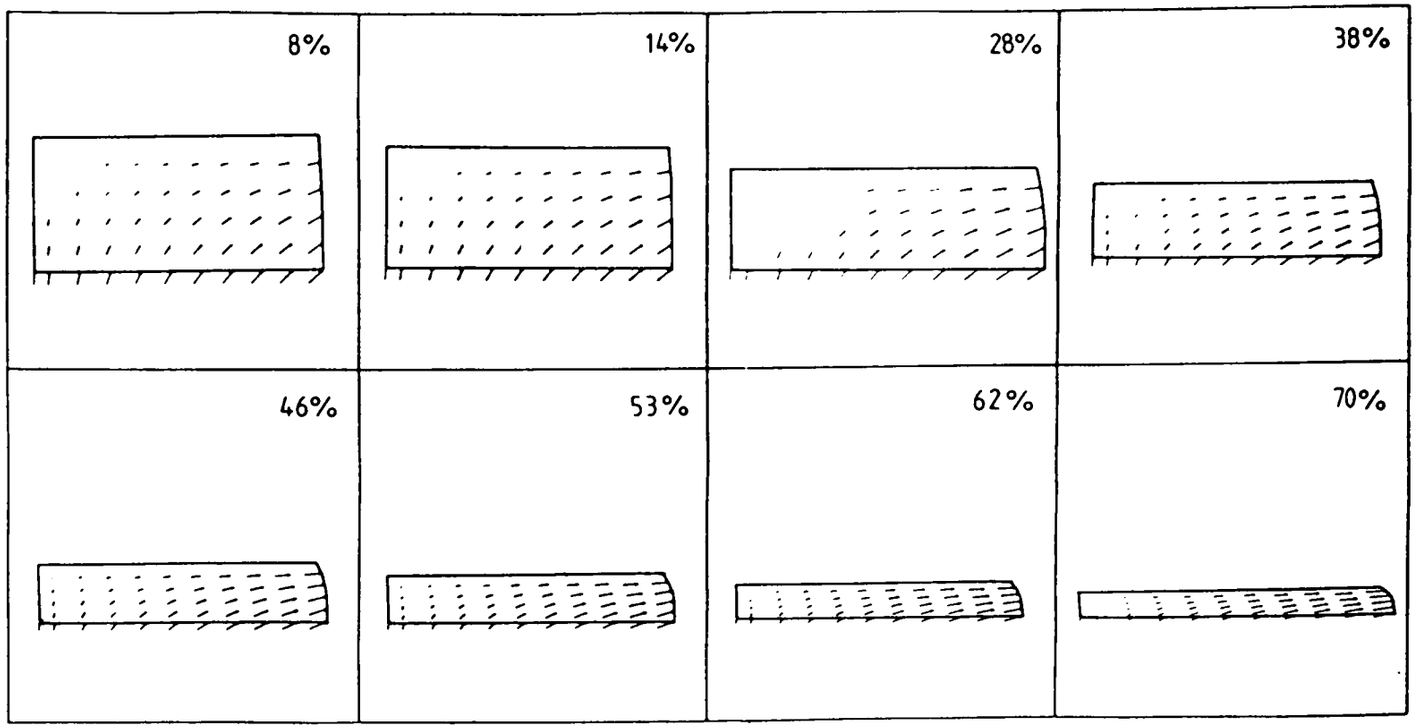

Figure 5.5(a)

Incremental displacement vectors for the simple upsetting of a 60-40 brass specimen model of initial H/D=0·5.

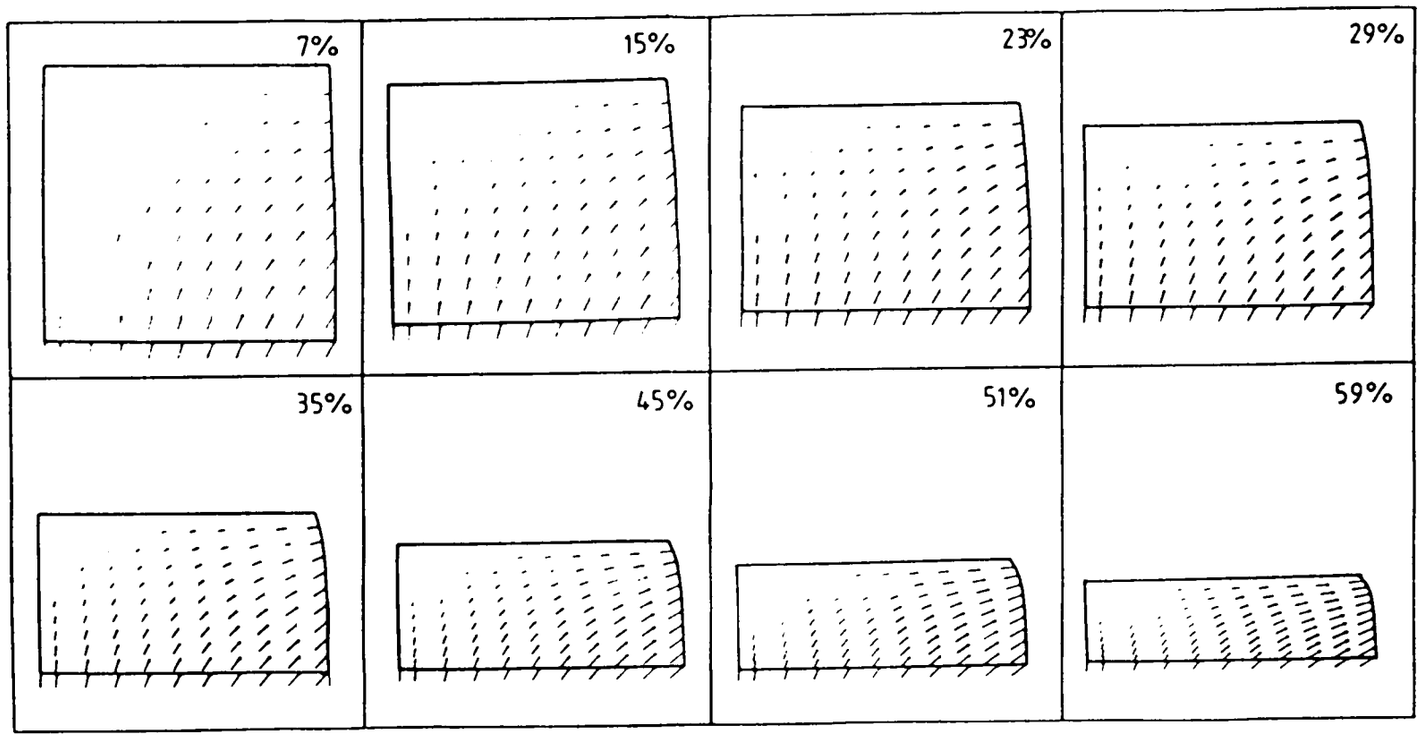

Figure 5.5(b)

Incremental displacement vectors for the simple upsetting of a 60-40 brass specimen model of initial H/D = 1·0 with m = 0·25.

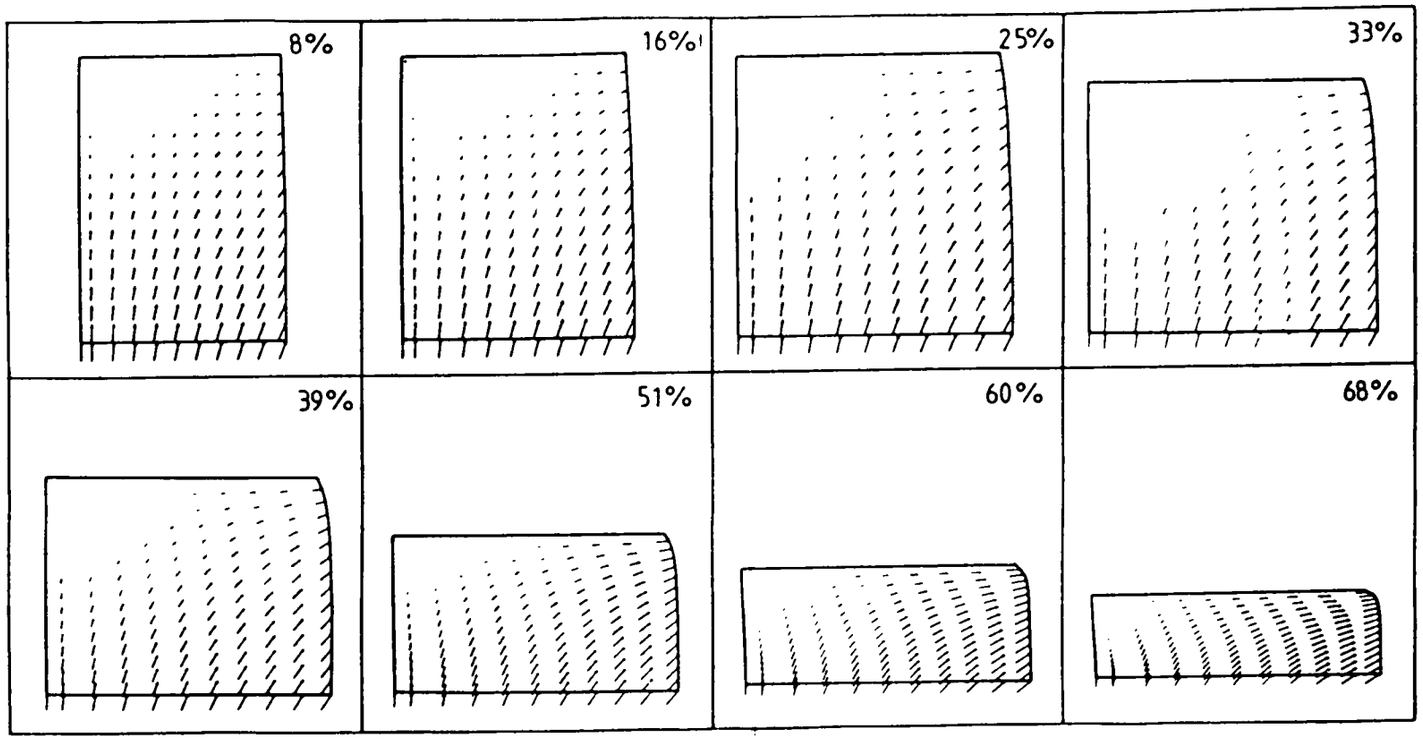

Figure 5.5(c)

Incremental displacement vectors for the simple upsetting of a 60-40 brass specimen model of initial H/D=1·5.

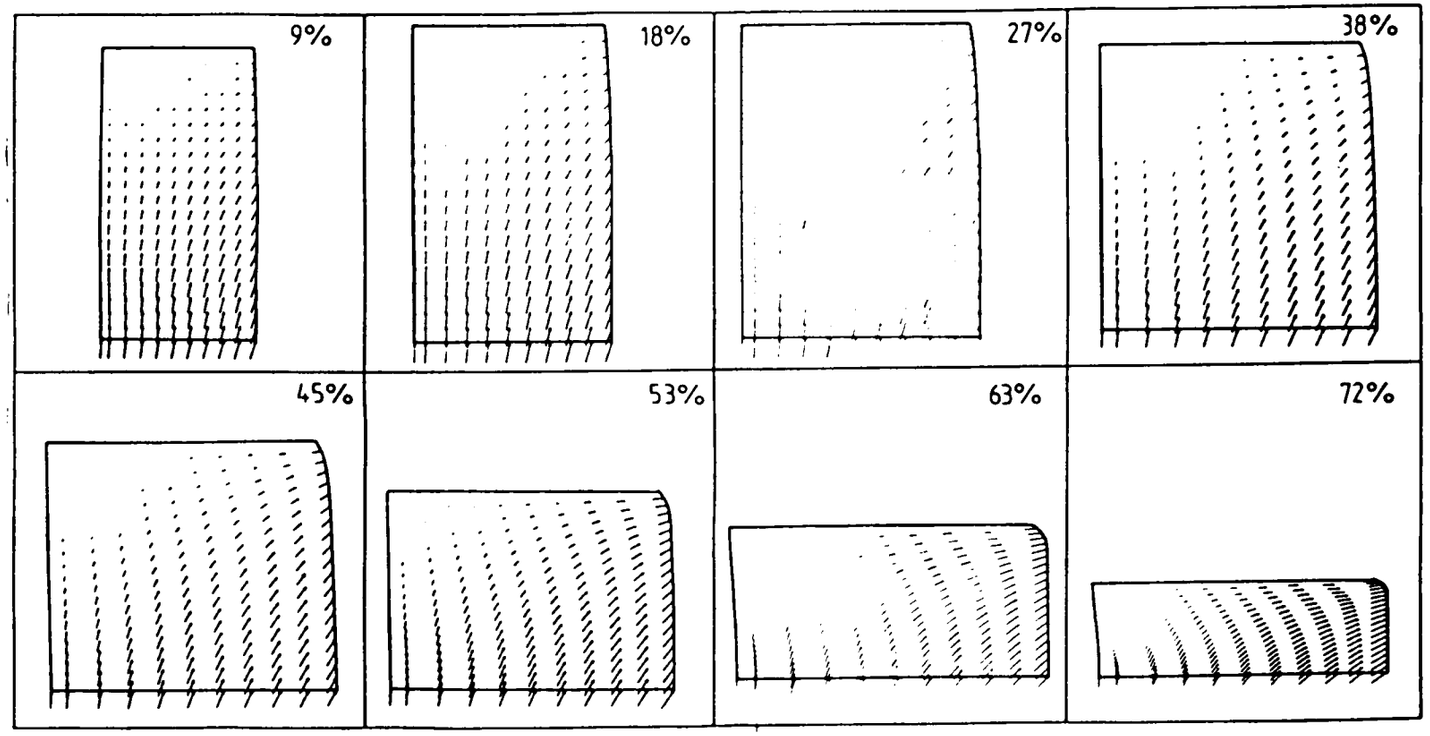

Figure 5.5(d)

Incremental displacement vectors for the simple upsetting of a 60-40 brass specimen model of initial H/D = 2·0.

The final illustration in the sequence of displacement vectors for the specimen with an initial height to diameter ratio of 2 shows that the leftmost column of nodes displayed do not remain in a straight line. This is because this layer of nodes are not actually on the axis but situated slightly to its right hand side (again a feature of the graphics program).

The plastic zone development diagrams for simple upsetting are shown in figure 5.6. These diagrams show the development of the region of plastic flow as deformation proceeds. Again, for each of the four aspect ratio specimens only one quarter of the billet has been displayed. The small sketch in the top right hand corner of each diagram shows the location of the quadrant modelled with respect to the complete specimen. All four sets of illustrations in figure 5.6 are not to the same scale, but are consistent for each aspect ratio model.

For the model with an initial aspect ratio of 0.5 the material is fully plastic after 2 increments and 0.3% reduction. A small volume of material near the die remains elastic after one increment, but less than 0.01% deformation later the complete model is behaving in a plastic manner. This pattern of plastic zone development is also apparent in the other three specimen aspect ratios examined, as figures 5.6(b) to 5.6(d) illustrate. All four models are fully plastic by a reduction in height of 1.0%.

Results have also been plotted on a graph of the type used by Kudo and Aoi to display their fracture locus (see figure 2.7). Figure 5.7 contains these finite-element strain path to fracture results. One set of values has been plotted for each aspect ratio model. The final value in each set, that value taken at the experimental level of deformation at fracture, has been plotted with a circle around it. Unlike the non-linear strain paths to fracture plotted by Kudo and Aoi, the finite-element values presented here give strain paths which are very

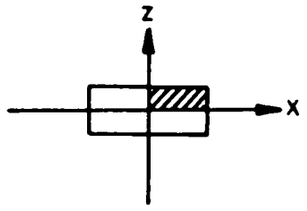

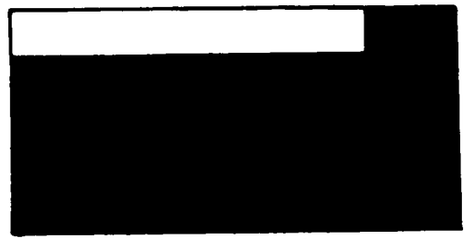

After 1 increment
0·27% deformation

After 2 increments
0·34% deformation

Figure 5.6(a)

Plastic zone development in the simple upsetting of 60-40 brass with initial height to diameter ratio of 0·5.

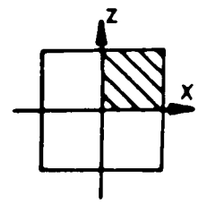

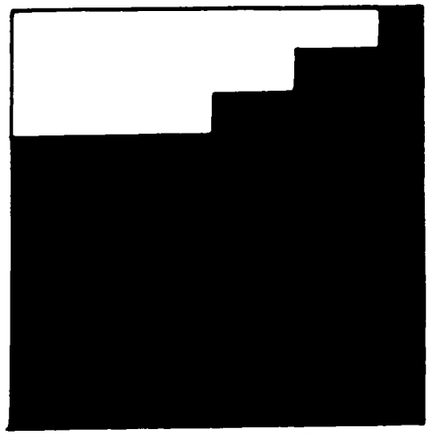

After 1 increment
0·30% deformation

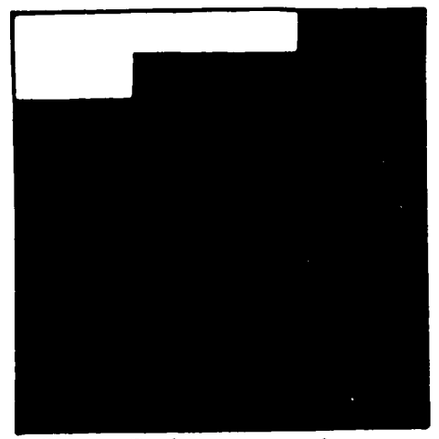

After 2 increments
0·38% deformation

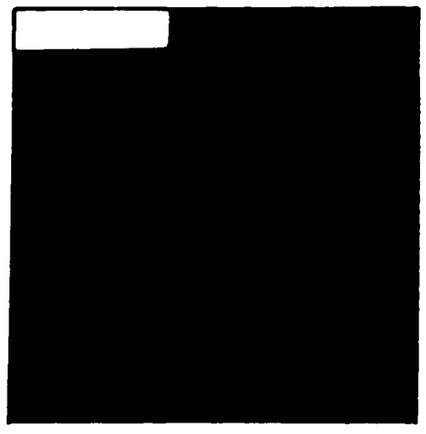

After 3 increments
0·60% deformation

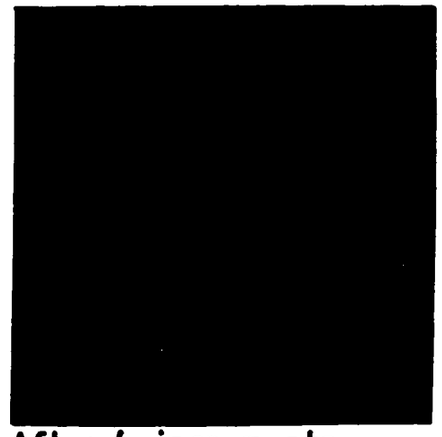

After 4 increments
0·76% deformation

Figure 5.6(b)

Plastic zone development in the simple upsetting of 60-40 brass with initial height to diameter ratio of 1·0.

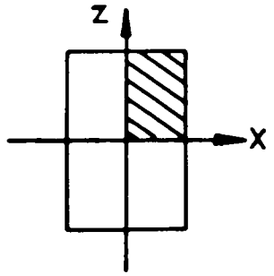

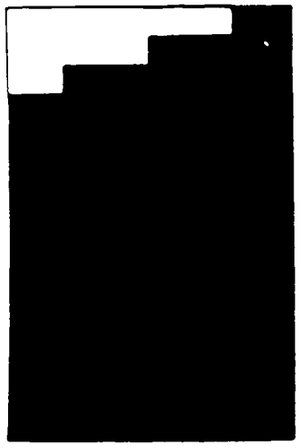

After 1 increment
0·3% deformation

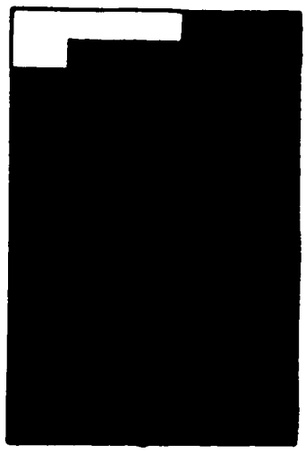

After 2 increments
0·5% deformation

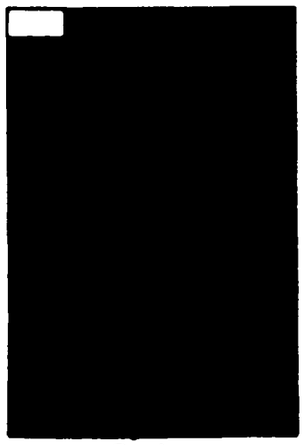

After 3 increments
0·7% deformation

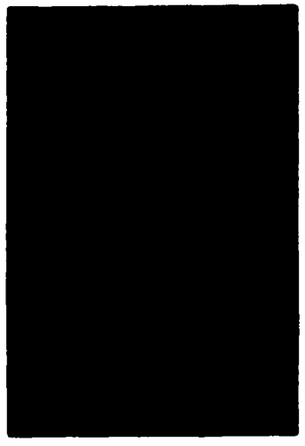

After 4 increments
1·0% deformation

Figure 5.6 (c)

Plastic zone development in the simple upsetting of 60-40 brass with initial height to diameter ratio of 1·5

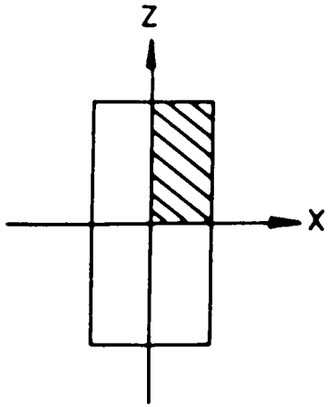

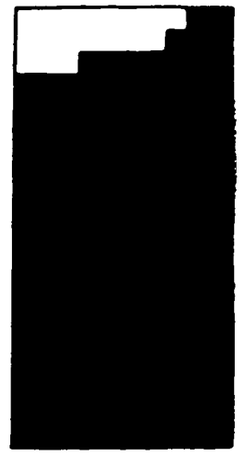

After 1 increment
0·3% deformation

After 2 increments
0·5% deformation

After 3 increments
0·7% deformation

Figure 5.6 (d)

Plastic zone development in the simple upsetting of 60-40 brass with initial height to diameter ratio of 2·0

Figure 5.7

Finite-element results plotted on a Kudo and Aoi fracture locus diagram.

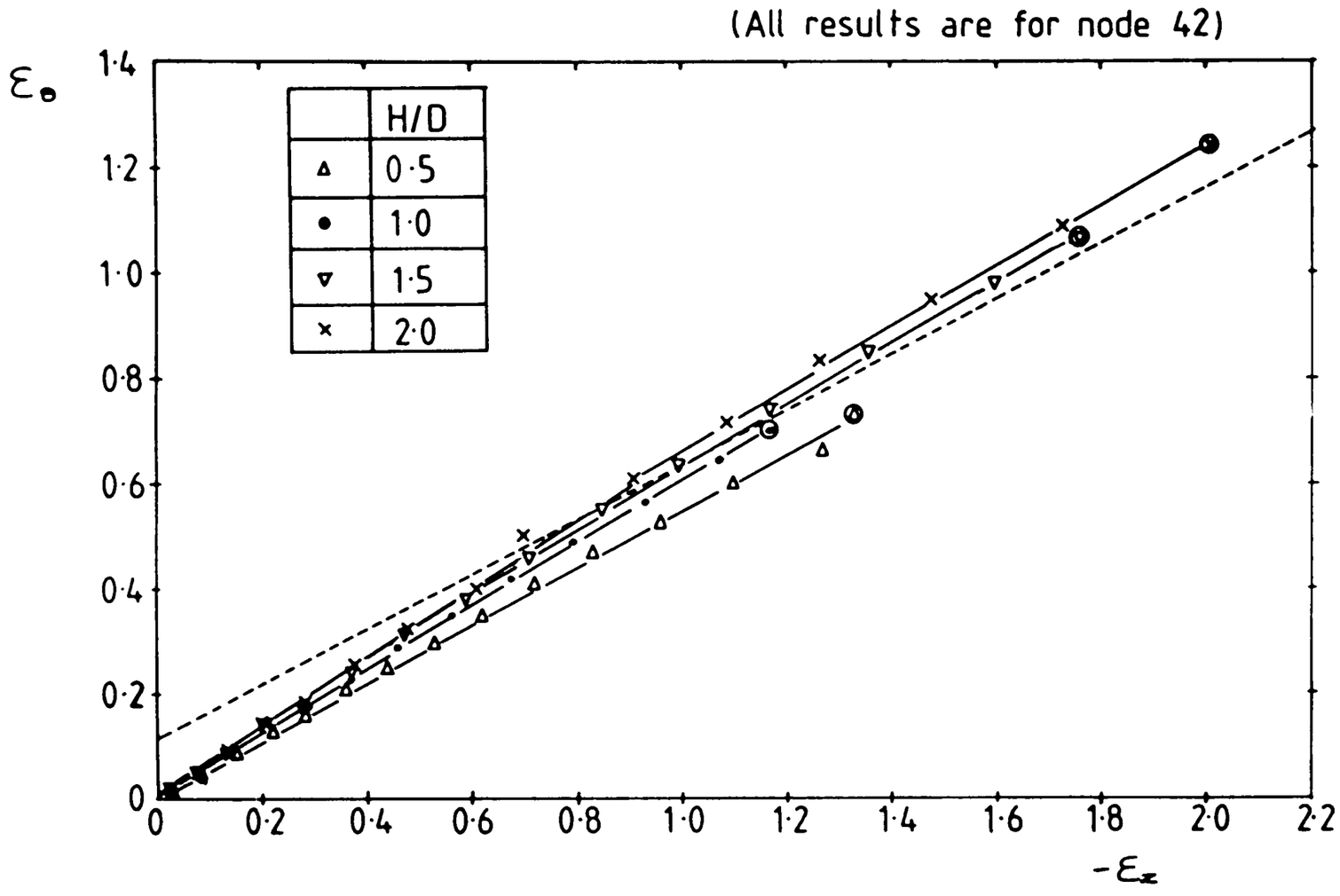

nearly linear, as the graph shows.

The dashed line has the same gradient as the fracture locus of Kudo and Aoi. Values obtained for the specimens which exhibited mixed-mode fracture are positioned slightly above this line, and those for longitudinal cracks slighly below it. It is not possible to draw this fracture locus with great accuracy as there are not enough numerical values to give a reliable intercept value with the axis. More finite-element values would therefore be required to demonstrate agreement with the principal surface strain fracture locus.

5.4.3 Assessment of various fracture criteria.

By using the finite-element program in conjunction with the fracture prediction program, as previously described in chapter 3 of this thesis, numerical predictions of the fracture initiation sites in simple upsetting were obtained by finding the node in the mesh at which the calculated value of each fracture criterion was at a maximum at the level of deformation at fracture found experimentally. These predicted sites were then compared with the crack initiation sites found experimentally and the comparisons presented in table 5.2 were made. A tick indicates that the experimental and numerically predicted sites of fracture initiation agree; a cross that they disagree.

The numbers displayed in the bottom right hand corner of each table element refer to the node number at which fracture initiation was predicted to occur. The location of these nodes is given in the deformed mesh diagrams in figure 5.8.

For both the McClintock and Atkins criteria, predictions can also be made of the plane of fracture. These are displayed in the top left hand corner of the appropriate table elements.

From table 5.2 it may be seen that four criteria have been found to predict successfully the fracture initiation sites found experimentally for all four aspect-ratio specimens. These are the generalised plastic strain and generalised plastic work criteria and those due to McClintock, Kaplan and Berg (1966) and Brozzo, DeLuca and Rendina (1972). The remaining criteria considered show partial agreement with experiment, that is they are capable of correctly predicting the experimental fracture initiation site for some but not all of the specimen geometries considered. The criteria due to Cockroft and Latham (1968), Ghosh et al (1976) and Oyane et al (1980) give correct

criterion / specimen	McClintock (1968)	McClintock et al (1966) (shear)	Ghosh	Oyane	Cockroft and Latham	Brozzo	Gen. plastic strain	Gen. plastic work	Norris	Atkins
H/D=0·5	zr(r) × 32	zr(z) √ 114	√ 217	√ 42	√ 52	√ 42	√ 42	√ 42	√ 42	θz × 84
H/D=1·0	rθ(r) √ 42	θz(θ) √ 114	√ 176	√ 42	× 371	√ 42	√ 42	√ 42	× 370	θz × 243
H/D=1·5	zr(r) √ 42	rθ(r) √ 83	× 154	√ 42	√ 527	√ 42	√ 42	√ 42	× 508	θz √ 302
H/D=2·0	rθ(r) √ 42	θz(z) √ 93	√ 589	× 312	× 218	√ 62	√ 42	√ 42	× 249	θz × 559

Table 5·2

Comparison of FE Predictions of fracture initiation site and experimental results for the simple upsetting of 60-40 brass.

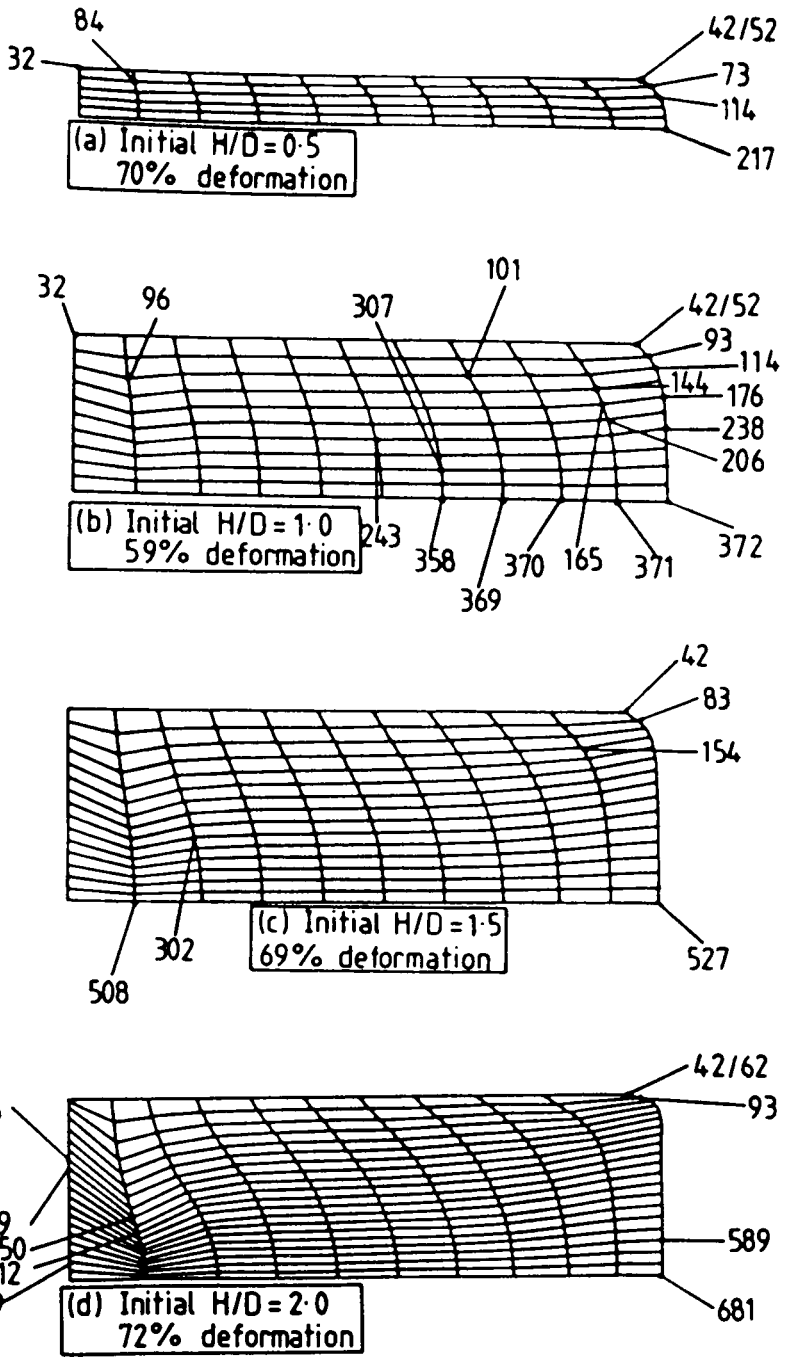

Figure 5.8

Deformed FE grids at the experimental level of deformation at fracture.

Node numbers refer to the fracture prediction sites.

predictions for three out of the four specimen geometries. It is possible that because the exact site of fracture initiation cannot be pinpointed there is wide agreement with many of the fracture criteria considered.

The remaining criteria, those of Norris et al (1978) and Atkins (1981) only give one correct fracture initiation site out of a total of four. Experimentally, surface cracks were found, that is cracks in the theta-z direction. The Atkins fracture criterion predictions give this plane for each of the four ratios but not at the correct fracture site, so these fracture plane predictions are not relevant.

The McClintock (1968) criterion does not produce any correct fracture plane predictions, but the criterion of McClintock et al (1966) does give correct fracture plane predictions for the specimens with initial aspect ratios of 1.0 and 2.0.

As reported in section 4.5.2 of chapter 4, an experimental determination of the actual critical value of generalised plastic work at fracture, the critical value of generalised plastic strain and of the tensile plastic work at fracture was made using a simple axisymmetric tensile test.

These critical values have been compared with finite-element predictions. The comparison of the predicted and experimental levels of deformation at fracture for the generalised plastic strain fracture criterion is presented in figure 5.9 and for the generalised plastic work criterion in figure 5.10.

The predicted level of deformation at fracture found from both sets of graphs and the value obtained experimentally for each mesh is summarised in table 5.3. Predictions from the work and strain criteria are the same, as also reported for the plane-strain side-pressing experiments in chapter 4. This is because the experimental curve terminates at a particular strain so the comparison on the basis of area is the same as

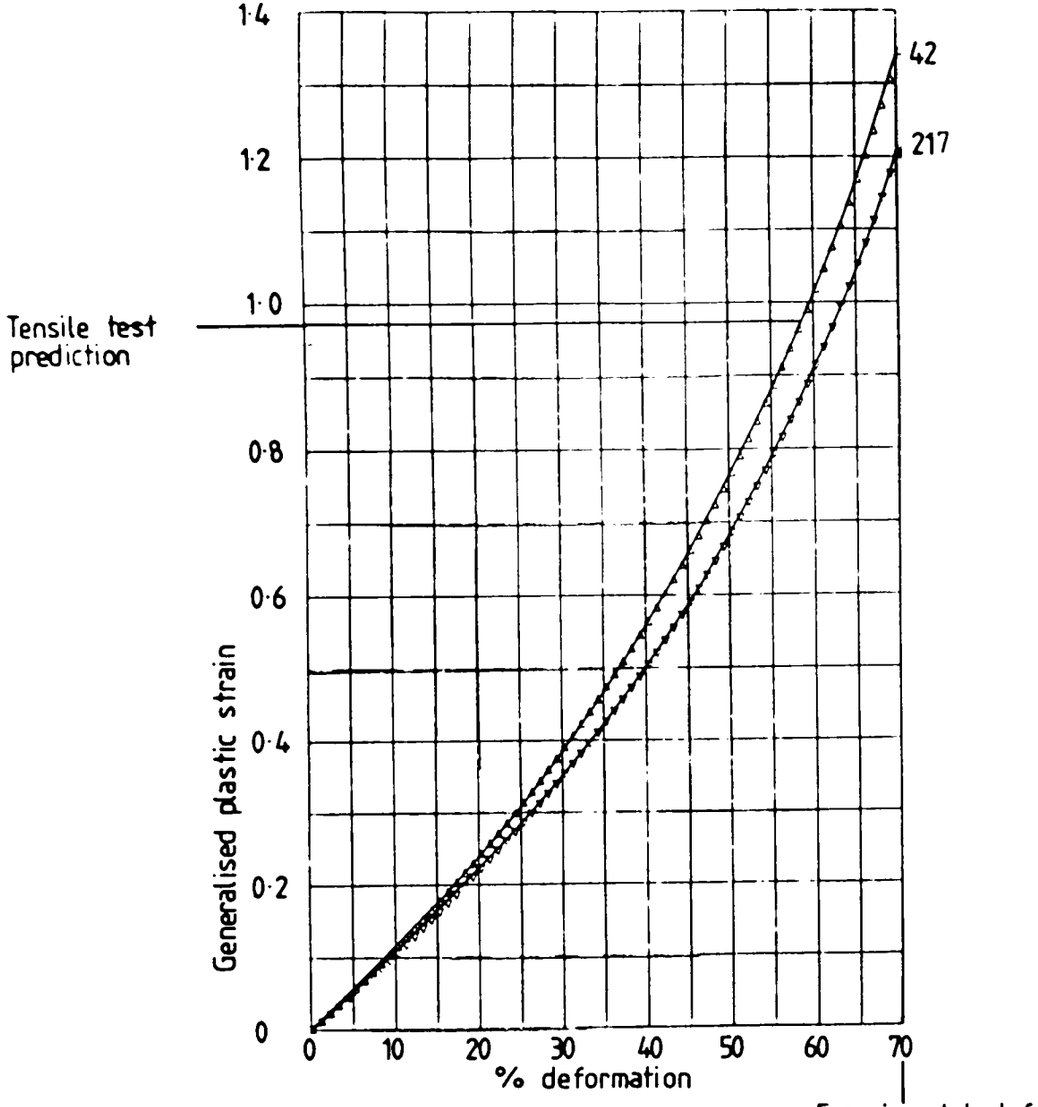

Figure 5.9(a)

Variation of FE generalised plastic strain in the upsetting of 60-40 brass with an initial height to diameter ratio of 0·5 for nodes 42 and 217.

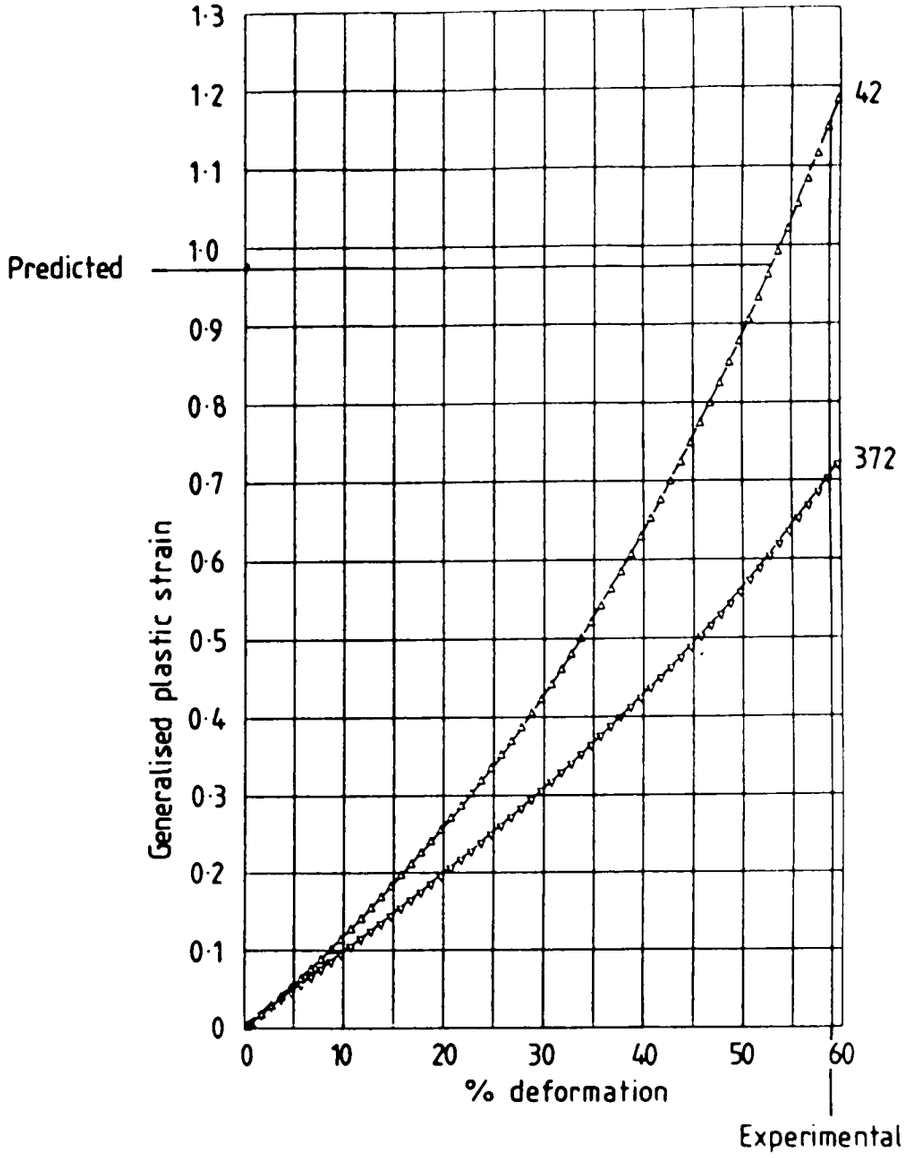

Figure 5.9(b)

Variation of FE generalised plastic strain in the upsetting of 60-40 brass with an initial height to diameter ratio of 1·0 for nodes 42 and 371.

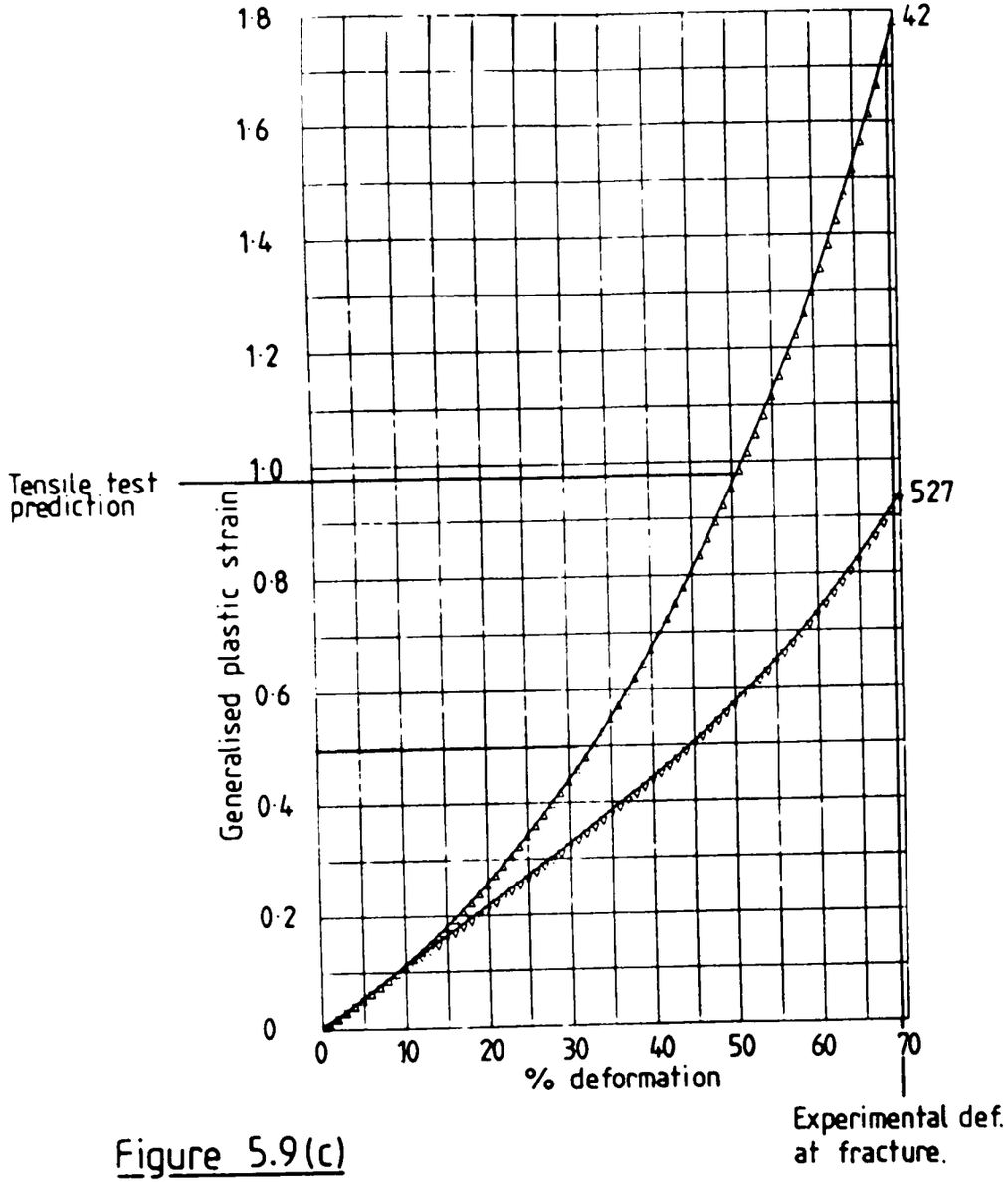

Figure 5.9(c)

Variation of FE generalised plastic strain in the upsetting of 60-40 brass with an initial height to diameter ratio of 1·5 for nodes 42 and 527.

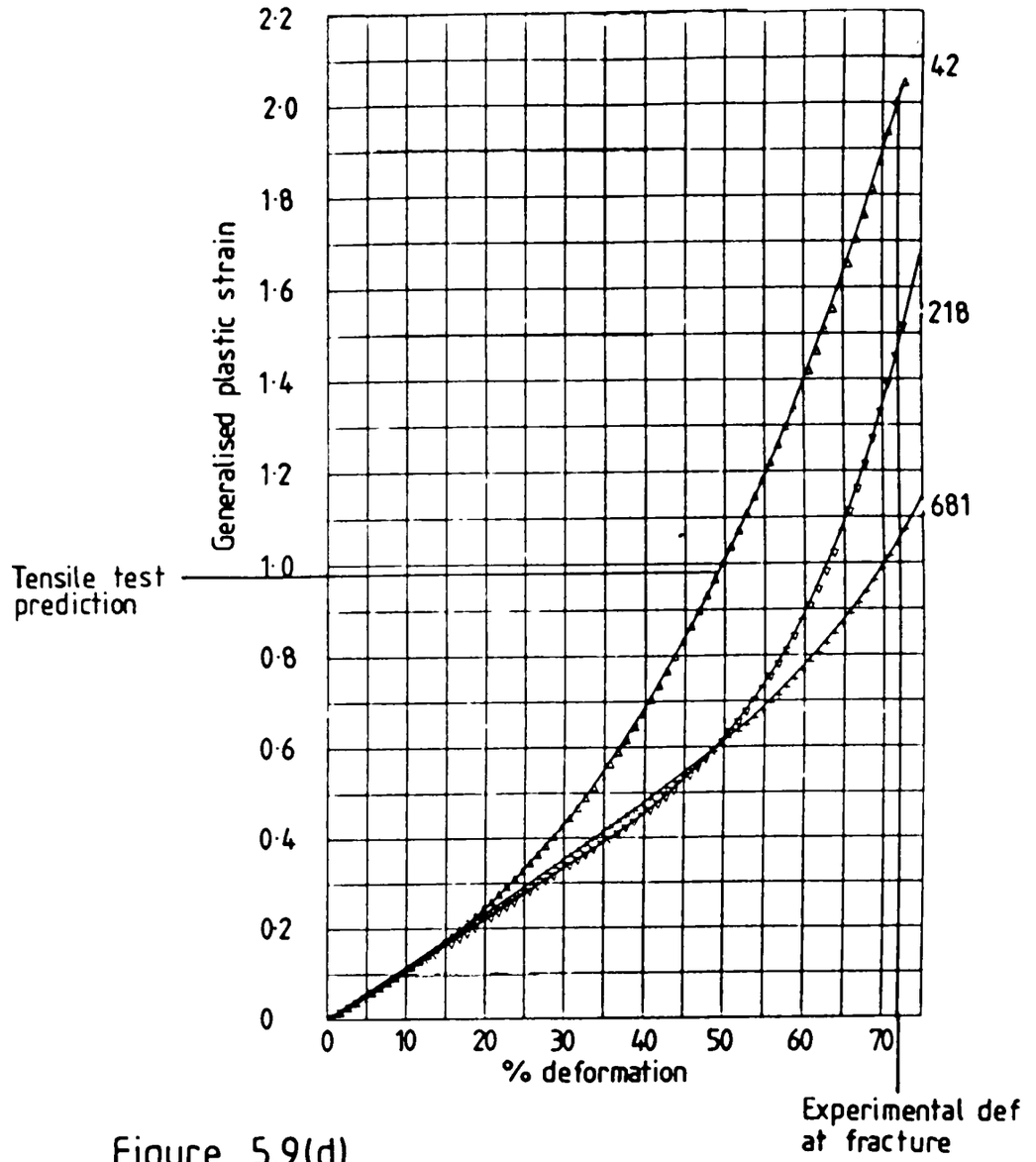

Figure 5.9(d)

Variation of FE generalised plastic strain in the upsetting of 60-40 brass with an initial height to diameter ratio of 2·0 for nodes 42, 218 and 681.

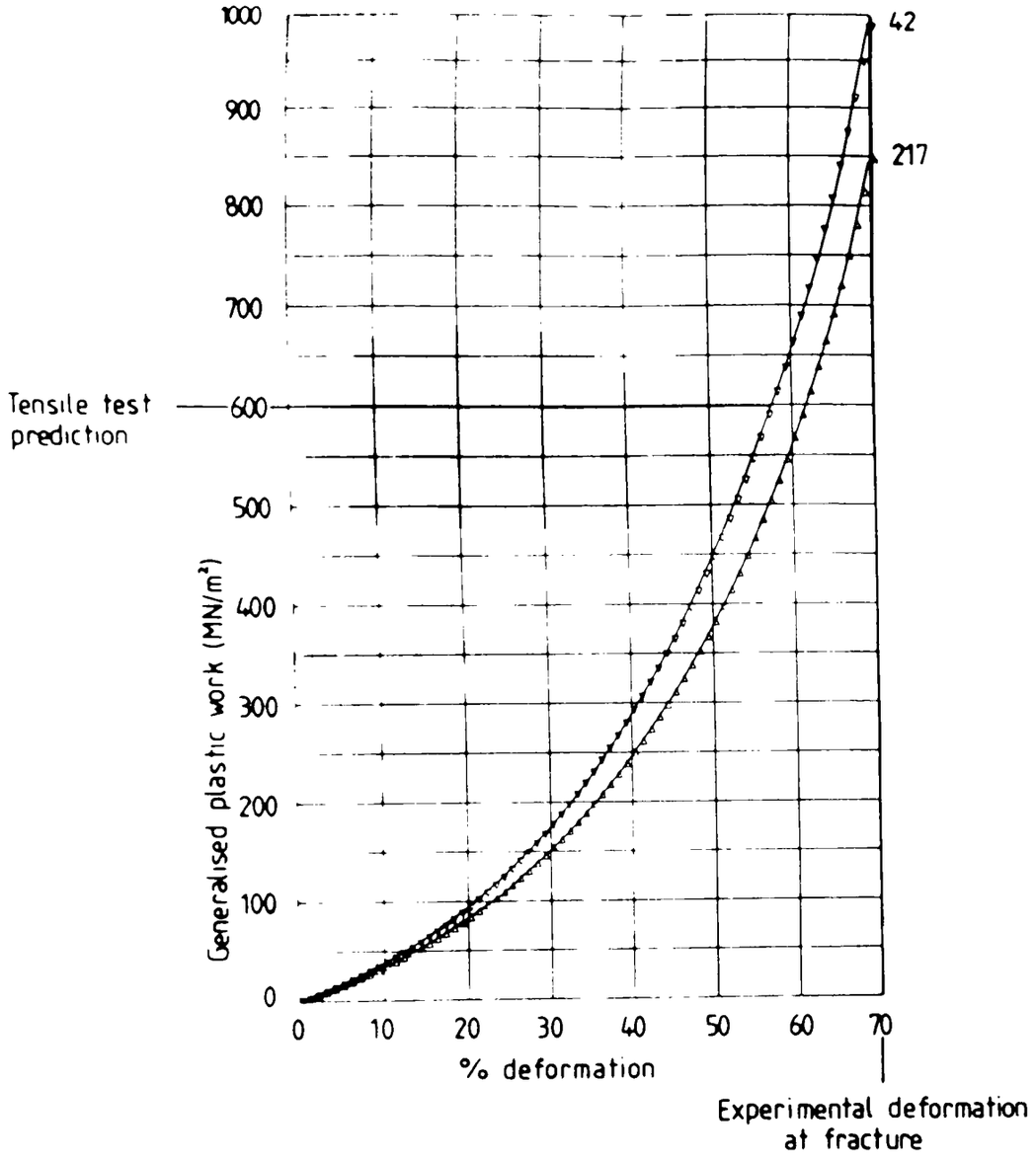

Figure 5.10(a)

Numerical calculation of the generalised plastic work fracture criterion from FE results for the upsetting of 60-40 brass with an initial height to diameter ratio of 0·5 for nodes 42 and 217.

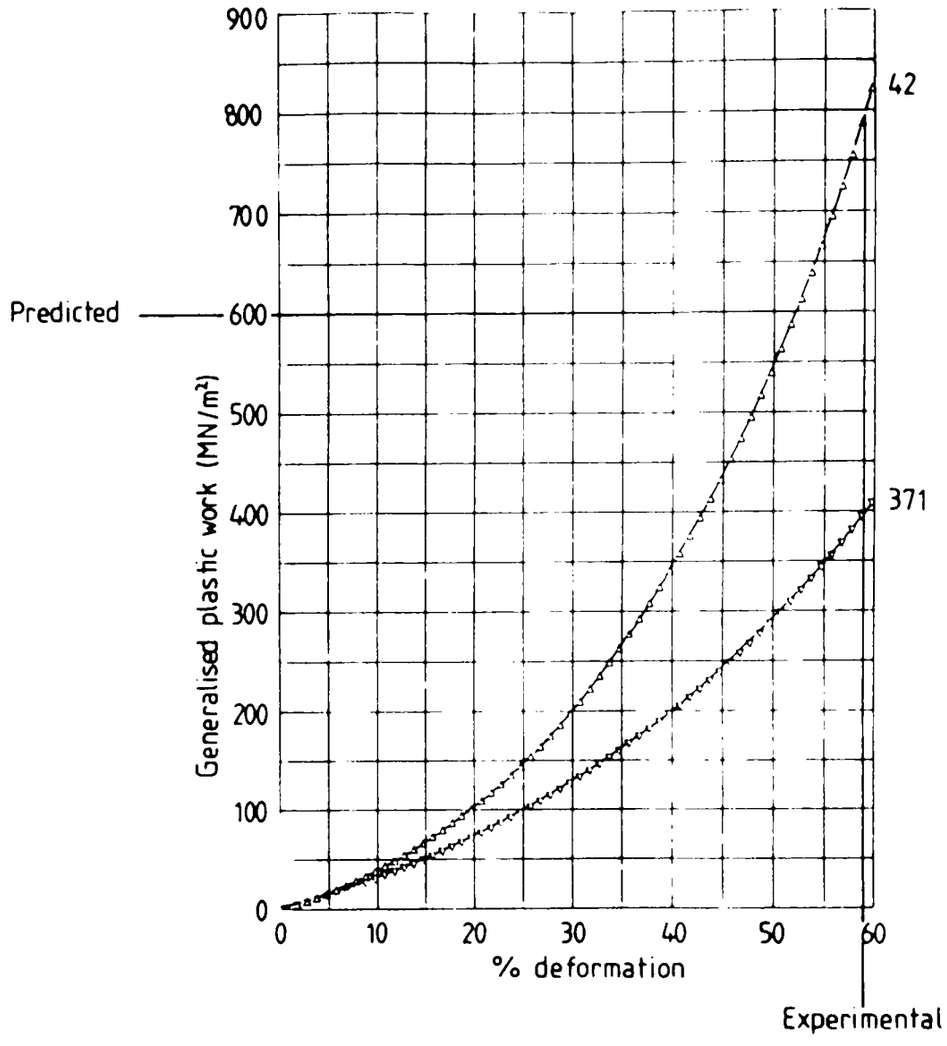

Figure 5.10(b)

Numerical calculation of the generalised plastic work fracture criterion from FE results for the upsetting of 60-40 brass with an initial height to diameter ratio of 1·0 for nodes 42 and 371.

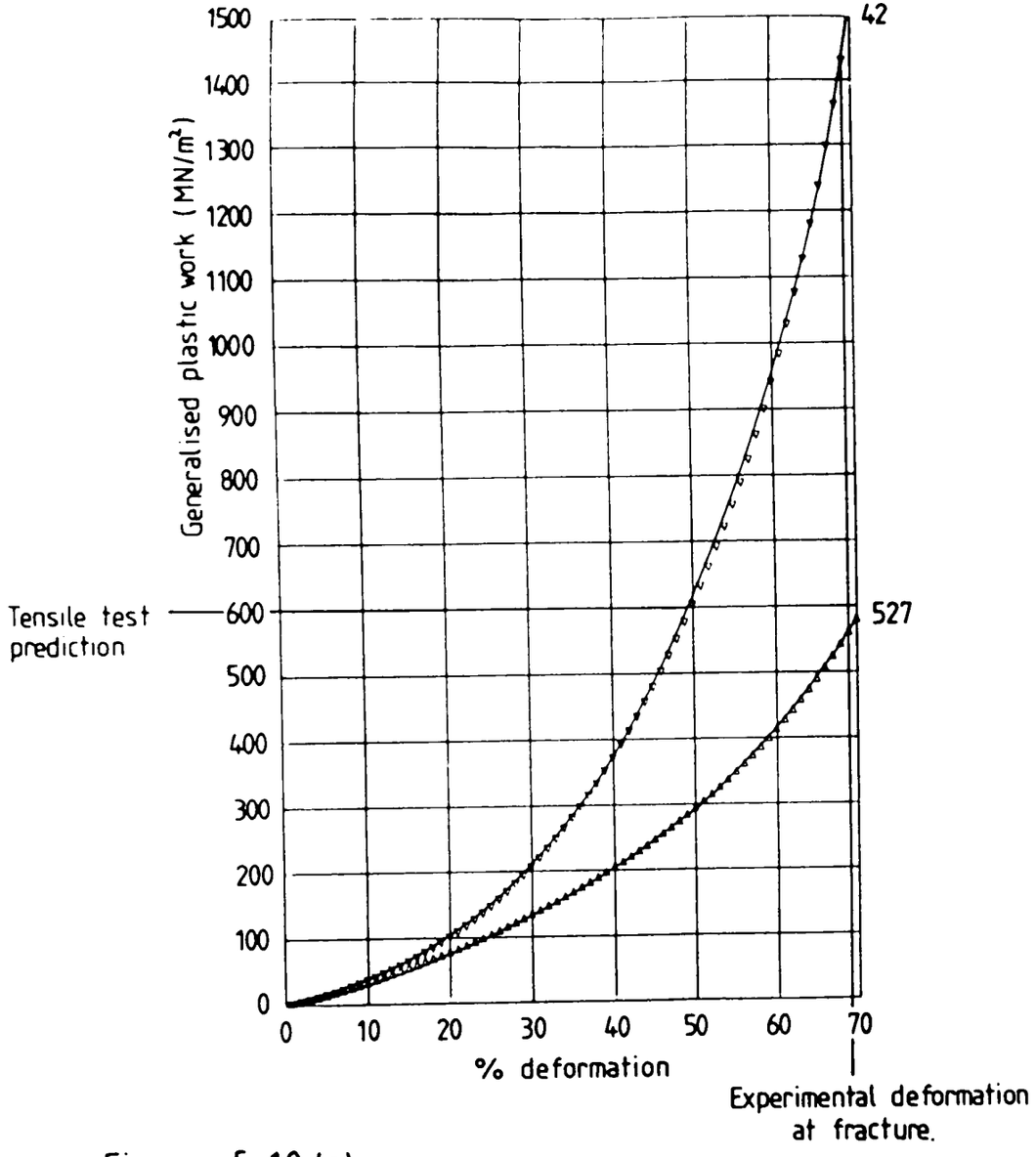

Figure 5.10 (c)

Numerical calculation of the generalised plastic work fracture criterion from FE results for the upsetting of 60-40 brass with an initial height to diameter ratio of 1·5 for nodes 42 and 527.

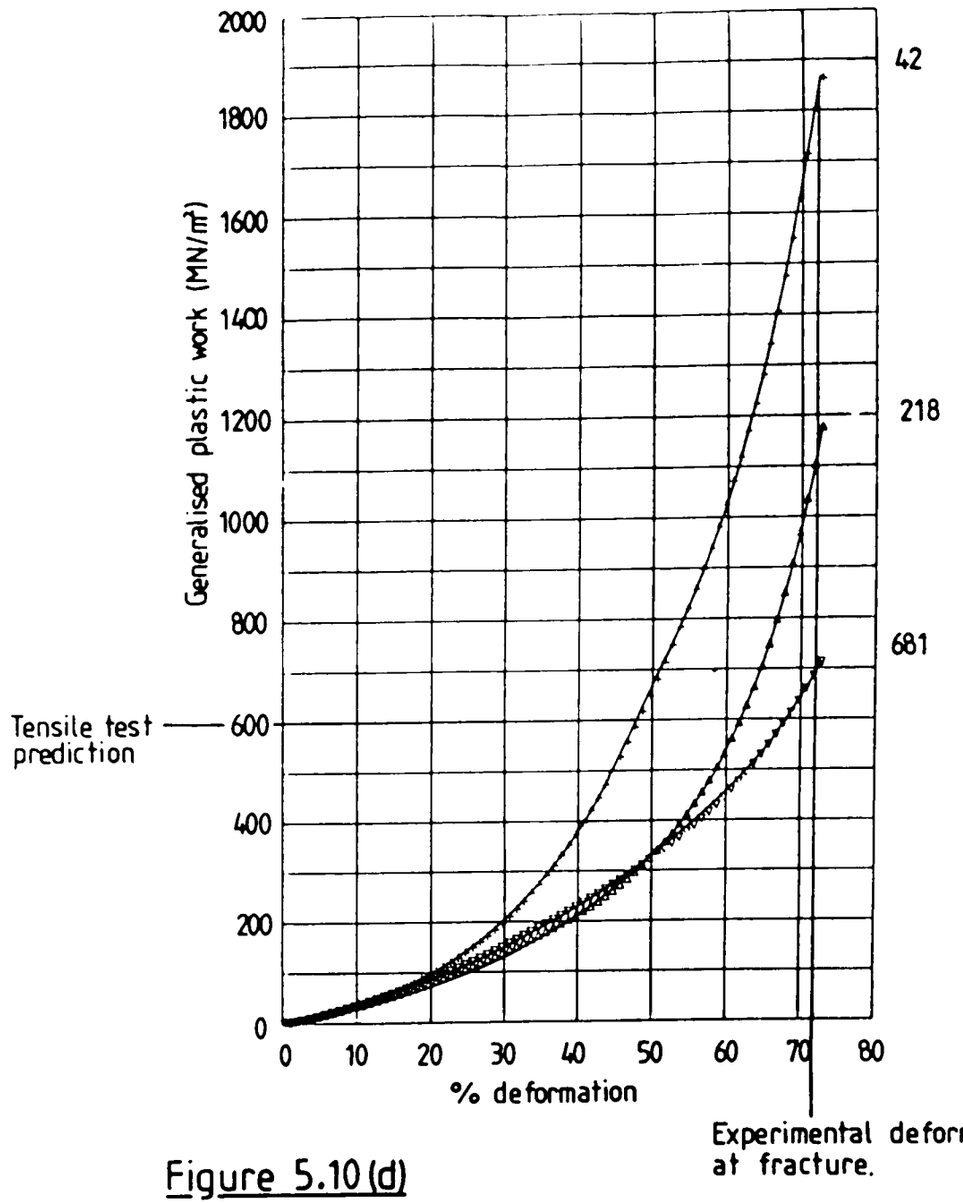

Figure 5.10 (d)

Numerical calculation of the generalised plastic work fracture criterion from FE results for the upsetting of 60-40 brass with an initial height to diameter ratio of 2·0 for nodes 42, 218 and 681.

H/D	Experimental	FE strain	FE work
0·5	70%	58%	58 %
1·0	59%	53 %	53 %
1·5	69%	51%	51%
2·0	72%	48%	48%

Table 5.3

Experimental and FE predicted levels of deformation at fracture for the simple upsetting of 60-40 brass.

on the basis of length on the strain axis.

Satisfactory work and strain predictions for specimens of initial height to diameter ratio of 0.5 and 1.0 have been obtained, but the tensile test predictions give levels of deformation at fracture approximately 20% too low for the taller cylinders. Referring back to Table 5.1, which shows the types of cracks obtained experimentally, it may be seen that these higher aspect-ratio specimens exhibit a mixed-mode type of fracture. Lower aspect-ratio specimens exhibited a Mode I (longitudinal) crack. Experimentally, it is possible that one part of the crack developed well ahead of the remainder but was not identified until the complete crack had been formed. The possible causes of these errors are discussed further in Chapter 8.

The graphs in figure 5.11 show how the numerical values of tensile plastic work vary with the level of deformation of the specimen. From these graphs it may be seen that the tensile test value of tensile plastic work at fracture of 540 MN/m^2 vastly overestimates the level of deformation of the specimen at fracture found experimentally. These results again highlight the failure of the Cockroft and Latham criterion to take into account the contribution to fracture from the work performed due to compressive stress.

Referring back to figure 5.3, which contains the ring test results for 60-40 brass and the finite-element calibration curves, it may be seen that there is a general disagreement between the theoretical form of the finite-element calibration curves and the distribution of experimental points. For the U series of tests, that is those which have been modelled using the finite-element program, an interface shear value, m, of 0.25 has been used. Although this is a reasonable average value over the entire reduction it underestimates the first two experimental points and overestimates the last two. In order to try to provide upper and lower bounds for the effect of this discrepancy on the

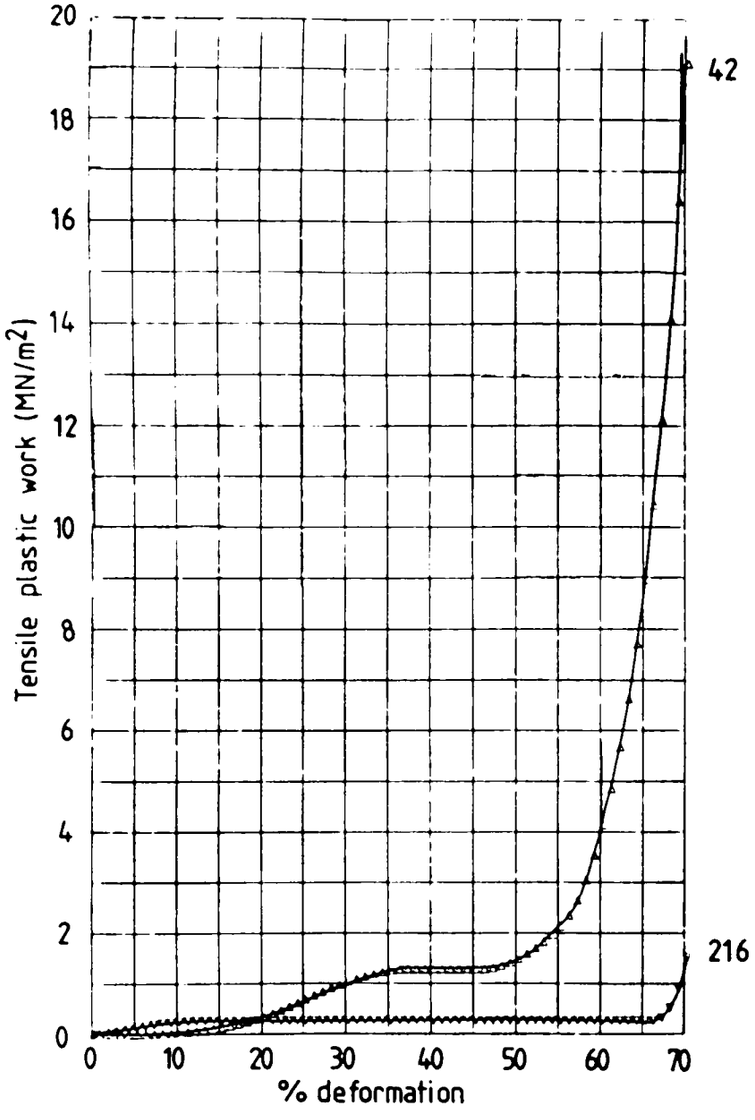

Figure 5.11(a)

Numerical calculation of the Cockroft and Latham fracture criterion from FE results for the upsetting of 60-40 brass with an initial height to diameter ratio of 0·5 for nodes 42 and 216.

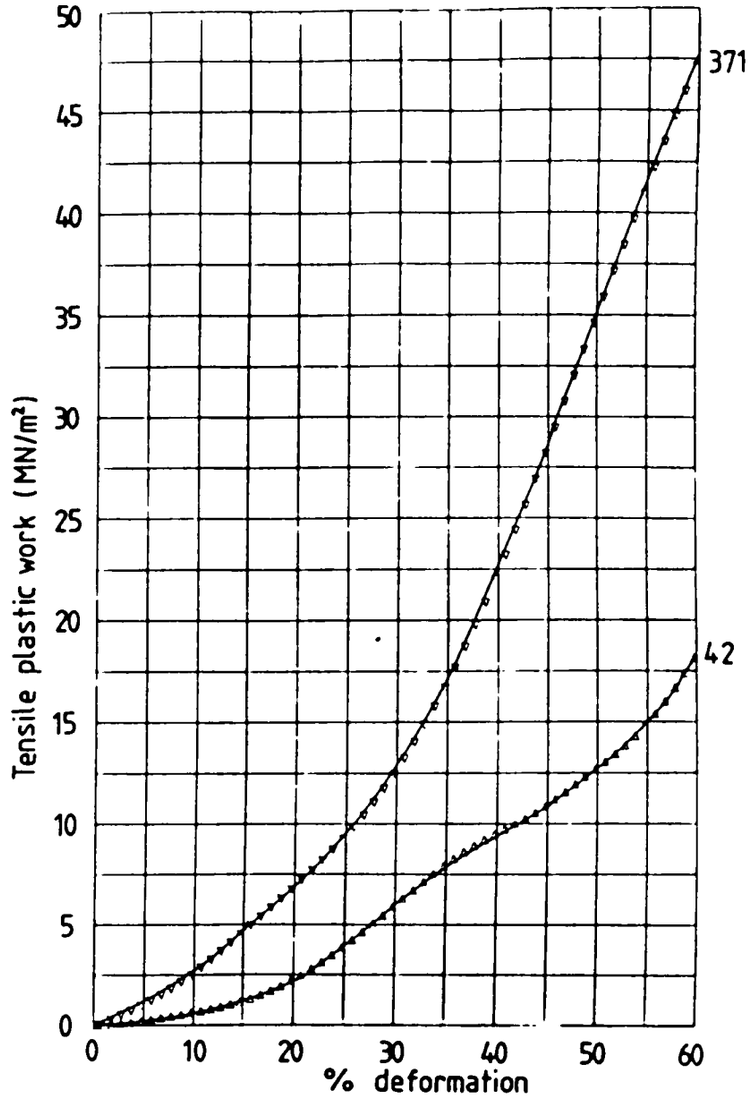

Figure 5.11(b)

Numerical calculation of the Cockroft and Latham fracture criterion from FE results for the upsetting of 60-40 brass with an initial height to diameter ratio of 1·0 for nodes 42 and 371.

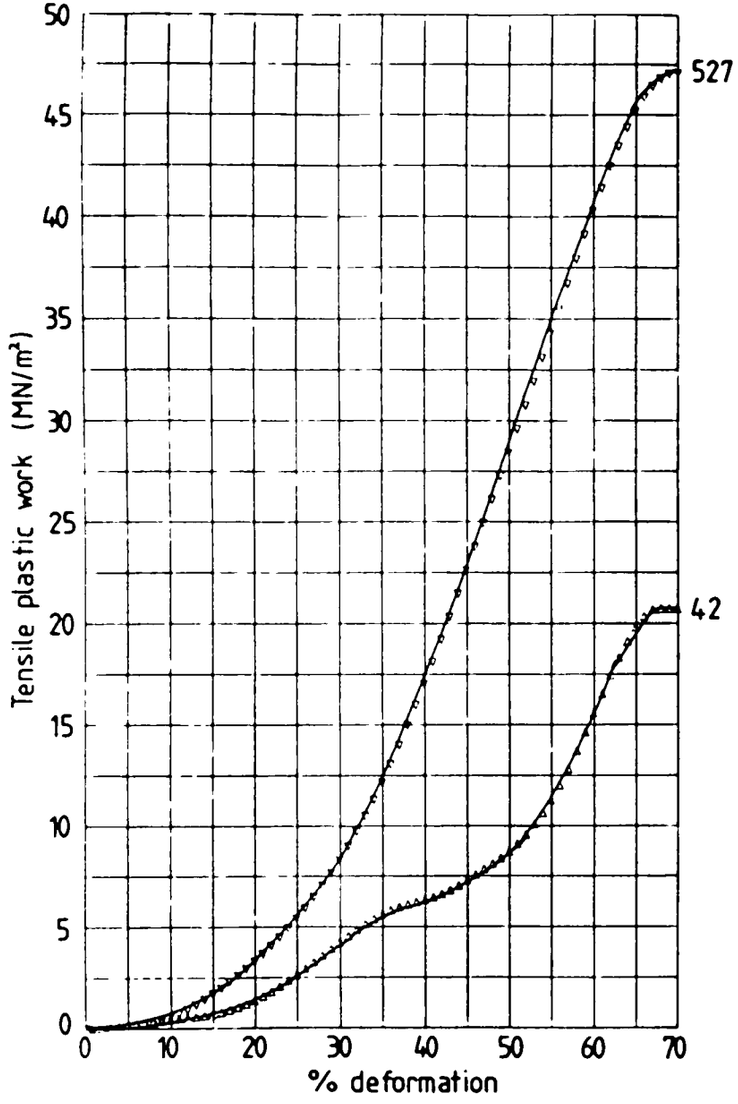

Figure 5.11(c)

Numerical calculation of the Cockroft and Latham fracture criterion from FE results for the upsetting of 60-40 brass with an initial height to diameter ratio of 1·5 for nodes 42 and 527.

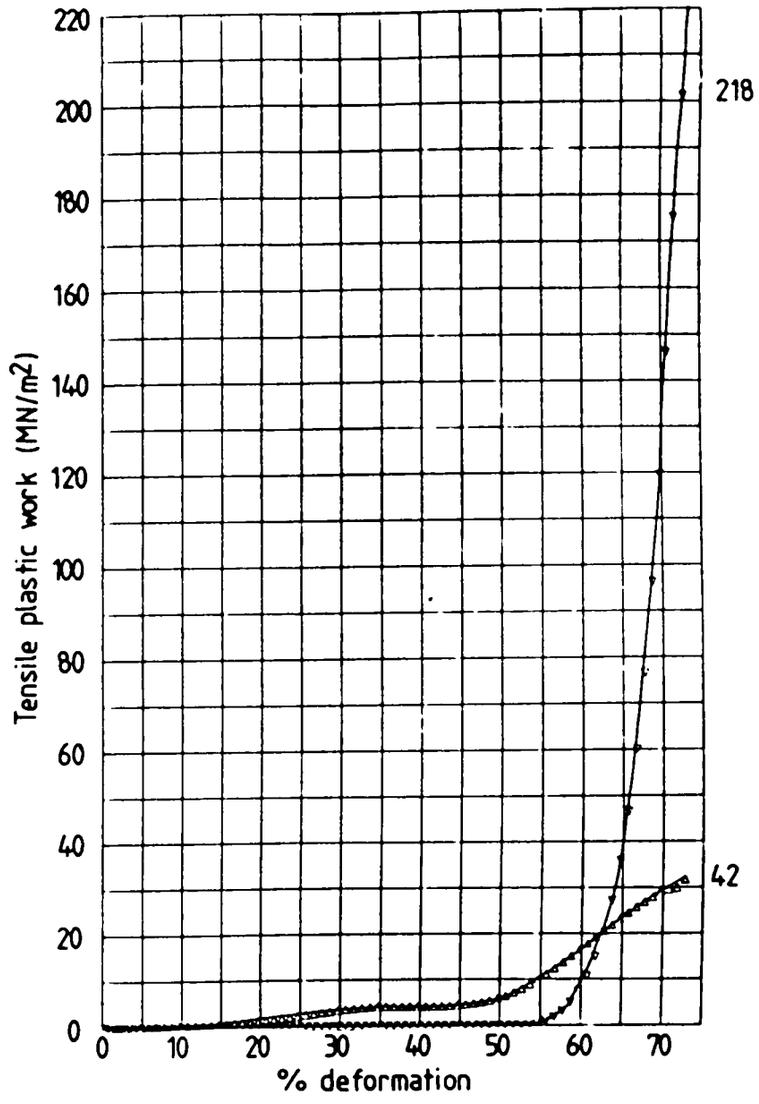

Figure 5.11(d)

Numerical calculation of the Cockroft and Latham fracture criterion from FE results for the upsetting of 60-40 brass with an initial height to diameter ratio of 2·0 for nodes 42 and 218.

prediction of the fracture initiation site and the level of deformation at fracture in the three criteria two more finite-element analyses were performed. The finite-element analysis for the model of the specimen with an initial height diameter ratio of 1.0 was repeated for the two additional interface shear values of 0.15 and 0.35. The comparison of these additional finite-element predictions of fracture initiation site and the experimental results are presented in Table 5.4 together with the results previously obtained for m = 0.25. From this table it may be seen that the fracture site predictions are unaltered for the following criteria:

1. McClintock (1968);
2. Brozzo et al (1972);
3. Norris et al (1978);
4. Oyane et al (1980);
5. Generalised plastic strain;
6. Generalised plastic work.

For those criteria with altered predictions of fracture site:

1. McClintock et al (1966).

This fracture initiation site prediction has changed from node 114 (see figure 5.8(b)) to node 93 for m = 0.15. This is one nodal spacing nearer the die, on the free surface of the specimen and therefore still corresponds to a correct surface crack prediction. For m = 0.35, node 96 is now predicted as the fracture initiation site. This node is near the central axis of the specimen and the fracture site prediction is therefore wrong. For both additional modelling levels of interface friction the zr plane is predicted, rather than the correct theta-r plane as for m = 0.25.

2. Cockroft and Latham (1968).

For this criterion all three predictions lie on the mid-height layer of nodes. For m = 0.15 the free surface node 372 has been

criterion / specimen	McClintock (1968)	McClintock et al (1966) (shear)	Ghosh	Oyane	Cockroft and Latham	Brozzo	Gen plastic strain	Gen plastic work	Norris	Atkins
m = 0·15	rθ √ 42	zr √ 93	× 165	√ 42	√ 372	√ 42	√ 42	√ 42	× 370	θz × 101
m = 0·25	rθ √ 42	θz √ 114	√ 176	√ 42	× 371	√ 42	√ 42	√ 42	× 370	θz × 243
m = 0·35	rθ √ 42	zr × 96	× 358	√ 42	× 371	√ 42	√ 42	√ 42	× 370	θz × 307

Table 5.4

Comparison of FE predictions of fracture initiation site and experimental results for the simple upsetting of 60-40 brass of initial H/D = 1·0 with three different modelling values of interface friction.

predicted. This, therefore, corresponds to a correct prediction. For the two higher levels of interface friction the predicted fracture initiation site moves one node towards the axis which is incorrect.

3. Ghosh (1976).

For m = 0.25 fracture is predicted to occur at node 176, on the free surface of the specimen. For m = 0.15 the predicted site is moved by one node into the body of the specimen. For m = 0.35 node 358 has been predicted. This is located on the mid-height layer of nodes, well into the body of the specimen.

4. Atkins (1981).

Here, all three fracture sites predictions are incorrect. However, the location of the predicted site is different for the three modelling levels of interface friction. For m = 0.15 node 101 has been predicted. This lies two nodes down in the material below the die, four nodes in from the free surface. For m = 0.25 node 243 has been predicted, this lies further down the model towards the mid-height layer of nodes, approximately half way between the axis and the free surface. For m = 0.35 fracture is predicted to start at node 307 which is located in the body of the specimen towards the mid-height plane of nodes. No changes in the predicted plane of fracture initiation have been found for these three modelling levels of interface friction.

Comparisons of the predicted and experimental levels of deformation at fracture for the tensile plastic work criterion are presented in figure 5.12 for the two additional modelling levels of interface friction. As previously found for all the specimen aspect ratios considered (see figure 5.11) the tensile test predicted a value of tensile plastic work of 540 MN/m^2 that vastly overestimates the level of deformation at fracture found experimentally.

Similarly obtained comparisons of the predicted and experimental levels of deformation at fracture for the generalised plastic strain and

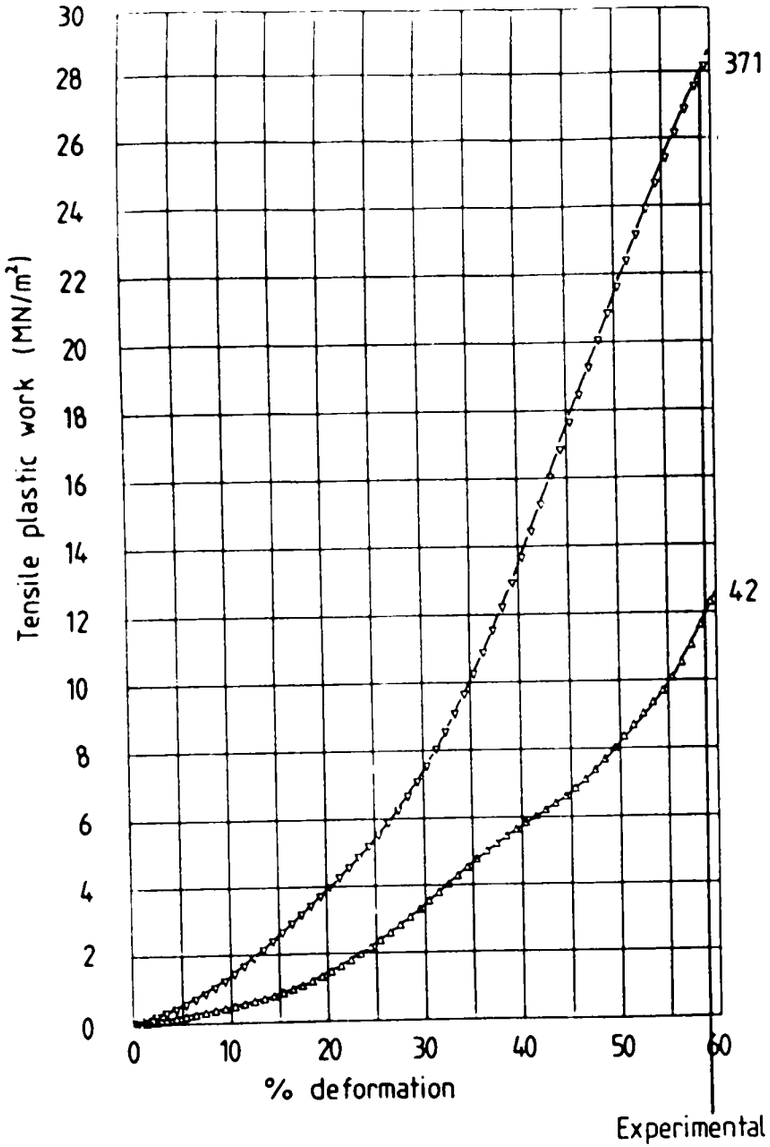

Figure 5.12(a)

Numerical calculation of the Cockroft and Latham fracture criterion from FE results for H/D = 1·0 with m = 0·15 for nodes 371 and 42.

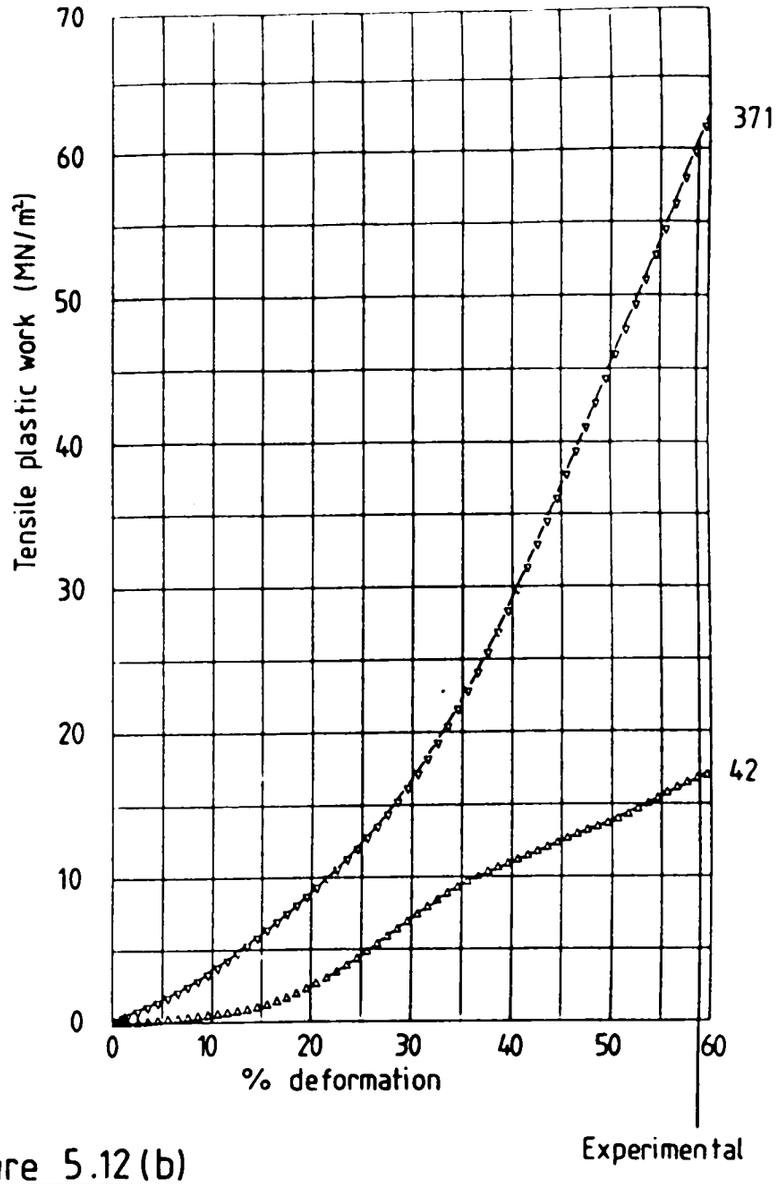

Figure 5.12(b)

Numerical calculation of the Cockroft and Latham fracture criterion from FE results for H/D = 1·0 with m = 0·35 for nodes 42 and 371.

generalised plastic work criteria are given in figures 5.13 and 5.14 respectively. Again, as expected, both these criteria give the same predictions and, together with the predictions previously obtained for the model using m = 0.25, are summarised in Table 5.5. From this table it may be seen that, in this case, there is a linear relationship between the interface shear factor, m, and the strain/work predictions. For m = 0.25 a level of deformation at fracture of 53% has been predicted, for m = 0.15 a level of 3% above this has been predicted, and for m = 0.35 a value 3% below this. Although work could be done to improve the agreement in general form between the finite-element calibration curves and experimental ring test results the system does not appear to be ill-conditioned and m = 0.25 provides a satisfactory average result.

From the results presented in this section it appears that the fracture criterion using a critical value of generalised plastic strain or work is not only capable of predicting that a surface fracture occurs in the upsetting of the brass specimens considered here, but also, when compared with the value of generalised plastic work at fracture calculated using a simple tensile test, provides a reasonable prediction of the level of deformation at fracture.

5.5 Conclusions.

Four criteria have been found to predict successfully the fracture sites found experimentally for all four aspect-ratio specimens considered. These are the generalised plastic strain and generalised plastic work criteria, and those due to McClintock, Kaplan and Berg (1966) and Brozzo, DeLuca and Rendina (1972).

For the generalised plastic work and strain criteria good agreement with the experimental level of deformation at fracture has been found for

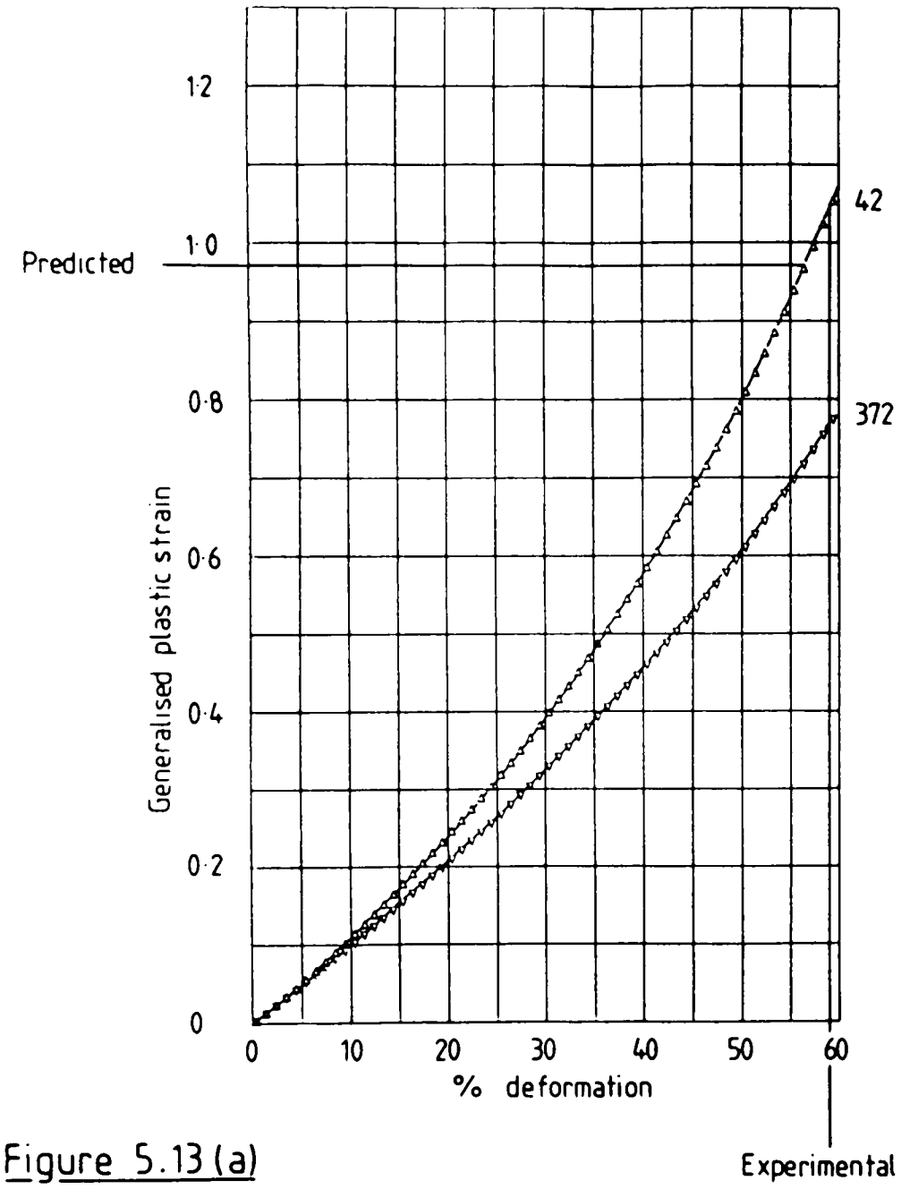

Figure 5.13(a)

Variation of FE generalised plastic strain for H/D = 1·0 with m = 0·15 for nodes 42 and 372.

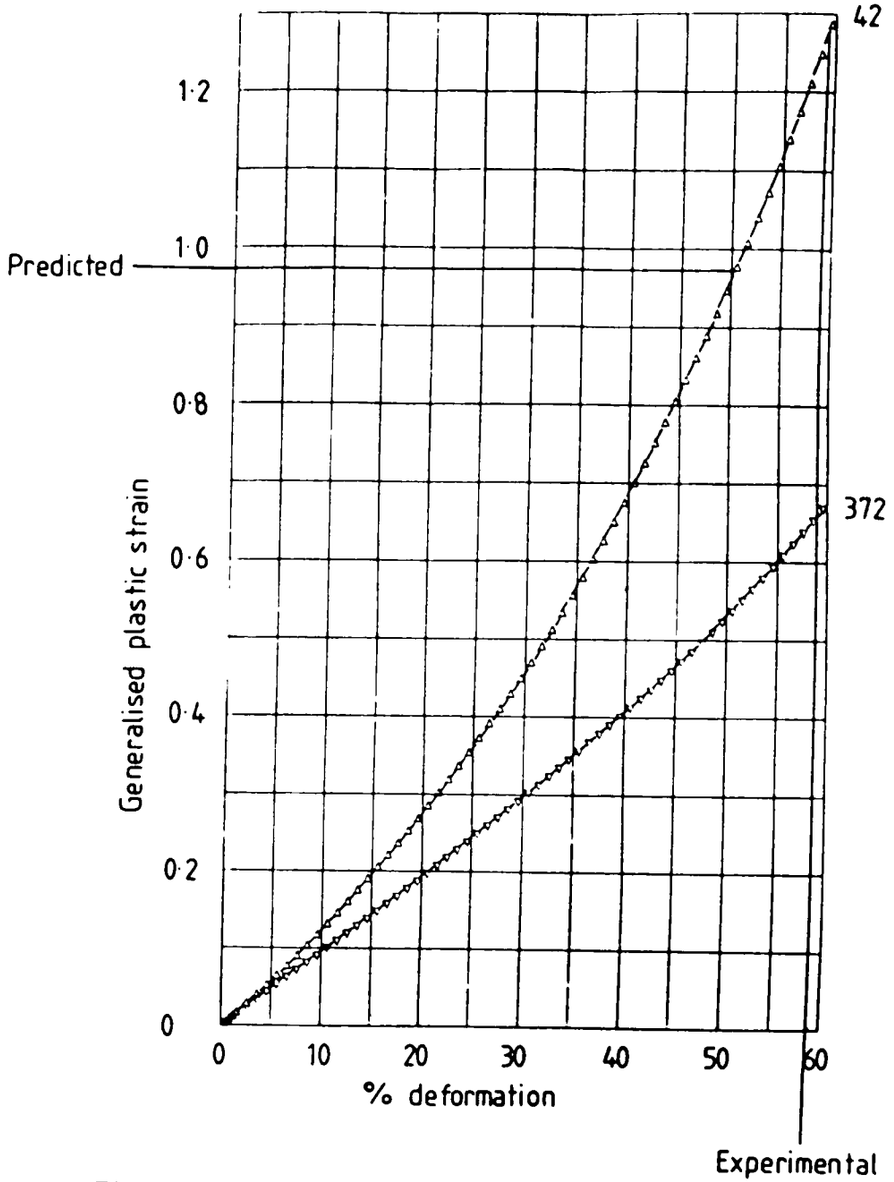

Figure 5.13(b)

Variation of FE generalised plastic strain for H/D = 1·0 with m = 0·35 for nodes 42 and 372

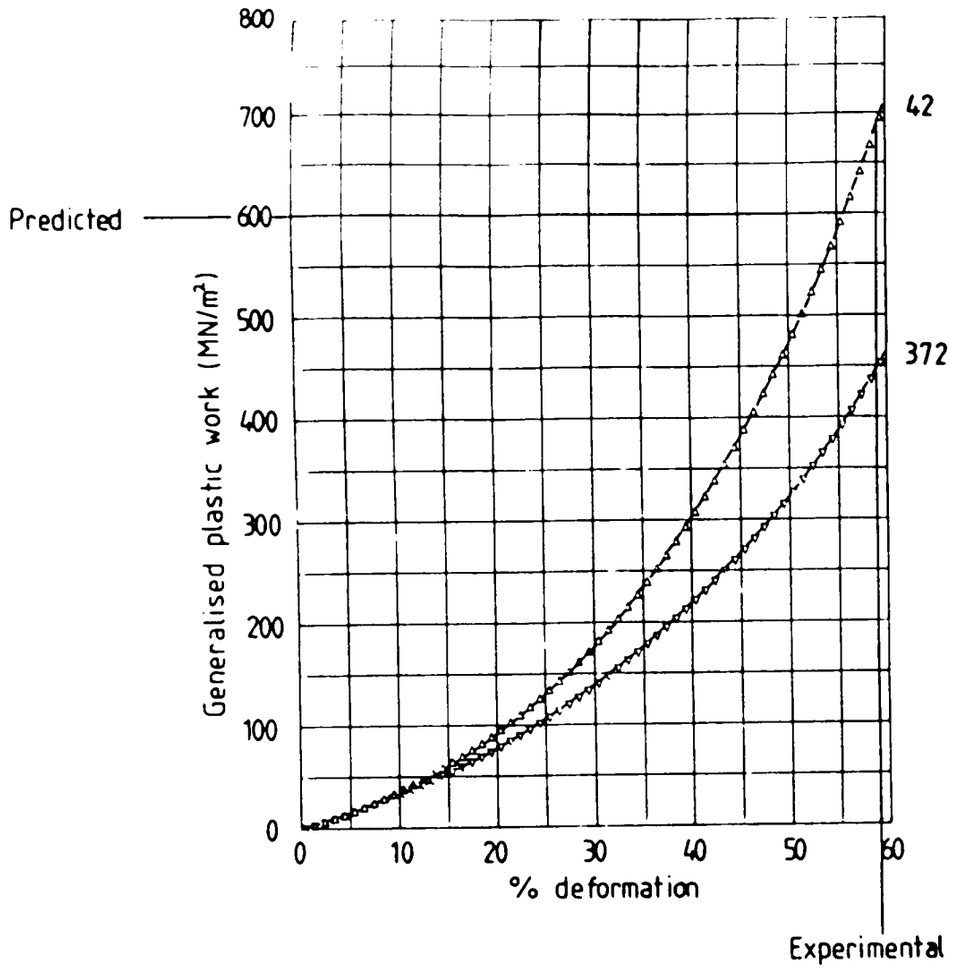

Figure 5.14(a)

Numerical calculation of the generalised plastic work fracture criterion from FE results for H/D = 1·0 with m = 0·15 for nodes 42 and 372

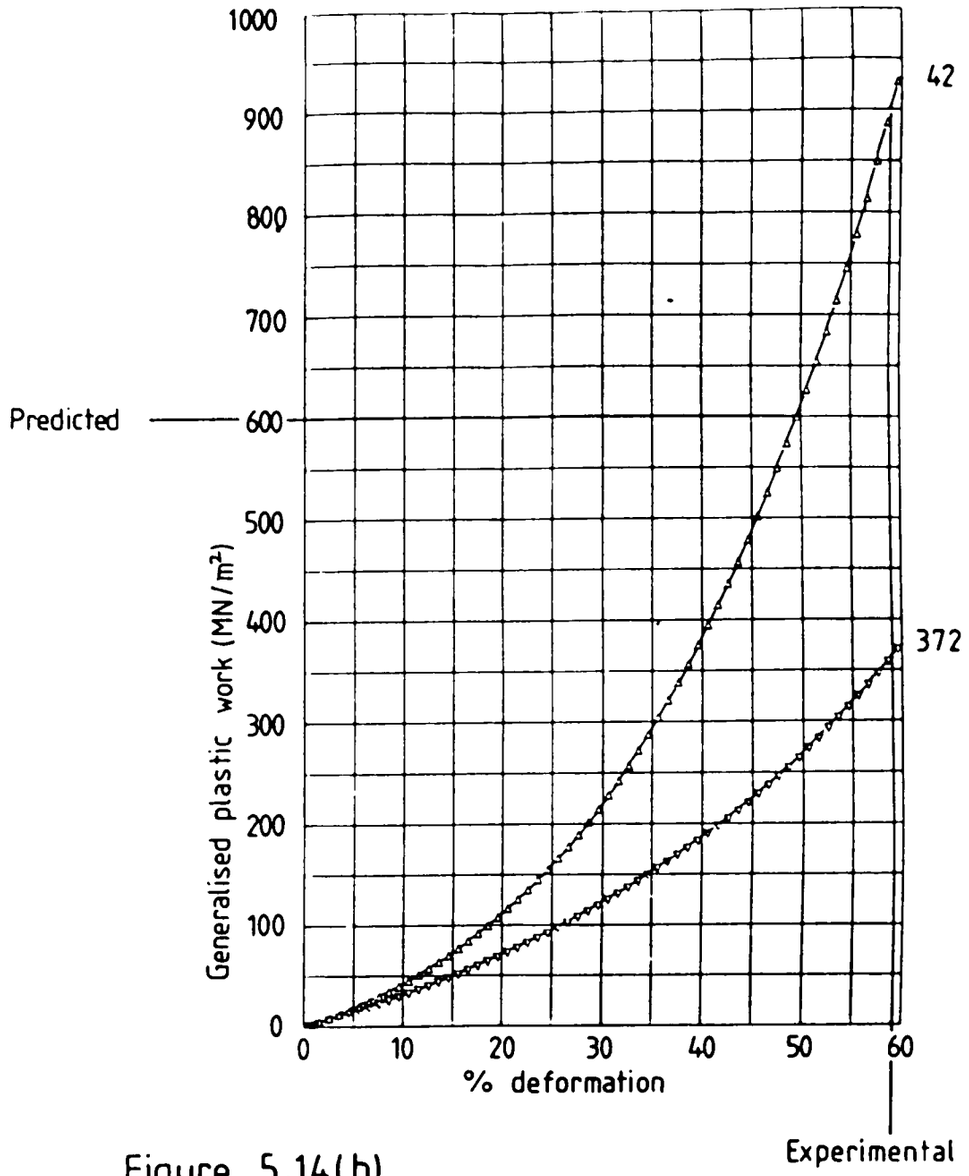

Figure 5.14(b)

Numerical calculation of the generalised plastic work fracture criterion from FE results for H/D = 1·0 with m = 0·35 for nodes 42 and 372.

H/D = 1·0

Experimental deformation at fracture = 59%

m	FE strain	FE work
0·15	56%	56%
0·25	53%	53%
0·35	50%	50%

Table 5.5

FE predicted levels of deformation at fracture for three modelling levels of interface shear factor, m.

specimens of initial aspect ratio 0.5 and 1.0, but predictions give levels of deformation at fracture approximately 20% too low for the taller cylinders. It is suggested that this may be due, in part, to experimental difficulties associated with measurement of the level of deformation at fracture initiation. Other possible causes are discussed in Chapter 8.

Chapter 6.

Strip Compression and Tension.

6.1 Introduction.

This chapter describes the experimental results and finite-element predictions obtained from three simple metalforming operations on 60-40 brass strip.

In the first of these operations, the strip specimen was subjected to a full width indentation until fracture occurred. In the second, a full width partial thickness indentation was produced and then the loading geometry was changed, the specimen being subjected to a tensile load, perpendicular to the indentation, transmitted through grippers on its ends, until fracture occurred.

In the third type of experiment an impression of the same position and dimensions as that produced by the second forging operation was milled in the specimen and then it was also pulled to fracture under tensile loading.

The dimensions of all these specimens and the experimental procedure are described in section 6.2. Section 6.3 presents details of the finite-element meshes used in the analysis of these problems and section 6.4 compares experimental and finite-element results. Finally, section 6.5 presents the conclusions of this chapter.

6.2 Specimen preparation and experimental procedure.

The 60-40 brass strip was supplied in three-metre lengths of 2.5cm wide and 0.32cm thick. It was used in the 'as received' condition after being cut into approximately 15 cm lengths.

In the first series of tests, strip specimens were compressed with two semi-cylindrical indentors until fracture occurred. This operation was performed on an Avery 600kN press using the sub-press shown in schematic

form in figure 6.1. Figure 6.1(a) shows the front view of the sub-press, and figure 6.1(b) a vertical section through AA. The dashed lines show the location of the strip specimen. Measurements of the level of deformation and corresponding load were recorded.

In the second series of tests the indentation operation was stopped after the load had reached 650 kN, that is after approximately 20% reduction of the original specimen thickness, and the specimen was prepared for the tensile loading stage. Markers were scribed, as shown in figure 6.2, using a tungsten carbide 'pencil', and their positions were measured using a Zeiss MP30 measuring projector ('Shadowgraph'). Each specimen was then gripped in the jaws of an Instron testing machine and pulled perpendicular to the axis of the initial groove, until fracture occurred. The positions of the markers were again measured and the lateral (surface) strain in the specimen calculated. Measurement of the minimum thickness of the specimen across the indentation before and after deformation enabled the thickness strain to be calculated. A series of indented specimens was pulled to various levels of tensile strain to give the deformation history.

In the third test, milled grooves of the same position and dimensions as the forged groove in the previous test were produced, and the same tensile testing procedure was followed.

6.3 Finite-element model.

The finite-element mesh of the undeformed strip specimen is presented in figure 6.3(a). It is only one element thick as all the deformation has been modelled as plane-strain.

One quarter of the specimen cross section has been modelled, deformation in the other quadrants follows from arguments of symmetry.

The strip compression operation was modelled using a moving cylindrical

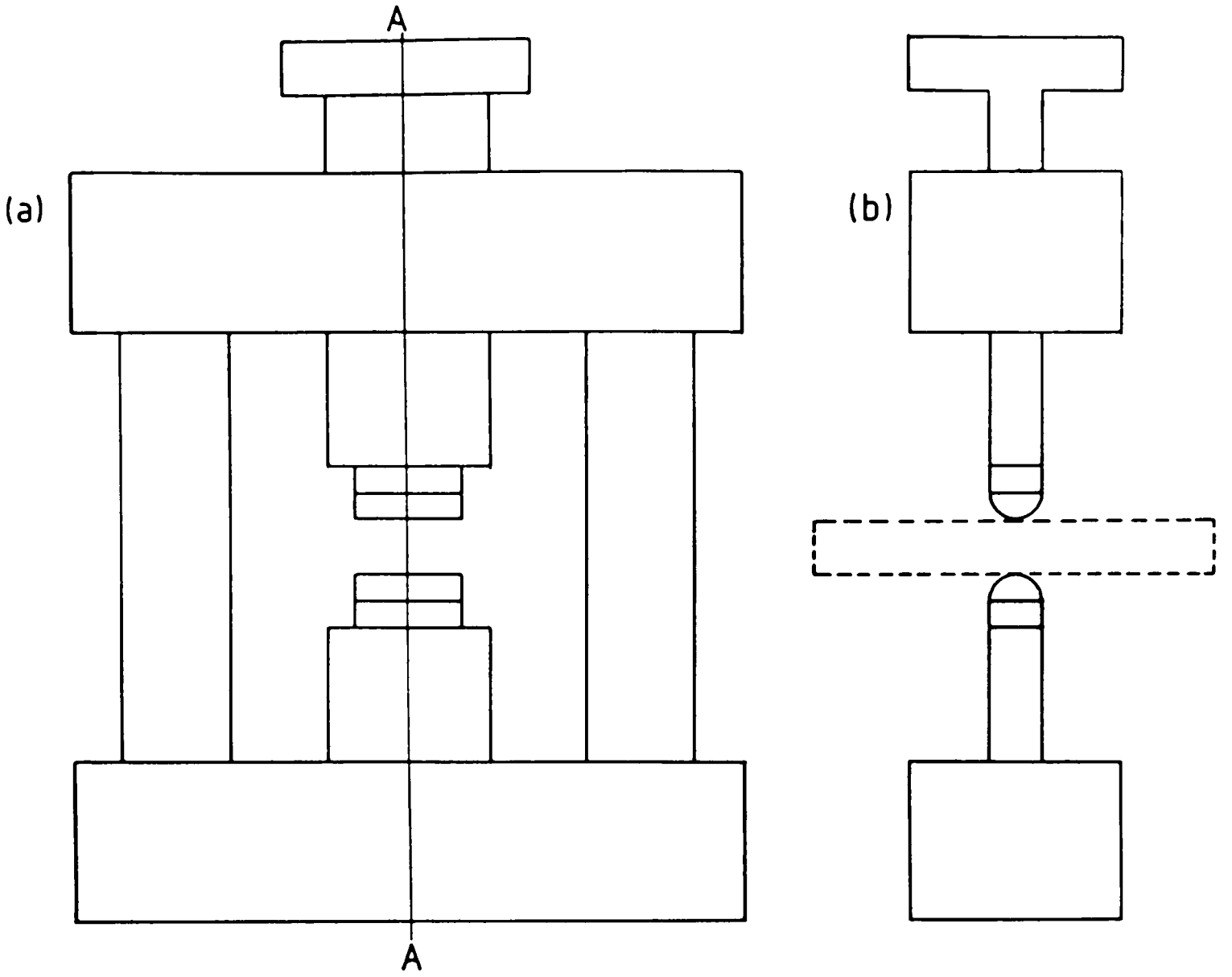

Figure 6.1 Die-set used for strip compression.

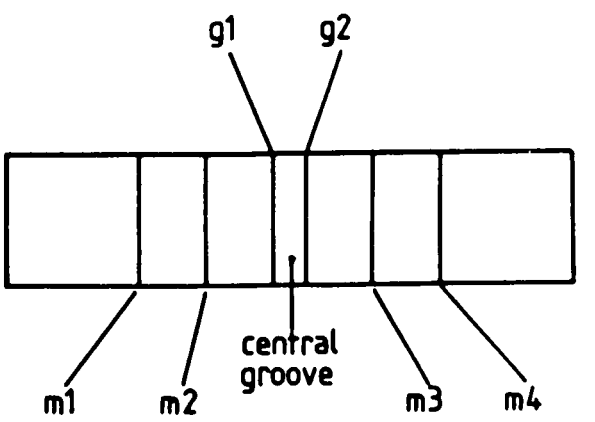

Figure 6.2

Position of strain measurement markers

(a) Undeformed

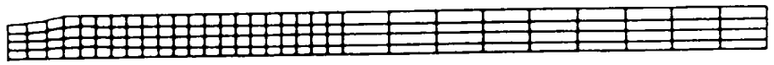

(b) After 20% compression

Figure 6.3

Finite-element meshes.

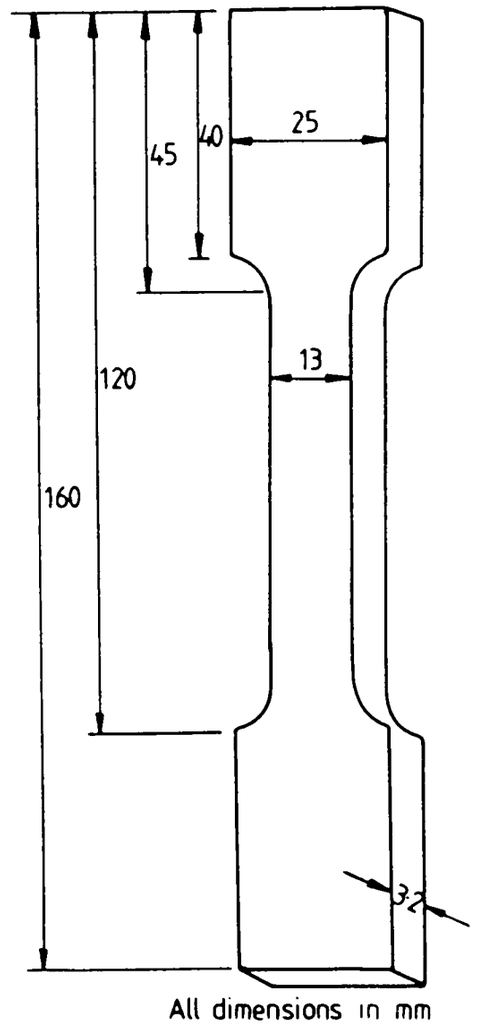

Figure 6.4(a)

Strip tension test specimen

boundary surface as the indentor. All the finite-element analyses were continued at least until the level of deformation at fracture found experimentally.

The nodal coordinates for the milled and forged strip analyses were taken from the results of the strip compression analysis after 20% deformation. This mesh is shown in figure 6.3(b). For the forged strip, the distribution of generalised plastic strain obtained from the end of the indentation simulation was also transferred to the new data file describing the state of the model at the start of the tensile testing stage.

The interface friction condition used in the indentation analysis was as previously found in section 4.3.2 of chapter 4, that is m = 0.25.

The constitutive relationship required for the modelling was determined using a standard strip tension test. The shape and dimensions of the specimens are shown in figure 6.4. The tests were carried out under uniaxial tension on a 100kN Instron testing machine at a cross head speed of 2 mm per minute. The extension of a 25mm gauge length was determined by an Instron extensometer driving the chart recorder. The stress and strain values were calculated from the load-extension data, and are shown in figure 6.4(b).

6.4.1 Experimental results.

This section contains the experimental results relating to the strip forming operations. Both deformation and fracture results are presented. The purpose of these experiments was to produce fracture sites and level of deformation at fracture data to be compared with the finite-element predictions (Section 6.4.3.).

Figure 6.5 shows the relationship between load and reduction for the strip indentation operation. No plastic deformation occurs at loads less

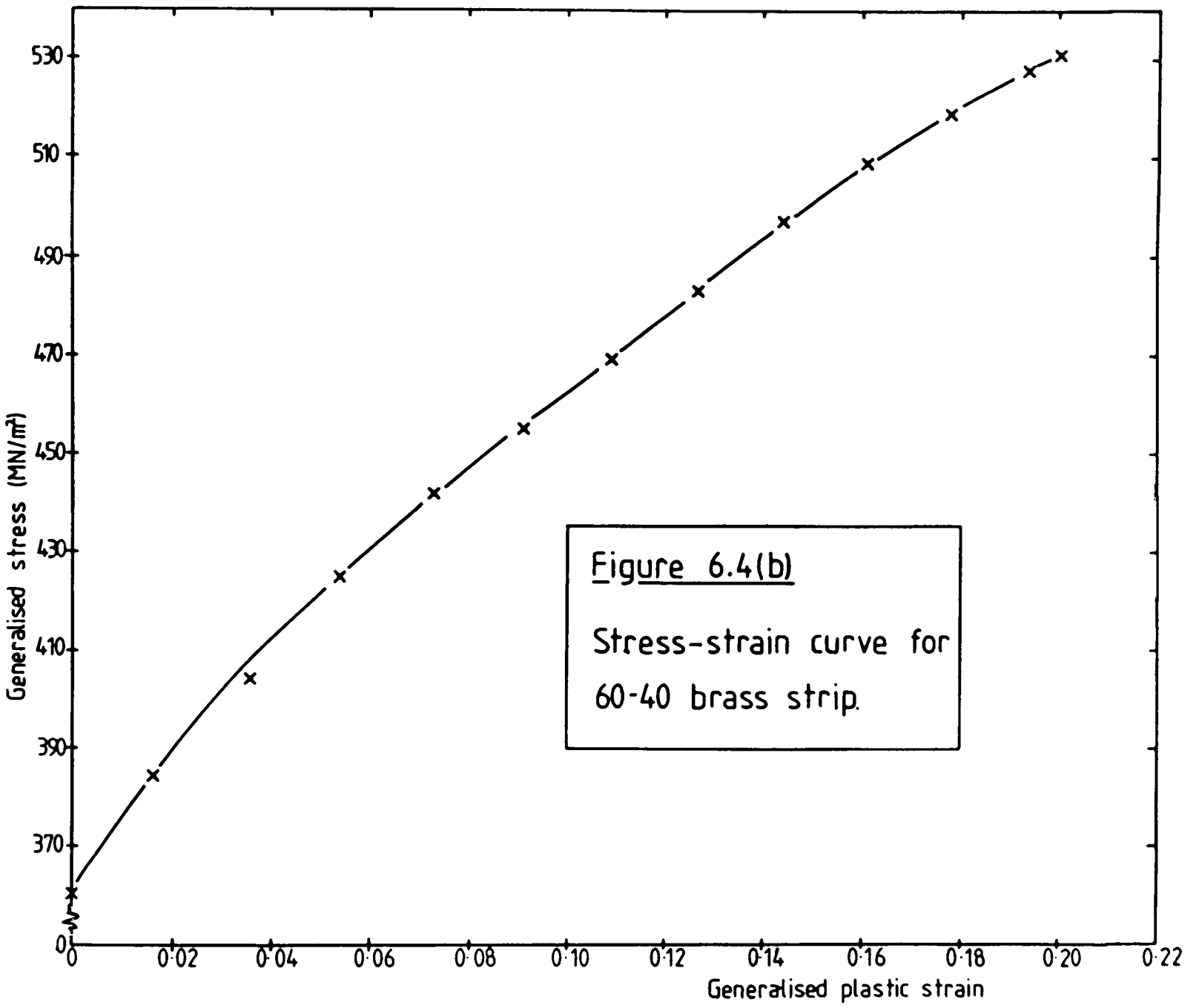

Figure 6.4(b)

Stress-strain curve for 60-40 brass strip.

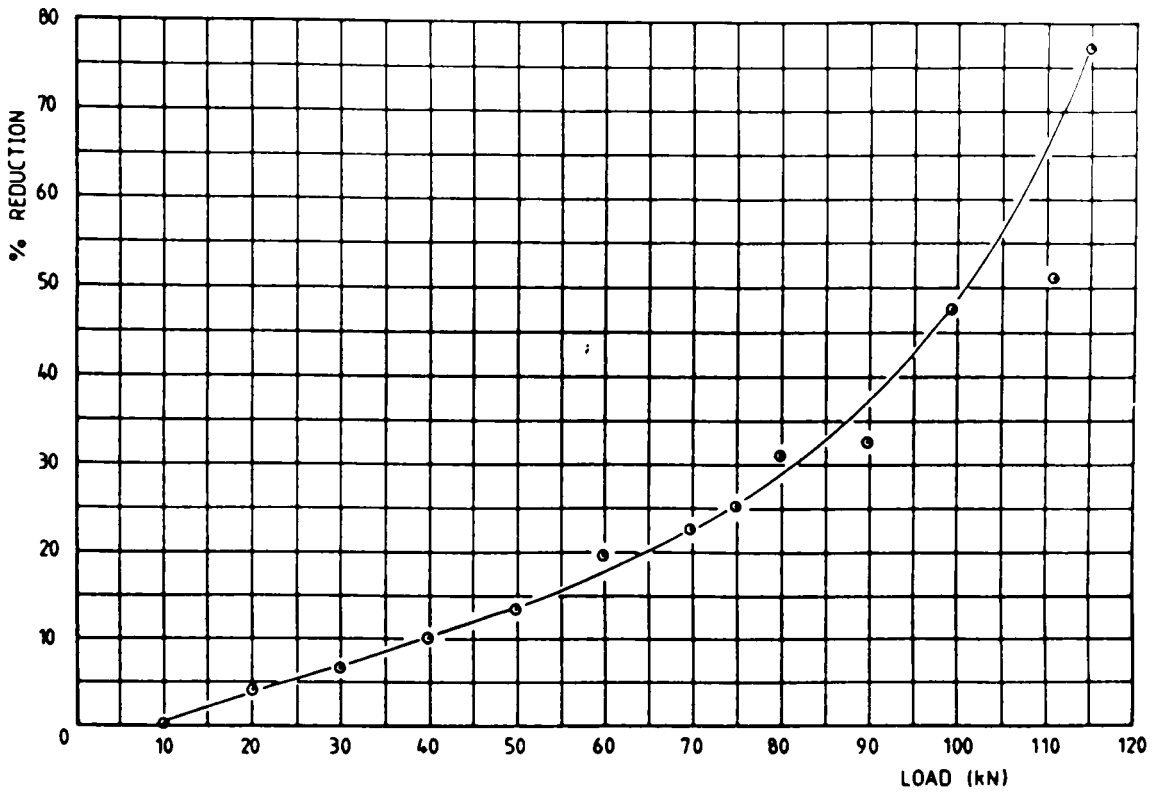

Figure 6.5

Relationship between load and percentage reduction in minimum thickness for the indentation of 60-40 brass strip.

than 10kN. There appears to be an approximately linear relationship between load and reduction up to about 55kN. After this a given load increment produces a correspondingly larger change in reduction. Fracture occurs across the minimum section of the neck at 77% reduction at a load of 115kN.

Figure 6.6 shows the surface strain distributions developed under tensile loading in the fractured milled and forged strip specimens. These strains were measured from the displacement of the scribed lines. Higher strains have been developed in the initially forged specimen than that with a milled groove. However, for the milled strip the deformation is more highly localised to the central groove than for the forged strip specimens. In both cases strain has been developed in the regions surrounding the centre groove. This is higher for the forged than the milled specimens as is also the strain gradient along the marked length of the specimen.

Figure 6.7 shows the experimental thickness strains across the minimum section of the indentation for the tensile deformation of the milled and forged strip specimens. On both graphs, the points plotted with circles around them indicate values for fractured specimens.

Reduction in the strip thickness for the milled specimens (Figure 6.7(a)) starts at a lower load than for the forged specimens. This is because the stress in the neck region has to reach a higher level in the forged specimen for plastic flow to occur, due to prior work hardening developed during the strip indentation operation. For both types of specimen the loads do not significantly increase once plastic flow in the neck region has begun. The thickness strains developed during the tensile test in the forged strip specimens at fracture were less than those developed in the milled strip specimens. The strip thickness at fracture of the minimum cross section used in the comparison with finite-element results is the average of the fractured specimens. For

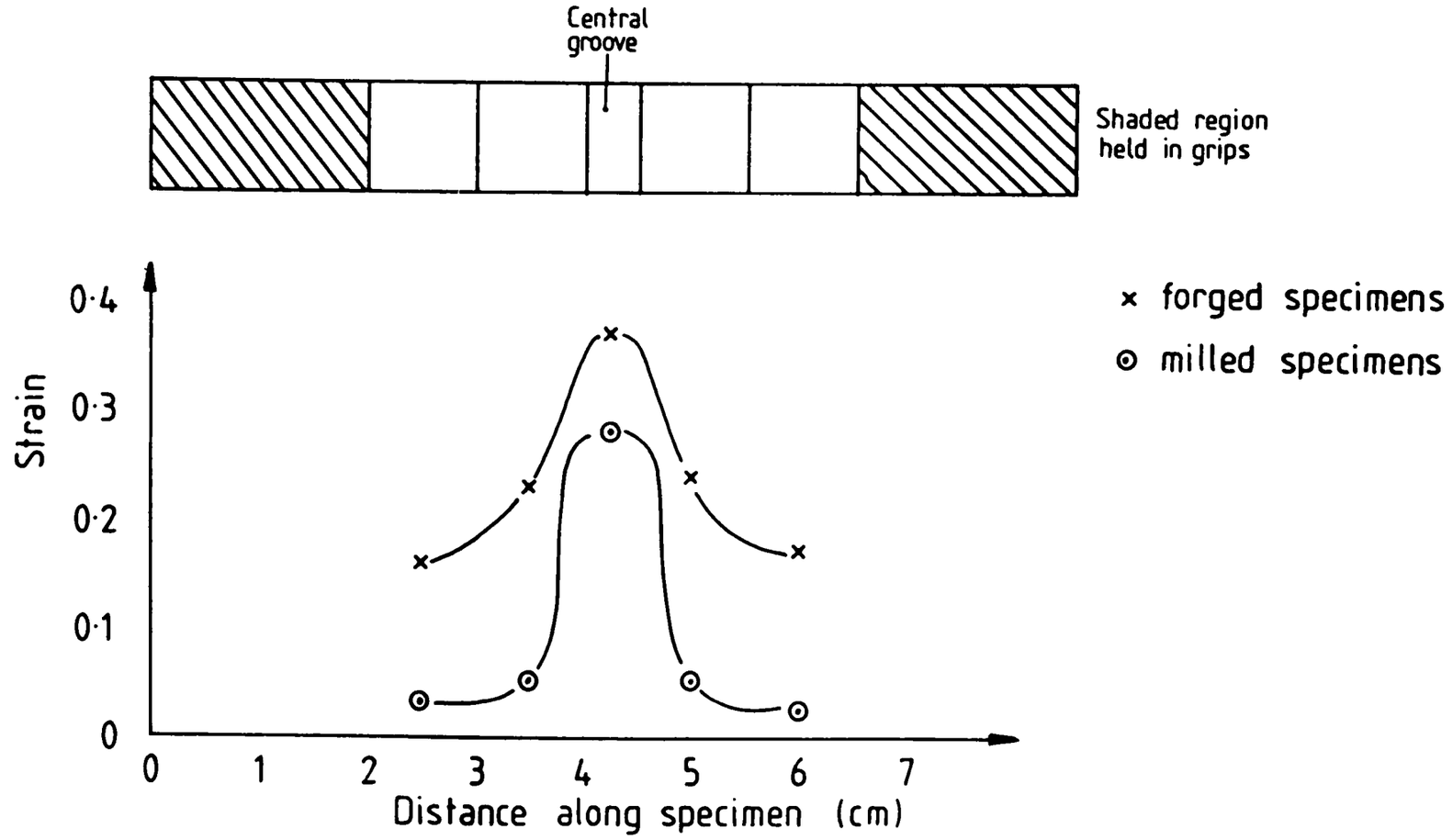

Figure 6.6.

Surface strain distribution in fractured strip specimens

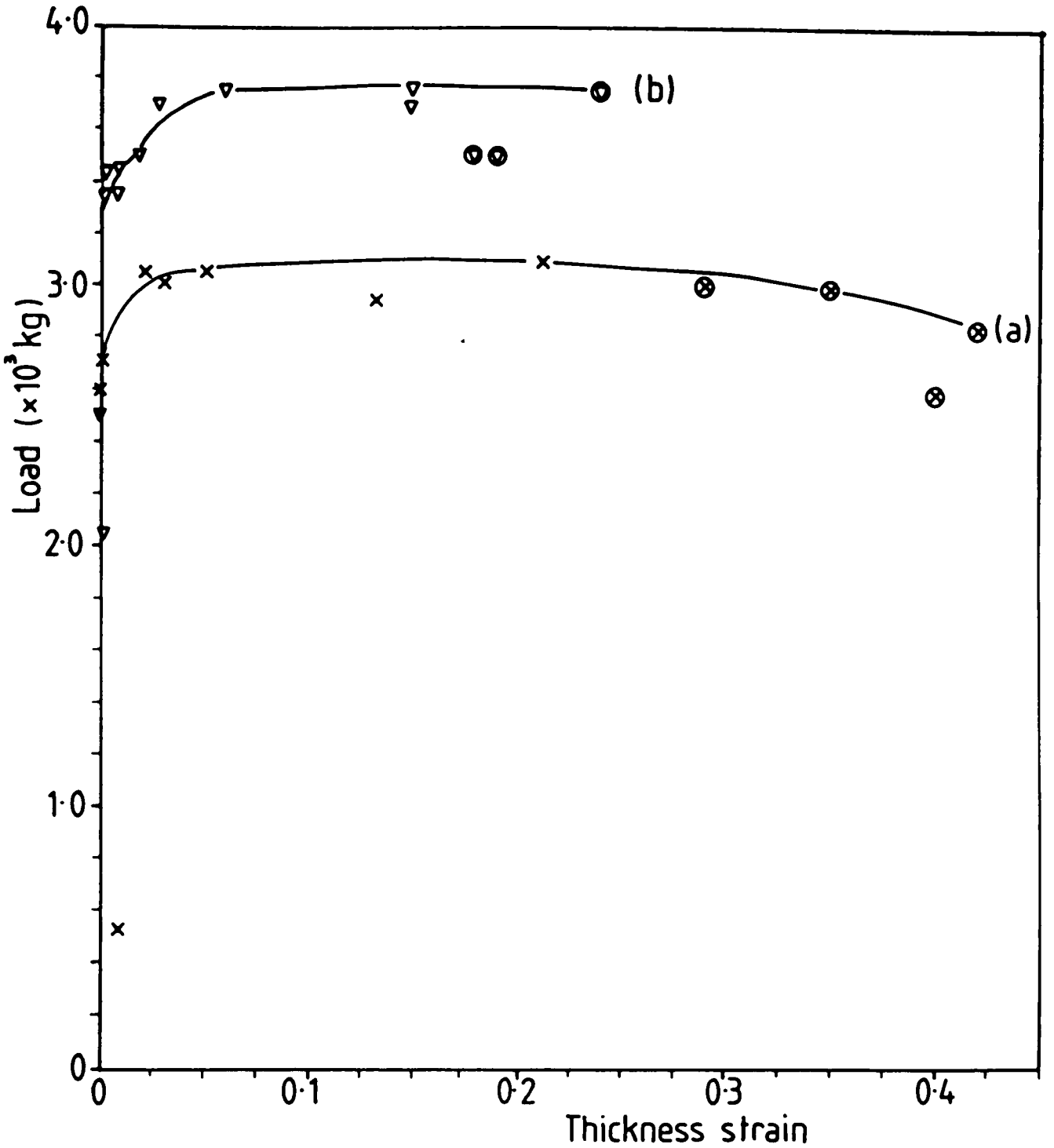

Figure 6.7

Experimental thickness strains for strip tension: minimum neck section. (a) milled (b) forged

the milled strip this is 1.26mm and the forged strip 2.08mm.

Figure 6.8 contains group photographs of the milled and forged groove specimens at three levels of deformation, and, for the final specimen in each group, fracture.

Scanning electron microscope (SEM) photographs of normal views of the fracture surfaces of the milled and forged specimens are presented in figure 6.9. These are fairly typical ductile fracture surfaces.

For one of the forged specimens it was possible to identify surface cracks before gross fracture occurred. An SEM photograph of three of the initiated cracks is shown in figure 6.10. These main cracks are perpendicular to the loading direction, although the separation of some of the material parallel to the loading direction may be observed. For the fractures in the other specimen types the fracture initiation site was not observed before gross separation of the two surfaces occurred.

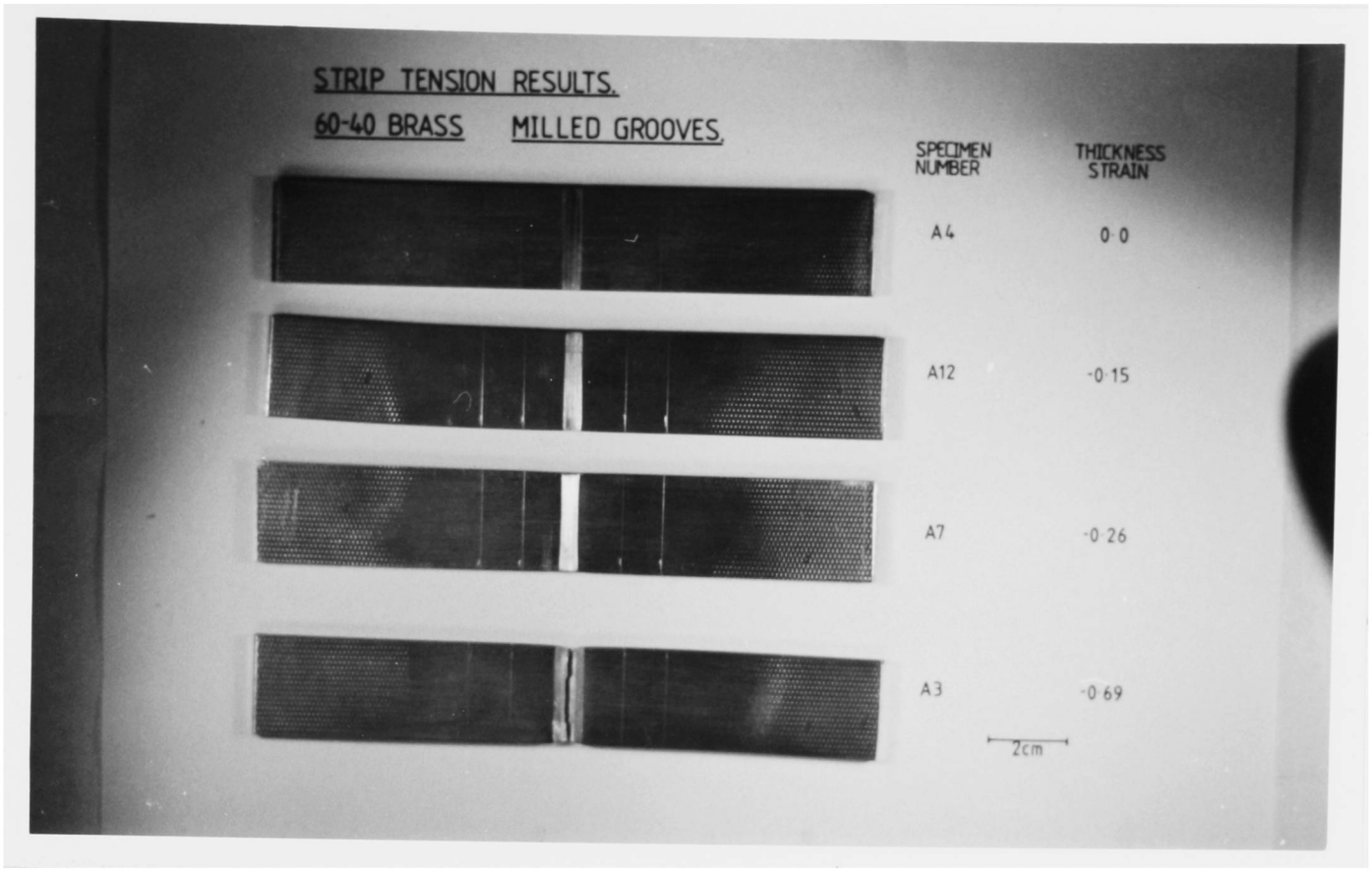

Figure 6.8(a)

Milled strip specimens.

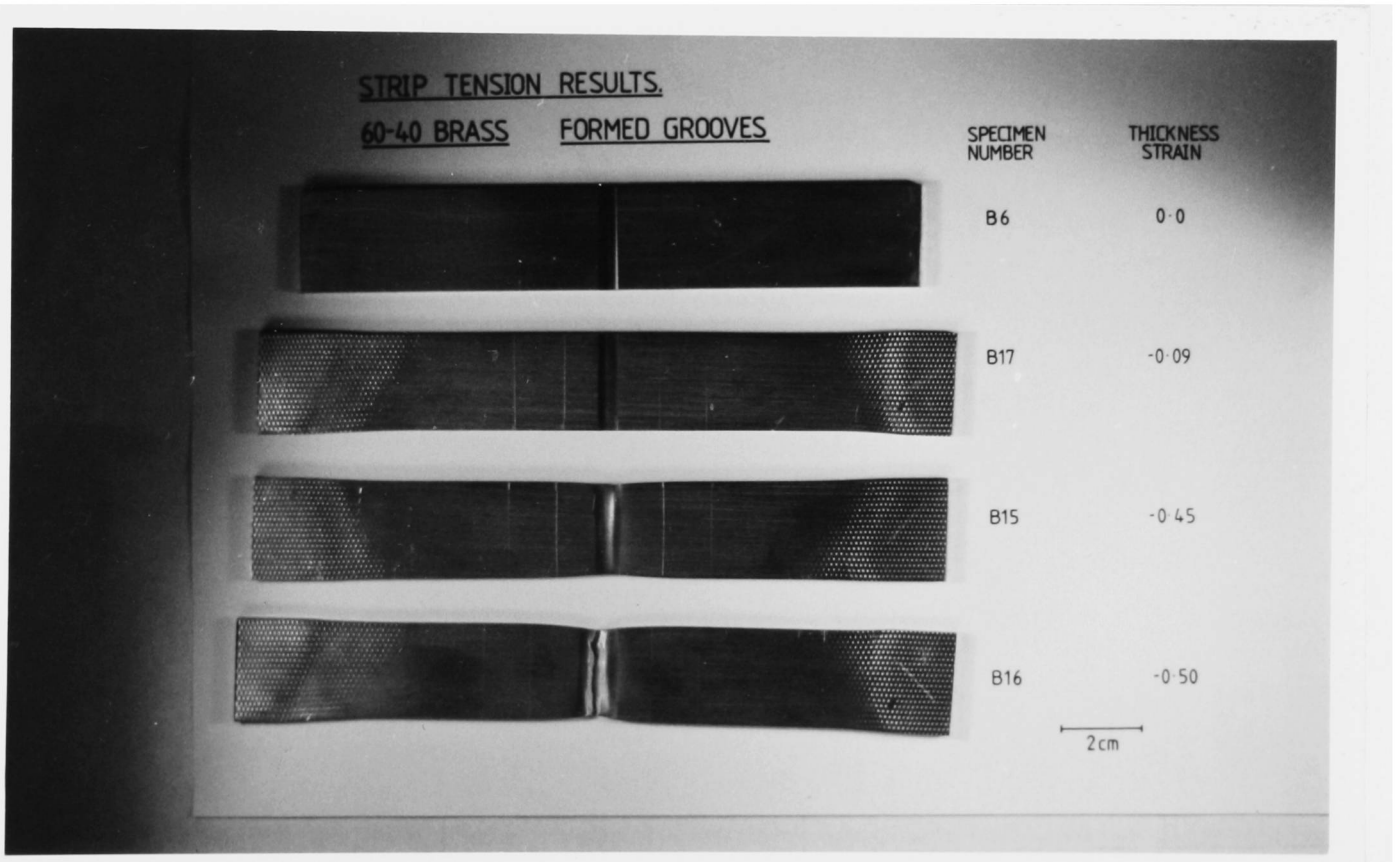

Figure 6.8(b)

Forged strip specimens.

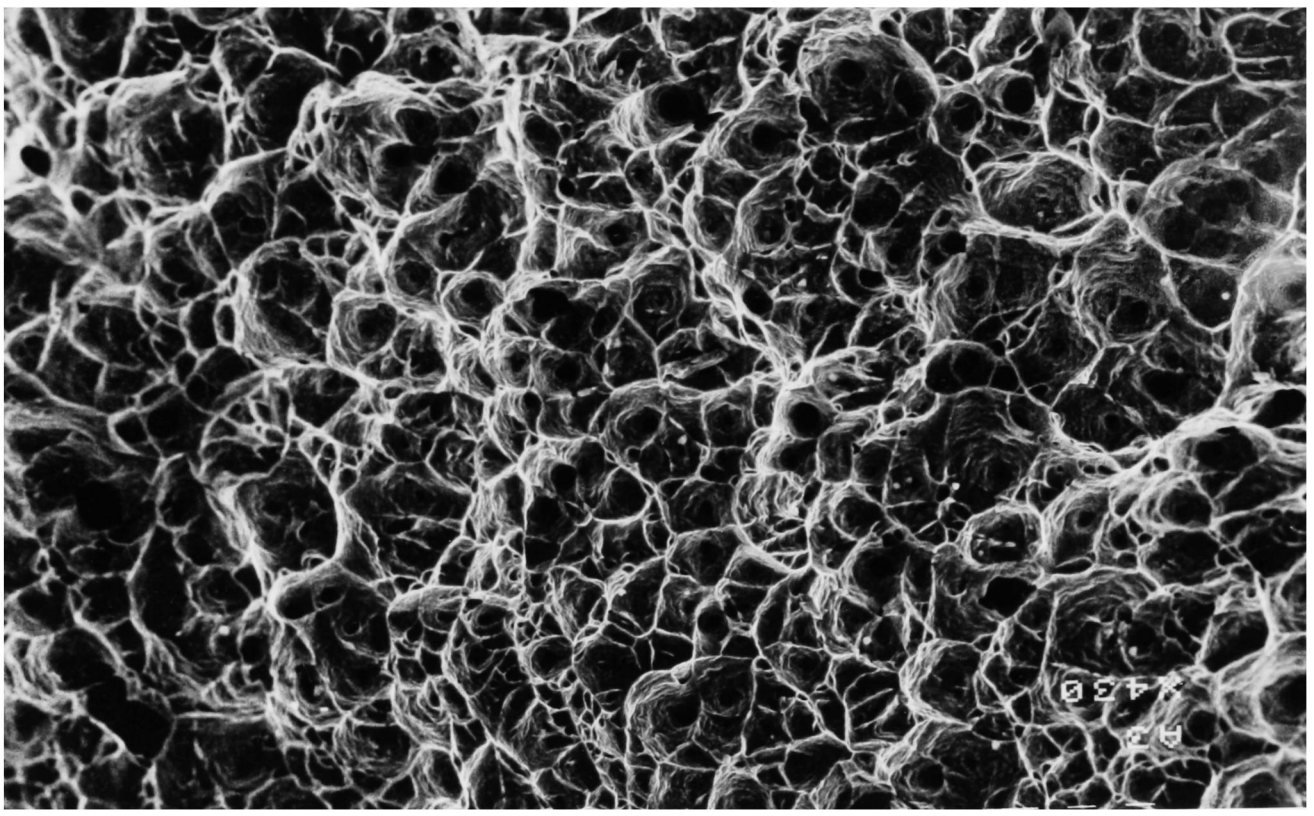

Figure 6.9(a)

Scanning electron microscope photograph of the milled strip fracture surface. (x430)

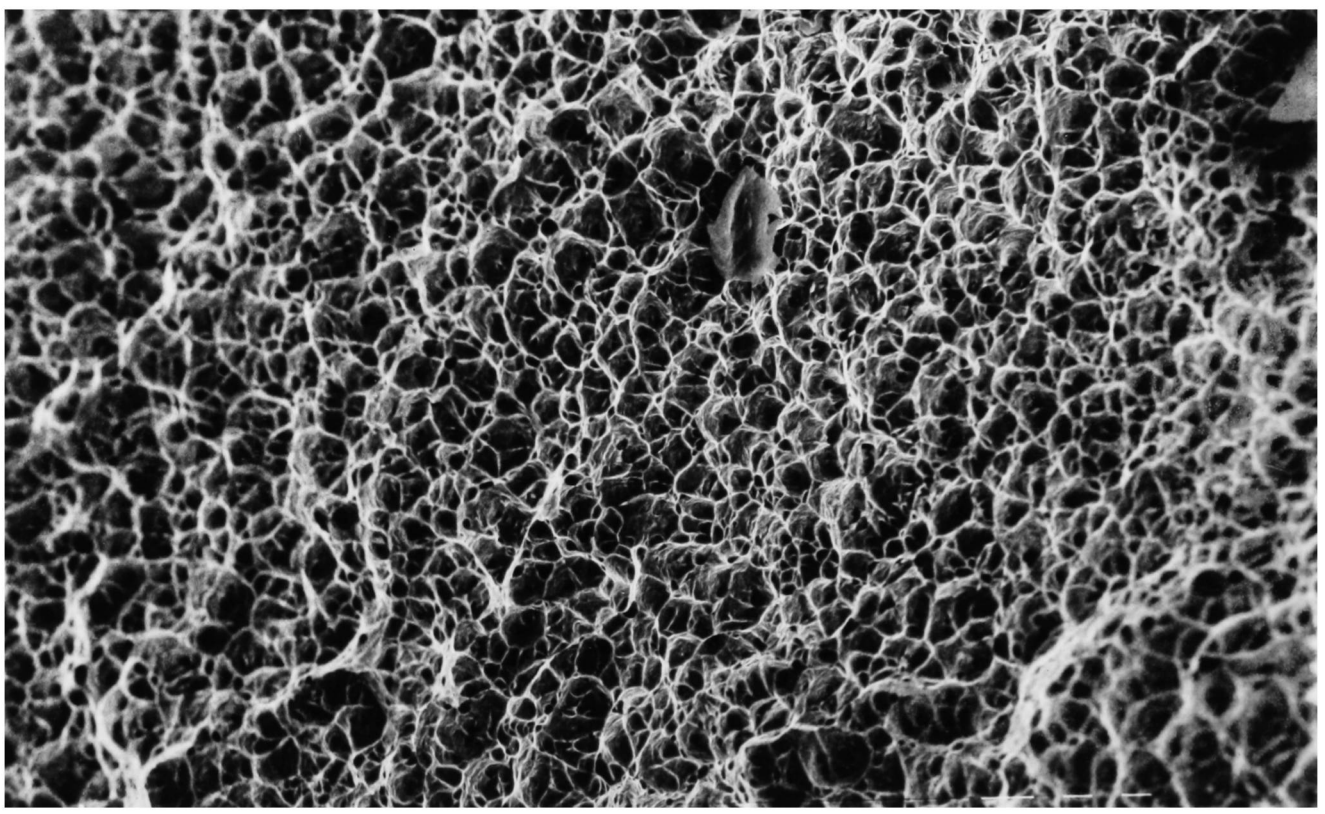

Figure 6.9(b)

Scanning electron microscope photograph of the forged strip fracture surface. (x430)

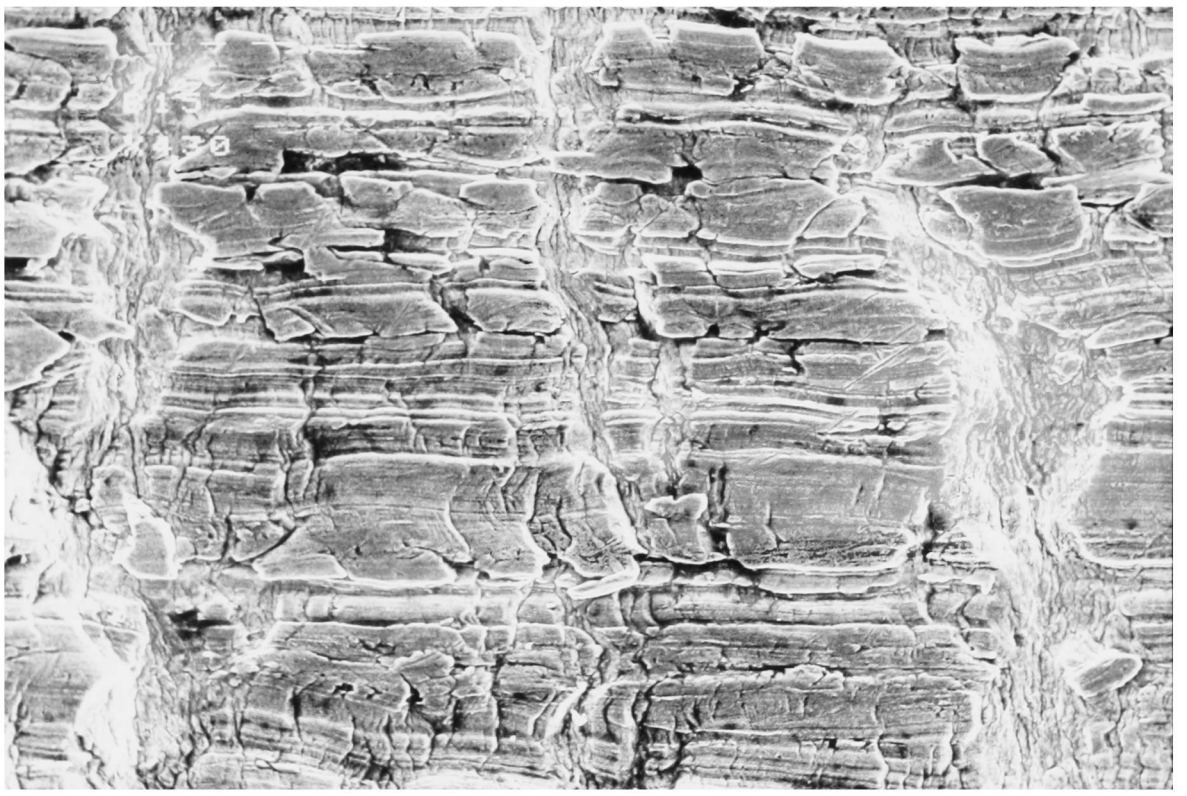

Figure 6.10

Three initiated cracks on the surface of a forged strip specimen. (x430)

6.4.2 Finite-element results.

Three sets of finite-element results are presented in this section; grid deformation patterns, incremental displacement vectors and plastic zone development diagrams. For all these illustrations only one quadrant has been modelled, the location of which is shown by a small sketch reproduced in each figure.

The plastic zone diagrams reveal where metal flow first starts and how this region of plastic flow develops as deformation proceeds. The grid deformation illustrations show the deformed finite-element grids after various levels of deformation. The incremental displacement vectors illustrate the direction and magnitude of the movement of a node during the most recent increment of deformation. These vectors have a relative magnitude of five when compared with the overall specimen dimensions. There are minor variations in the scale of each diagram due to the automatic scaling routines in the finite-element program. Even so, the changes in the flow patterns which occur as the deformation proceeds may be clearly identified. For all the results presented in this section the final illustration in each sequence is at the level of deformation at fracture found experimentally.

For the strip compression operation, figure 6.11(a) shows the plastic zone developed after various depths of indentation up to the experimental level of deformation at fracture. These illustrations show that the plastic zone develops steadily as deformation proceeds so that only the indented region and a small region extending into the specimen behave in a plastic manner.

The plastic zone development, for the tensile test simulation, for the model with an initially milled groove is presented in figure 6.11(b). The reduced section of the initially milled groove is the first

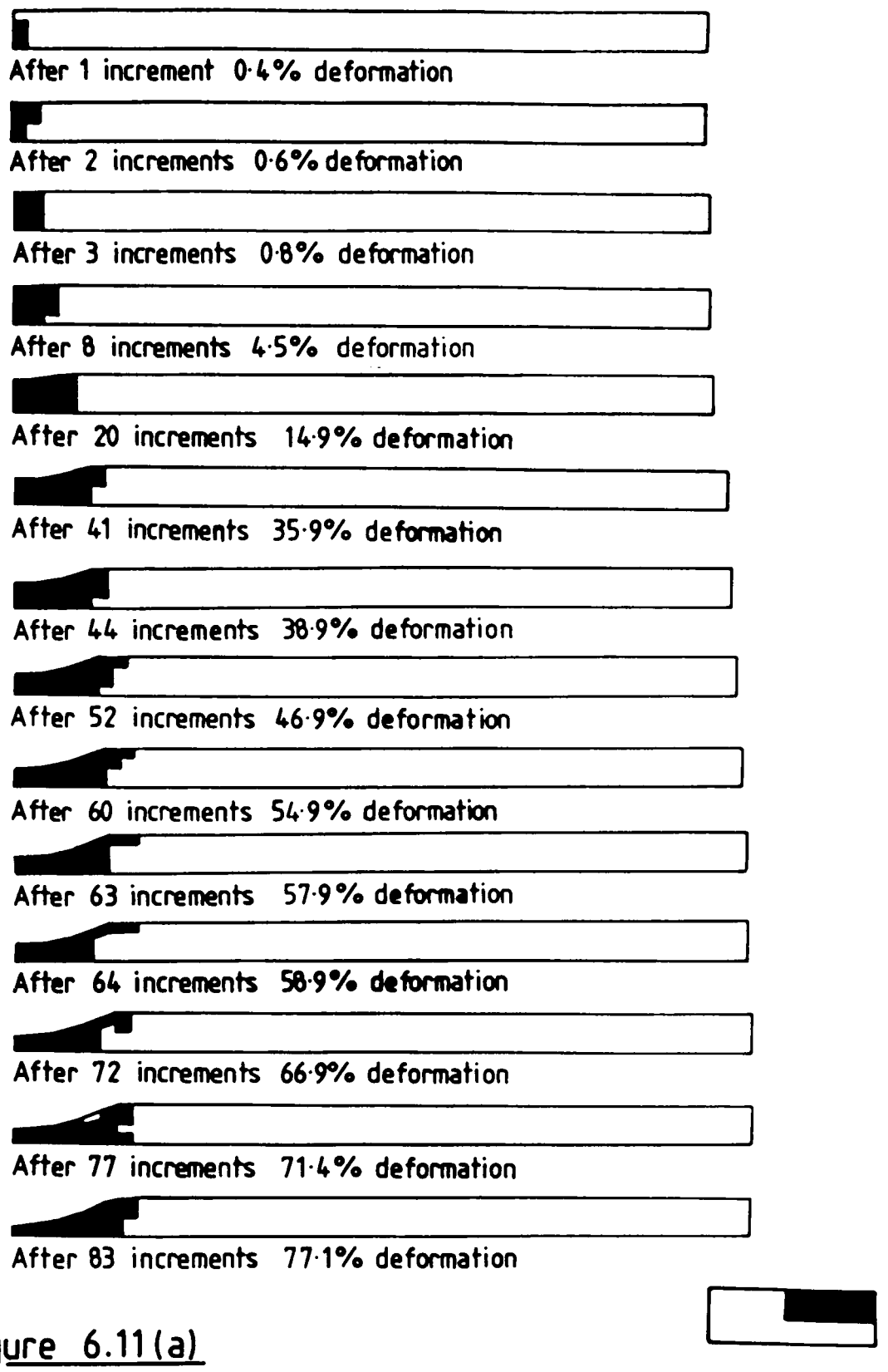

Figure 6.11(a)

Plastic zone development in brass strip after various depths of indentation.

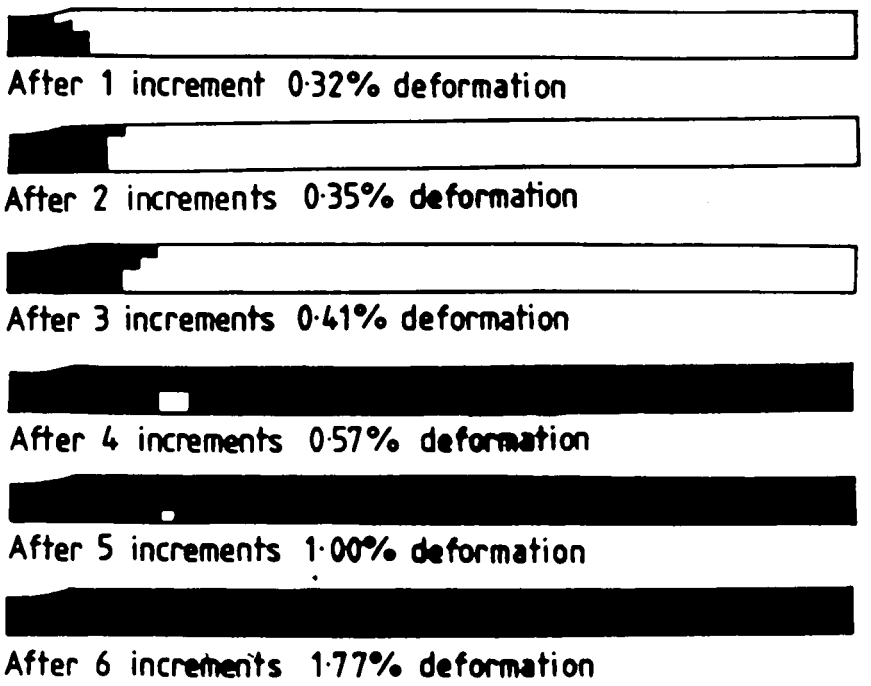

Figure 6.11(b)

Plastic zone development in the tensile deformation of brass strip with a milled indentation.

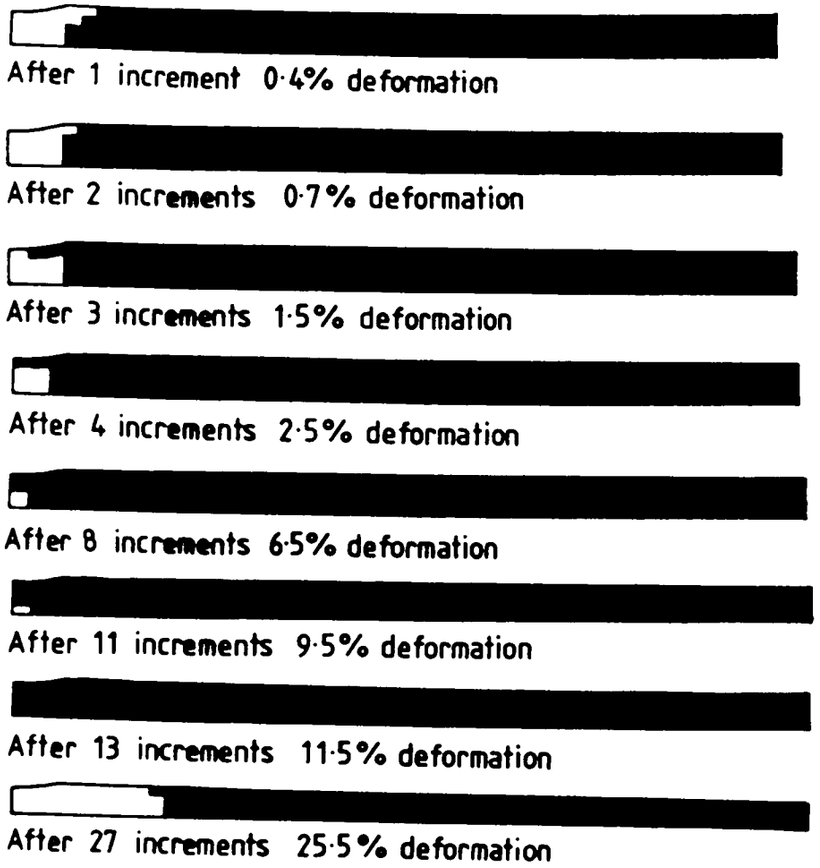

Figure 6.11(c)

Plastic zone development in the tensile deformation of brass strip with a forged indentation.

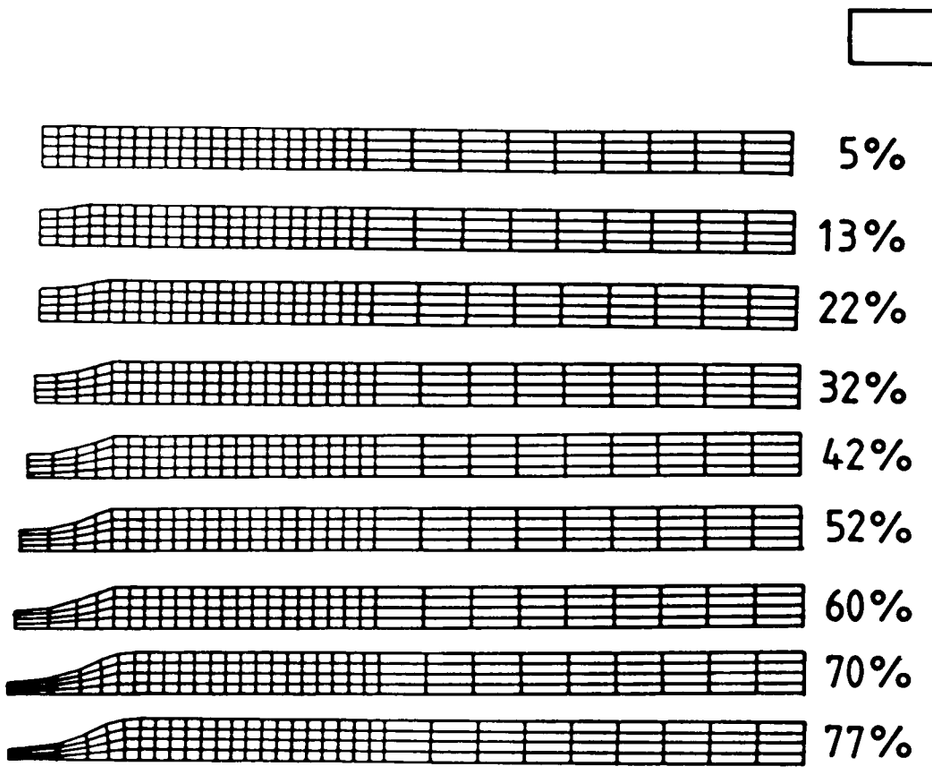

Figure 6.12(a)

Finite-element grid distortions for the model of 60-40 brass strip after various depths of indentation.

part of the model to behave in a plastic manner. This plastic zone then extends into the remainder of the specimen so that by 1.8% overall elongation the complete specimen is stressed above initial yield. For the forged strip model (Figure 6.11(c)) the initially indented region is the last part of the specimen to go plastic, as it has work hardened due to deformation in the previously performed indentation. Not until 11.5% overall elongation is the complete specimen predicted to behave in a plastic manner. However, by the level of deformation at fracture found experimentally the end of the specimen near the grips has started to neck, with the area around the original forged groove now behaving in an elastic manner. This does not agree with experiment and will be considered in more detail with respect to the other finite-element results presented in this section.

For the strip indentation model the formation of the neck region is clearly shown by both the deformed grids in figure 6.12(a) and the incremental displacement vectors in figure 6.13(a), and is predicted to be very highly deformed by the time fracture was observed experimentally. As expected, no deformation is visible away from the indented region.

The finite-element models for the forged strip and milled strip tension analyses both start with an initial indentation corresponding to 20% reduction in the original thickness.

For the milled strip tension analysis, as shown by the deformed grids in figure 6.12(b), and the incremental displacement vectors in figure 6.13(b), the neck has deformed much more before fracture occurs than for the initially forged strip.

For the forged strip model deformation appears to become localised in the region near the grips. This does not occur experimentally and suggests that the modelling assumption of plane-strain may not be valid up to this high level of extension.

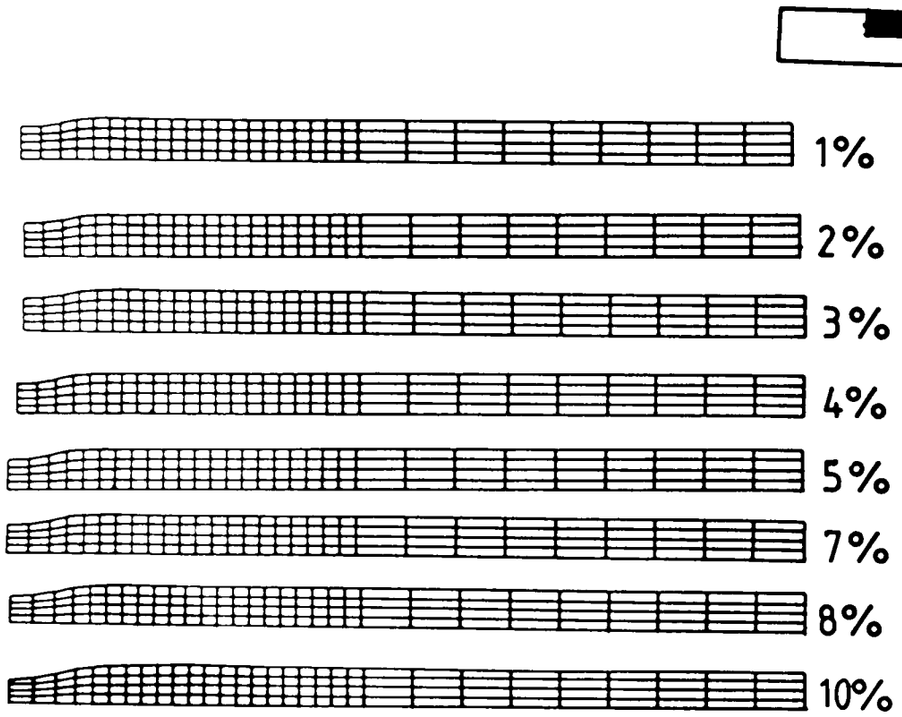

Figure 6.12(b)

Finite-element grid distortions for milled brass strip after various levels of overall extension.

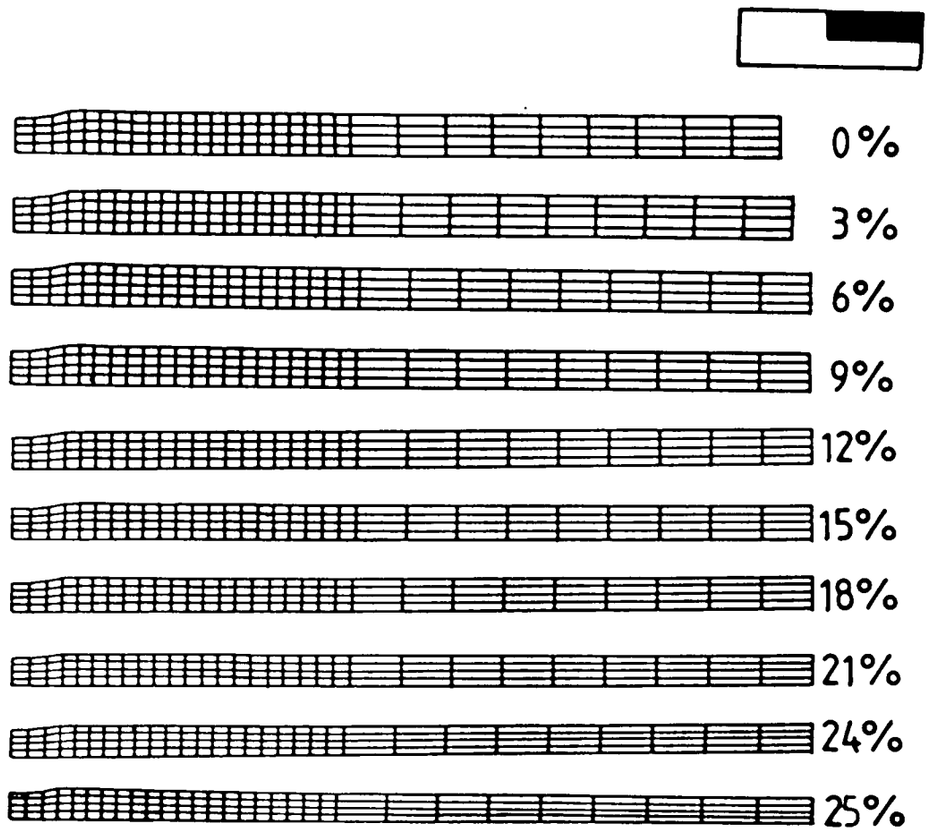

Figure 6.12(c)

Finite-element grid distortions for forged brass strip after various levels of overall extension.

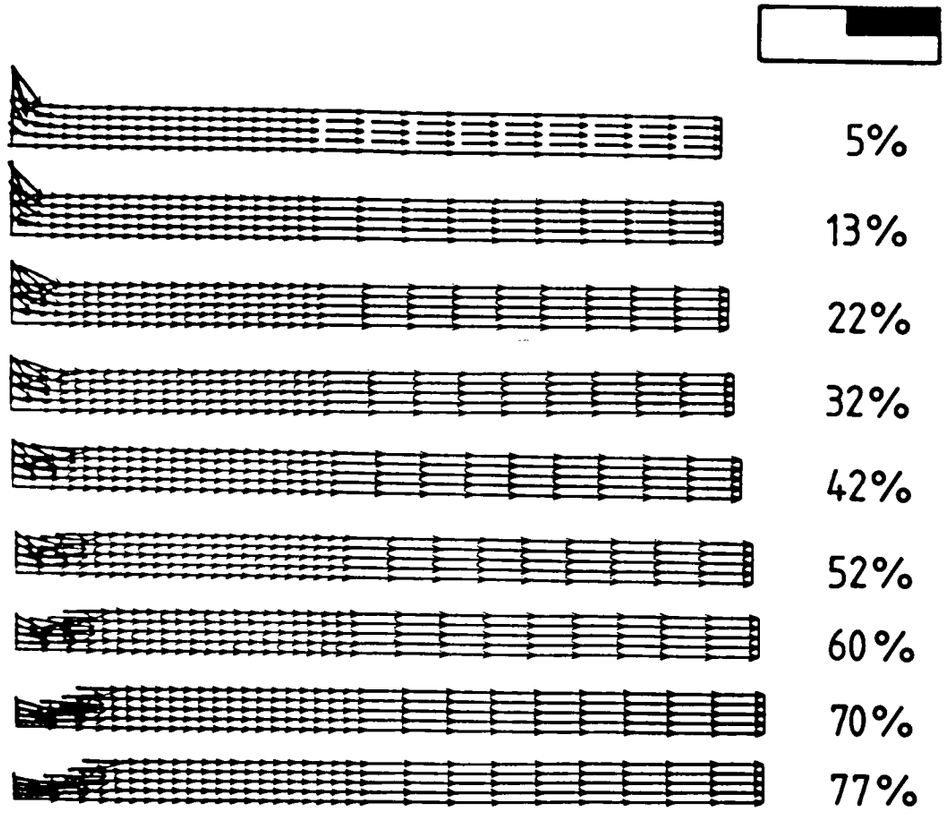

Figure 6.13(a)

Incremental displacement vectors for the finite-element analysis of strip compression.

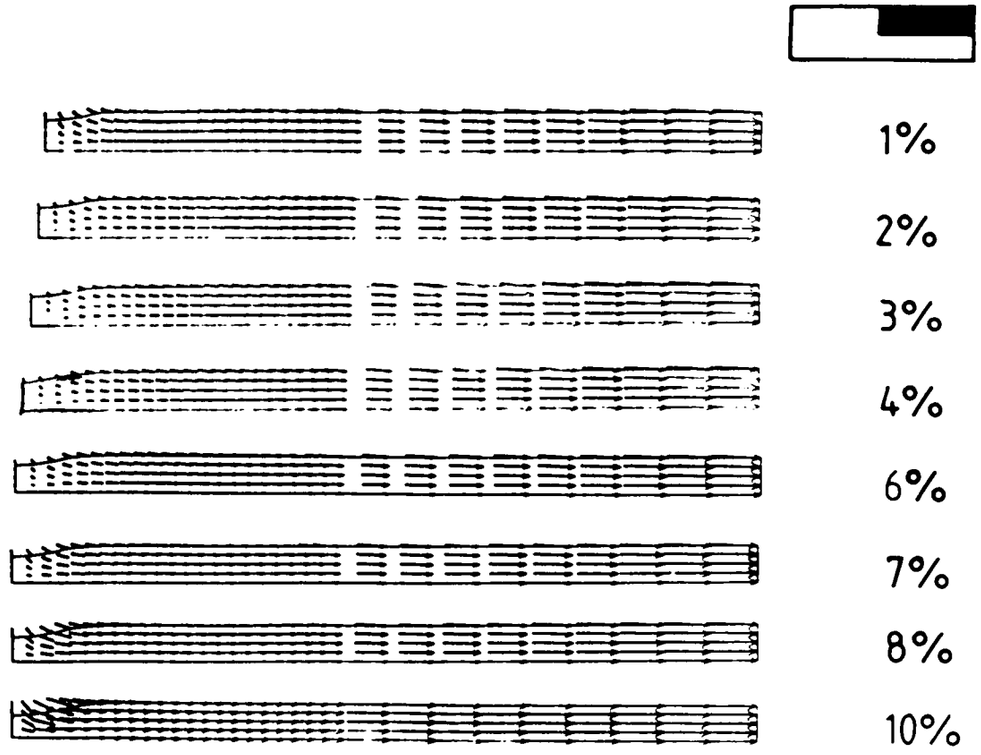

Figure 6.13(b)

Incremental displacement vectors for the finite-element analysis of milled strip tension.

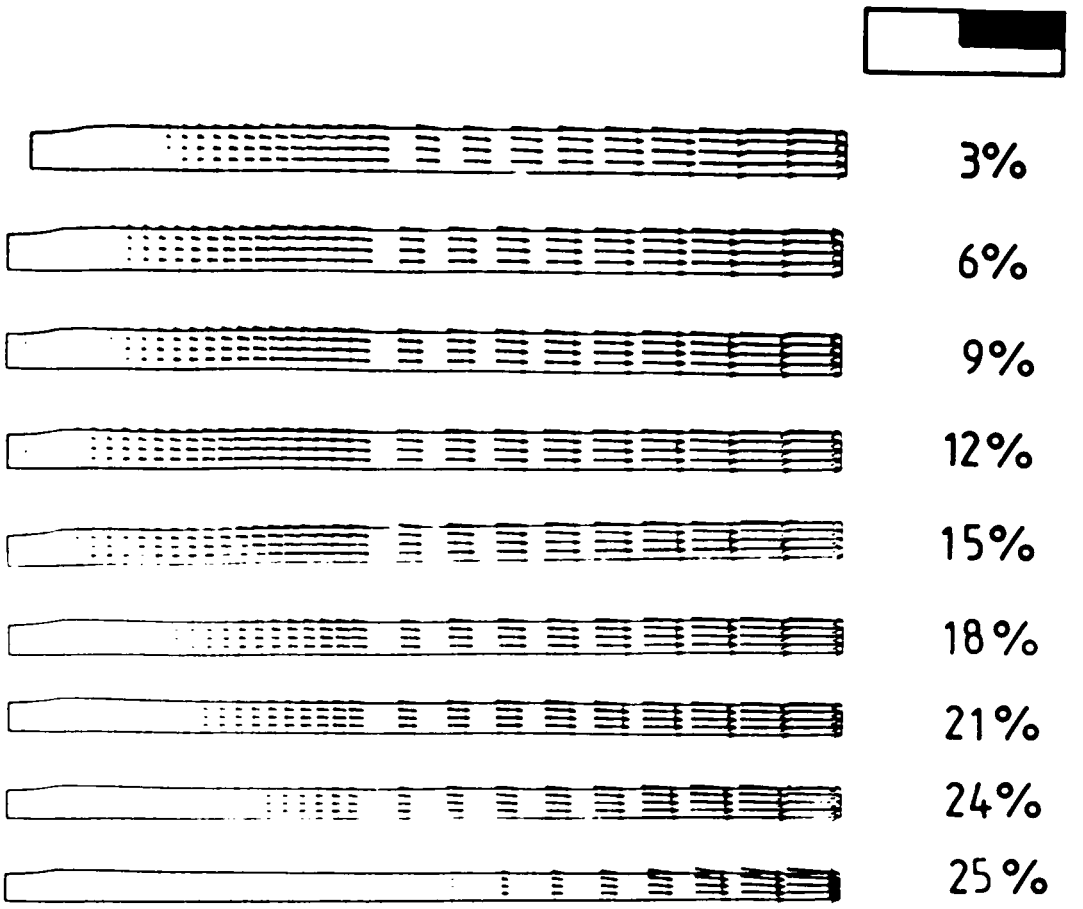

Figure 6.13(c)

Incremental displacement vectors for the finite-element analysis of forged strip tension.

This flow localisation is more clearly illustrated by the incremental displacement vectors shown in figure 6.13(c). By 25% elongation no deformation at all is occurring in the half of the model near the initial indentation. As the previously presented plastic zone development diagram (figure 6.11(c)) showed, the leftmost quarter of the model is behaving in an elastic manner by 25% deformation. The minimum neck thickness calculated by the finite-element program for the forged strip is 2.4mm compared with the 2.08mm found experimentally. Referring back to the group photographs presented in figure 6.8 it may be seen that there is some lateral strain across the necked region of the fractured specimen. This could obviously not be reproduced in the plane-strain finite-element model and suggests that a fully three dimensional model would be required to obtain better agreement with experiment.

For the milled strip, the minimum neck thickness calculated by the finite-element program is 1.35mm compared with the 1.26mm found experimentally. Here, the agreement is much better and figure 6.8 shows that there is much less lateral strain across the necked region of the fractured specimen than for the forged specimen.

6.4.3 Assessment of various fracture criteria.

By using the finite-element program in conjunction with the fracture accumulation program, as previously described in chapter 3 of this thesis, numerical predictions of the fracture initiation sites in the strip compression and tension operations were obtained. For each fracture criterion the node in the finite-element mesh at which the accumulated criterion value was a maximum at the level of deformation at fracture found experimentally was located. These sites were then compared with those found experimentally and the comparisons are

presented in Table 6.1. A tick indicates that the experimental and numerically predicted sites of fracture initiation agree; a cross that they disagree. The numbers displayed in the bottom right hand corner of each table element refer to the node number at which fracture initiation has been predicted to occur. The location of these nodes is given in the deformed mesh diagrams in figure 6.14.

For the McClintock and the Atkins criteria, prediction of the plane of fracture may also be made. These are displayed in the top left hand corner of the appropriate table elements.

From Table 6.1 it may be seen that only two criteria successfully predict the experimental fracture initiation site for all three strip deformation operations. These are the generalised plastic strain and generalised plastic work criteria. The criterion of McClintock, Kaplan and Berg (1972) does not predict the correct fracture initiation site for any of the operations considered. The remaining criteria considered show partial agreement with experiment, that is they are capable of correctly predicting the experimental fracture initiation site in some but not all of the strip deformation operations considered. The criteria due to Cockroft and Latham (1968), Brozzo, DeLuca and Rendina (1972), Norris, Reaugh, Moran and Quinones (1978), Oyane, Sato, Okimoto and Shima (1980) and Atkins (1981) give correct predictions for two out of the three cases. The remaining criteria, those of McClintock (1968) and Ghosh (1976) give only one correct fracture initiation site out of the total of three.

Experimentally, fractures occur in the yz plane. Neither of the McClintock fracture criteria or the Atkins criterion have correctly predicted this fracture plane.

As previously described in section 4.5.2 of chapter 4, an experimental determination of the critical value of generalised plastic strain at fracture, the critical value of generalised plastic work and

criterion / specimen	McClintock (1968)	McClintock et al (1966) (shear)	Ghosh	Oyane	Cockroft and Latham	Brozzo	Gen. plastic strain	Gen plastic work	Norris	Atkins
strip compression	zx × 198	zx × 266	× 279	√ 320	√ 319	√ 319	√ 319	√ 319	√ 192	zx √ 191
forged strip	zx × 140	zx × 313	× 342	× 123	× 123	× 123	√ 320	√ 320	× 187	xy × 325
milled strip	xy √ 319	xy × 199	√ 256	√ 319	√ 320	√ 320	√ 320	√ 320	√ 320	zx √ 320

Table 6.1

Comparison of FE predictions of fracture initiation site and experimental results for strip compression and tension.

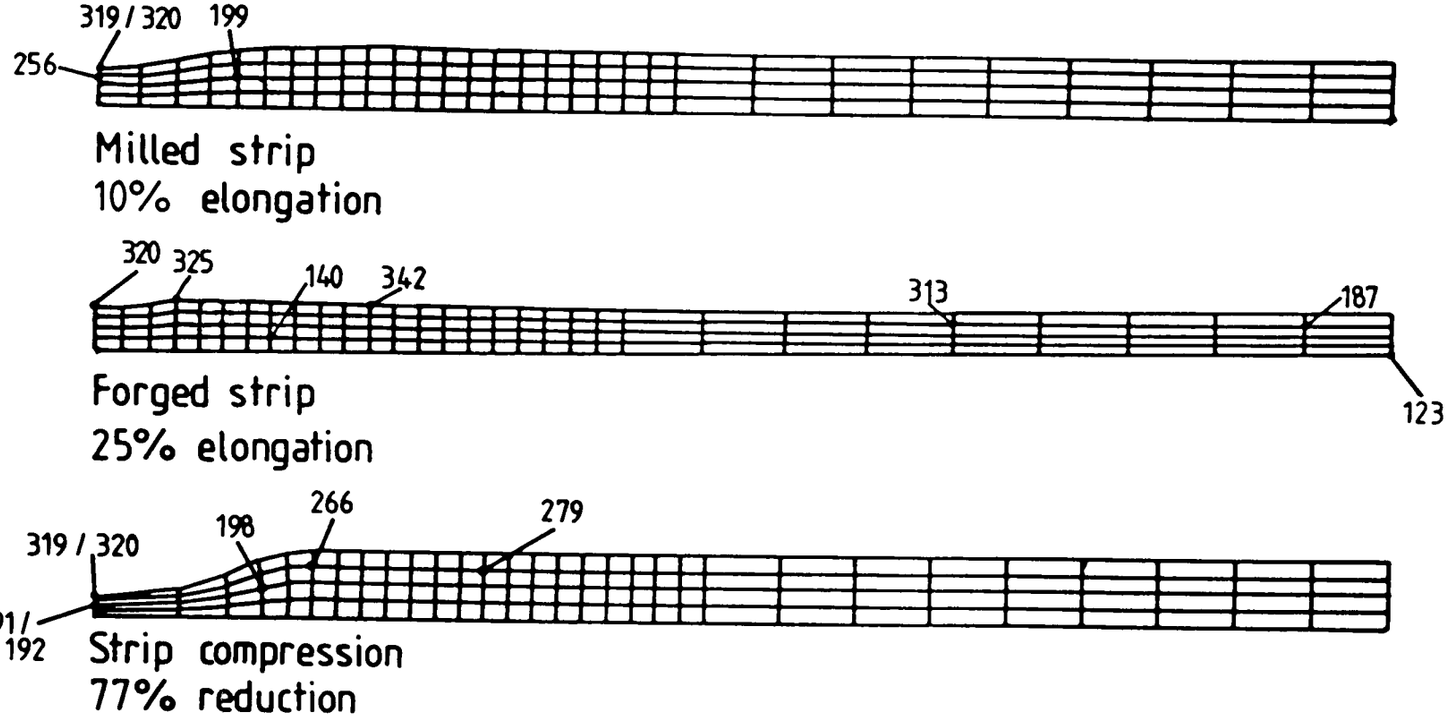

Figure 6.14

Deformed FE grids at the experimental level of deformation at fracture.

of the critical value of the Cockroft and Latham tensile plastic work at fracture was made, this time using a strip tension test. These critical values have been compared with the finite-element predictions. The comparison of the predicted and experimental levels of deformation at fracture for the generalised plastic strain criterion is presented in figure 6.15 and for the generalised plastic work criterion in figure 6.16. On each of the graphs for the forged strip results, the first 20% on the deformation axis refers to the compression operation, and the remainder to the tension operation.

The predicted level of deformation at fracture from both sets of graphs and the values obtained experimentally are summarised in Table 6.2. Predictions from the work and strain criteria are the same, as also reported for the plane-strain side-pressing in chapter 4 and the simple upsetting in chapter 5.

For the strip compression operation the generalised plastic strain and work criteria give a reduction in the minimum section of the indented region of 48% compared with 77% found experimentally. As described previously, the prediction was made using a simple strip tensile test, and the operation considered here is a compressive one. The strains developed under this compressive stress system would therefore be expected to delay fracture initiation. This is discussed further in chapter 8.

For the tensile deformation of the brass strip containing a milled groove the finite-element program has calculated a value of generalised plastic strain at the experimental level of deformation at fracture of 0.54 (work: 307 MN/m^2) compared with 0.74 (work: 450 MN/m^2) from the strip tension test. These results are in much better agreement than for the strip compression operation. However, the indentation would be expected to allow fracture to initiate before a non-necked specimen as has been predicted and a more accurate prediction may be possible if,

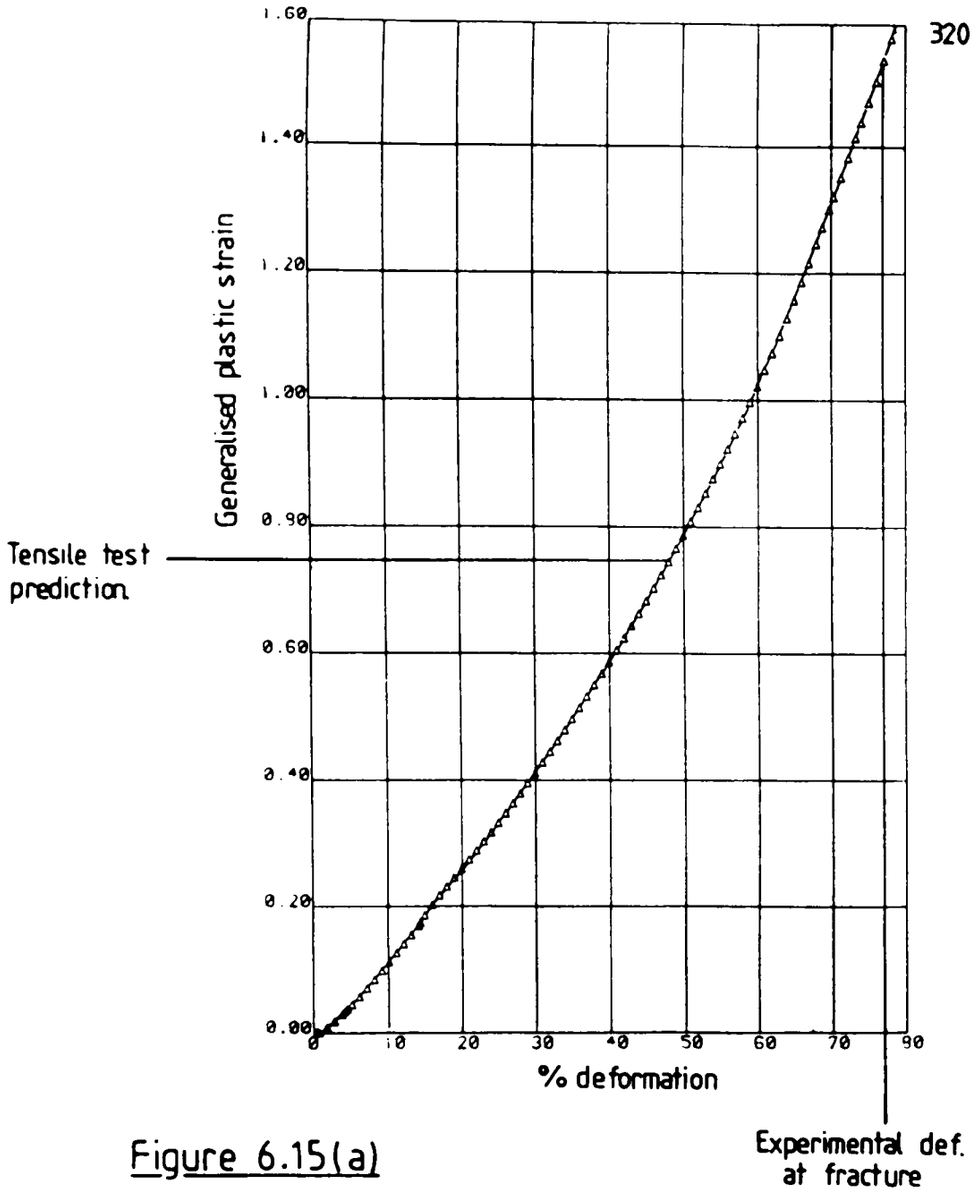

Figure 6.15(a)

Variation of FE generalised plastic strain for the compression of brass strip (node 320)

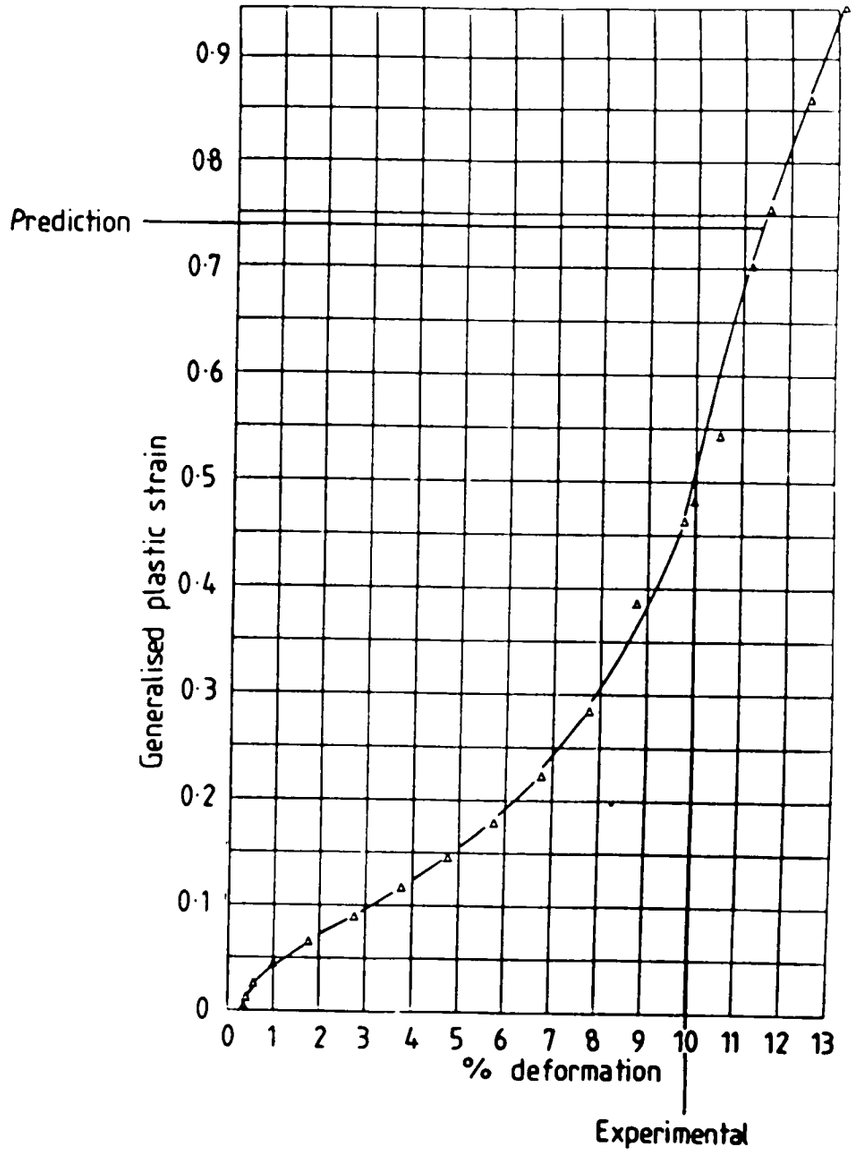

Figure 6.15(b)

Variation of FE generalised plastic strain for the tensile deformation of brass strip with a milled groove (node 320).

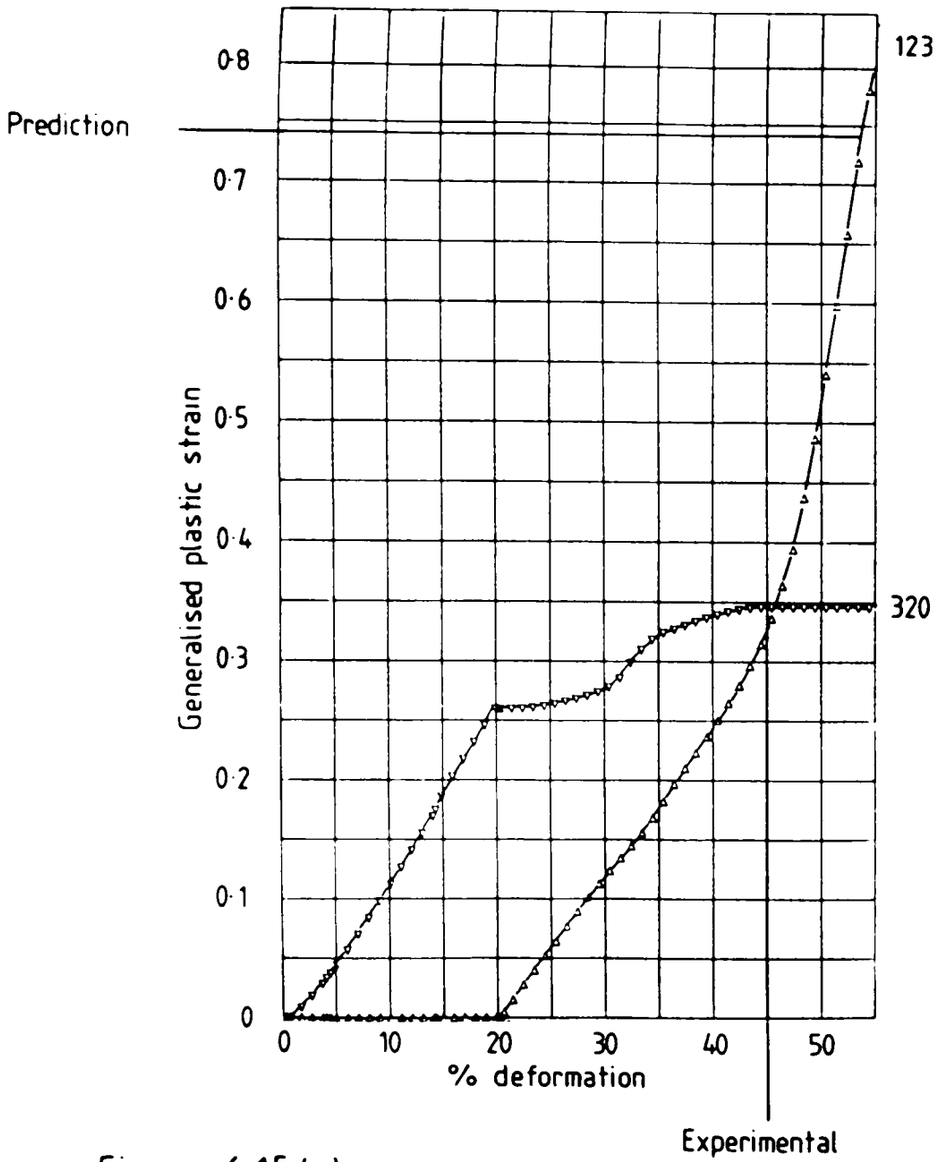

Figure 6.15(c)

Variation of FE generalised plastic strain for the tensile deformation of brass strip with a forged groove (nodes 123 and 320).

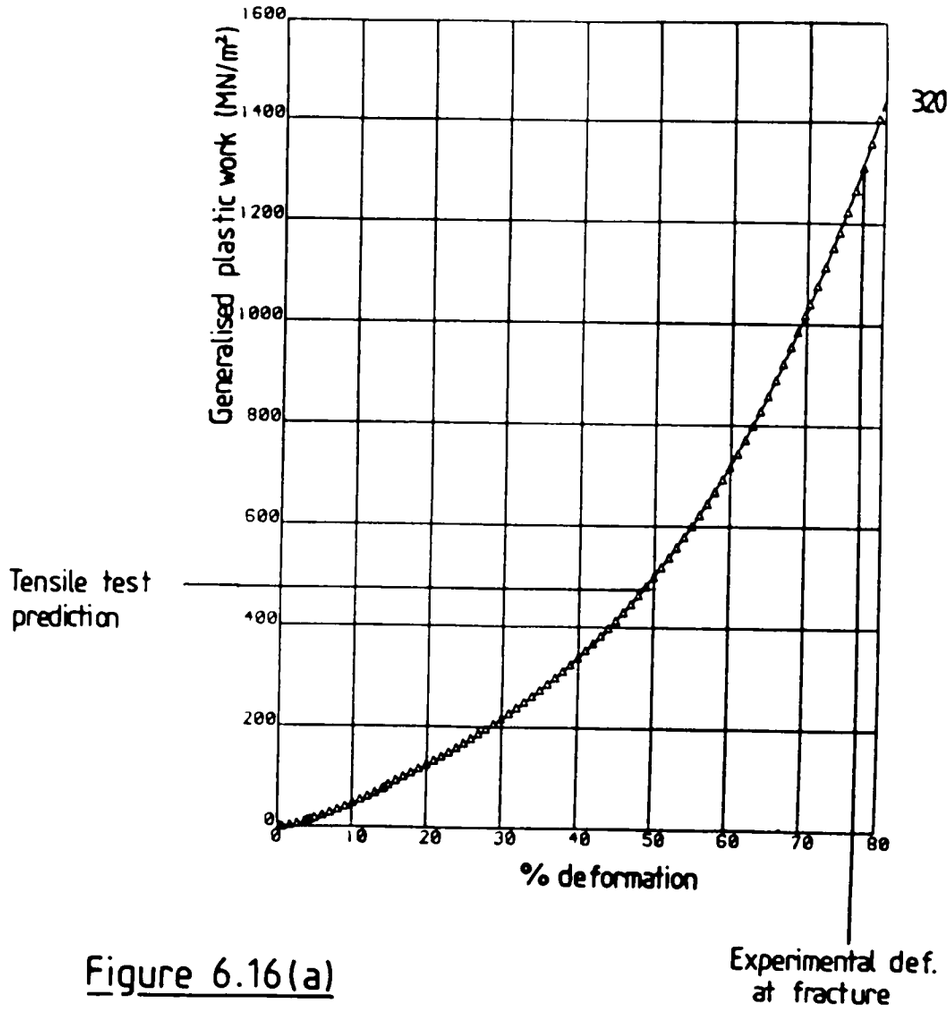

Figure 6.16(a)

Numerical calculation of the generalised plastic work fracture criterion from FE results for the compression of brass strip (node 320).

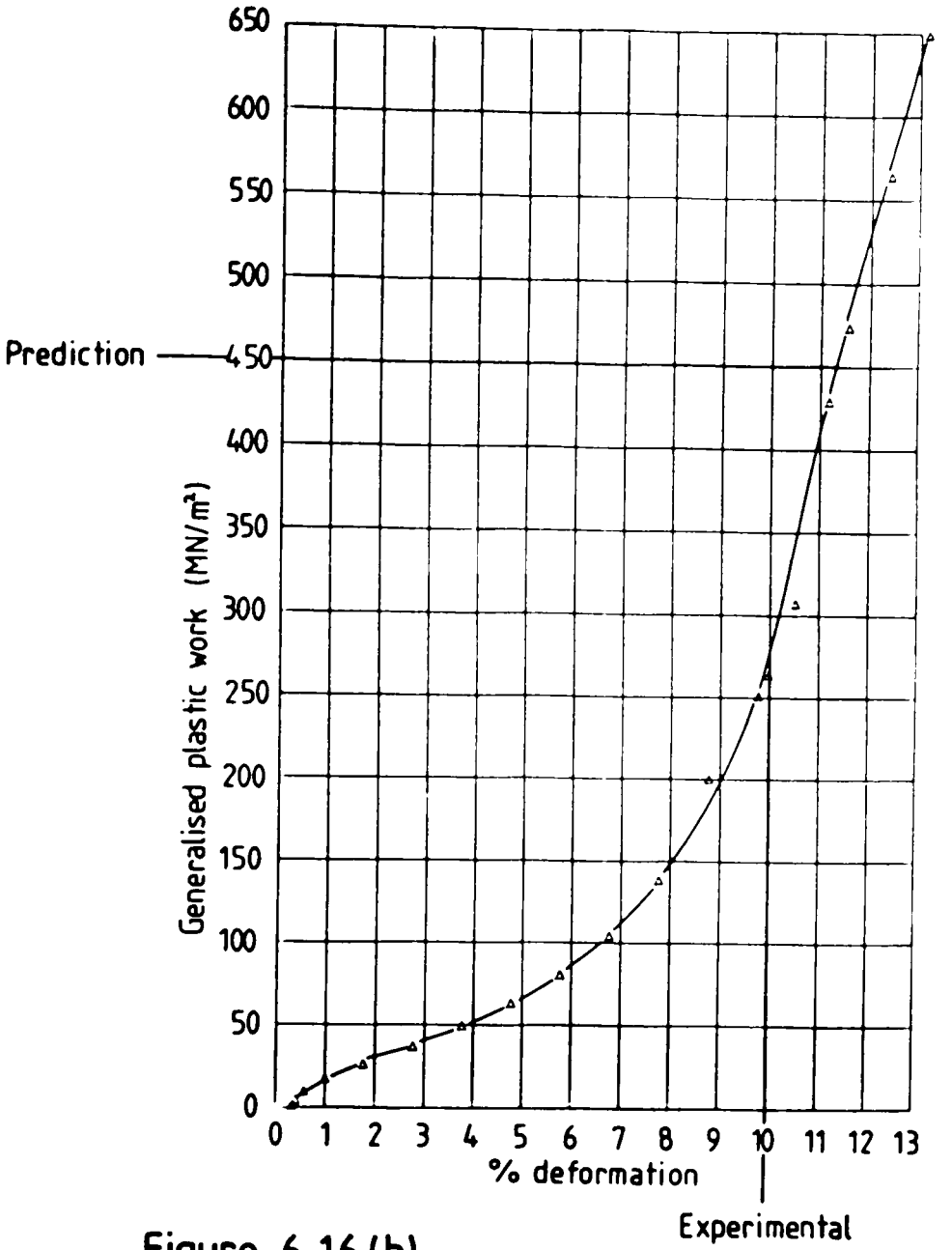

Figure 6.16(b)

Numerical calculation of the generalised plastic work fracture criterion from FE results for the tensile deformation of brass strip with a milled groove. (node 320).

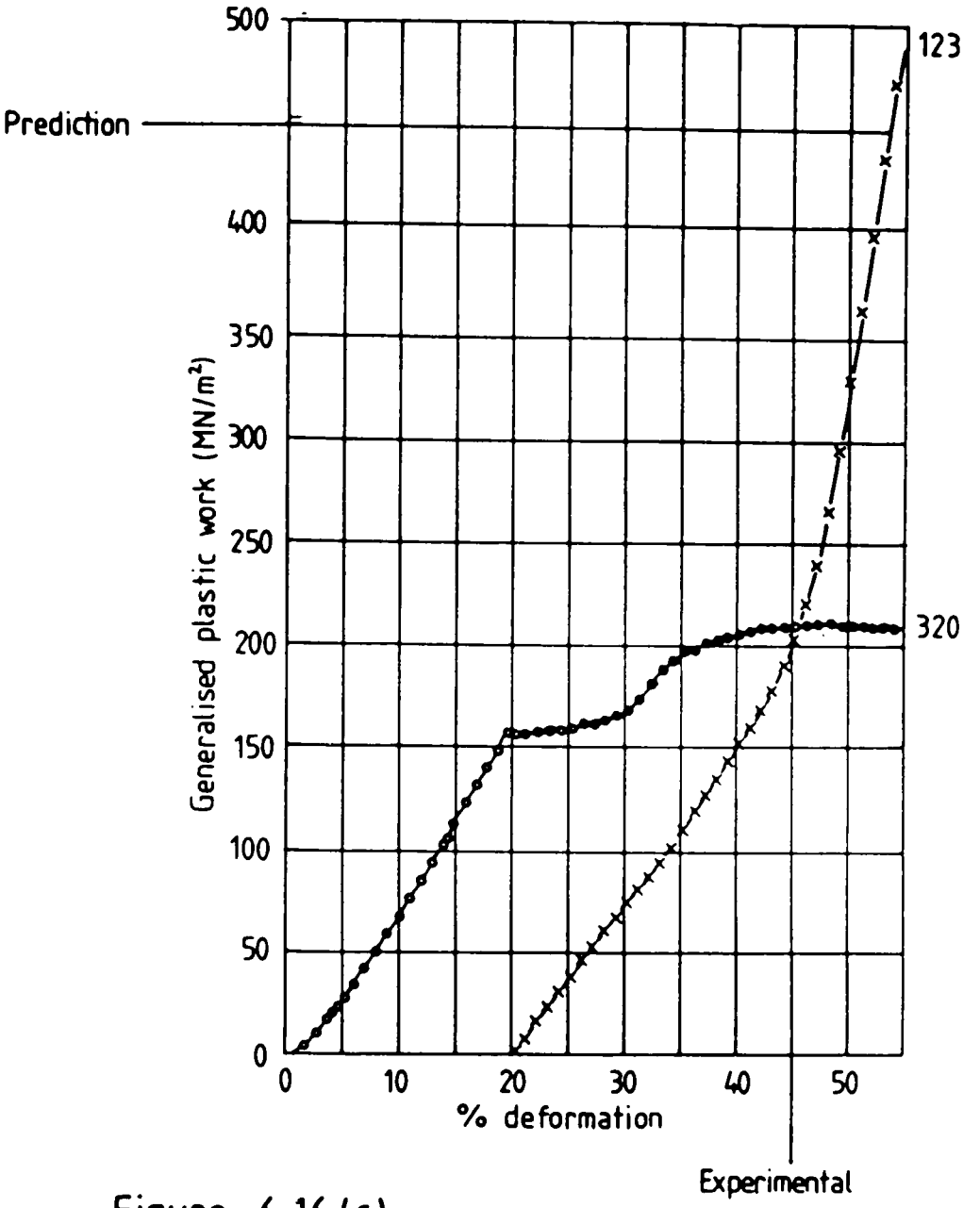

Figure 6.16(c)

Numerical calculation of the generalised plastic work fracture criterion from FE results for the tensile deformation of brass strip with a forged groove (nodes 123 and 320).

Model	Experimental	Finite-element	
		Work	Strain
Compression	77% reduction of min section	48%	48%
Forged	25% Elongation	33%	33%
Milled	10% Elongation	11·5%	11·5%

Table 6.2

Experimental and predicted deformations at fracture.

again, the effect of hydrostatic stress on the critical value of plastic strain at fracture were taken into account. This possibility is considered further in Chapter 8. For brass strip with a forged groove the finite-element technique has calculated a value of generalised plastic strain at the experimental level of deformation at fracture of 0.35 (work: 170 MN/m^2) compared with the 0.74 (work: 450 MN/m^2) found from the tensile test.

A significant contribution to the differences found here may be due to the inability of the plane-strain finite-element mesh to model accurately the experimental conditions, as previously described in section 6.4.3. It is suggested that this agreement would be improved by a fully three dimensional finite-element model.

The graphs in figure 6.17 show how the numerical values of Cockroft and Latham's tensile plastic work vary with the level of deformation of the specimen. For the strip compression operation (Figure 6.17(a)) the tensile test value underestimates the experimental level of deformation at fracture. This result again highlights the failure of the Cockroft and Latham criterion to take into account the contribution to fracture from the work performed due to compressive stresses.

For the brass strip with a milled groove the tensile test value slightly overestimates the level of deformation at fracture found experimentally. This result shows good agreement as the experimental conditions are very similar to those investigated by Cockroft and Latham.

For the brass strip with a forged groove the fracture initiation site found experimentally was not correctly predicted by the Cockroft and Latham criterion. The level of deformation at fracture predictions are, therefore, not meaningful and are not shown.

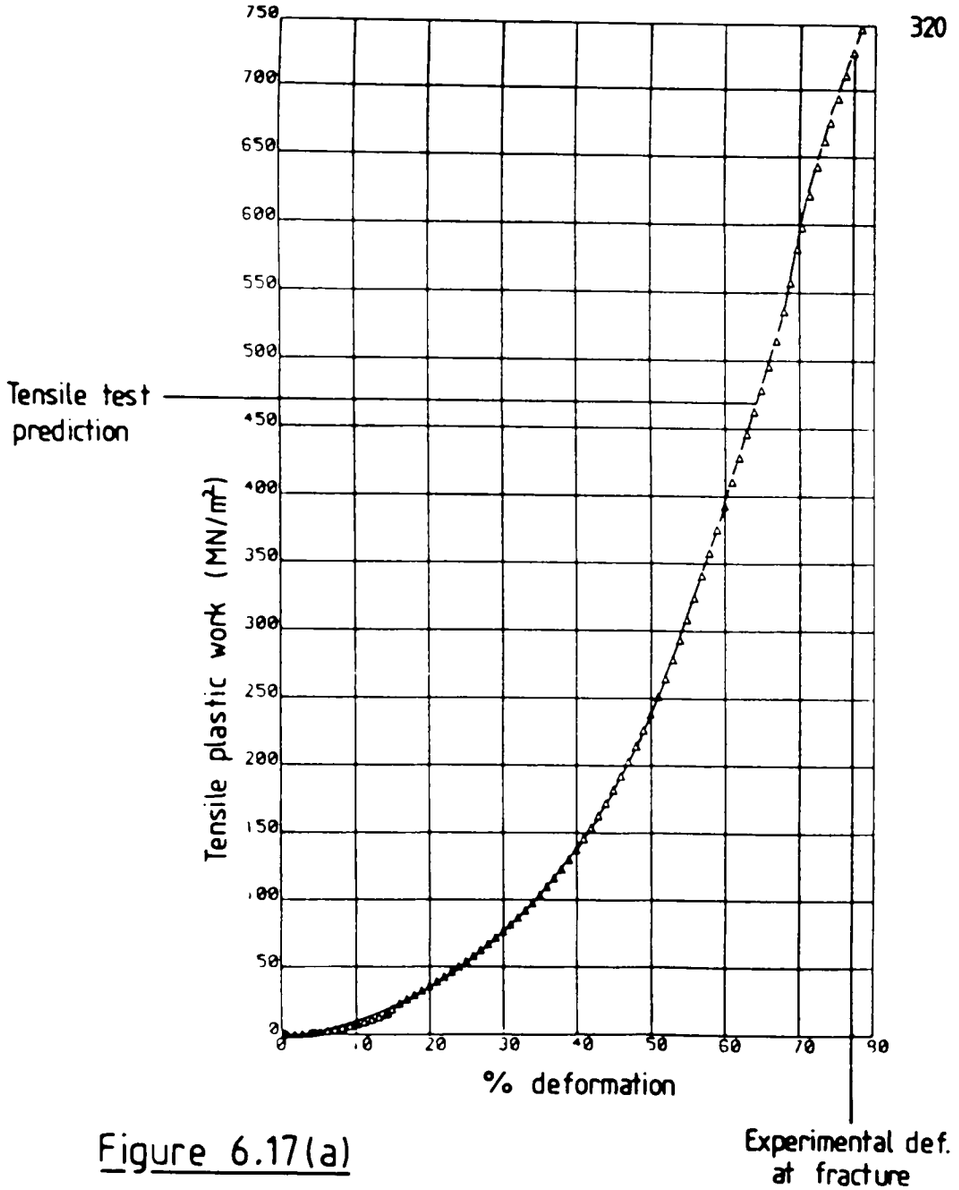

Figure 6.17(a)

Numerical calculation of the Cockroft and Latham fracture criterion from FE results for the compression of brass strip (node 320).

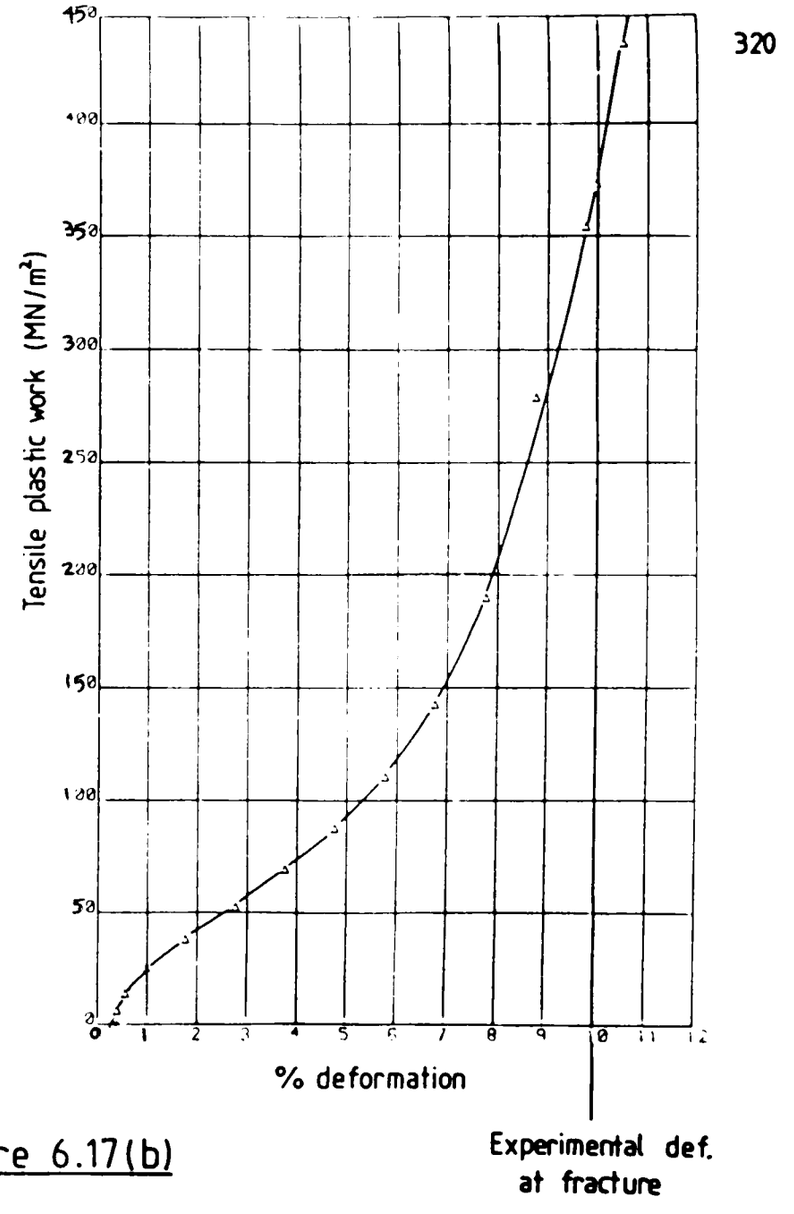

Figure 6.17(b)

Numerical calculation of the Cockroft and Latham fracture criterion from FE results for the tensile deformation of brass strip with a milled groove for node 320.

6.5 Conclusions.

Good agreement has been found for the finite-element and experimental deformation results for the strip compression and milled strip tension operations. For the forged strip tension operation the results do not agree with experiment and it is suggested that a three dimensional finite-element model would produce better agreement.

Only the generalised plastic strain and generalised plastic work criteria have been found to predict successfully the fracture initiation sites found experimentally for all three strip deformation operations. Chapter 8 considers further the errors in the predicted levels of deformation at fracture.

Chapter 7.

Axisymmetric extrusion.

7.1 Introduction.

This chapter describes the experimental results and finite-element predictions obtained for the extrusion of a circular rod into that of a smaller diameter.

Both 60-40 brass and 7075 aluminium alloy have been extruded as described in section 7.2. Section 7.3 describes the finite-element mesh used in the analyses and section 7.4 presents the finite-element and experimental results. Finally, section 7.5 gives the conclusions of this chapter.

7.2 Specimen preparation and experimental procedure.

Circular section rods of both 60-40 brass and 7075 aluminium alloy were used in this study of axisymmetric extrusion. The brass was used in its 'as received' condition (see Section 4.3.2) but the aluminium alloy supplied had been produced by a different manufacturing route from that used in chapter 4. In this case the material had been produced as cold rolled plate, rather than continuous cast rod, and hence had the characteristic inhomogeneous microstructure shown in figure 7.1. A more homogeneous structure was required for critical tests of identifying fracture initiation. The method of heat treatment used to homogenise the structure is given in Appendix B.

A stress-strain curve of the heat treated material, determined using a compression test as described in section 4.3.2, is shown in figure 7.2. The materials were extruded as illustrated in figure 7.3 where the diameter of the circular section rod is reduced. Tests were done quasi-statically at room temperature. Experiments were performed for

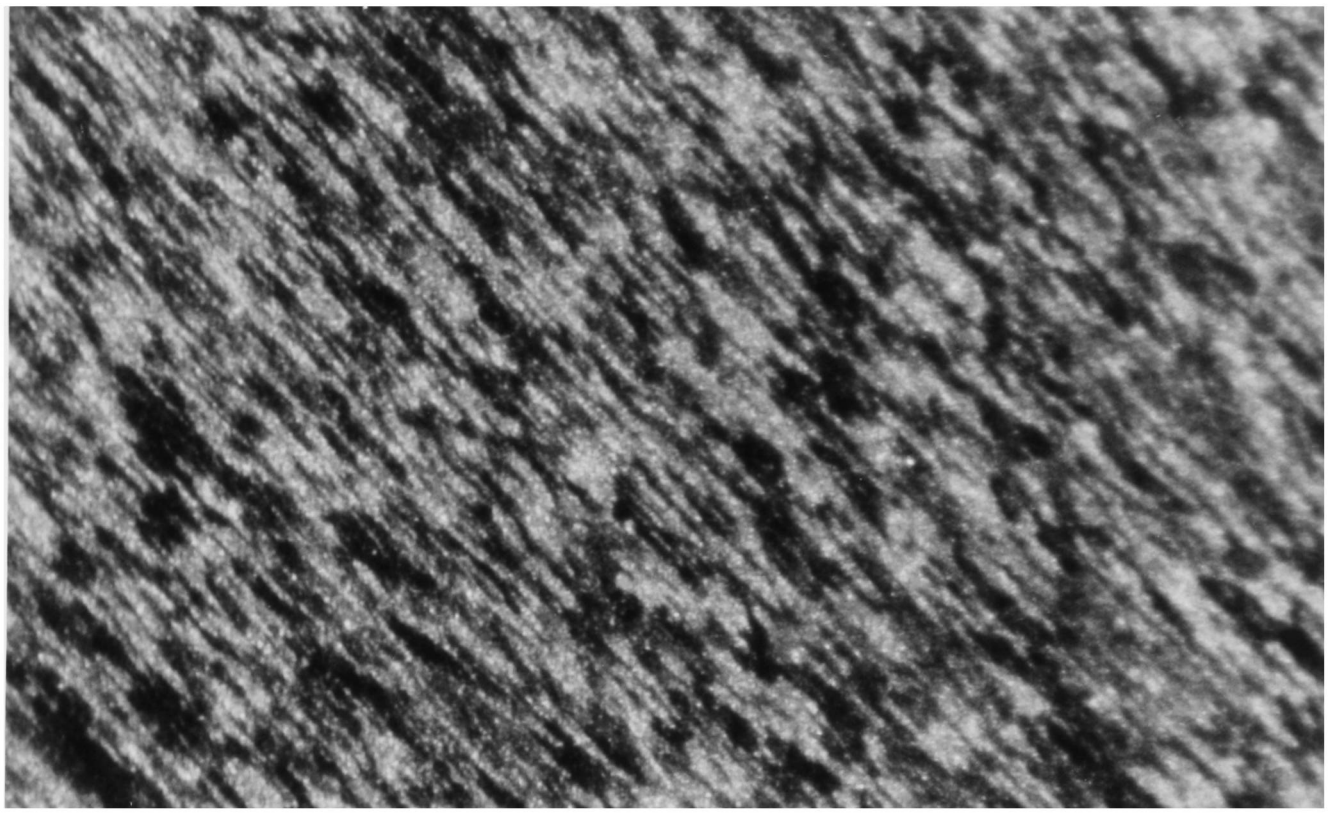

(a) Transverse (x80)

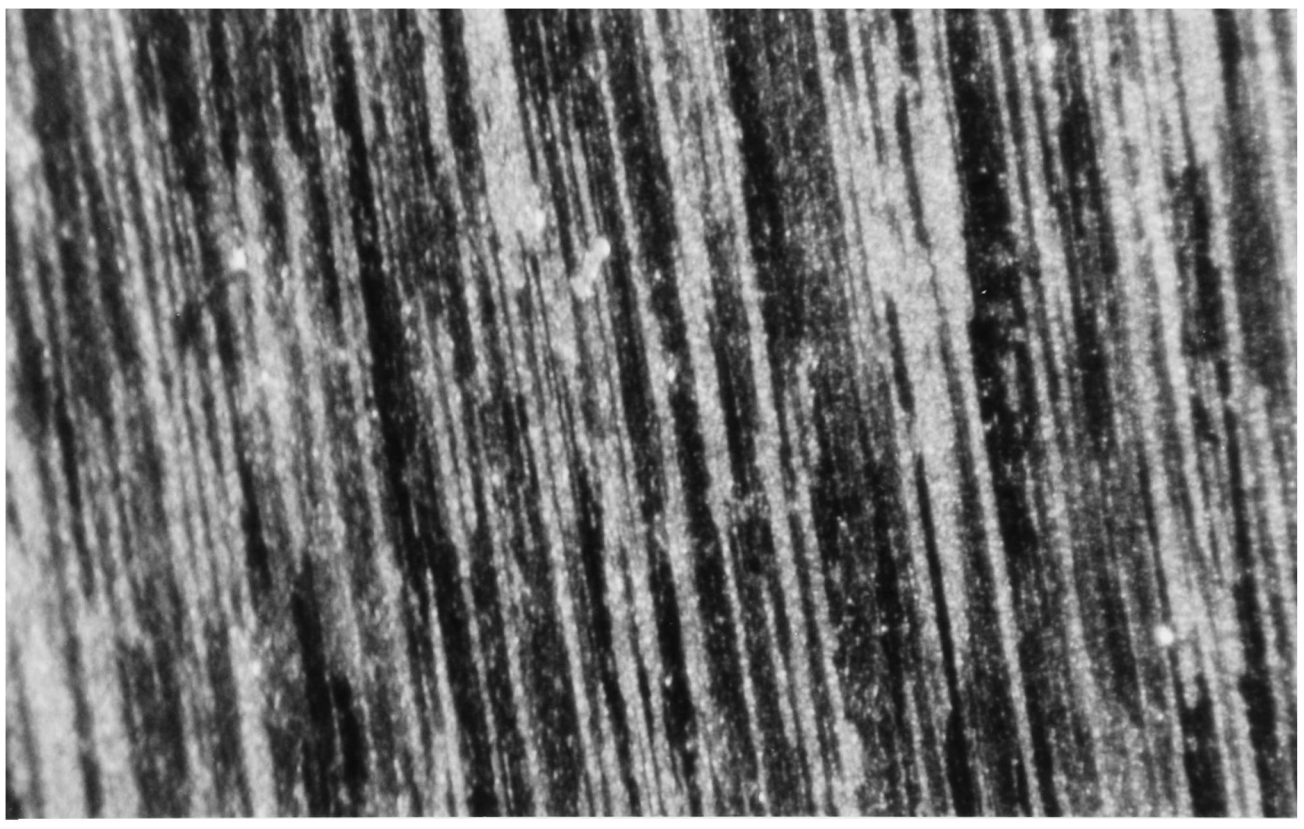

(b) Longitudinal (x80)

Figure 7.1

Microstructure of 7075 aluminium alloy (plate stock).

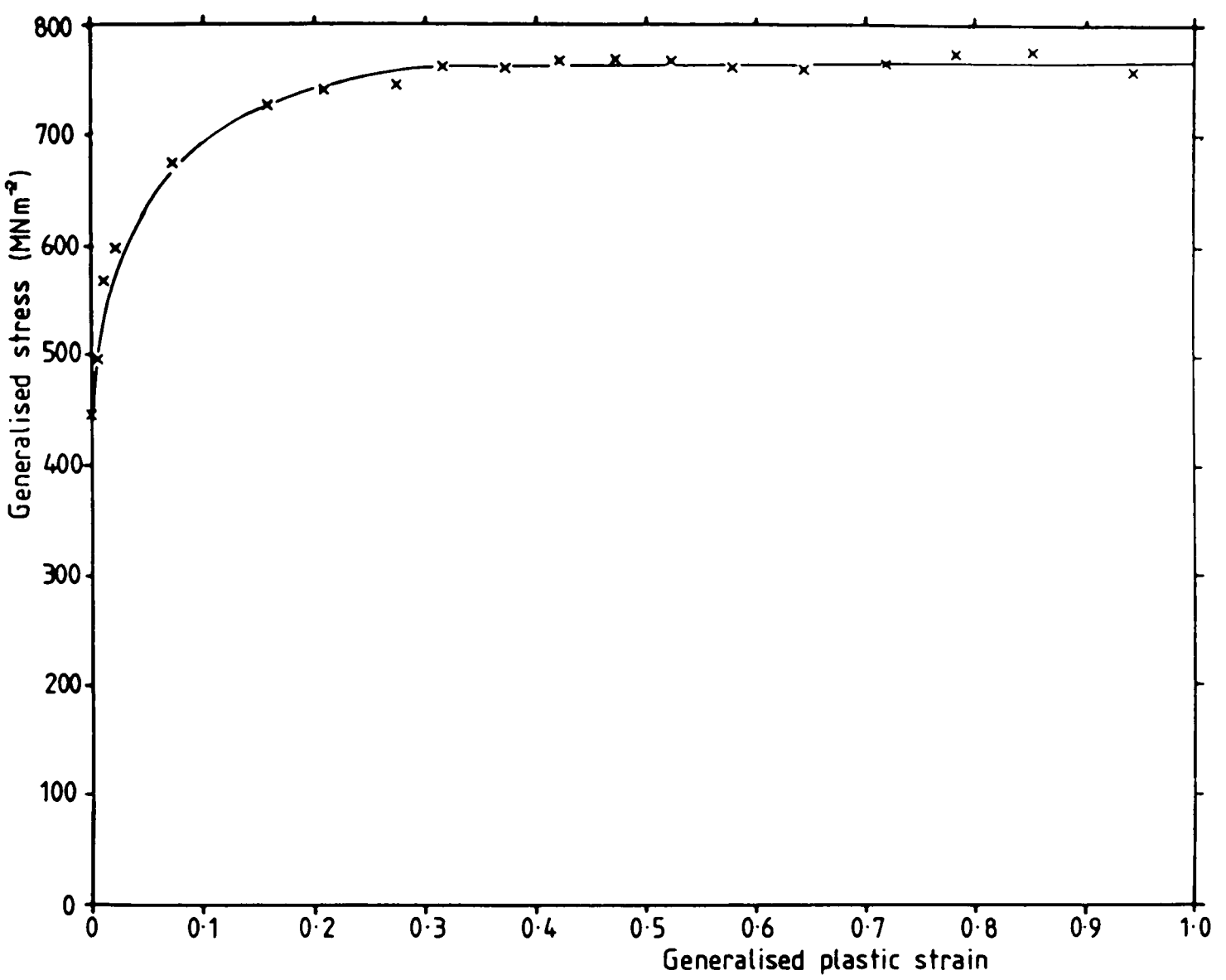

Figure 7.2 Compression test stress-strain curve for 7075 aluminium alloy (heat treated plate).

the three different reductions in area of 34%, 61% and 77%. In all tests the dies were well lubricated with lanolin. The specimens were carefully examined after deformation for the appearance of cracking.

7.3 Finite-element model.

The axisymmetric extrusion of both 60-40 brass and 7075 aluminium alloy for 61% reduction in area was selected for modelling using the finite-element method. For both materials the three reductions studied experimentally all cracked in the same mode (see Section 7.4.1). The experimental results for the 61% reduction allow the fracture initiation sites to be identified at an earlier stage than for the other reductions. It therefore seems suitable to be modelled numerically. Figure 7.4 shows the finite-element mesh used and its dimensions. An 18^{o} segment of the cylindrical rod has been utilised. Based on the 'Ring test' results presented in figure 7.5 an interface shear factor, m, of 0.1 was used on the dies, land and container. (This test has previously been described in section 4.3.3).

The constitutive relationship obtained from the compression test reported in Section 7.2 was used to model the variation in stress with plastic strain.

In order to constrain the model to simulate extrusion properly a number of theoretical boundary conditions have to be constructed. In principle this is fairly easy, however in practice this modelling problem has shown up a number of deficiencies and difficulties encountered in using the finite-element program and will therefore be described in detail.

The first problem found concerned the modelling of the sloping part of the dies. Obviously, a conical boundary surface would be the most appropriate one to use. Unfortunately, no conical boundary surface is

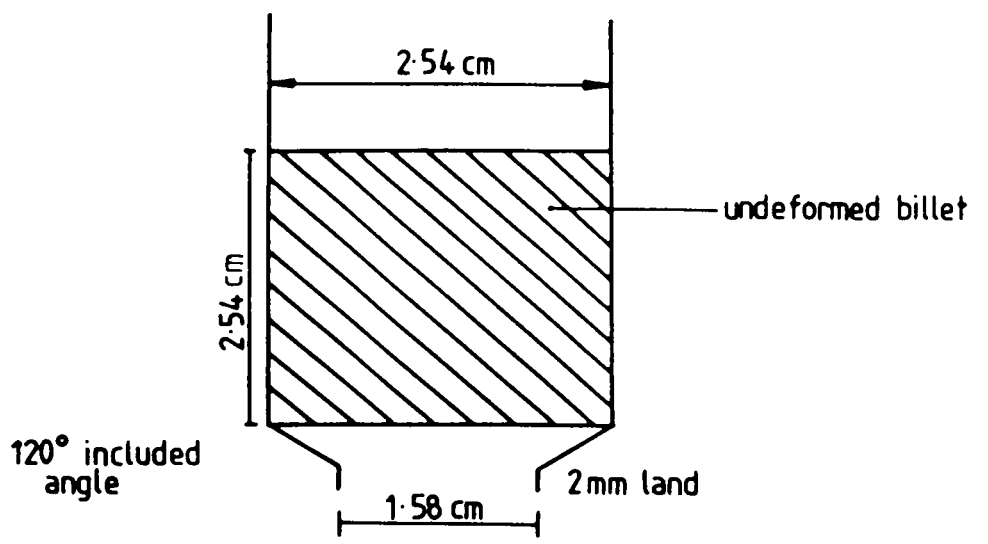

Figure 7.3

Sketch of extrusion geometry.

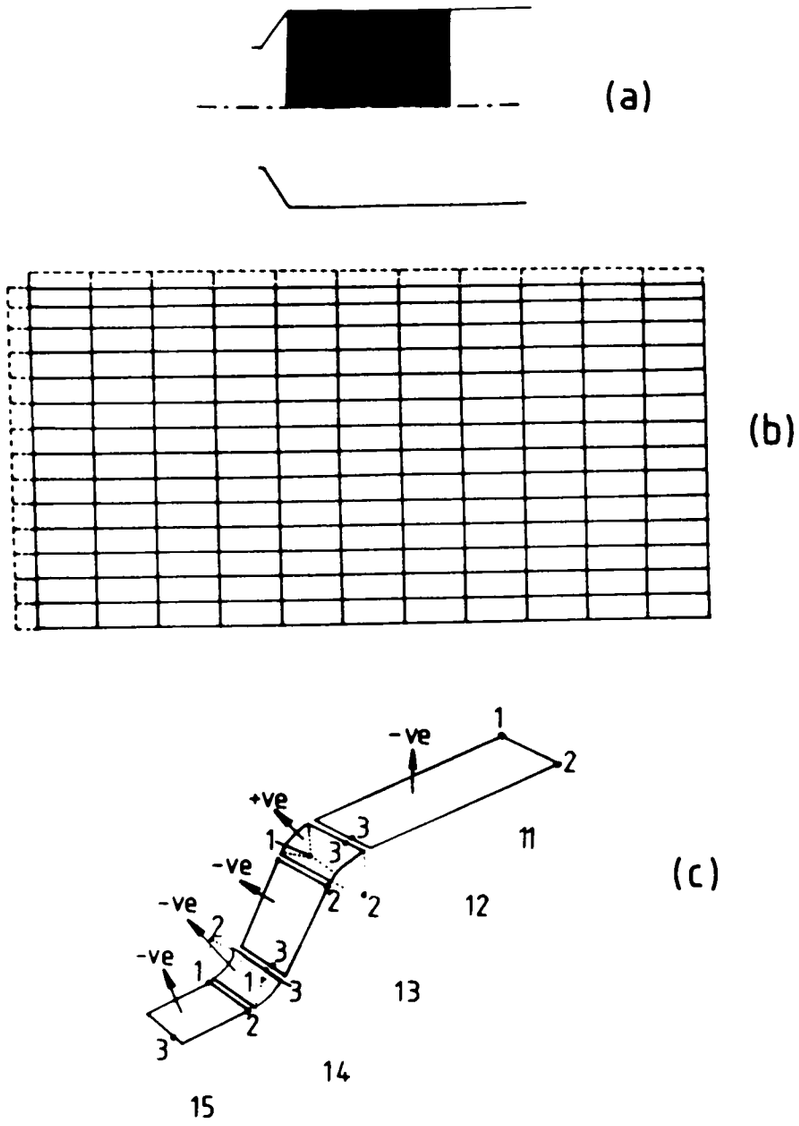

Figure 7.4

Finite-element model

(a) Half of complete cross section is modelled

(b) FE mesh (dotted lines indicate friction layer)

(c) Arrangement of boundary planes

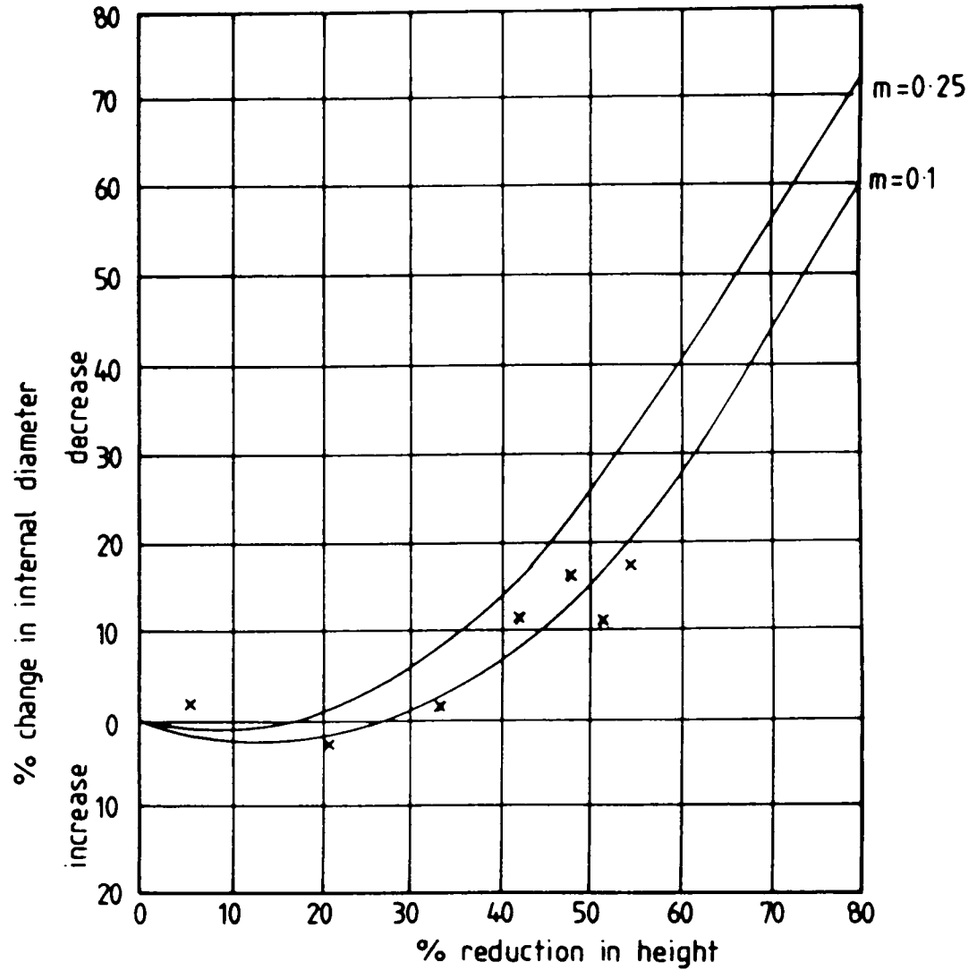

Figure 7.5

Ring test results for 7075 aluminium alloy (plate) lubricated with lanolin and finite-element calibration curves.

available within the program and the problem has to be modelled using a single layer of elements constrained by an intersecting constraining condition and a boundary plane as shown in figure 7.6.

An additional problem arose because node 57 (shown in figure 7.7) remained stuck at the intersection between boundary planes 11 and 13. Consequently very large strains were generated in this area. In order to aleviate this a partially cylindrical boundary surface (boundary 12) was introduced joining the two plane surfaces and modelling a radius of curvature of 1mm as shown in figure 7.4.

The third problem concerned the constraining conditions used to ensure that the material continues to flow within the 18^{o} segment throughout the deformation process (see figure 7.6). Unfortunately, these constraining conditions also resulted in the outermost nodes in contact with the boundary planes moving out and violating the original segment constraining condition, as shown in figure 7.8. The two additional boundary planes marked 61 and 62 were introduced (figure 7.9) so that all the deformation was confined to the 18^{o} segment. Using this arrangement of boundary planes revealed yet another problem this time concerning the deformation of the friction layer. For the top row of elements, as shown in figure 7.4, the billet nodes are moved by the program onto the new boundary planes, so that the corresponding friction layer nodes move onto their secondary surfaces, two nodes on to plane 61 and two nodes onto plane 62. This meant that the friction layer elements had now no volume, all the nodes of each element being on the same plane. The stiffness of these friction layer elements could not be calculated, and the analysis failed.

If the boundary surfaces are renumbered so that the top die boundary surface is encountered after the boundary surfaces constraining the material to remain as an 18^{o} segment then the program will move the friction layer node onto the top die boundary surface. Again running

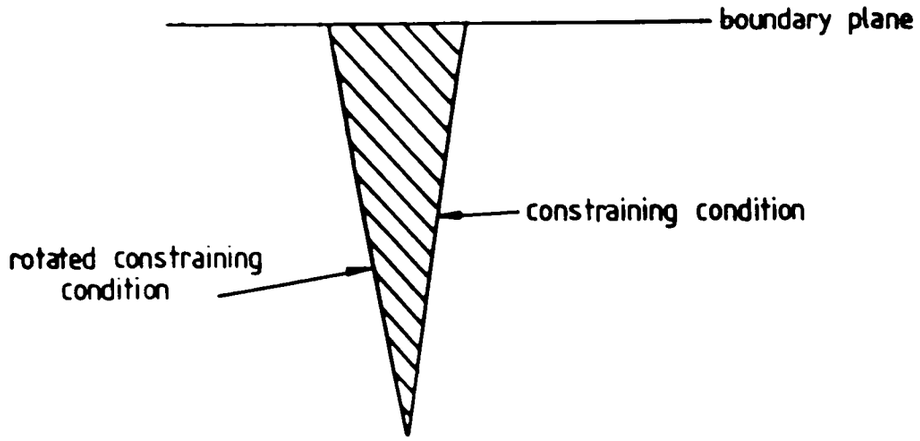

Figure 7.6

Intersecting boundary planes

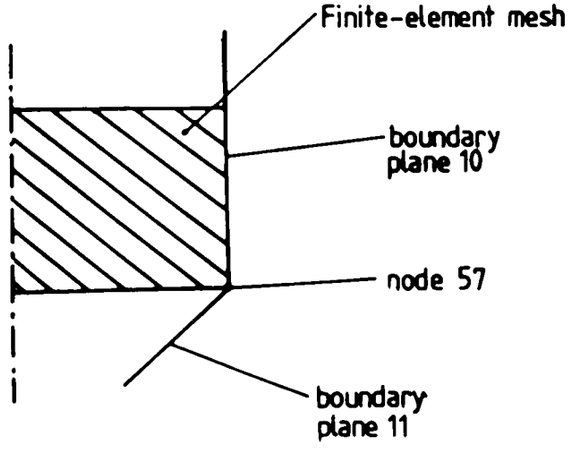

Figure 7.7

Position of the node at the intersection of boundary planes 10 and 11.

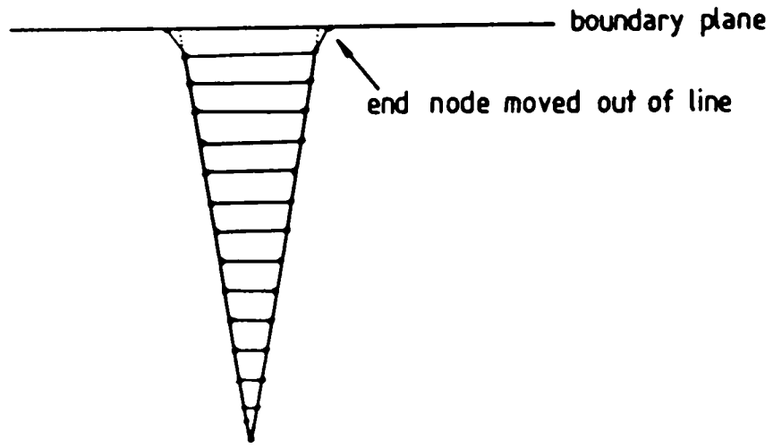

Figure 7.8

Violation of constraining conditions.

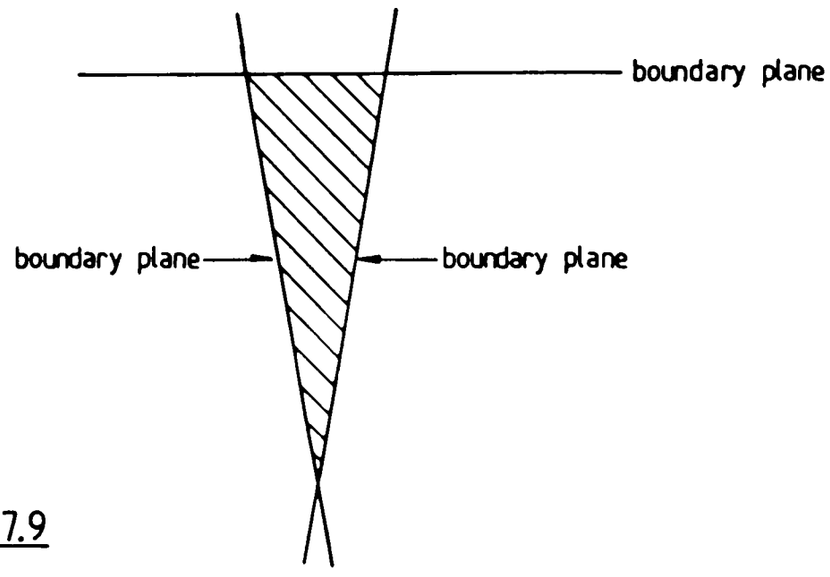

Figure 7.9

Segment showing additional boundary surfaces.

these data on the computer shows that this solution cures the problem for all but the leading edge of nodes which have no where else to go but the segment boundary surfaces, and the analysis fails again.

It would appear that the finite-element program, and in particular the friction layer technique, is not sophisticated enough to cope with multiboundary-surface problems and much work needs to be done on its development. For the purpose of this analysis the small lateral nodal movement (of the order of 0.1mm) of the top nodes away from the 18^{o} segment will unfortunately have to be tolerated.

This description of the problems found in the boundary surface specification illustrates the types of computational problems encountered in trying to model many metalforming analyses. This clearly illustrates that the original data specification for finite-element analyses of metalforming problems demands considerable time and effort. The finite-element analysis was eventually run until the same level of deformation at fracture as that found experimentally was reached.

7.4 Results and discussion.

7.4.1. Experimental Results.

As described in section 7.2 circular section rods of both 60-40 brass and 7075 aluminium alloy were extruded using dies to give the three different reductions in area of 34%, 61% and 77%. Photographs of the fractured specimens for 61% reduction in area are shown in figure 7.10. Figure 7.10(a) refers to 60-40 brass, while figure 7.10(b) refers to 7075 aluminium alloy. Fractures were found to have initiated on the outside surface of the specimen and grow towards its axis on an inclined plane. This mode of fracture is commonly referred to as 'fir-tree'

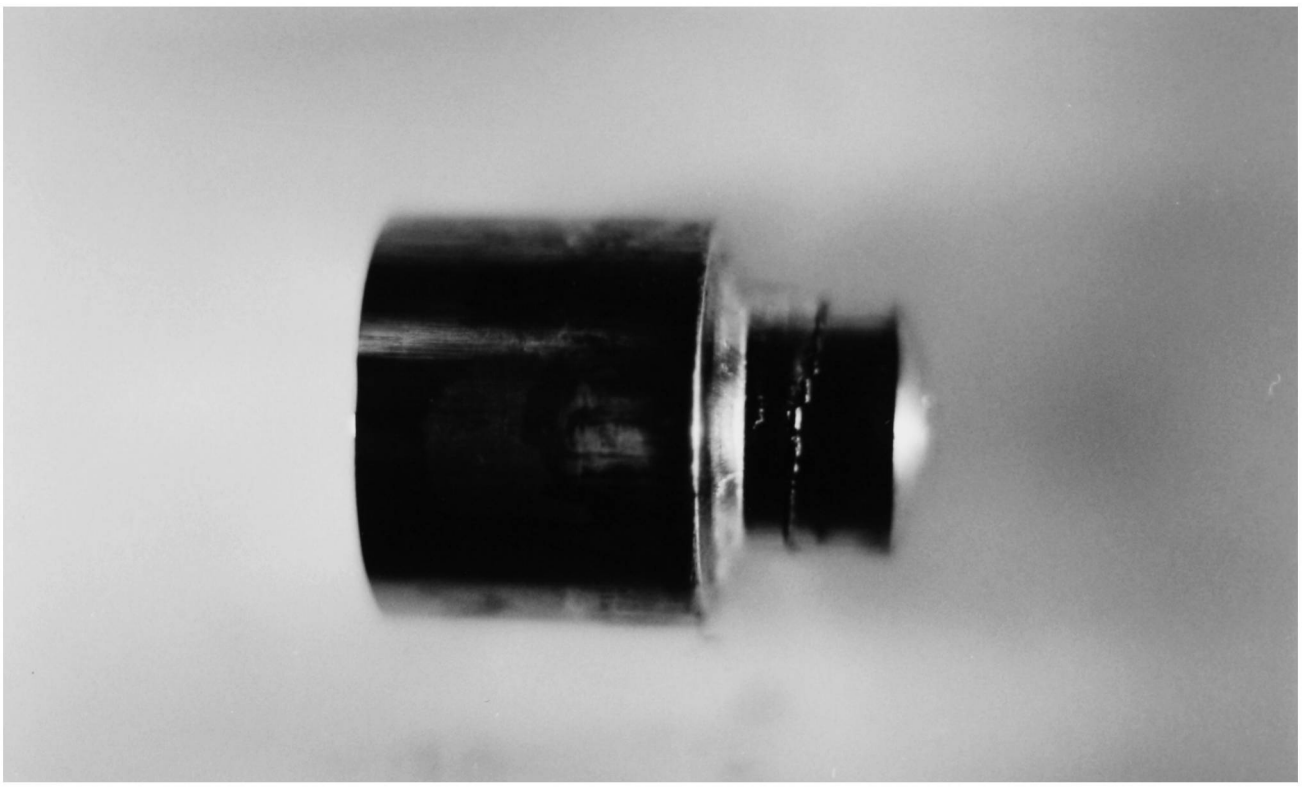

(a) 60-40 Brass

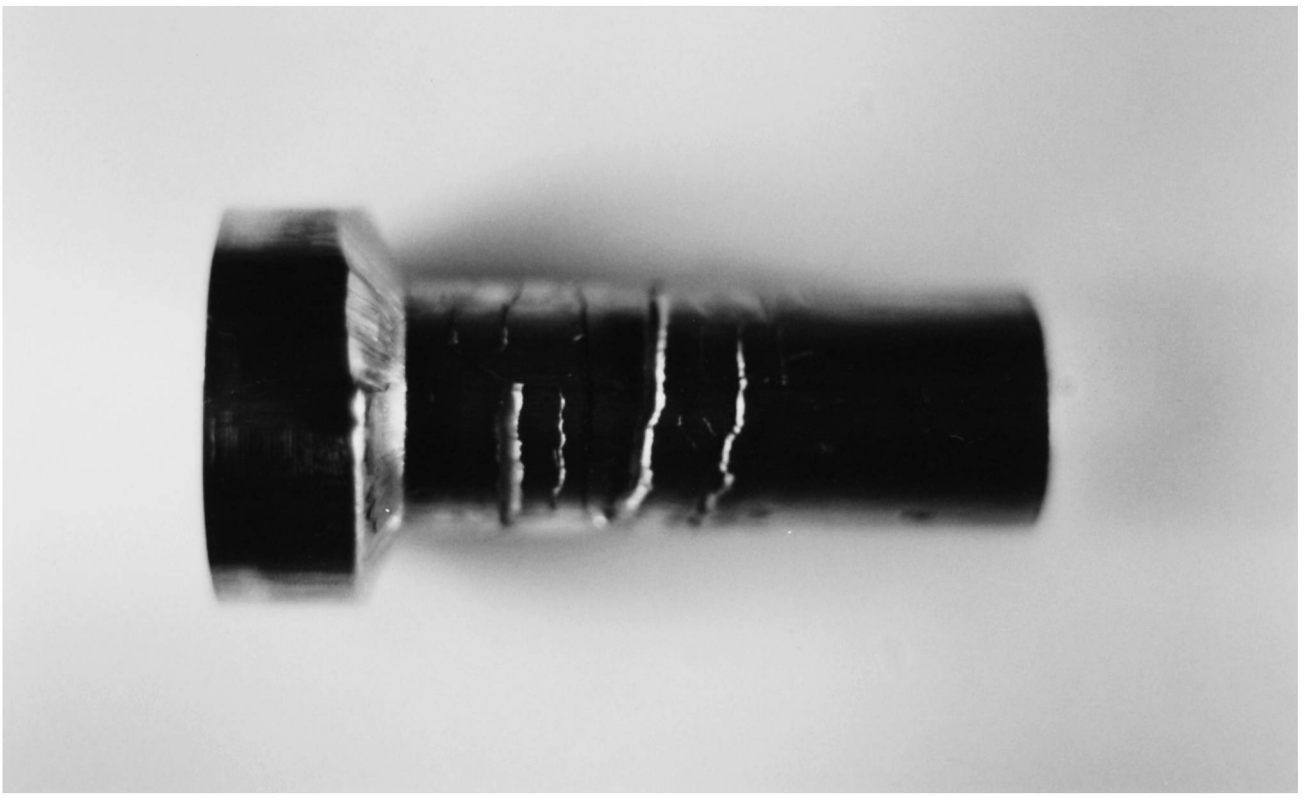

(b) 7075 aluminium alloy

Figure 7.10

Fir-tree cracking in extrusion.

cracking. A fully developed fracture therefore has a conical profile. All the specimens tested, that is both materials and the full range of reductions, cracked in this same mode. Several cracks were found on the outside surface of each specimen.

For the brass specimen the first crack was found to occur after approximately 10% of the length of the undeformed bar had been extruded. For 7075 aluminium alloy the corresponding deformation was 23%.

Figure 7.11 shows scanning electron microscope photographs of the fractured surfaces of both materials. These are characteristic of ductile fracture surfaces produced by shear.

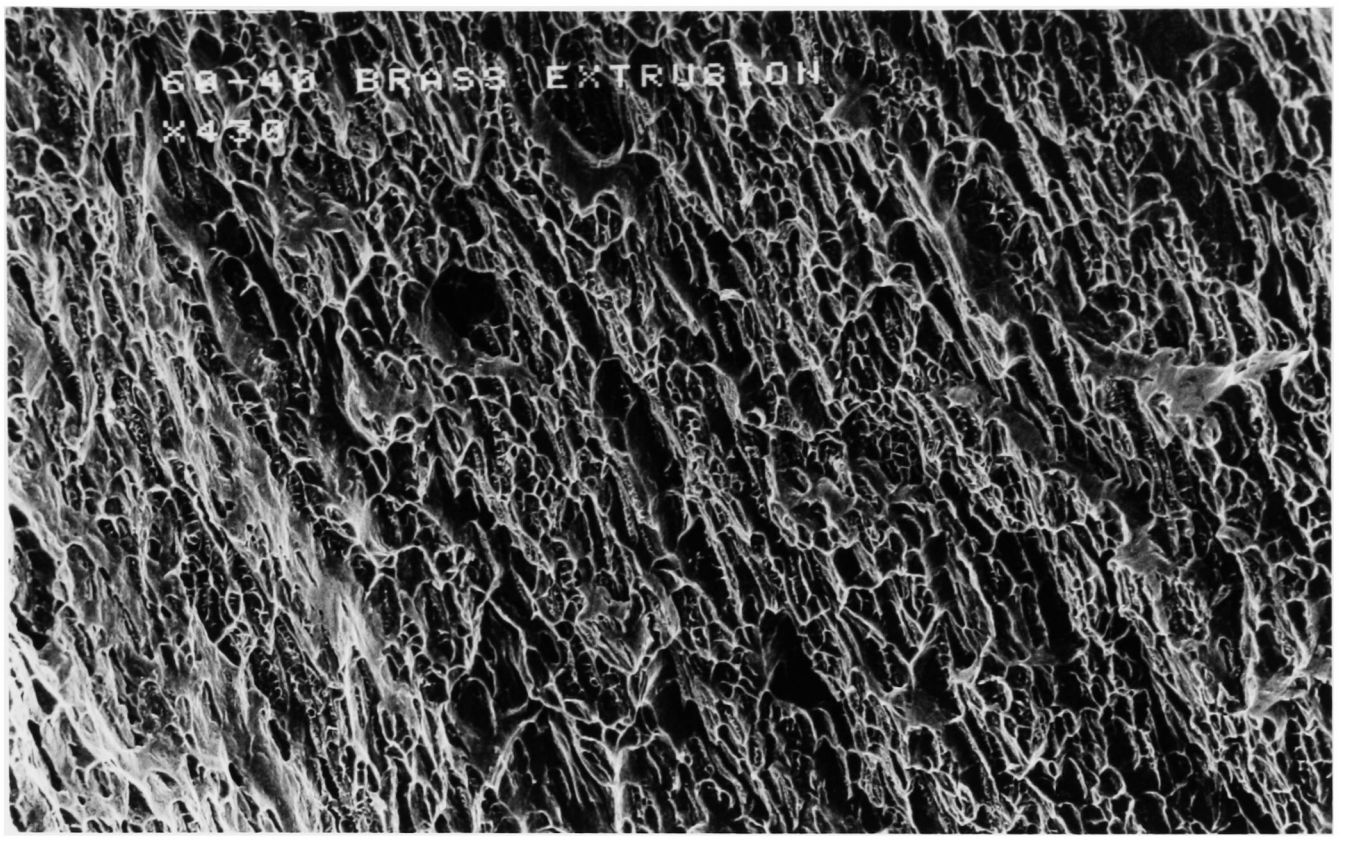

(a) 60-40 brass (x430)

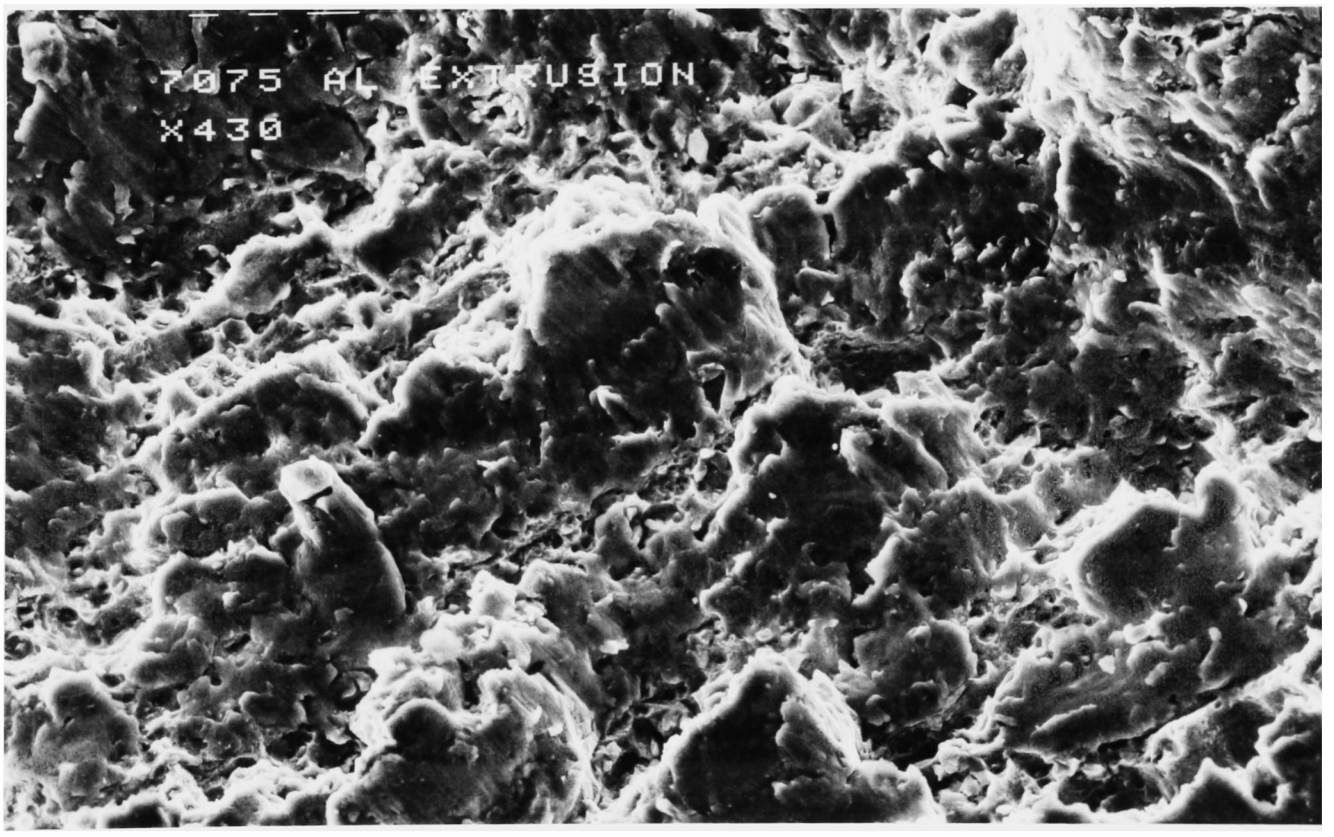

(b) 7075 aluminium alloy (x430)

Figure 7.11

Scanning electron microscope photographs of fracture surfaces in extrusion.

7.4.2 Finite-element results.

This section examines some of the deformation results produced by the finite-element analysis. The first of these concerns the way in which the plastic zone is initiated and develops as deformation proceeds. Results obtained for the axisymmetric extrusion of 60-40 brass and 7075 aluminium alloy are presented in figure 7.12. In each case the diagrams refer to only half of the complete specimen cross section. The percentage deformation figures by the side of each plastic zone diagram refer to the percentage of the original length of the bar which has been pushed past the entrance to the reduction die. The illustrations presented for both the materials are at corresponding levels of deformation, as far as the numerical technique will allow.

For 60-40 brass all the material directly in contact with the die and container has yielded by 0.9% deformation of the original bar. Thus for a complete billet these plastic zone results predict an outer sleeve of plastic material enclosing an inner core of elastic material. By 3.3% deformation the lower half of the billet, being that nearest to the reduction die entrance, behaves in a plastic manner leaving a region in the upper half of the billet, extending diagonally towards the die surface, to behave elastically. Later diagrams in the sequence show that this elastic region progressively gets smaller until at 8% deformation only a very small area in the top left hand corner of the model remains elastic. The pattern of plastic zone development is very similar for the 7075 aluminium alloy. However, this material tends to have a more localised plastic zone for a corresponding level of deformation. This is due to the difference in work hardening rates of the two materials: the 60-40 brass has the higher work hardening rate and therefore the more diffuse plastic zone.

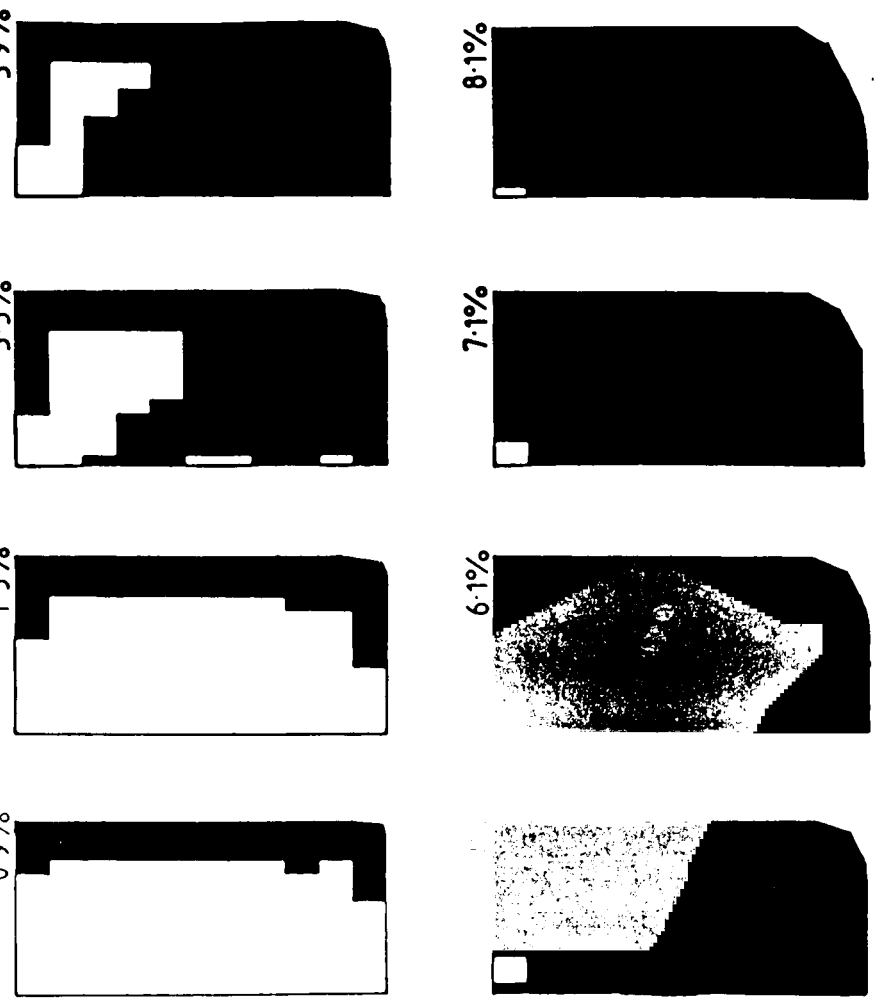

Figure 7.12(b)

Plastic zone development in the extrusion of 60-40 brass.

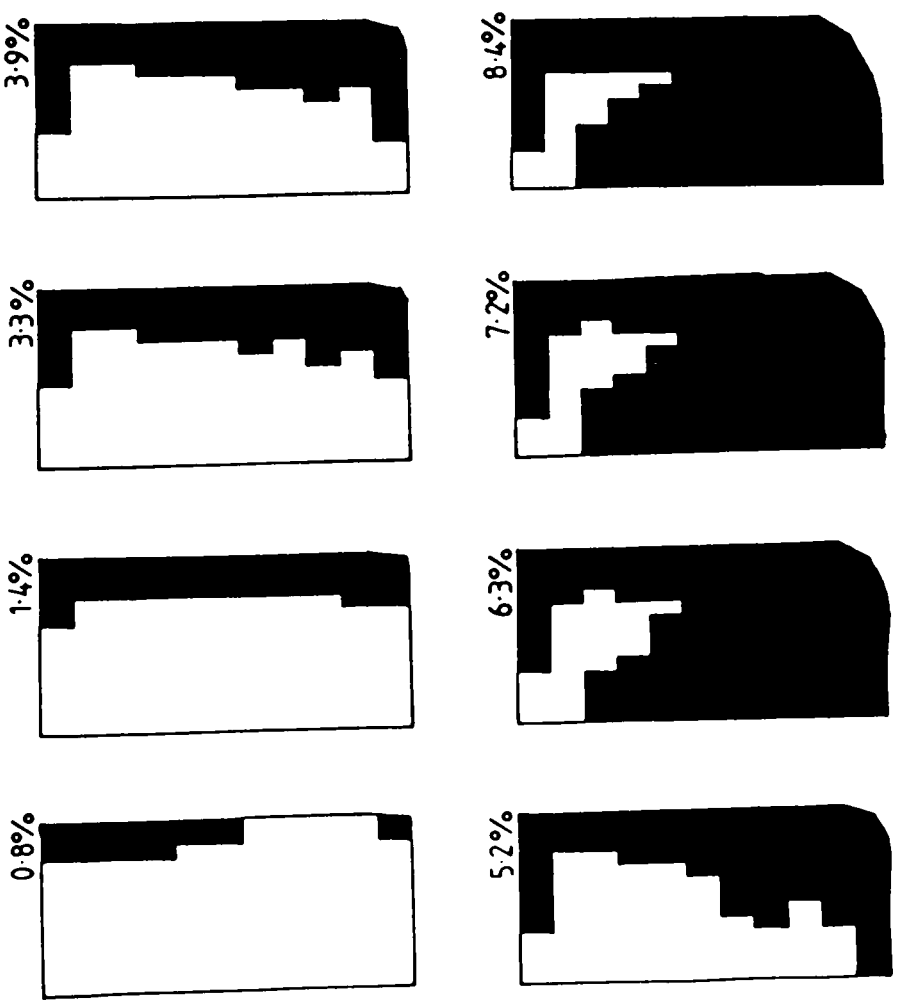

Figure 7.12(a)

Plastic zone development in the extrusion of 7075 aluminium alloy.

The incremental displacement vectors illustrate the direction and magnitude of the movement of a node during the latest increment of deformation. Deformation of the workpiece was simulated within the finite-element program by applying a specified displacement in the vertical direction to the end layer of nodes.

The automatic scaling of the graphics program means that the diagrams are not all drawn to the same scale, but the changes in the flow patterns which occur as the deformation proceeds may be identified.

The magnitude of the prescribed displacement during the increment of deformation being examined is shown by the arrows indicating movement of the top layer of nodes. All the arrows have been magnified by approximately four in order to make the flow trends more easily identifiable. Figure 7.13(a) presents these incremental displacement vectors for the extrusion of 60-40 brass. Instantaneous images of the pattern of metal flow at eight stages are shown, starting from the point where the billet model is at the entrance to the reduction die until just over 20% of the model has moved past the entrance of this die.

Deformation occurs first in the region of the model in contact with the reduction die and continues to be localised to this region until the die volume has been completely filled and the material is starting to be extruded from it. A dead zone then develops along this die around which material flows. This dead zone formation subsequently allows a much smoother flow path.

As figure 7.13(b) shows, the flow pattern for the extrusion of 7075 aluminium alloy is very similar to that of 60-40 brass; the incremental displacement vectors for axisymmetric extrusion presented here do not show any differences between the metal flow patterns for 60-40 brass and 7075 aluminium alloy.

The distorted grids are given in figure 7.14. Axonometric views of the finite-element mesh are given at six different levels of

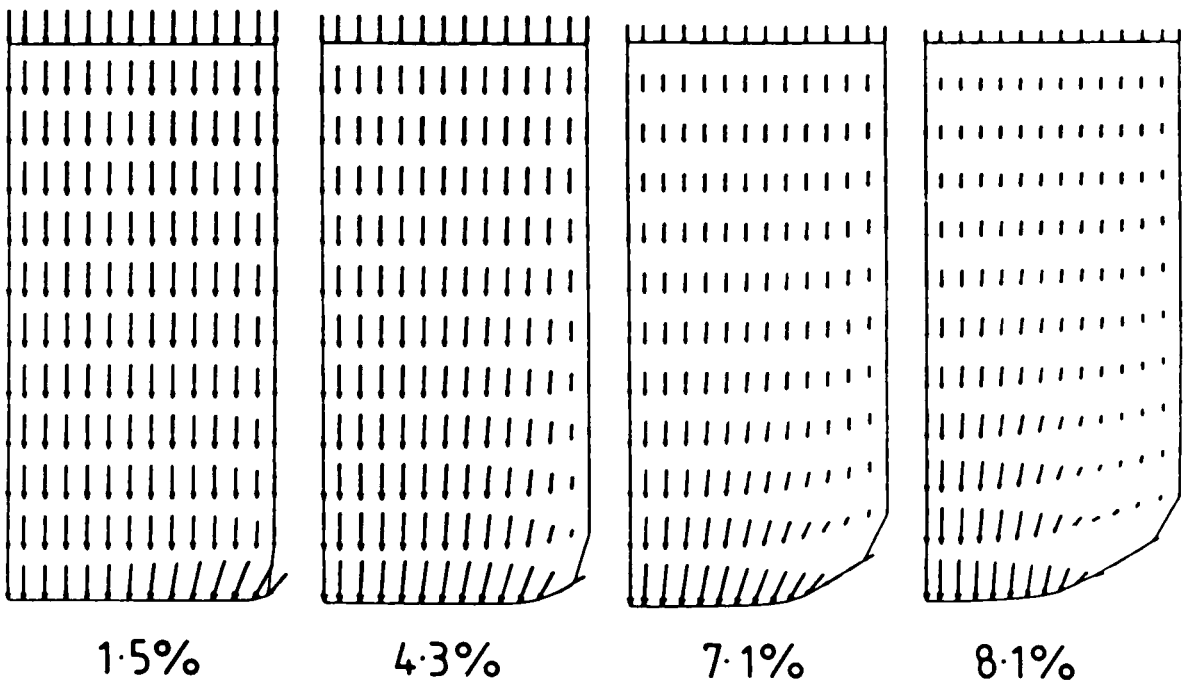

Figure 7.13(a)

Incremental displacement vectors for the extrusion of 60-40 brass.

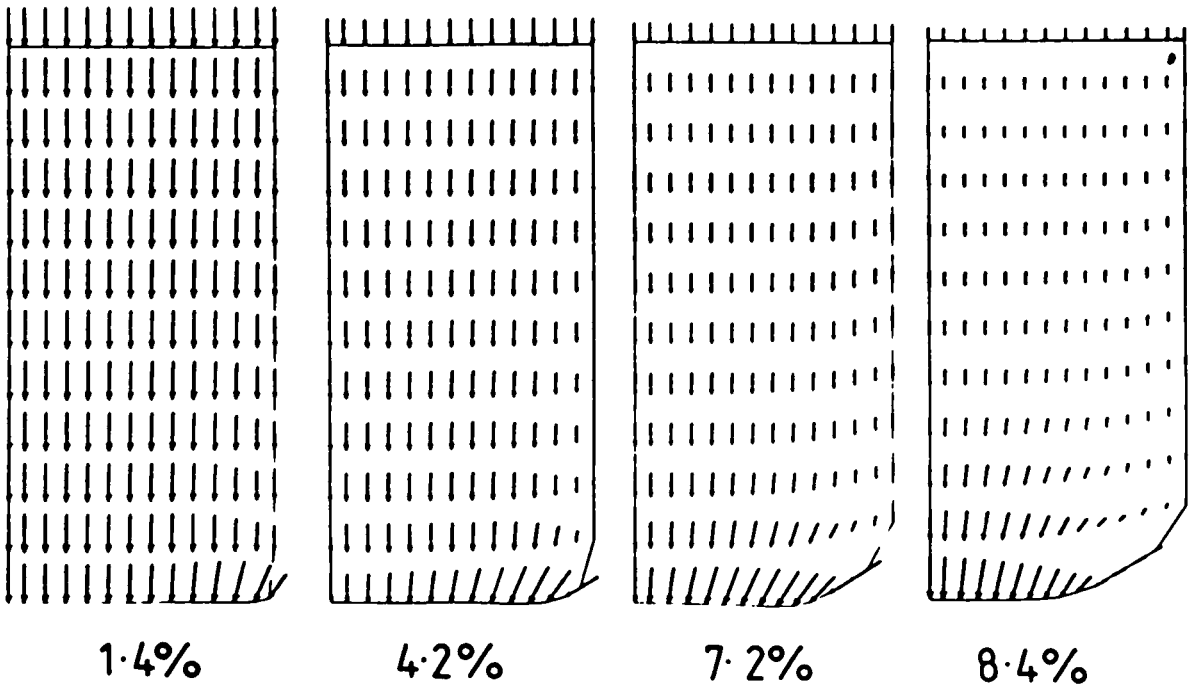

Figure 7.13(b)

Incremental displacement vectors for the extrusion of 7075 aluminium alloy.

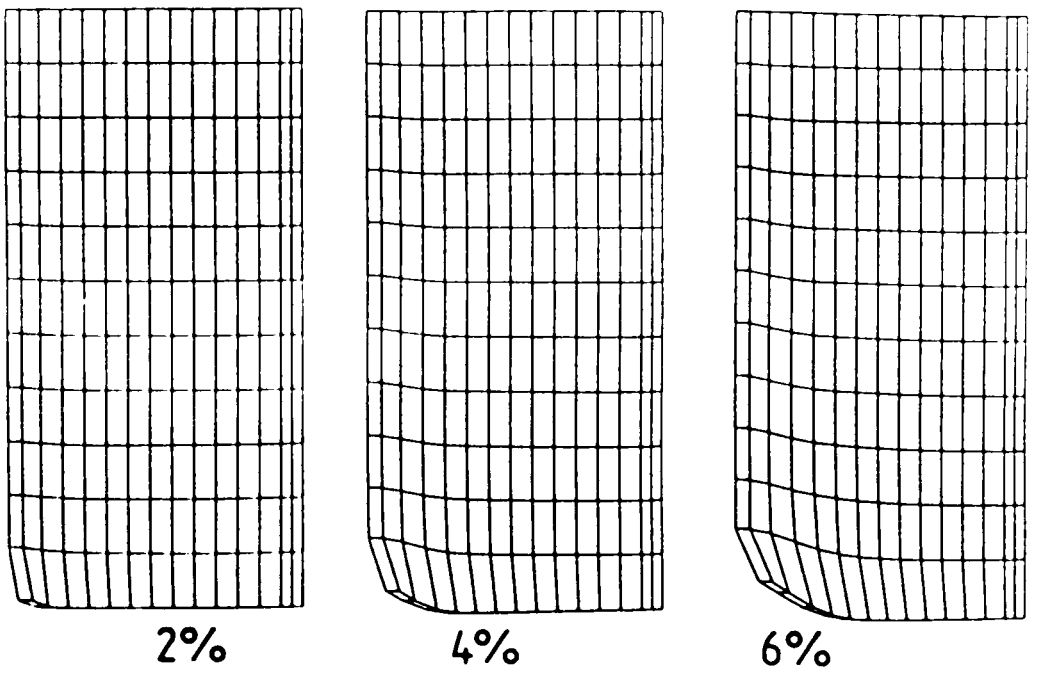

Figure 7.14 (a)

Distortion of the finite-element grids in the extrusion of 60-40 brass.

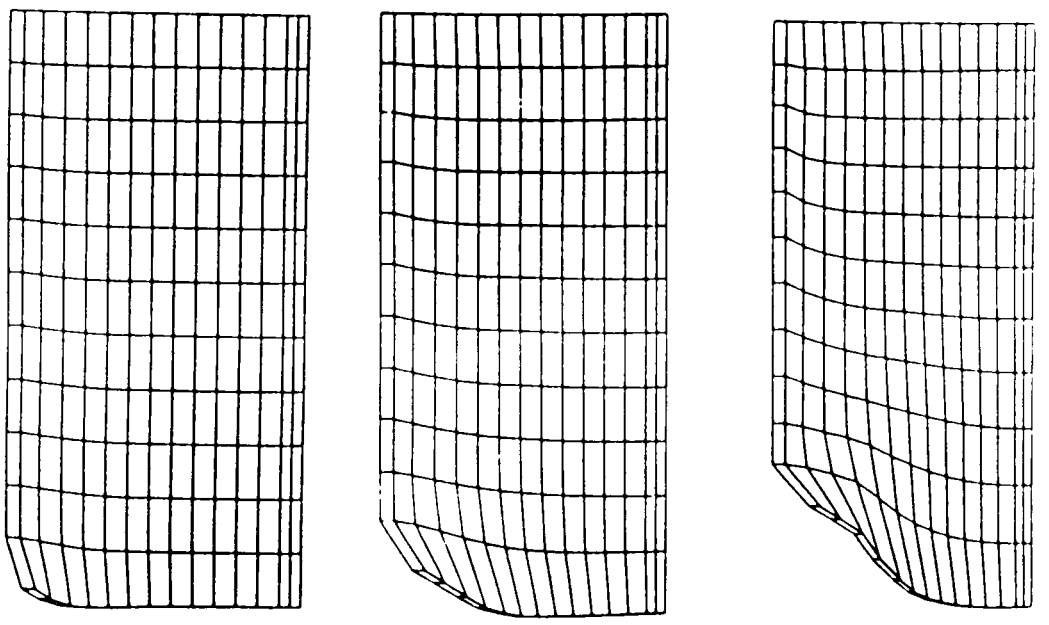

Figure 7.14(b)

Distortion of the finite-element grids in the extrusion of 7075 aluminium alloy.

deformation. The final illustration in each sequence is at the reduction at which fracture was observed in the parallel sequence of experimental tests. As would be expected, the finite-element grids for both materials become most heavily distorted in the region around the reduction die. For 7075 aluminium alloy the distortion at the experimental reduction at fracture is correspondingly more severe because of the higher value of this reduction.

Finally, figure 7.15 shows the finite-element axial stress distributions at the experimental level of deformation at fracture for both the materials studied. For 60-40 brass the axial stress is compressive throughout the mesh with the highest stress in the right hand corner, being the periphery of the surface of the billet model. The axial stress levels fall towards the die exit. Due to the higher level of deformation at fracture of 7075 aluminium alloy the axial stress levels are very much higher than for 60-40 brass. As figure 7.15(a) shows very high tensile axial stresses are present near the reduction die exit. Some tensile stress remains in the extrudate.

A similarly located transition from compressive to tensile stresses in extrusion has also been observed in the elastic-plastic finite-element results of Tekkaya and Roll (1984) previously presented in figure 1.22.

This section has contained some of the results produced in the finite-element analysis of rod extrusion. No direct comparisons with experimental results are available, although in the case of the axial stress distributions for 7075 aluminium alloy the same trends have been observed in previously published results. However, all the results presented here do serve to illustrate the flexibility of the finite-element approach.

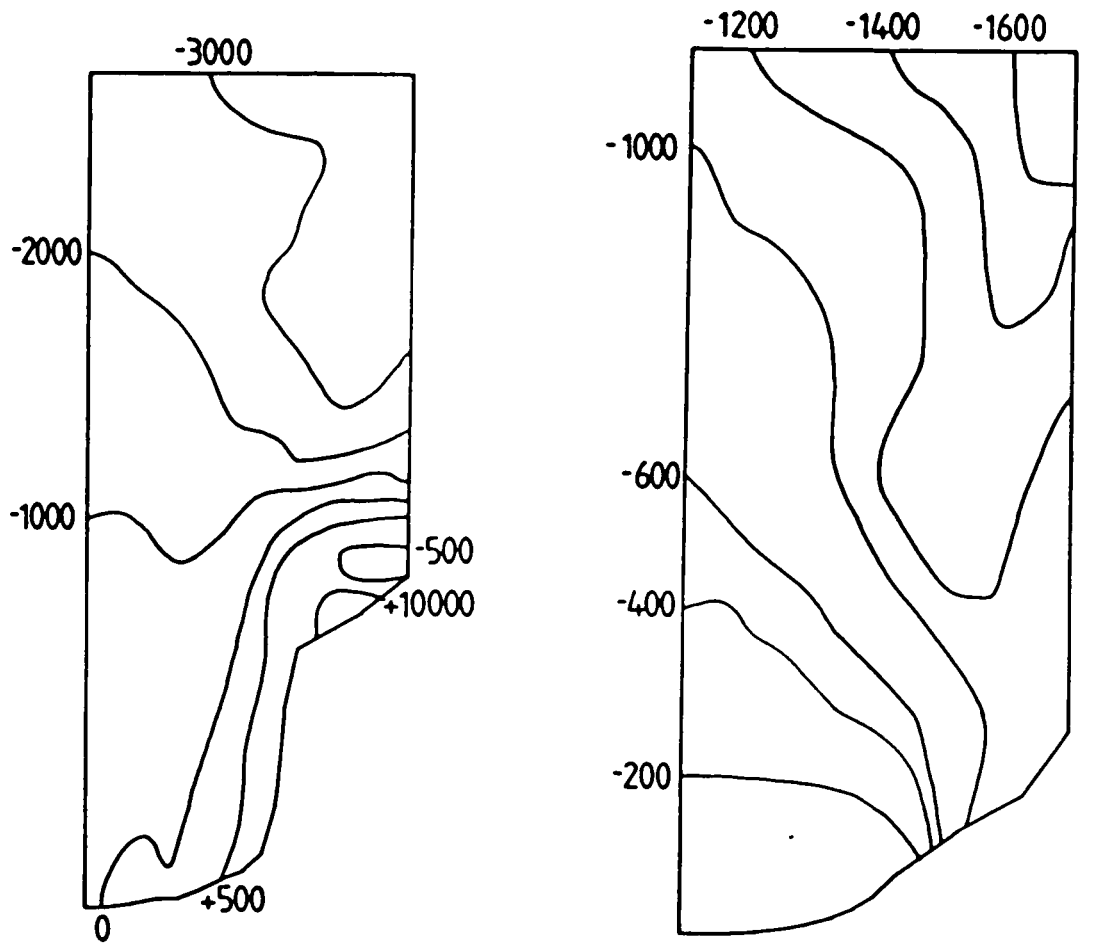

(a) 7075 Aluminium alloy 23% deformation

(b) 60-40 Brass 10% deformation

Figure 7.15

Finite-element axial stress distributions (σ_x) for axisymmetric extrusion at the experimental level of deformation at fracture.

(Units: MN/m^2)

7.4.3 Assessment of various fracture criteria.

By using the finite-element program in conjunction with the fracture accumulation program, as previously described in section 4.5.2, numerical predictions of the fracture initiation site in the axisymmetric extrusion of 60-40 brass and 7075 aluminium alloy were obtained by finding the node in the mesh at which the accumulated value of each fracture criterion was a maximum at the level of deformation at fracture found experimentally. These predicted sites were then compared with the experimental crack initiation site and the results presented in Table 7.1 were arrived at. A tick indicates that the experimentally and numerically predicted sites of fracture initiation agree; a cross that they disagree.

The numbers displayed in the bottom right hand corner of each table element refer to the node at which fracture initiation was predicted to occur. The location of these nodes is given in the deformed mesh diagrams in figure 7.16. For the McClintock and Atkins criteria predictions can also be made of the plane of fracture. These are displayed in the top left hand corner of the appropriate table elements. From this table it may be seen that seven of the criteria examined successfully predict the experimental fracture initiation site for both the materials considered, these criteria being due to McClintock (1968), Cockroft and Latham (1968), Brozzo et al (1972), Oyane et al (1980), Atkins (1981) and the critical values of generalised plastic strain and work. The fracture criterion of Norris et al (1978) exhibits partial agreement with the experimental results, that is it predicts the correct fracture site for the extrusion of brass but not for the aluminium alloy. The remaining criteria examined, being those due to McClintock et al (1966) and Ghosh (1976) did not show any agreement at all with the experimental results.

criterion / specimen	McClintock (1968)	McClintock et al (1966) (shear)	Ghosh	Oyane	Cockroft and Latham	Brozzo	Gen. plastic strain	Gen plastic work	Norris	Atkins
60-40 brass	zr √ 40	θz × 202	× 350	√ 37	√ 51	√ 38	√ 53	√ 53	√ 85	rθ √ 53
7075 Al	rθ √ 41	rθ × 322	× 329	√ 41	√ 40	√ 41	√ 40	√ 40	× 226	rθ √ 40

Table 7.1

Comparison of FE predictions of fracture initiation site and experimental results for the extrusion of 60-40 brass and 7075 aluminium alloy.

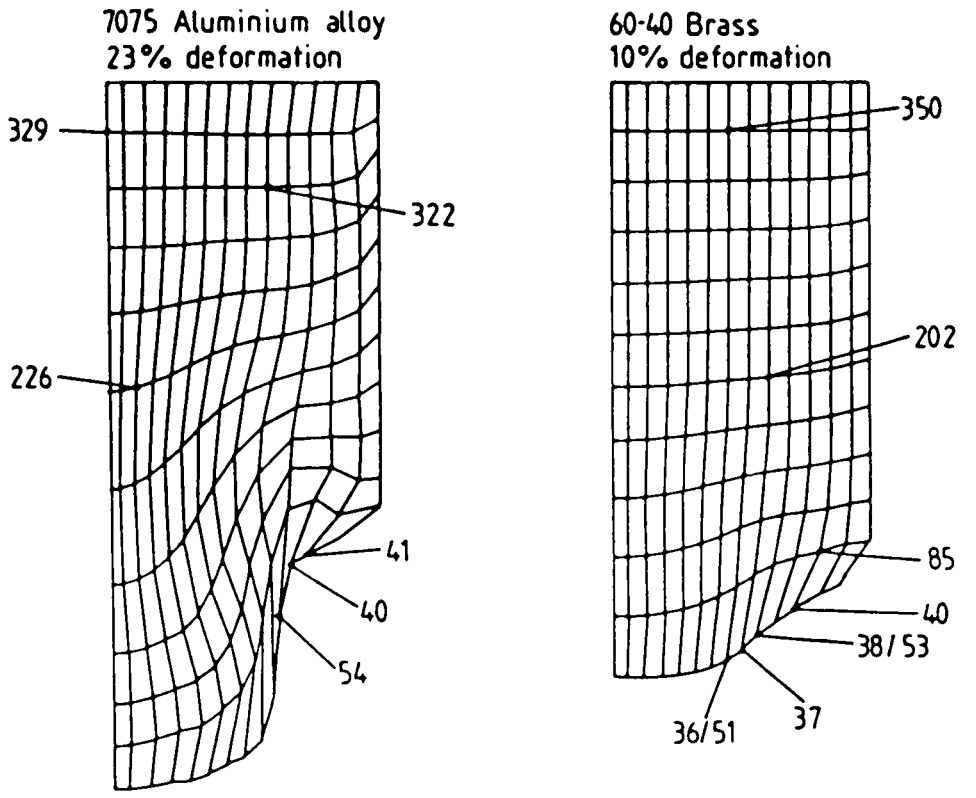

Figure 7.16

Deformed FE grids at the experimental level of deformation at fracture.

Experimentally, fractures occurred on the r-theta plane, as successfully predicted by the Atkins criterion for both the materials studies here. The criterion of McClintock (1968) predicts the correct fracture plane for the aluminium alloy but not for the brass, while that due to McClintock and co-workers (1966) does not produce any correct fracture plane predictions.

As with the results presented in previous chapters, an experimental determination of the value of generalised plastic work, generalised plastic strain and tensile plastic work at fracture was made using an axisymmetric tensile test. The results relating to 60-40 brass as presented in section 4.2.2 may be used here, but a new determination relating to 7075 aluminium alloy needed to be made due to the difference in methods by which the stock was produced.

The predicted and experimental values of tensile plastic work for both materials have been compared and are presented in figure 7.17. For the extrusion of 60-40 brass, fracture was found to occur experimentally after approximately 10% of the length of the undeformed bar had been extruded past the reduction die entrance. As figure 7.17(a) shows the tensile test value of tensile plastic work at fracture greatly overestimates the deformation found experimentally. For 7075 aluminium alloy, where 23% of the length of the undeformed bar had been extruded past the entrance to the reduction die, the opposite situation has been found, as figure 7.17(b) shows the tensile test value considerably underestimates the deformation obtained experimentally.

Comparisons of the predicted and experimental levels of deformation at fracture for the generalised plastic work fracture criterion are given in figure 7.18 and for the generalised plastic strain criterion in figure 7.19. As reported in the previous results chapters the generalised plastic work and strain criteria produce the same predictions. Figures 7.18(a) and 7.19(a) refer to 60-40 brass where the

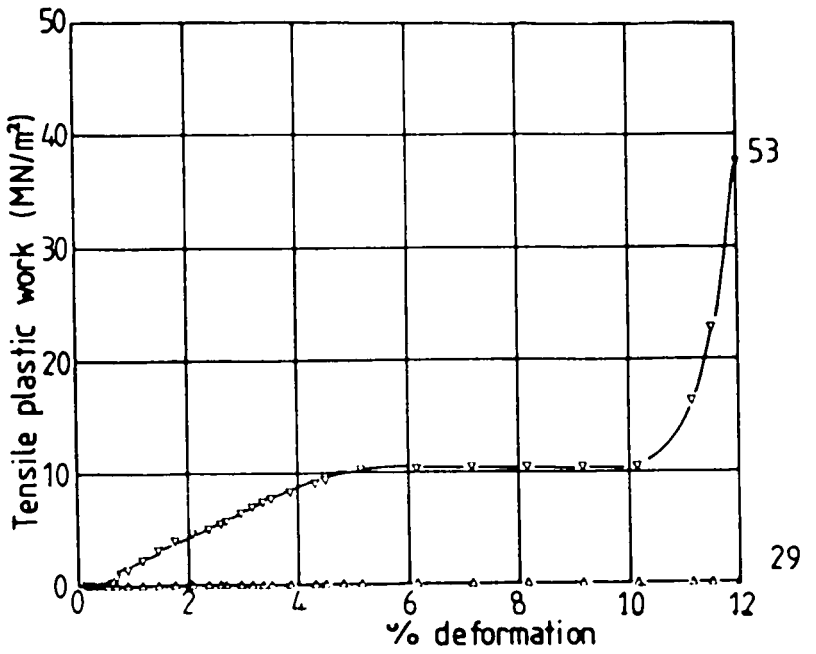

Figure 7·17(a).

Numerical calculation of the Cockroft and Latham fracture criterion for the extrusion of 60-40 brass from FE results for nodes 29 and 53.

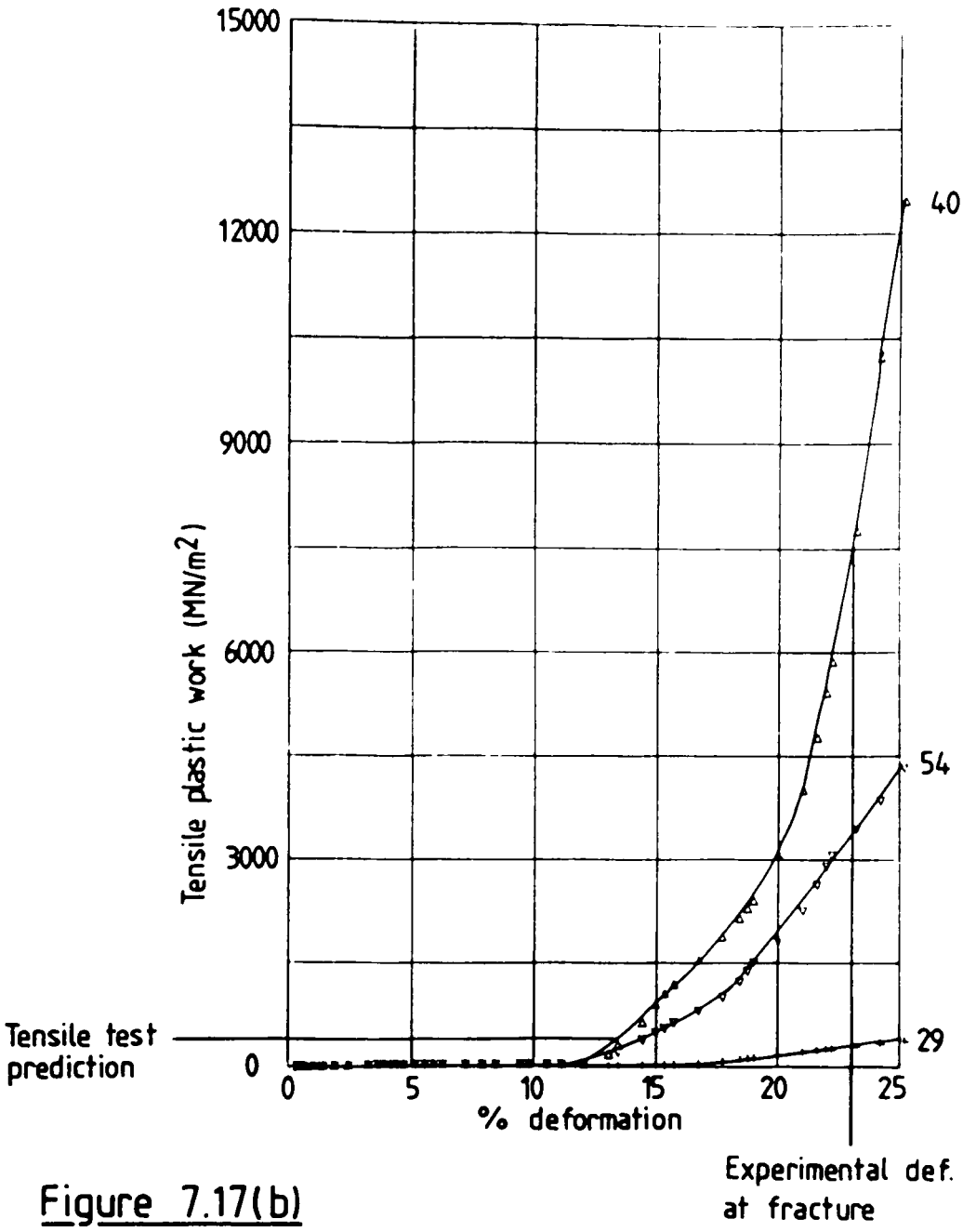

Figure 7.17(b)

Numerical calculation of the Cockroft and Latham fracture criterion from FE results for the extrusion of 7075 aluminium alloy for nodes 29, 40 and 54.

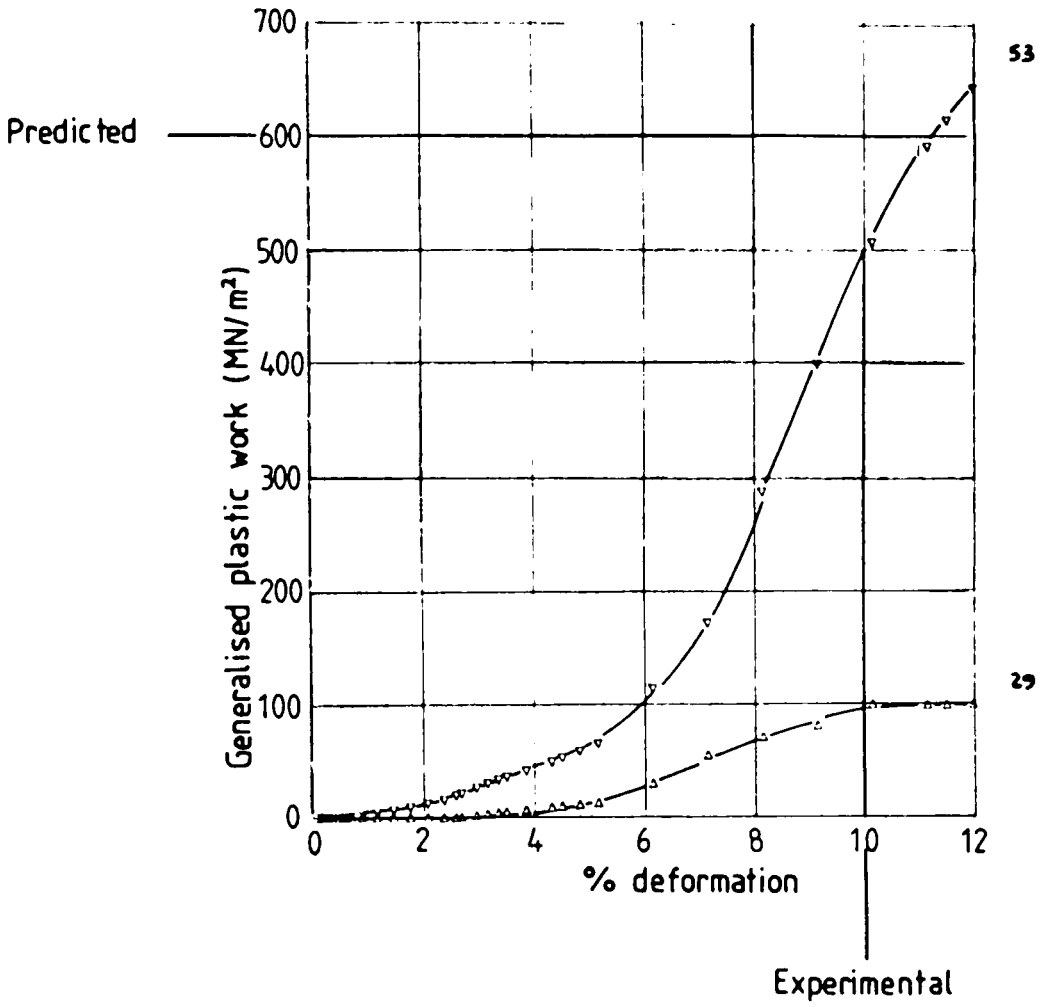

Figure 7·18(a).

Numerical calculation of the generalised plastic work fracture criterion for the extrusion of 60-40 brass from FE results for nodes 29 and 53.

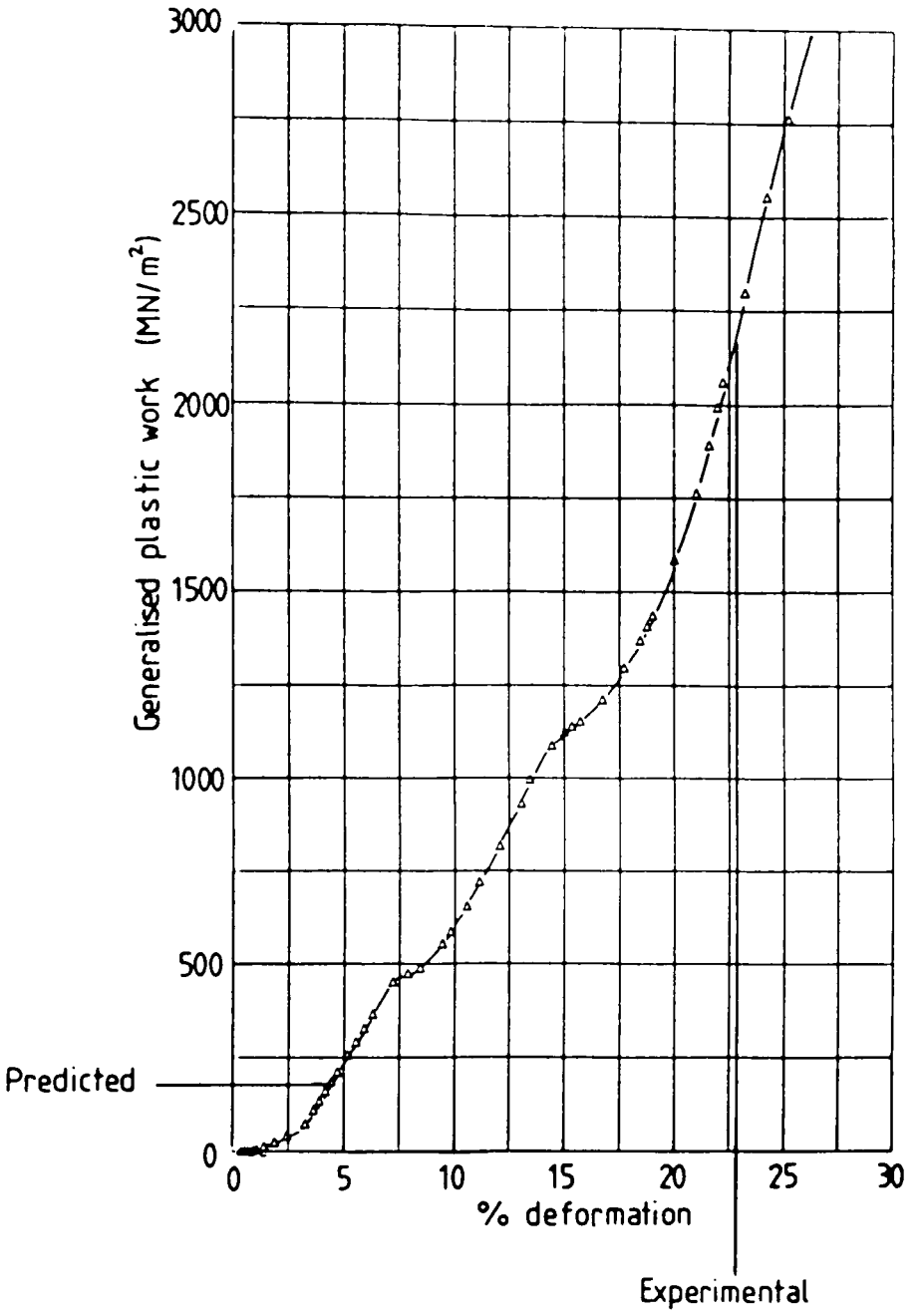

Figure 7·18(b).

Numerical calculation of the generalised plastic work fracture criterion for the extrusion of 7075 aluminium alloy from FE results for node 40.

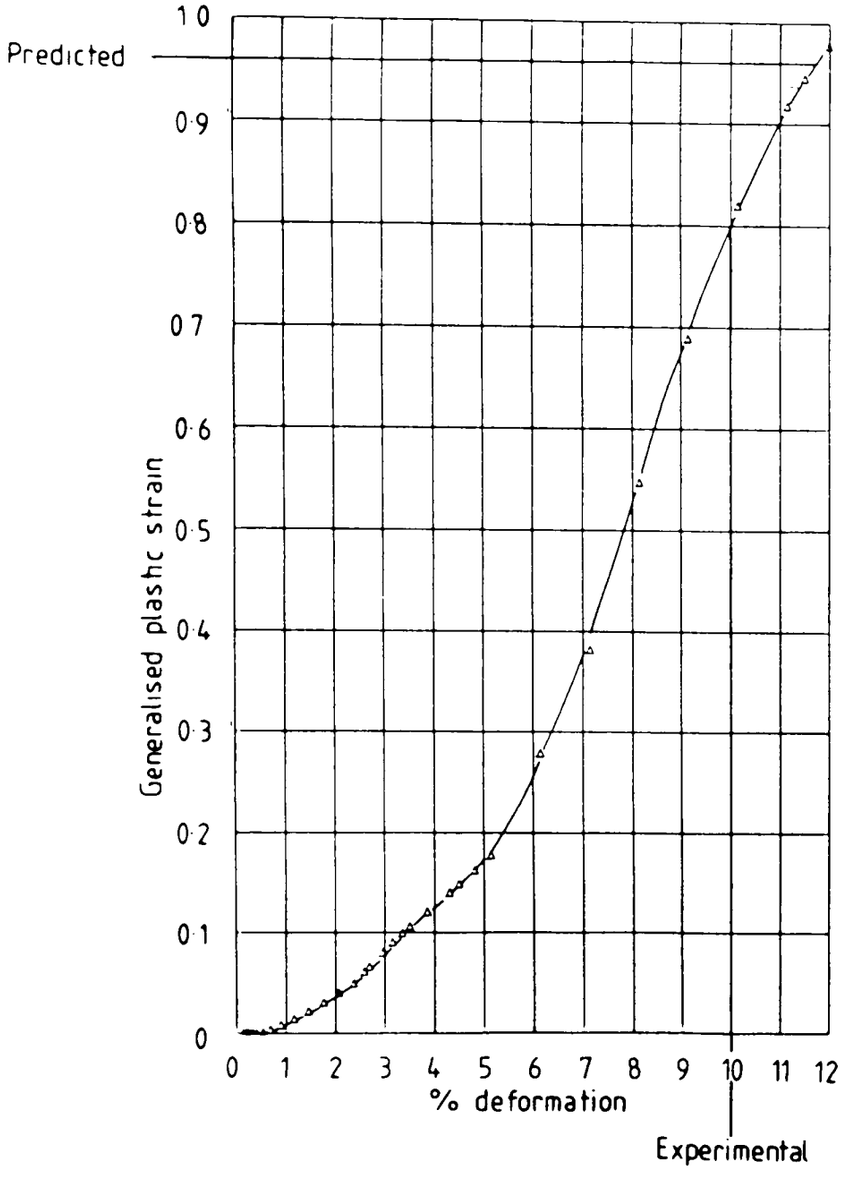

Figure 7.19(a)

Variation of FE generalised plastic strain for the extrusion of 60-40 brass (node 53)

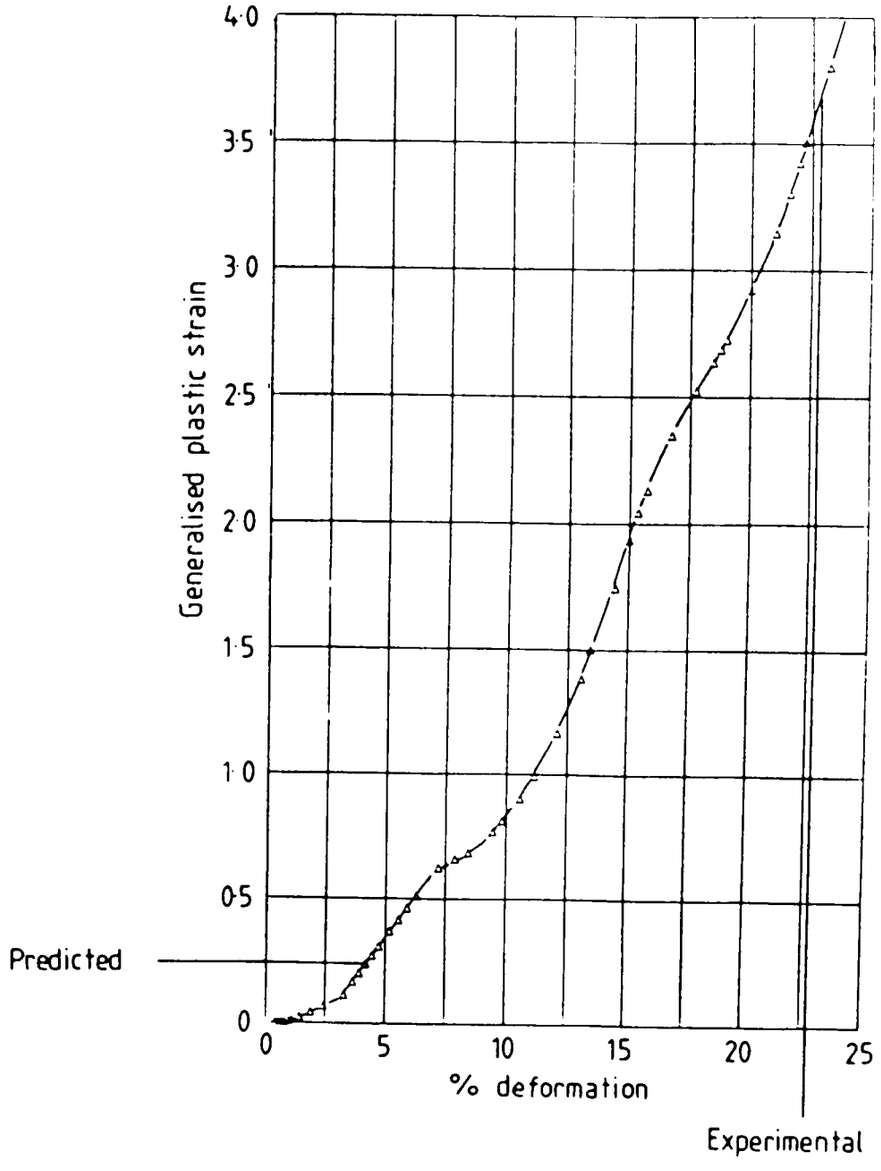

Figure 7.19(b)

Variation in FE generalised plastic strain for the extrusion of 7075 aluminium alloy for node 40.

tensile test value and the finite-element values are in very good agreement. However, the predictions are not so good for the extrusion of 7075 aluminium alloy (Figures 7.18(b) and 7.19(b)). Here, as with the prediction of tensile plastic work, the tensile test value of generalised plastic strain/work at fracture considerably underestimates the deformation found experimentally. One very important limitation of using the critical value of generalised plastic strain/work as a fracture criterion is that it does not take into account variations in hydrostatic stress which are well known to influence the onset of fracture (as classically described by Bridgman (1952)).

Figure 7.20 shows the finite-element hydrostatic stress distributions at the experimental level of deformation at fracture. For 60-40 brass, where good agreement with the generalised plastic strain/work predictions has already been found, the hydrostatic stress is compressive throughout the mesh and varies from -1600 MN/m^2 at the top end to -400 MN/m^2 in the region near the die exit. However, the situation is very different for 7075 aluminium alloy where the tensile test value considerably underestimates the deformation found experimentally. Here the hydrostatic stress distribution in figure 7.20(b) shows that high tensile hydrostatic stresses are experienced by material along and emerging from the reduction die. Figure 7.21 presents the variation in hydrostatic stress with level of deformation calculated in the finite-element analysis. The node at which the generalised plastic work criterion predicts fracture will be initiated experiences a compressive hydrostatic stress up to approximately 13% deformation after which, as the graph shows, the calculated values increase very rapidly to give a value of +7000 MN/m^2 at 23% reduction.

Comparison of the fracture results from extrusion with the value of generalised plastic strain/work calculated in a simple tensile test may therefore not be very meaningful.

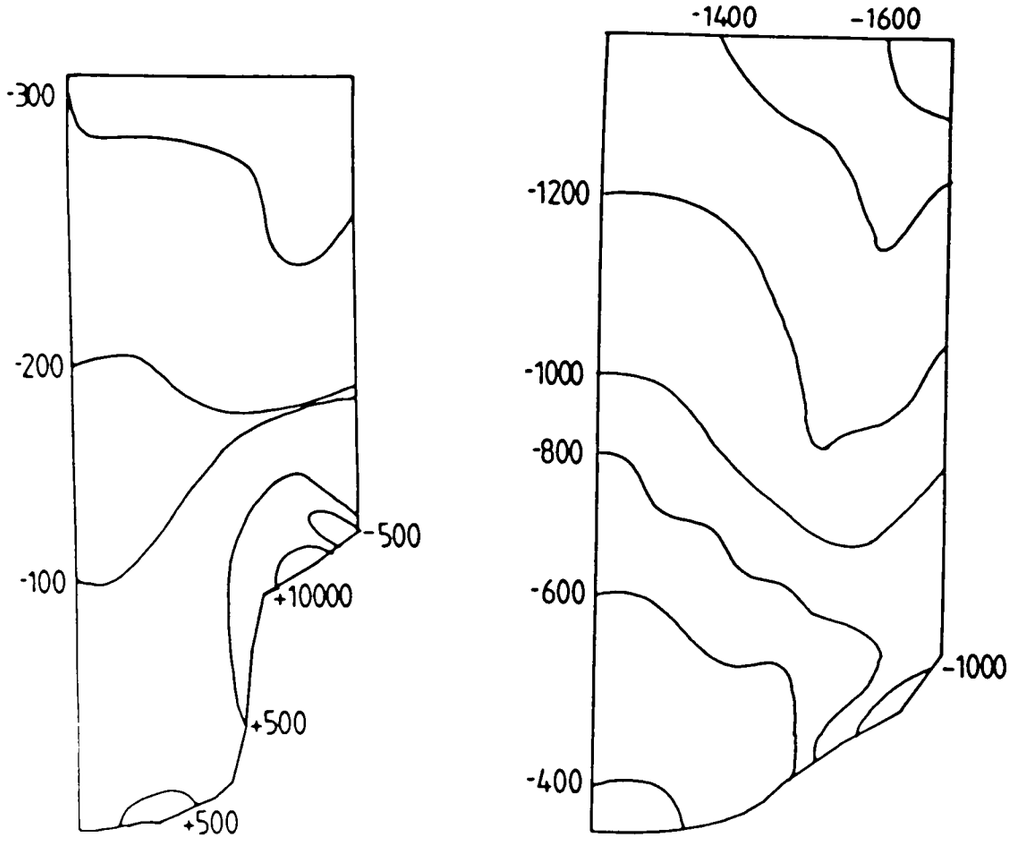

(a)
7075 Aluminium alloy
23% deformation

(b)
60-40 Brass
10% deformation

Figure 7.20

Finite-element hydrostatic stress distributions for axisymmetric extrusion at the experimental level of deformation at fracture.

(Units. MN/m^2)

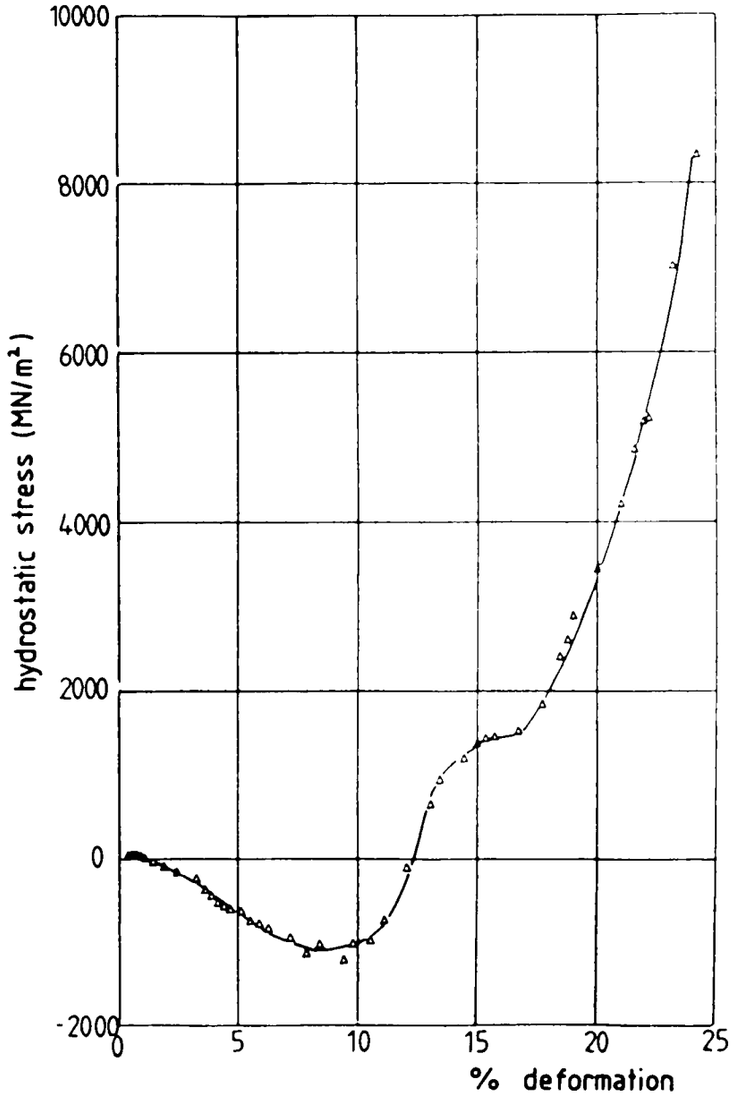

Figure 7·21.

Variation of hydrostatic stress in the extrusion of 7075 aluminium alloy (node 40).

The differences in the level of deformation at fracture predictions found here are further examined in chapter 8.

7.5 Conclusions.

The occurrence of fir tree cracking found experimentally in the extrusion of 60-40 brass and 7075 aluminium alloy rod has been compared with predictions from a number of published continuum fracture criteria. Seven of the criteria examined successfully predict the fracture initiation site, being those due to McClintock (1968), Cockroft and Latham (1968), Brozzo et al (1972), Oyane et al (1980), Atkins (1981) and the critical values of generalised plastic strain and work at fracture.

The generalised plastic strain and work criteria have successfully predicted the level of deformation at fracture for brass, but not for the aluminium alloy. These predictions are considered further in Chapter 8.

Chapter 8.

Discussion.

8.1 Introduction.

In this thesis experimental and numerical analyses for a number of simple metalforming operations have been conducted. The numerical results, produced by finite-element analysis, have been used to give predictions of fracture initiation site, for a total of ten previously published fracture criteria. These site predictions have been compared with experiment. For the generalised plastic strain and work, and Cockroft and Latham criteria, predictions of the level of deformation at fracture have also been examined. This chapter presents a summary of all the analyses and experiments. Section 8.2 looks at the complete set of fracture site predictions and section 8.3 explores the influence of hydrostatic stress in an attempt to identify causes of some discrepancies observed between experiment and theoretical predictions. Finally, section 8.4 presents the conclusions of this chapter.

8.2 Fracture Initiation Predictions.

Table 8.1 contains a summary of the success and failure of each of the fracture criteria in predicting the fracture site for all the simple metalforming operations examined in this thesis. Only the generalised plastic strain and generalised plastic work criteria successfully predict the experimental fracture initiation site for all the geometries considered.

On the basis of the work presented here it does not appear possible to distinguish between generalised plastic work and generalised plastic strain as a fracture criterion. Not only do they produce the same site predictions, but also the same level of deformation at fracture

	Model	McClin (1968)	McClin (1966)	Ghosh	Oyane	Cockroft and Latham	Brozzo	Work and strain	Norris	Atkins
Side-pressing	Brass circular					√	√	√		
	7075 circular					√	√	√		
	7075 H/W=1·33							√		√
	7075 H/W=2·03							√		√
Upsetting	H/D = 0·5		√	√	√	√	√	√	√	
	H/D = 1·0	√	√	√	√		√	√		
	H/D = 1·5	√	√		√	√	√	√		
	H/D = 2·0	√	√	√			√	√		
Strip	Compression			√	√	√	√	√	√	√
	Milled	√		√	√	√	√	√	√	√
	Forged							√		
Extrusion	7075	√			√	√	√	√		√
	Brass	√			√	√	√	√		√

Table 8.1

predictions, as the results in previous chapters have indicated. This is because both parameters are linked by the material stress-strain curve; if generalised plastic strain has been increased then so must work be increased by a related amount, and vice versa, so that both always give the same predictions.

Table 8.1 shows the wide agreement obtained for a range of fracture criteria particularly for simple upsetting. This may be due to the rapid propagation of the crack observed in these experiments, which made it impossible to identify the fracture initiation site. A theoretical prediction was therefore deemed correct if it indicated a free surface fracture.

Predictions based on the void growth fracture criteria, being those due to McClintock, Kaplan and Berg (1966), McClintock (1968), Ghosh (1976) and Oyane et al (1980), have not shown widespread agreement with the experimental fracture initiation sites.

The experimental results presented here suggest that both the 60-40 brass and the aluminium alloy exhibit a high initiation strain and a high rate of crack propagation. (Confirmation of this has been found in the literature for 7075 aluminium alloy (Broek, 1973)). This has been suggested by the generally good agreement with the energy arguments for crack initiation, and why those criteria based on hole growth have been generally unsuccessful. These criteria are based on voids being present in a body before deformation commences and thus having zero initiation strain, and modelling how the voids grow as deformation proceeds. They are therefore applicable to materials with a low initiation strain so voids are present very early in the deformation sequence, and a low rate of crack propagation, so that the growth phase is the important one.

The tensile plastic work criterion of Cockroft and Latham (1968) has produced good agreement with experiment where large tensile stresses have been present, as in the central region of the initially circular

section plane-strain side-pressed specimens. However, it has been unsuccessful where the contribution to the plastic strain/work integral due to compressive stresses has been found to be important, as for example in the plane-strain side-pressed specimens initially with machined flats.

The fracture criterion due to Brozzo et al (1972), a modification of the Cockroft and Latham criterion to incorporate the effect of hydrostatic stress, has been slightly, but not significantly, more successful.

The fracture initiation site predictions from the Norris et al (1978) and Atkins (1980) fracture criteria, which contain an explicit dependence on strain increment ratios, have not been very successful. However, it has been shown that generalised plastic work contains an implicit dependence on the strain increment ratio history (Atkins and Mai, 1985) and it may be that these ratios, nevertheless, are important parameters in fracture initiation.

With respect to the level of deformation at fracture predictions, it is not necessary to consider both generalised plastic work and generalised plastic strain as both have been previously shown to produce the same predictions, therefore only generalised plastic strain will be considered here. As table 8.2 shows, in some cases quite considerable discrepancy is apparent between the tensile test value of generalised plastic strain at fracture and the corresponding finite-element value of generalised plastic strain at the experimental level of deformation at fracture. The following section of this chapter deals with the effect of hydrostatic stress.

	Model	T.T. $\bar{\varepsilon}$ at fracture	F.E. $\bar{\varepsilon}$ at fracture	% diff.
Side-pressing	Brass circular	0·97	1·08	11
	7075 circular	0·32	0·34	6
	7075 H/W=1·33	0·32	0·30	-6
	7075 H/W=2·03	0·32	0·32	0
Upsetting	H/D = 0·5	0·97	1·34	38
	H/D = 1·0	0·97	1·18	22
	H/D = 1·5	0·97	1·78	84
	H/D = 2·0	0·97	2·04	110
Strip	Compression	0·74	1·54	108
	Milled	0·74	0·54	-27
	Forged	0·74	0·35	-53
Extrusion	7075	0·24	3·80	1480
	Brass	0·97	0·82	-15

Table 8.2

Generalised plastic strain at fracture comparisons.

8.3 Effect of Hydrostatic stress.

As mentioned at the end of section 8.2 and quantified in table 8.3 some not inconsiderable differences exist between the finite-element and tensile test values of generalised plastic strain at fracture. One possible explanation for these differences may be due to the different levels of hydrostatic stress at fracture in the operations considered, the effect of which has been classically described by Bridgman (1952). It is the purpose of this section to examine the finite-element predictions of hydrostatic stress for each test geometry and see if they may be related to the level of generalised plastic strain at fracture. Figures 8.1, 8.2 and 8.3 show the limits of finite-element calculated hydrostatic stress obtained for a given finite-element generalised plastic strain at the experimental level of deformation at fracture. Figure 8.1 shows the values obtained for the various test geometries machined from 60-40 brass rod stock; Figure 8.2 for continuous cast 7075 aluminium alloy, and figure 8.3 for 60-40 brass strip. One set of values cannot be included in these graphs, that referring to 7075 extrusion, where the specimens were machined from plate stock. This result will be set aside for the purposes of this discussion as there are no other results from the same source with which to compare it.

The crosses on these graphs show the average of the hydrostatic stress values calculated by the finite-element program up to the experimental level of deformation at fracture. The bars marked show the range of hydrostatic stress calculated by the finite-element program during the complete deformation sequence leading up to fracture. The graphs from which these values have been obtained, showing the variation in finite-element hydrostatic stress with level of deformation in each test geometry, are given in Appendix C. The hydrostatic stress for the

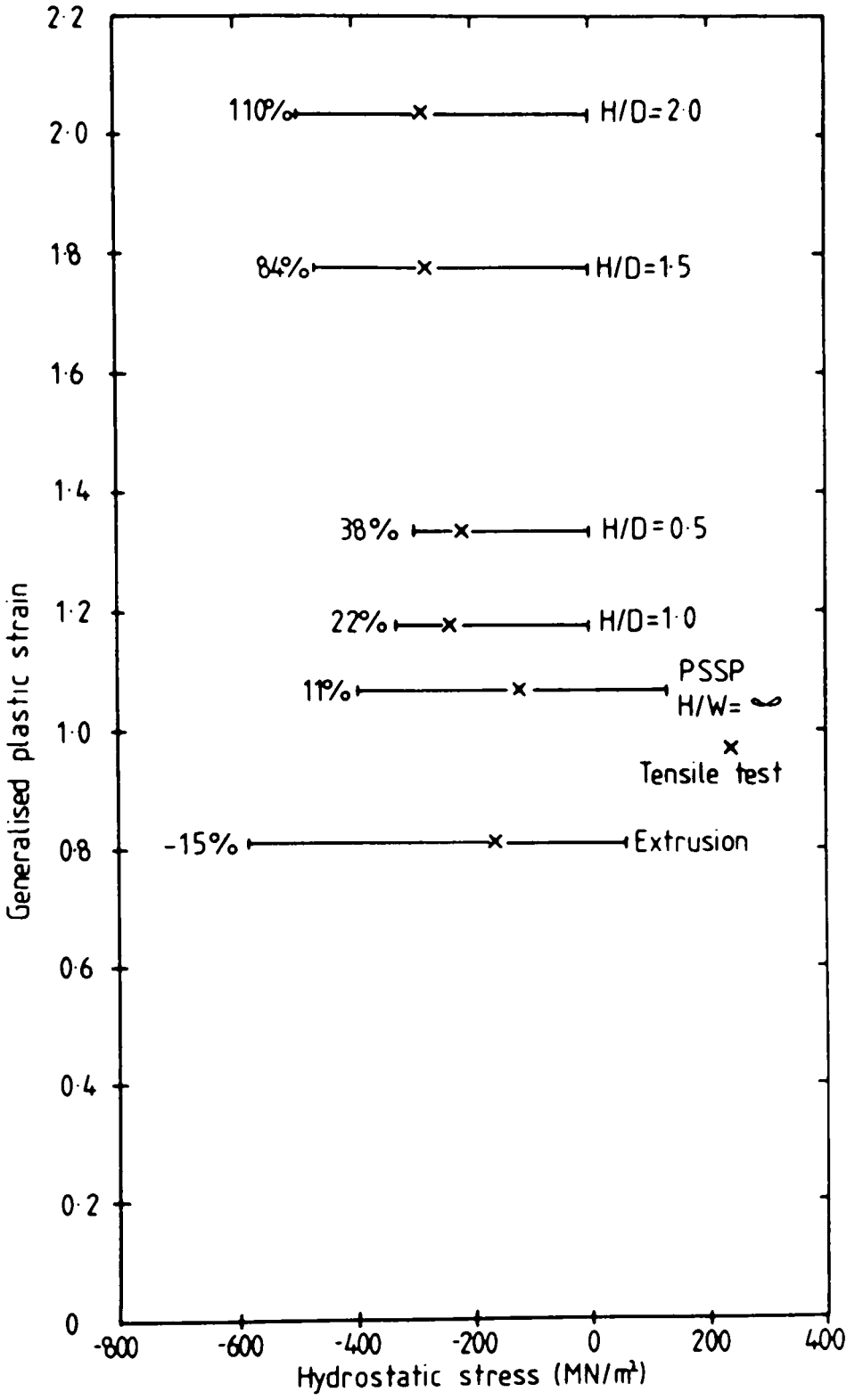

Figure 8·1

Generalised plastic strain at fracture plotted against hydrostatic stress for brass rod

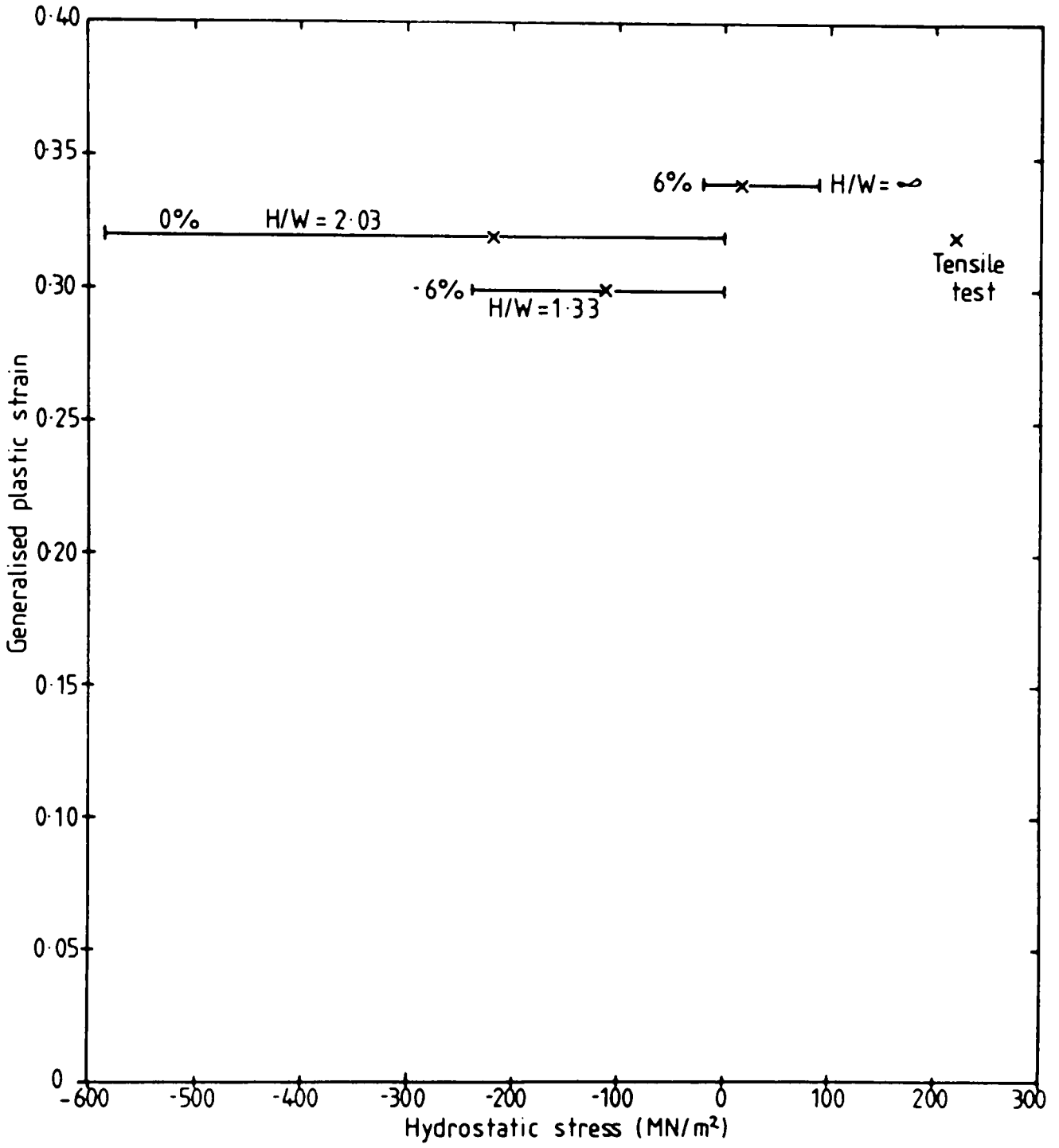

Figure 8.2

Generalised plastic strain at fracture plotted against hydrostatic stress for the plane-strain side-pressing of 7075 aluminium alloy.

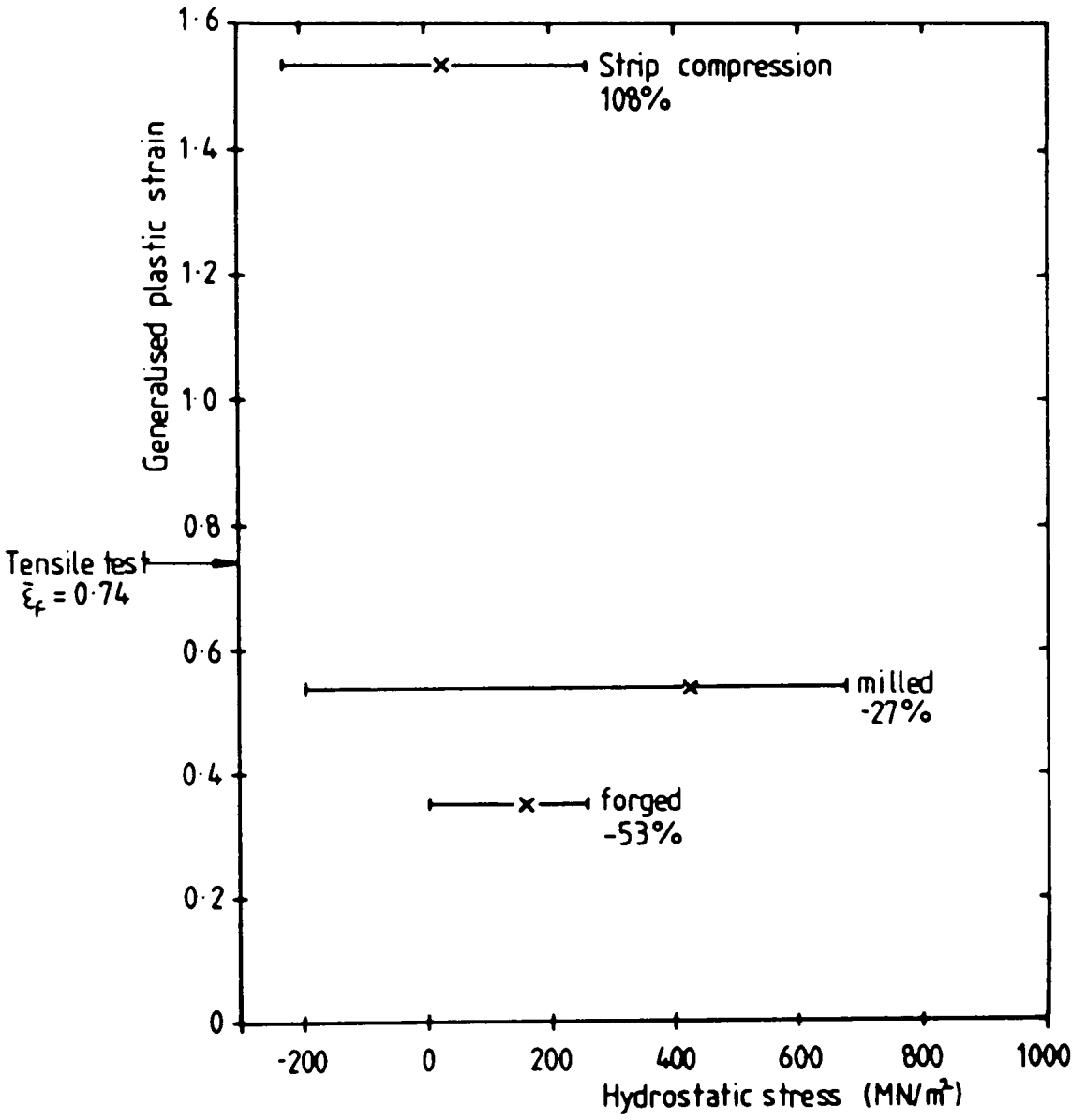

Figure 8.3

Generalised plastic strain at fracture plotted against hydrostatic stress for the deformation of brass strip.

experimental tensile tests, calculated as suggested by Bridgman (1944), is also plotted in figure 8.1 for brass and figure 8.2 for aluminium alloy. The percentage deformation figures to the left of each plotted point give the difference between the generalised plastic strain at fracture in the tensile test and the finite-element calculated generalised plastic strain values at the level of deformation at fracture found experimentally. Attention is focussed here on figure 8.1, the graph for 60-40 brass rod, although the other graphs have a very similar form.

As shown on the graph it is not possible to identify a trend through the points which indicates larger generalised plastic strain values at fracture under conditions of compressive hydrostatic stress. A linear relationship would be expected to be an oversimplification, but these results do not indicate that the errors in the level of deformation at fracture predictions found in the work presented in this thesis can be explained by reference to the state of hydrostatic stress.

8.4 Conclusions.

Consideration of a range of continuum fracture criteria calculated for a number of simple test geometries using the finite-element technique has revealed that only the fracture criteria based on a critical value of generalised plastic strain at fracture, (and the equivalent fracture criterion of a critical value of generalised plastic work) are capable of correctly predicting the experimental fracture initiation sites for the complete range of processes considered. Errors in the levels of deformation at fracture predictions cannot be explained with reference to finite-element values of hydrostatic stress.

Conclusions and Further Work.

The work presented in this thesis has further demonstrated the capabilities of the elastic-plastic finite-element technique in the analysis of metalforming operations.

The four simple metalforming operations of plane-strain side-pressing, simple upsetting, strip compression and tension, and axisymmetric extrusion have been considered. In all of the operations the finite-element calculated stress and strain values have been used to predict the fracture initiation sites from a range of published fracture criteria.

Only the fracture criteria of a critical value of generalised plastic strain, and the equivalent criterion of a critical value of generalised plastic work, have correctly predicted the fracture initiation sites found experimentally in all the specimen geometries considered. For these successful criteria predictions have also been made of the level of deformation at fracture. However, significant differences are revealed when these predictions are compared with experiment. Subsequent investigation has shown that these differences cannot be related to the level of hydrostatic stress calculated by the finite-element program.

Further work needs to be done to investigate the source of the disagreement between the numerical predictions and experiment.

Once this has been done the technique could be applied to more industrially relevant geometries. Analysis of metal flow in an automobile connecting rod has already been examined by Pillinger (1984) but as yet no analysis of fracture initiation sites has been performed.

Improvement could also be made in a number of ways to the

finite-element program used. Most importantly, this concerns the modelling of interface friction with respect to the general disagreement between the finite-element and experimental form of the ring test results. Attention needs to be focussed on this problem.

The availability of a conical boundary surface would have helped in the analysis of extrusion presented in chapter 7.

Adequate pre- and post-processing programs would have reduced the time required for data preparation and improved the clarity of results presented in the analyses of all the metalforming operations examined in this thesis.

Summary

This thesis has described the use of elastic-plastic finite-element analysis in an investigation of fracture initiation in metalforming. Finite-element calculated stress and strain distributions were used to obtain fracture initiation site predictions from continuum fracture criteria due to the following investigators:

1. McClintock, Kaplan and Berg (1966);
2. McClintock (1968);
3. Cockroft and Latham (1968);
4. Brozzo, DeLuca and Rendina (1972);
5. Ghosh (1976);
6. Norris, Reaugh, Moran and Quinones (1978);
7. Oyane et al (1980);
8. Atkins (1981);
9. Generalised plastic strain;
10. Generalised plastic work.

Four sets of numerical and experimental results have been compared. These relate to the operations of plane-strain side-pressing, simple upsetting, strip compresion and tension, and axisymmetric extrusion.

Only the generalised plastic strain criterion (and the equivalent criterion of generalised plastic work) have correctly predicted the experimentally obtained fracture initiation sites in all the geometries examined.

Errors in the level of deformation at fracture predictions cannot be explained with reference to the finite-element values of hydrostatic stress.

References.

ALEXANDER, J.M. & LENGYEL, B. (1964)
J. Inst. Met. 93, pp 137-145
'On the cold extrusion of flanges against high hydrostatic pressure'

ALEXANDER, J.M. & PRICE, J.W.H. (1977)
18th MTDR Conference, pp267-274
'Finite-element analysis of hot metal forming'

ARGON, A.G., IM, J. & SAFOGLU, R. (1975)
Met Trans 6A, pp 825-837,
'Cavity formation from inclusions in ductile fracture'

ARGON, A.S. (1973)
ASM Metal Park Ed S.I. Oh
Chapter 7 in 'The inhomogeneity of plastic deformation' : 'stability of plastic deformation'

ATKINS, A.G. (1981)
Metals Science (February)
'Possible explanation for unexpected departures in hydrostatic tension - fracture strain relations'

ATKINS, A.G. & MAI, Y-W (1985)
Ellis Horwood
'Elastic and plastic fracture'

AVITZUR, B (1968a)
McGraw Hill
'Metal forming : processes & analysis'

AVITZUR, B (1968b)
Trans ASME J Eng Ind pp 79-81
'Analysis of central bursting defects in extrusion and wire drawing'

BOWDEN, F.P. & TABOR, D. (1964)
Clarendon Press, Oxford
'The friction and lubrication of solids. Part 2'

BRIDGMAN,P.W. (1952)
McGraw Hill
'Studies in large plastic flow and fracture'

BRIDGMAN, P.W. (1944)
Trans ASM 32 pp 553-574
'The stress distribution at the neck of a tension specimen'

BROEK, D. (1973)
Eng Fract Mech 5, pp55-66
'The role of inclusions in ductile fracture and fracture toughness'

BROZZO, P., De LUCA, B & RENDINA, R (1972)
Sheet metal forming & formability.
Proc. 7th Biennial Congress of the Int deep drawing research group
'A new method for the prediction of the formability limits of metal sheets'

CHANDA, S.K. (1982)
Private communication

CHEN,C.C. & KOBAYASHI, S. (1980)
Process modelling - fundamentals and applications to metals. ASM, pp167.
'Rigid plastic finite-element analysis of plane-strain closed-die forging'

COCKROFT, M.G. & LATHAM, D.J. (1968)
J. Inst. Met. 96, pp 33-39
'Ductility and the workability of metals'

COCKROFT, M.G. & LATHAM, D.J. (1966)
NEL report number 240.
'A simple criterion of fracture for ductile materials'

COFFIN, L.F. & ROGERS, F.C. (1967)
GE Research and development centre, Schenectady, New York. Technical information series number 67-C-047
'Structural damage in metalworking'

COLLINS, I.F. (1969)
Int. J. Mech Sci 11, pp 971-978
'Slip-line field solutions for compression and rolling with slipping friction'

COOK, M. & LARKE, E.C. (1945)
J Inst Met 71, pp 371-390
'Resistance of copper and copper alloys to homogeneous deformation in compression'

CRAMPHORN,A.S., BRAMLEY,A.N. & McDERMOTT,R.P. (1976)
Proc 4th NAMR conference, pp80-86.
'UBET related developments in forging analysis'

DAVIDENKOV,N.N. & SPIRIDOVA,N.I. (1946)
Proc Am Soc Test Mater 46, pp 1147-1158
'Mechanical methods of testing: Analysis of the state of stress in the neck of a tension test specimen'

DODD,B., STONE,R. & BAI,Y. (1985)
Res Mechanica 13, pp265-273
'Fracture in upset forging of cylinders of magnesium alloy'

DODD,B. & KUDO,H. (1980)
Int J Mech Sci 22, pp67-71
'Slip-line field for mid-plane cracking or splitting in sheet drawing'

DUNG, N.L., KLIE, W. & MAHRENHOLTZ, O. (1980)
Mech Res Comm 7, pp33-38
'Analysis of plastic flow with a simplified finite-element method'

ERTURK, T. (1979)
Proc 3rd Int Conf on the mechanical behaviour of materials, Cambridge.
'Measurement of bulk formability and the effect of second phase particles - An application of the upset test'

FARMER, L.E. & OXLEY, P.L.B. (1971)
J. Mech PHYS SOLIDS 19 369-388
'A slip line field for plane strain extrusion of a strain-hardening material'

FORD, H. & ALEXANDER, J.M. (1977)
Ellis Horwood
'Advanced mechanics of materials'

FREUDENTHAL, A.M. (1950)
'The inelastic behaviour of engineering materials and structures
John Wiley

GARNER, J.N. & RICE, W.B. (1974)
Am CIRP, 23, pp69-
'An experimental investigation of central burst formation during hydrostatic extrusion using wax to simulate metal'

GHOSH, A.K. (1976)
Met Trans 7A, pp 523-533
'A criterion for ductile fracture in sheets under biaxial loading'

GILLEMOT, L.F. (1976)
Eng Fract Mech 8, pp 239-253
'Criterion of crack initiation and spreading'

GOODS, S.H. & BROWN, L.M. (1979)
Acta Metallurgica 27, pp 1-15
'The nucleation of cavities by plastic deformation'

HAMPTON, S.J., ANDRIACCHI, T.P. & GALANTE, J.O. (1980)
J. Biomech 13, pp 443-448
'Three dimensional stress analysis of the femoral stem of a total hip prosthesis'

HANCOCK,J.W. & MACKENZIE,A.C. (1976)
J Mech Phys Solids 24, pp147
'On the mechanisms of ductile fracture in high strength steels subjected to multi-axial stress states'

HARTLEY, P. (1979)
Ph.D. Thesis, University of Birmingham
'Metal flow and homogeneity in extrusion forging'

HARTLEY, P., STURGESS, C.E.N. & ROWE, G.W. (1980)
Int J Mech Sci 22, pp 743-753
'Influence of friction on the prediction of forces, pressure distributions and properties in upset forging'

HARTLEY, P., STURGESS, C.E.N. & ROWE, G.W. (1979)
Int J Mech Sci 21, pp 301-311
'Friction in finite-element analyses of metalforming processes'

HARTLEY,P., STURGESS,C.E.N. & ROWE,G.W. (1978)
Proc 6th NAMRC, Florida, pp212-219.
'A finite-element analysis of extrusion forging'

HENCKY, H. (1923)
Zeits ang Math Mech 3, pp241

HILL, R. (1950)
Clarendon Press, Oxford
'The mathematical theory of plasticity'

HILL, R., LEE, E.H. & TUPPER, S.J. (1951)
Trans ASME J Appl Mech 18, pp 46
'A method of numerical analysis of plastic flow in plane-strain and its application to the compression of a ductile material between rough plates'

HILL,R., LEE,E.H. & TUPPER,S.J. (1946)
Proc 6th Int Cong Appl Mech, Paris

HOPSON, M.W., WEINMANN, K.J., HENDRICKSON, A.A. & ROWE, G.W. (1974)
Proc. 2nd NAMRC, pp 239-254
'The use of the fibre structure of high-purity aluminium for the study of metal flow in plastic deformation'

IWATA, K., OSAKADA, K. & FUJINO, S (1972)
Trans ASME J Eng Ind, 94, pp 697-703
'Analysis of hydrostatic extrusion by the finite-element method'

JAIN, S.C. & KOBAYASHI, S. (1970)
Proc 11th Int MTDR, Birmingham
'Deformation & fracture of an aluminium alloy in plane-strain side-pressing'

JOHNSON,W. (1959)
Proc I Mech E 173, pp61-72
'Estimation of upper-bound loads for extrusion and coining operations'

JOHNSON, W. & KUDO, H. (1962)
Manchester University Press
'The mechanics of metal extrusion'

JOHNSON, W. & MAMALIS, A.G. (1977)
Proc 17th MTDR Conference, Birmingham 1976. Macmillan Press, pp607-
'Defects in metalworking processes'

JOHNSON, W., MELLOR, P.B. & WOO. D.M. (1958)
J Mech Phys Solids 6, pp 203
'Extrusion through single hole staggered and unequal multi-hole dies'

KIVIVUORI, S. & SULONEN, M. (1978)
Ann CIRP 27, pp141-145
'Formability limits and fracturing modes of uniaxial compression specimens:

KOBAYASHI, S. (1970)
Trans ASME, J Eng Ind 92, pp391-399
'Deformation characteristics and ductile fracture of 1040 steel in simple upsetting of solid cylinders & rings'

KORHONEN, A.S. (1980)
Acta Polytechnica Scand. Chemistry including Metallurgy series, no. 144, Helsinki.
'Localisation of plastic flow and ductile fracture in metals'

KUDO,H. (1960a)
Int J Mech Sci 1, pp57-83
'An upper-bound approach to plane-strain forging and extrusion - I'

KUDO,H. (1960b)
Int J Mech Sci 1, pp229-252
'An upper-bound approach to plane-strain forging and extrusion - II'

KUDO, H. & AOI, K. (1967)
J Japan Soc Plast 8, pp17
'Effect of compression test condition upon fracturing of a medium carbon steel'

KUDO,H. & MATSUBARA,S. (1978)
IUTAM symposium, Tutzing, Germany.
In 'Metalforming plasticity', Ed. H. Lippmann.
'Joint examination project of the validity of various numerical methods for the analysis of metalforming processes'

KUHN, H.A. & DIETER, G.E. (1977)
ICF4 (Volume 1), Waterloo, Canada.
'Workability in bulk forming processes'

KUHN, H.A., LEE, P.W. & ERTURK, T. (1973)
Trans ASME J Eng Mat 95, pp213-218
'A fracture criterion for cold forming'

KUHN,H.A. & LEE,P.W. (1971)
Met Trans 2, pp3197-3202
'Strain instability and fracture at the surface of upset cylinders'

LATHAM, D.J., COCKROFT, M.G. & TWEEDIE, E.S. (1968)
Metal Forming, July, pp 196-200 and Metal Forming, August, pp 221-225
'An assessment of the compression test for determining mechanical properties'

LATHAM, D.J. & COCKROFT, M.G. (1966)
NEL Report number 216
'The effect of the stress system on the workability of metals'

LEE, C.H., IWASAKI, H. & KOBAYASHI, S. (1973)
Trans ASME J Eng Ind 95, pp 283-291
'Calculation of residual stresses in plastic deformation processes'

LEE, C.H. & KOBAYASHI, S. (1973)
Trans ASME J Eng Ind 95, pp865-873
'New solutions to rigid-plastic deformation problems using a matrix method'

LEE, C.H. & KOBAYASHI, S. (1971)
Trans ASME J Eng Ind 93, pp445
'Analysis of axisymmetric upsetting and plane-strain side-pressing of solid cylinders by the finite-element method'

LEE, E.H. (1976)
Office of Naval Research ONR-ARPA-N0014-75-C-0923 Sudam no. 76-1
'The basis for an elastic-plastic code'

LEE, E.H., MALLETT, R.L. & YANG, W.H. (1977)
Comp Meth Appl Mech Eng 10, pp339-353
'Stress and deformation analysis of the metal extrusion process'

LEE, E.H. & McMEEKING, R.M. (1978)
Trans ASME J eng Ind 100, pp386-7
'Concerning analysis of central burst in metal forming'

LEE, P.W. & KUHN, H.A. (1973)
Met Trans 4, pp969-974
'Fracture in cold upset forging - a criterion and model'

MALE, A.T. & COCKROFT, M.G. (1964)
J Inst Met 93, pp 38-46
'A method for the determination of the coefficient of friction of metals under conditions of bulk plastic deformation'

MARCAL, P.V. & KING, I.P. (1967)
Int J Mech Sci 9, pp 143-155
'Elastic-plastic analysis of two-dimensional stress systems by the finite-element method'

McCLINTOCK, F.A. (1968)
Trans ASME J Appl Mech 35, pp 363
'A criterion for ductile fracture by the growth of holes'

McCLINTOCK, F.A., KAPLAN, S.M. & BERG, C.A. (1966)
Int J Mech Sci 2, pp 614
'Ductile fracture by hole growth in shear bands'

NAGAMATSU,A., MUROTA,T. & JIMMA,T. (1971)
Bull JSME 14, pp331-338
'On the non-uniform deformation of material in axially symmetric compression caused by friction'

NAGTEGAAL, J.C. & DeJONG, J.E. (1980)
in 'Computational methods in non-linear mechanics', North Holland publishing company, Ed J.T. Oden, pp303-309
'Some computational aspects of elastic-plastic large strain analysis'

NAGTEGAAL, J.C., PARKS, D.M. & RICE, J.R. (1974)
Comp Meth in Appl Mech & Eng 4, pp 153-177
'On numerically accurate finite-element solutions in the fully plastic range'

NORRIS, D.M., REAUGH, J.E., MORAN, B. & QUINNONES, D.F. (1978)
J Eng Mat Tech 100, pp 279-286
'A plastic-strain, mean-stress criterion for ductile fracture'

OH, S.I. & KOBAYASHI, S. (1976)
AFML-TR-76-61
'Theories on flow and fracture in metalforming processes. Part 2. A theory on ductile fracture in metalworking processes'

OH, S.I., CHEN, C.C. & KOBAYASHI, S. (1979)
Trans ASME 101, pp
'Ductile fracture in axisymmetric extrusion and drawing. Part 2. Workability in extrusion and drawing'

OH, S.I., LAHOTI, G.D. & ALTAN, T. (1982)
Proc First International Conference in Industrial Forming Processes'. University of Swansea. Pineridge Press, pp145-154.
'Application of FEM to industrial metalforming processes'

OSMAN,F.H. & BRAMLEY,A.N. (1982)
Proc first International conference on numerical methods in industrial forming processes. 12-16 July 1982. Pineridge Press, Swansea, pp333-342.
'An incremental analytical technique for forging and extrusion of metals'

OYANE, M., SATO, T., OKIMOTO, K. & SHIMA, S. (1980)
J. Mech Work Tech 4, pp 65-81
'Criteria for ductile fracture and their applications'

OYANE, M. (1972)
Bull JSME 15, pp1507-1513
'Criteria of ductile fracture strain'

PILLINGER, I. (1984)
PhD thesis, University of Birmingham
'The prediction of metal flow and properties in three-dimensional forging using the finite-element method'

PILLINGER, I., HARTLEY, P., STURGESS, C.E.N. & ROWE, G.W. (1982)
1st Int Conf in Numerical Methods in Industrial Forming Processes. University College Swansea. July 12-16th, pp123-134.
'An elastic-plastic finite-element analysis of the radial expansion of a thick-walled hollow cylinder and analytical validation'

PRAGER, W. & HODGE, P.G. (1951)
John Wiley, New York
'Theory of perfectly plastic solids'

PRANDTL, L. (1921)
Z angew Math Mech 1, pp 15
'On the penetration hardness of plastic materials and the hardness of indentors'

PRANDTL, L. (1920)
Nachr Ges Wiss Gottingen volume 74

PRICE, J.W.H. & ALEXANDER, J.M. (1979)
Int J Mech Sci 21, pp417-430
'Specimen geometries predicted by computer model of high deformation forging'

PRICE, J.W.H. & ALEXANDER, J.M. (1976)
Second Int Symp on finite-elements in flow problems, Santa Margherita Ligure, Italy.
'The finite-element analysis of two high temperature metal deformation processes'

RAO, S.S. (1982)
Pergammon International Library
'The finite-element method in engineering'

RICE, J.R. & TRACEY, D.M. (1973)
Numerical and computer methods in structural mechanics.
Ed. S.J. Fenvers et al. Academic Press.
'Computational fracture mechanics'

RICE, J.R. & TRACEY, D.M. (1969)
J Mech Phys Solids 17, pp 201-217
'On the ductile enlargement of voids in triaxial stress fields'

RICHARDS, T.H. (1977)
Ellis Horwood, Sussex
'Energy methods in stress analysis'

ROWE, G.W. (1979)
Edward Arnold
'Elements of metalworking theory'

ROWE, G.W. & HARTLEY, P. (1977)
Proc 5th NAMRC, Amhurst, pp 204-210
'Computer analysis of progressive deformation in extrusion forging'

SANTIAGO, J.M. & WISNIEWSKI, I.H.L. (1982)
1st Int Conf in Numerical Methods in Industrial Forming Processes. University College, Swansea. July 12-16th
'Implementing the Besseling-White plasticity model in the Adina finite-element program'

SHAH, S.N. & KOBAYASHI,, S. (1976)
AFML-TR-76-61
'Theories on flow and fracture in metalforming processes. Part 1. A theory of metal flow in axisymmetric piercing and extrusion'

SOWERBY,R., CHANDRASEKARAN,N., DUNG,N.L. & MAHRENHOLTZ,O. (1985)
VDI-Forschung im Ingenieurwesen 51
'The prediction of damage accumulation during upsetting tests based on McClintock's model'

SPENCER, A.J.M. (1980)
Longman
'Continuum mechanics'

STARK, P.A. (1970)
Macmillan, New York.
'Introduction to numerical methods'

TABOR, D. (1951)
Oxford University Press
'The hardness of metals'

TEKKAYA, A.E. & ROLL, K. (1984)
Proc. Conf. Numerical methods for non-linear problems, Vol. 2. Ed. C Taylor et al. Pineridge Press, Swansea.
'Analysis of metal forming processes by different finite-element methods'

THORNTON, J.N. & BRAMLEY, A.N. (1980a)
Proc. I Mech Eng 194, pp 9-15
'An approximate method for predicting metal flow in forging and extrusion operations'

THORNTON, J.N. & BRAMLEY, A.N. (1980b)
Proc I Mech Eng 194, 53-55
Discussion on (1980a)

YAMADA, Y., YOSHIMURA, N & SAKURAI, T. (1968)
Int J Mech Sci 10, pp 343-354
'Plastic stress-strain matrix and its application for the solution of elastic-plastic problems by the finite-element method'

ZIENKIEWICZ, O.C., JAIN, P.C. & ONATE, E. (1978)
Int J Solids Struct 14, pp15-38
'Flow of solids during forming and extrusion: some aspects of numerical solutions'

ZIENKIEWICZ, O.C. & GODBOLE, P.N. (1975)
J Strain Analysis 10, pp 180-183
'A penalty function approach to problems of plastic flow of metals with large surface deformations'

ZIENKIEWICZ, O.C., VALLIAPAN, S. & KING, I.P. (1969)
Int J Num Methods Eng 1, pp 75-100
'Elasto-plastic solutions of engineering problems. Initial stress, finite-element approach'

ZIENKIEWICZ, O.C. (1977)
McGraw Hill
'The finite-element method'

Appendices.

Appendix A:

Structure of the finite-element incremental post-processing file.

Record	Contents	Type
1	increment number,def, time, work, number of nodes (nnd), number of elements (nl), jobname, date, title	int,real,real,real, int,int,char*10, char*10,char*78
2	node numbers	real(nnd)
3	node coordinates	real(3*nnd)
4	nodal stress components	real(6*nnd)
5	nodal incremental strain components (elastic+plastic)	real(6*nnd)
6	nodal incremental plastic strain components	real(6*nnd)
7	nodal generalised plastic strain	real(nnd)
8	nodal temperature	real(nnd)
9	nodal contact values	int(nnd)
10	element rotational values	char(nl)*10
11	element yield values	int(nl)

Appendix B:

Heat treatment of cold rolled 7075 aluminium plate.

1. Cut plate into smaller pieces, about 25 cm square.

2. Heat as quickly as possible to 460°C. Keep at this temperature for one hour.

3. Quench in cold water (tap water will do). The plate must be taken from the furnace to the water quench as quickly as possible. The plate should be agitated while submerged in the quenchant.

N.B. This is the stage most likely to influence the final structure. A tensile or hardness test may be useful to check the consistency of each piece of the plate. Any anomolous piece may be reheated as in stage 2.

4. Heat to 135°C at 20°C per hour. Keep at this temperature for 16 hours. Cool in air. (This is the peak age temper T651, which should produce a very brittle structure, more brittle than the original plate).

Notes.

The pieces of plate may be heated together provided an air gap is maintained between the pieces. The pieces should be quenched individually. The complete heat treatment sequence should be completed within a couple of days.

(This sequence suggested by Dr T Davies of Alcan Plate, 16th October 1984).

Appendix C:

Finite-element hydrostatic stress graphs.

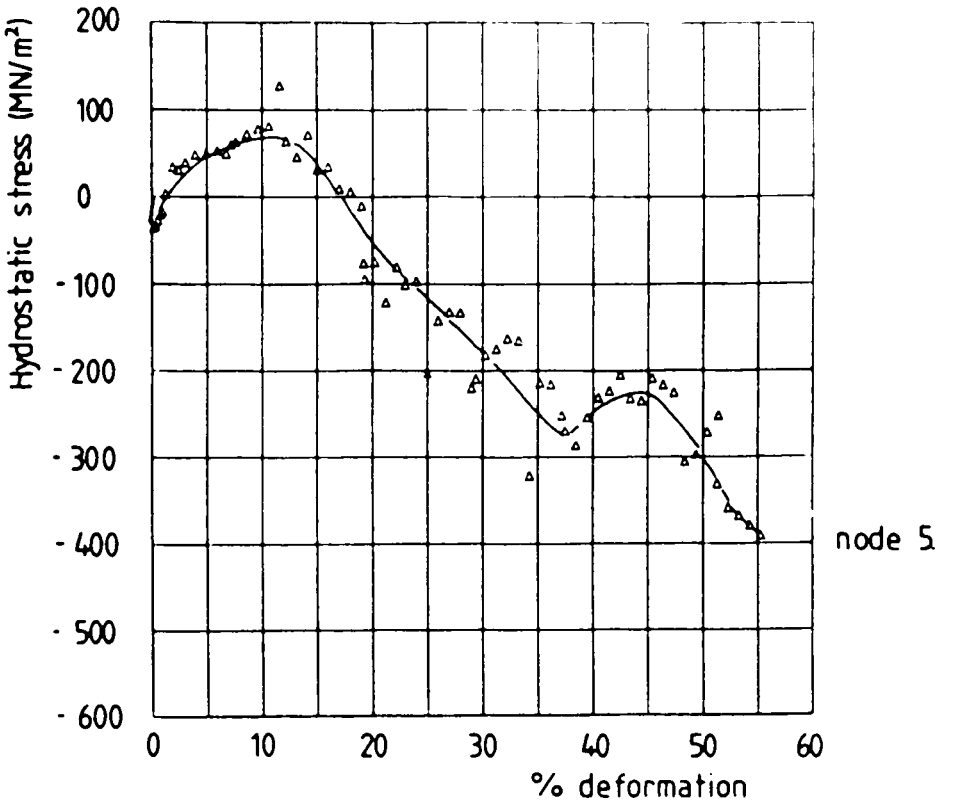

Figure C.1

Variation of FE hydrostatic stress for the plane-strain side-pressing of initially circular section brass.

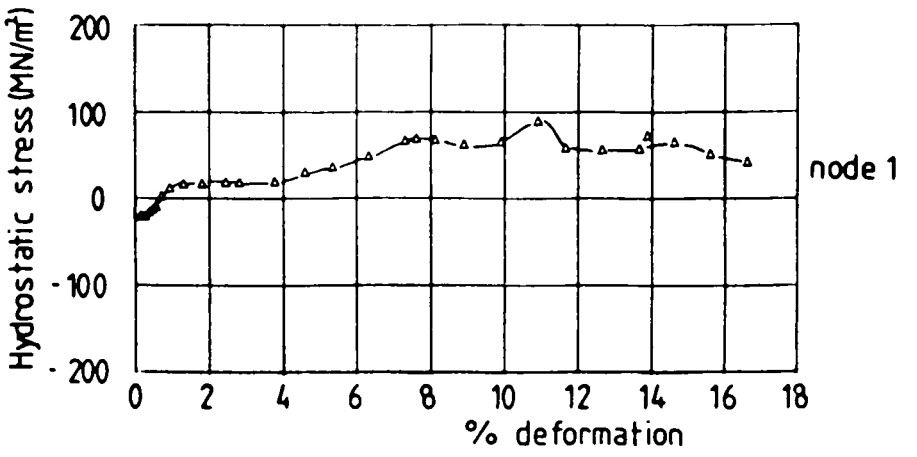

Figure C.2

Variation of FE hydrostatic stress for the plane-strain side-pressing of 7075 aluminium alloy with an initially circular cross section for node 1.

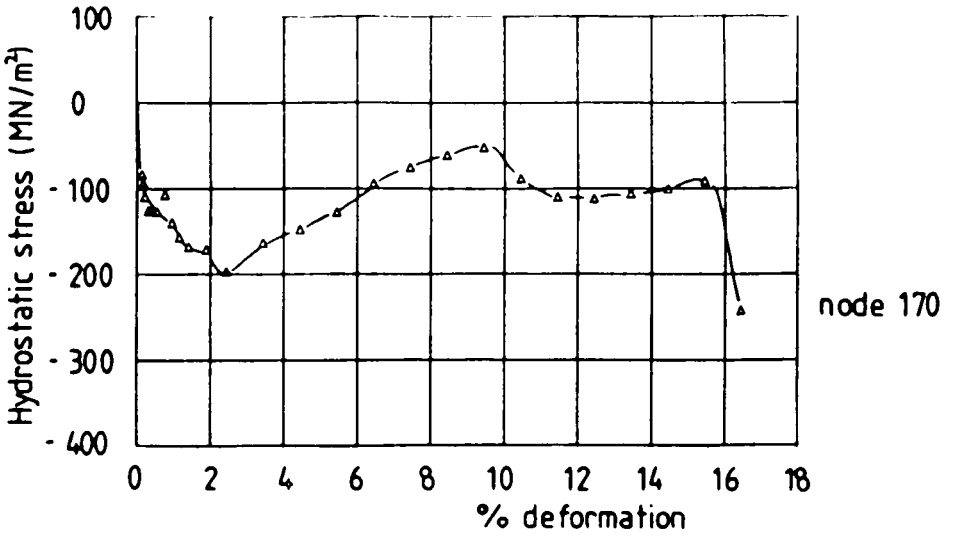

Figure C.3

Variation in FE hydrostatic stress for the plane-strain side-pressing of 7075 aluminium alloy with initial H/W = 1·33 for node 170.

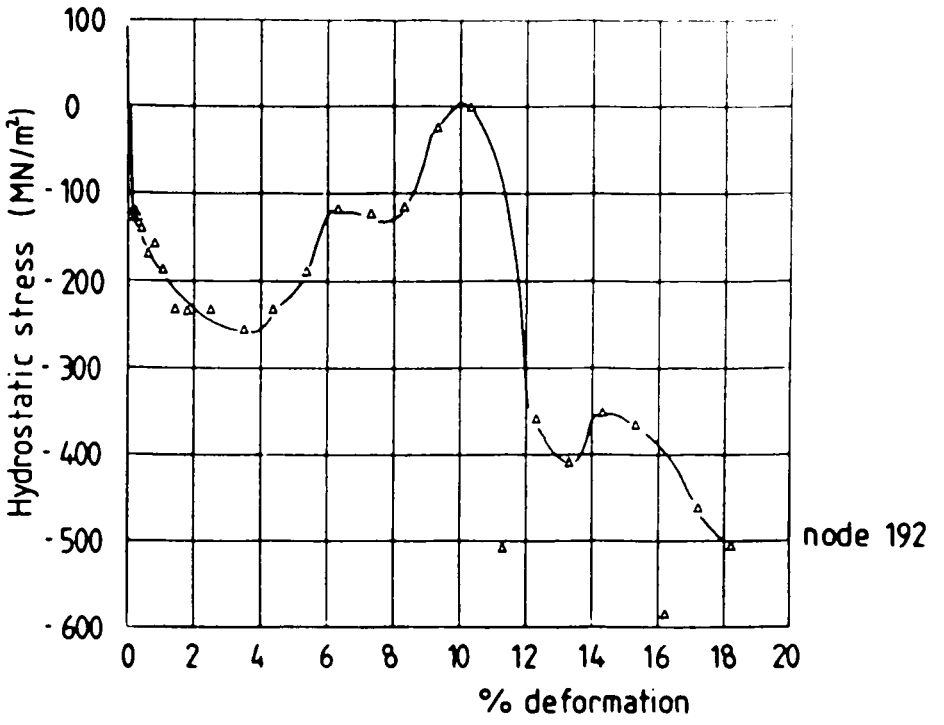

Figure C.4

Variation of FE hydrostatic stress for the plane-strain side-pressing of 7075 aluminium alloy with initial H/W = 2·03 for node 192.

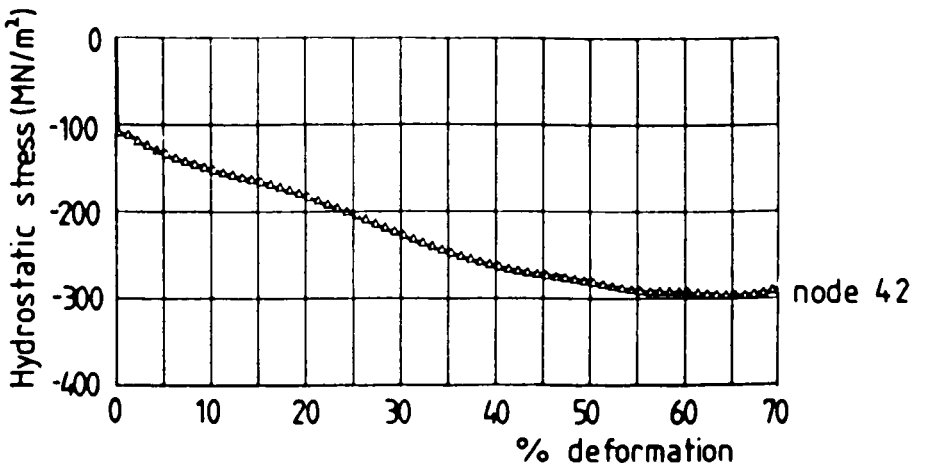

Figure C.5

Variation of FE hydrostatic stress for the simple upsetting of brass of initial H/D = 0·5 for node 42.

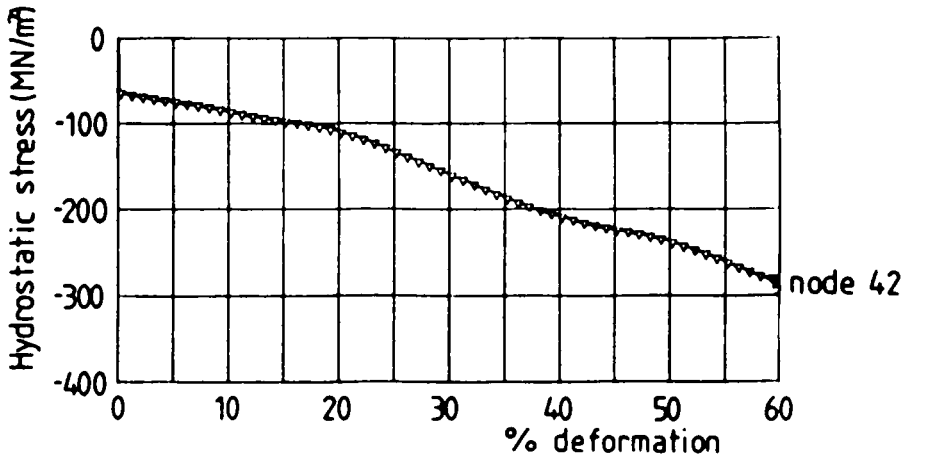

Figure C.6

Variation of FE hydrostatic stress for the simple upsetting of brass of initial H/D = 1·0 for node 42.

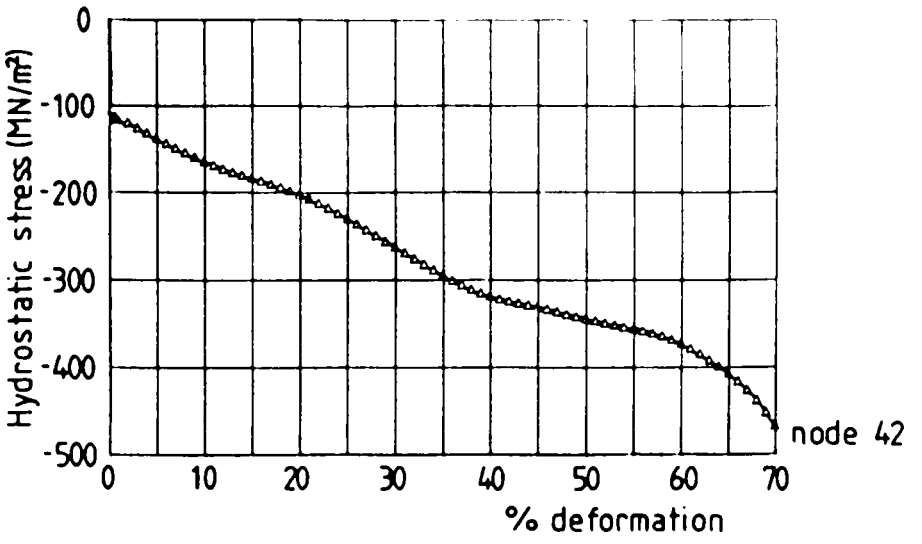

Figure C.7

Variation of FE hydrostatic stress for the simple upsetting of brass of initial H/D=1·5 for node 42.

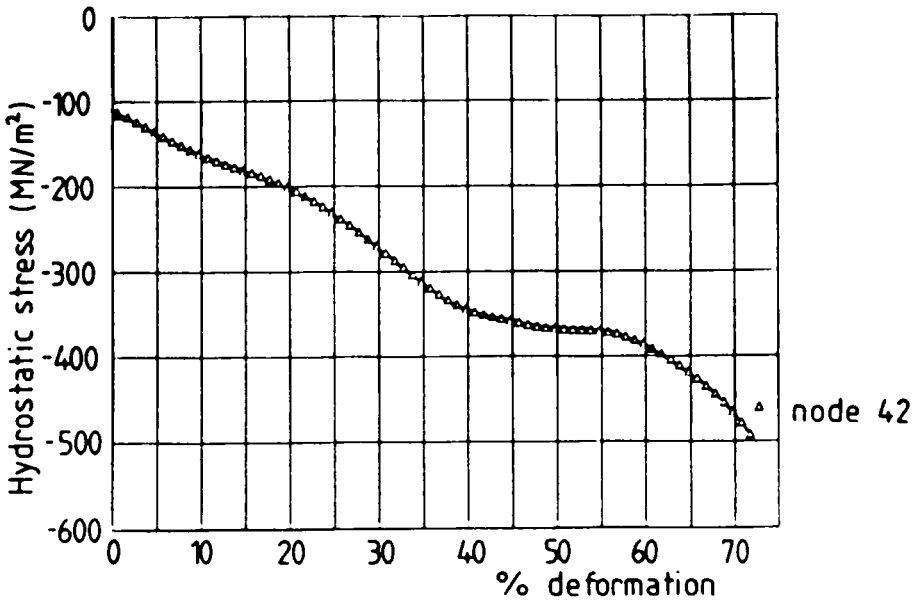

Figure C.8

Variation of FE hydrostatic stress for the simple upsetting of brass of initial H/D = 2·0 for node 42.

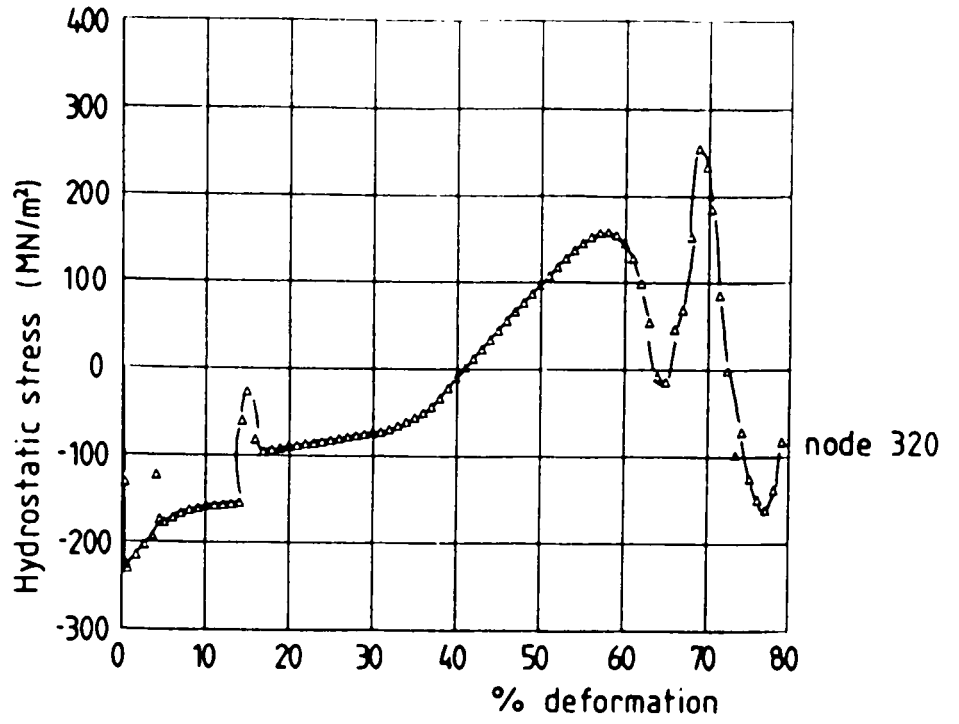

Figure C.9

Variation of FE hydrostatic stress for the compression of brass strip for node 320.

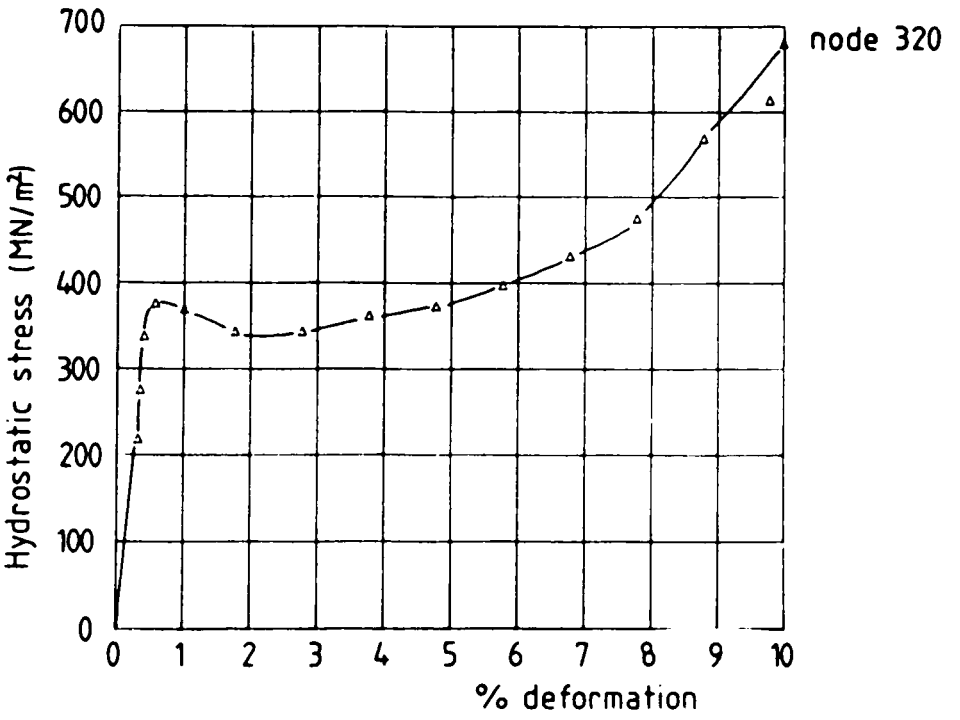

Figure C.10

Variation of FE hydrostatic stress for the tensile deformation of milled brass strip for node 320.

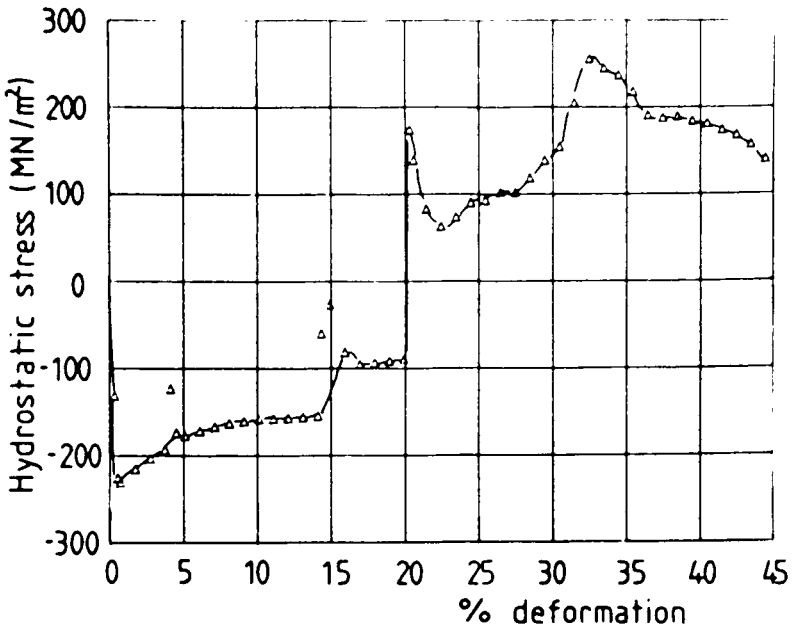

Figure C.11

Variation of FE hydrostatic stress for the tensile deformation of forged brass strip for node 320.

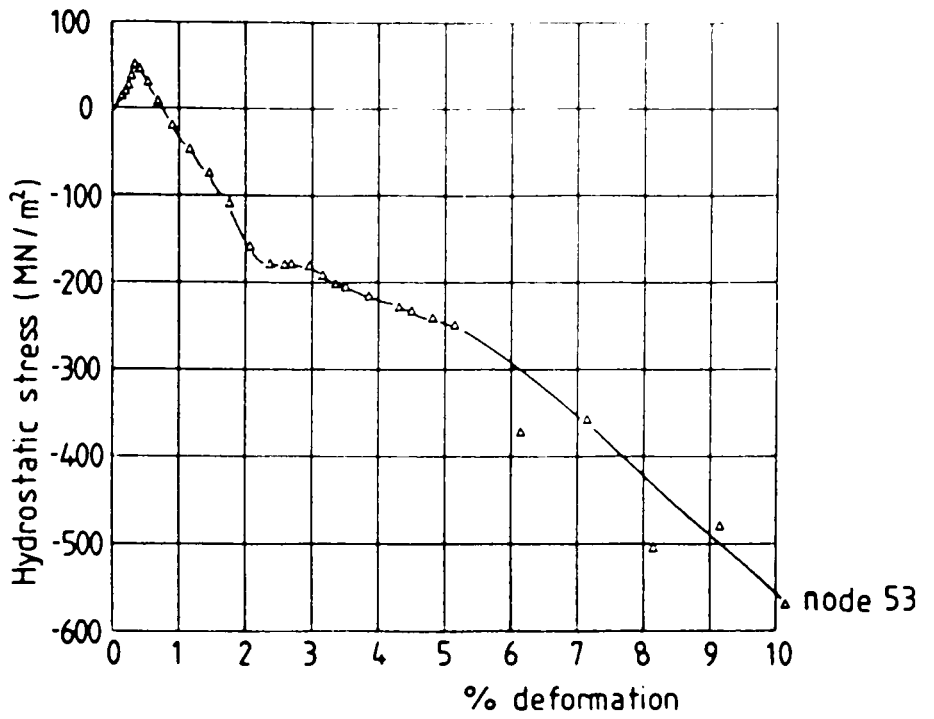

Figure C.12

Variation of FE hydrostatic stress for the extrusion of brass for node 53.

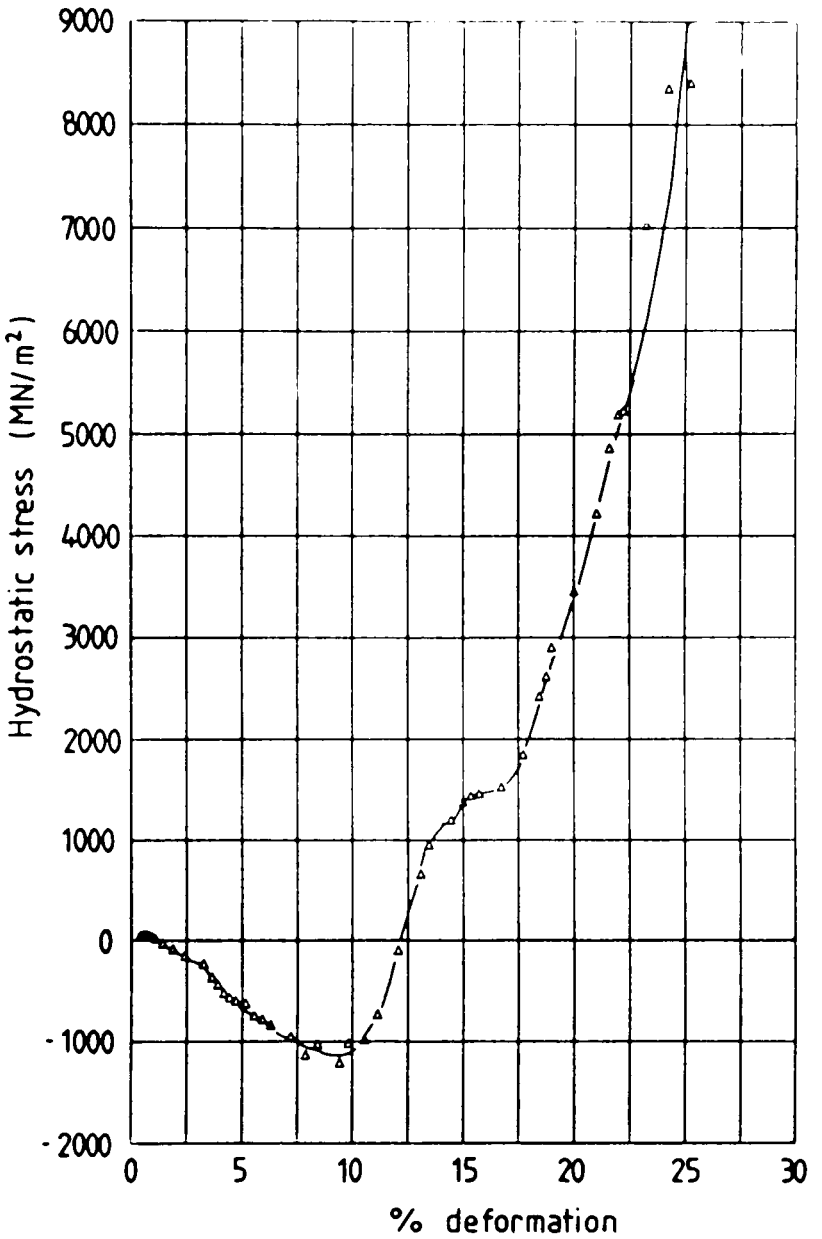

Figure C.13

Variation of FE hydrostatic stress for the extrusion of 7075 aluminium alloy for node 40.

Appendix D:

Published work.

S.E.Clift, P.Hartley, C.E.N.Sturgess & G.W.Rowe (1985)

'Fracture initiation in plane-strain forging'

Proc 25th International Machine Tool Design and Research Conference,

University of Birmingham, pp 413-420.

FRACTURE INITIATION IN PLANE STRAIN FORGING

S. E. CLIFT, P. HARTLEY, C. E. N. STURGESS and G. W. ROWE
University of Birmingham, UK

SUMMARY

This paper presents a preliminary investigation of the ability of elastic-plastic finite-element simulations to predict the initiation of ductile fracture in bodies undergoing large plastic deformation.

Plane-strain forging of 7075 aluminium alloy of circular cross section and two geometries with machined flats was analysed using the finite-element method and examined experimentally. The predictions of generalised strain distribution were confirmed by local hardness tests.

Fractures were found to initiate at, a) the centre of the circular section billet, and b) from the surfaces under the die for the geometries with machined flats. These fractures then appeared to propagate along bands of high shear strain.

Four fracture criteria were used in conjunction with the finite-element analysis to predict the site of the initiation of the fractures; These were generalised plastic work (Freudenthal (1)), tensile plastic work (Cockroft and Latham (2)), a modified tensile plastic work criterion (Brozzo et al (3)) and a criterion proposed by Ghosh (4). According to the generalised plastic work criterion, fracture should start at the centre of the initially circular-section billet but near the corner under the die when flats had been machined on the billet, as found experimentally. The two tensile plastic work criteria predicted failure at the centre for both geometrical forms, and the Ghosh criterion failed to predict a correct failure site at all.
The level of deformation at fracture was compared with experiment for the generalised plastic work and tensile plastic work criteria. Here, only the generalised plastic work criterion gave satisfactory correlation.

INTRODUCTION.

Metalforming operations may be limited by surface or internal cracks developing in the workpiece. Thus, it is important to identify the conditions within the deforming workpiece which may lead to fracture. Action may then be possible to modify the forming process to produce sound and reliable products.

The process by which fractures occur in metalforming has been widely modelled as one of void initiation and growth, followed by subsequent coalescence to form a crack. Based on this idea, criteria for ductile fracture have been suggested by McClintock et al (5,6) and Rice and Tracey (7). Marciniak and Kuczynski (8) proposed a model of ductile fracture which considered localised thinning between voids. Parmar and Mellor (9) tried to establish a relationship between density changes due to void growth and plastic strain while Oyane et al (10) proposed criteria for ductile fracture of both initially pore-free and pore containing materials.
Other criteria concentrate more on the the continuum effects of the microscopic processes leading to ductile fracture. Freudenthal (1) postulated that generalised plastic work is the critical parameter at fracture. Cockroft and Latham (2) consider the effects of the maximum principal tensile stress over the plastic strain path to fracture. Although this criterion includes an implicit dependence on hydrostatic stress, Brozzo et al (3) chose to include an additional explicit dependence. Ghosh (4) proposed a criterion based on the statistical process of the shear joining of voids in the stretch forming of sheet materials.

Recent developments in finite-element techniques for the study of metalforming problems has now made it possible to investigate in detail the predictions which can be obtained using many of these fracture criteria.

A limited investigation into the use of finite element techniques in fracture prediction has been performed by Oh, Chen and Kobayashi(11) who concluded that this type of application of finite-element theory is a valid one but that a more accurate computational formulation than that available at the time was required. Osakada and Mori(12) have also used finite-element stress and strain distributions to predict ductile fracture. However, their criterion falls into the same category as those of McClintock et al and Rice and Tracey which all require substantial experimentation to determine parameters required to produce a fracture prediction. It is obviously advantageous to keep the number of experimentally determined parameters in any fracture criterion to a minimum. Therefore those criteria which consider the continuum effects of the processes leading to ductile fracture and can most easily be used in conjunction with finite-element stress and strain fields (1-4) are considered in this paper.

The metalforming operation selected for study here is plane-strain side-pressing, sometimes referred to as transverse upsetting. This is of practical importance as an early stage in the manufacture of turbine blades, and has been previously examined by Jain and Kobayashi(13). They compared the metal flow and fractures obtained experimentally with results from a slip-line field analysis. The direction of propogation of the crack observed in the

experiments appeared to follow the calculated slip lines. Their analysis, however, was restricted to infinitesimal deformation steps and the material had to be modelled as rigid-perfectly plastic, so both elastic deformation and the effects of work hardening were ignored. The region of the workpiece in which fracture initiated was not identified experimentally and a theoretical prediction of fracture site was not possible using this theory.

Lee and Kobayashi(14) later used a two dimensional elastic-plastic finite-element formulation to study this operation. Their analysis provided more detailed information of the stress and strain distributions, both during and at the end of the deformation, but these were not used to predict fracture.

An elastic-plastic finite-element formulation using the Von Mises yield criterion and Prandtl-Reuss flow rule has been used for the work presented in this paper. This approach is capable of modelling strain hardening and contains several enhancements which allow the accurate calculation of large strains when deformation and rotations are both present (15).

PLANE STRAIN FORGING EXPERIMENTS

The specimens of 7075 aluminium alloy were 20mm diameter cylinders, 36.5mm long, made in two halves with a flat transverse interface, constrained in length by a close-fitting container and a suitable shim. This ensured approximately plane strain deformation when transversely compressed between flat parallel dies at room temperature, and at a low strain rate (less than 0.001 per second), to the required level of deformation. The deformed specimens were removed at regular intervals of deformation and examined for the appearance of any fractures in the mating surface. If any were observed the test was stopped; if not the specimens were again cleaned and carefully relocated to continue the deformation. The stress-strain curve for this material is shown in figure 1. Three different geometric cross sections were compressed in the experiments: (i) A full circular cross section, (ii) the same nominal rod as in (i) but with two diametrically opposed machined flats so that the height H was 2.03 times the contact width W, and (iii) as (ii) but with H/W = 1.33. The three geometries are illustrated in figure 2. No lubricant was used in any of the tests and the contact surfaces were cleaned with acetone. The ratio, m, of interfacial shear stress to the shear yield stress of the material, was found from ring tests with specimens machined from the same bars as those used for the side-pressing experiments to be approximately 0.25 (16).

Metal flow. All specimens with an initially circular cross-section displayed a mode of deformation which began in the areas immediately in contact with the dies. At a later stage, the deformation became more concentrated on diagonal shear bands. With the machined flats on the specimen the deformation again concentrated on diagonal shear bands but dead zones were present beneath the dies.

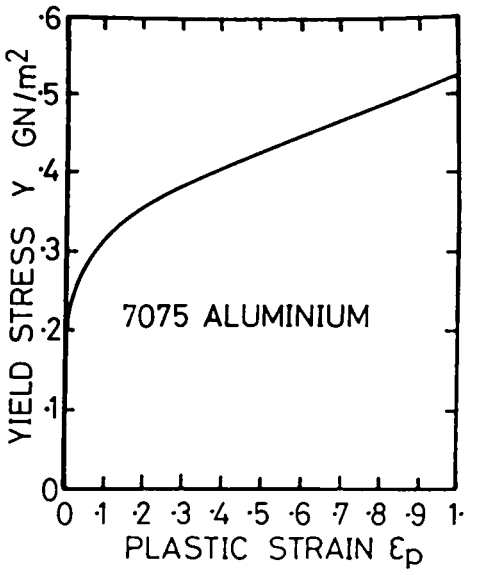

Figure 1.
Stress-strain curve for 7075 aluminium alloy.

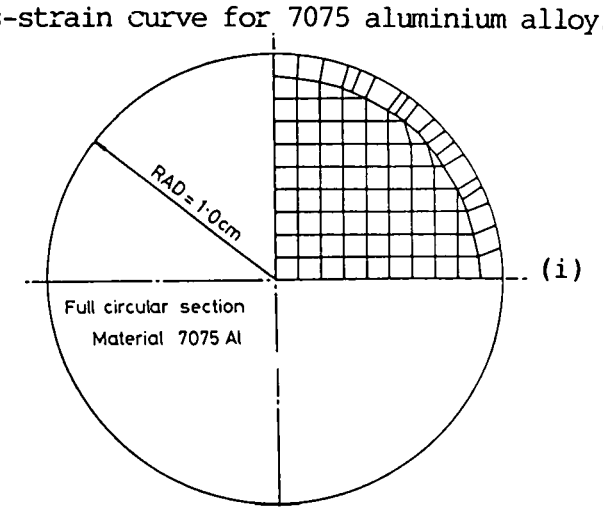

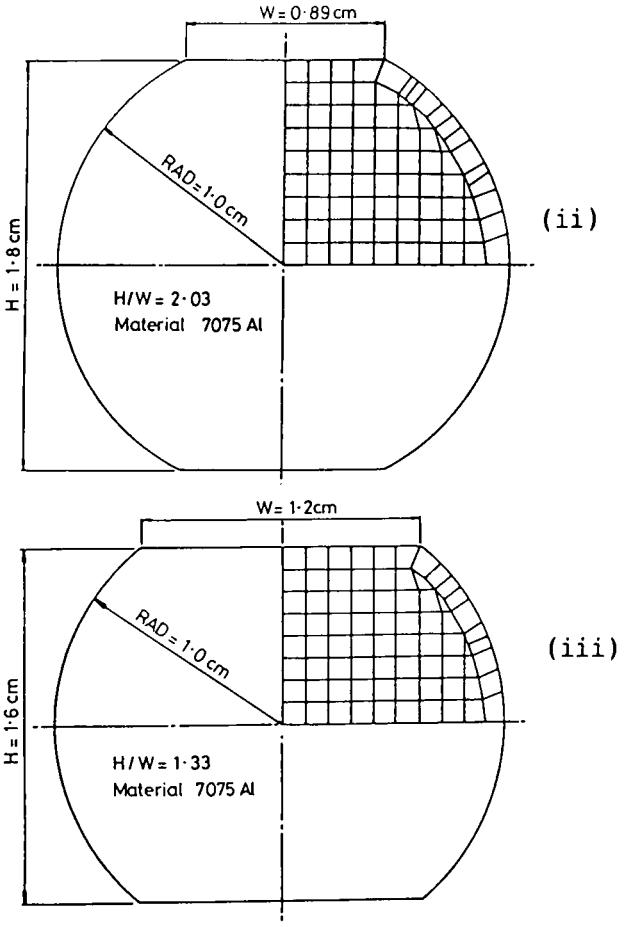

Figure 2.
Initial finite-element meshes for (i) a full circular cross section, (ii) specimen with initial height to width ratio of 2.03, (iii) specimen with initial height to width ratio of 1.33.

Deformation and fracture of 7075 aluminium alloy. Figure 3 illustrates the fractures observed in the tests. Although it was difficult to ascertain the exact point of fracture initiation, it was possible to identify the area of the specimen where fractures first appeared.

For those specimens having an initially circular cross section, this was at the centre of the specimen, with an overall reduction in height of 16%. For the specimens with machined flats, the fractures started from a point in the material in contact with the dies, close to the free surface. For an initial height to contact width ratio of 2.03 fracture occurred at 18% deformation, and for the second geometry with flats which had an initial ratio of 1.33, fracture occurred at 16% deformation. The results obtained indicate a strong dependency of the fracture initiation site on the initial geometry of the specimen, but the level of deformation at fracture was not so critically dependent on geometry. In each case the fracture that propagated through the specimen followed a path similar to the directions of maximum shear strain indicated by the slip-line fields of Jain and Kobayashi (13).

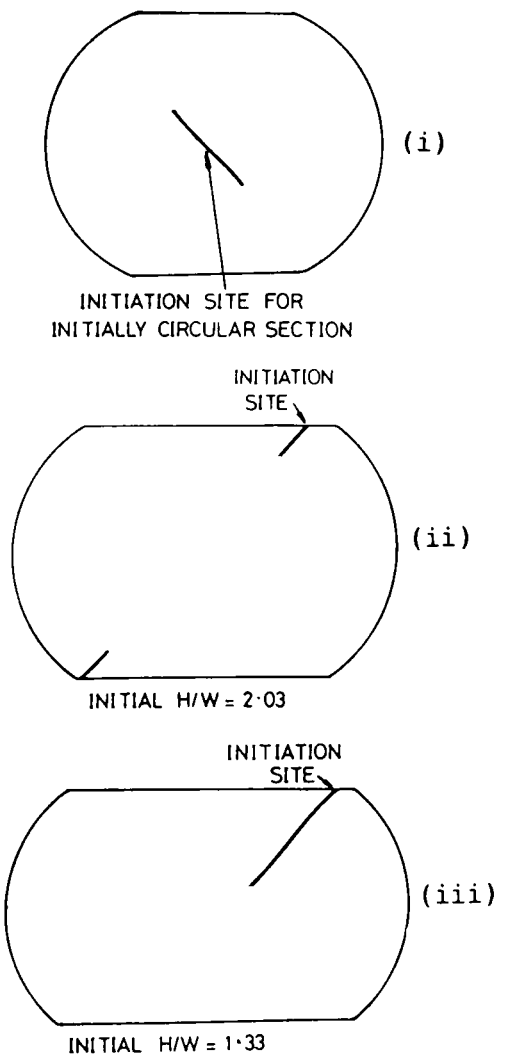

Figure 3.
Sketches to illustrate the initiation sites of experimentally observed fractures for (i) initially circular section, (ii) initial H/W = 2.03, (iii) initial H/W = 1.33. For the initially circular section the fracture propagated away from the central region. For specimens with machined flats fracture propagated towards the central region.

FINITE ELEMENT RESULTS.

Figure 4(i) illustrates the development of the plastically deforming regions for the circular section model, (for simplicity only one quadrant is illustrated). It is clear that deformation is restricted to regions close to the compressing platens during the early stages of side-pressing and spreads across the model at approximately 0.9% reduction in height. Figures 4(ii) and 4(iii) for the geometries with machined flats show greater deformation near the centre of the model initially but very similar patterns after about 1% reduction.

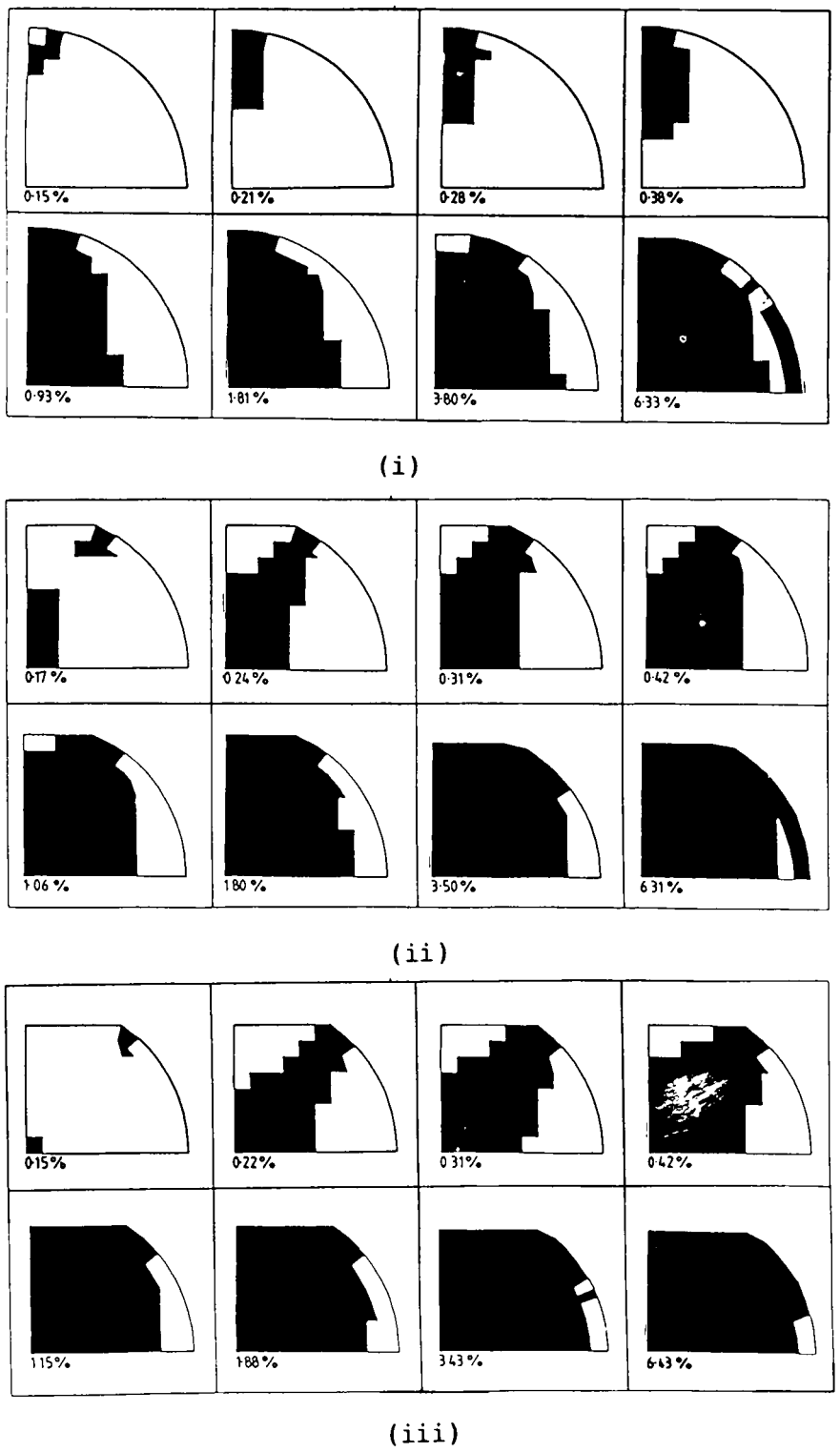

Figure 4.
Finite-element prediction of the development of the plastically deforming regions for (i) initially circular section, (ii) initial H/W = 2.03, (iii) initial H/W = 1.33.

The distorted finite-element grids at the level of deformation at which fracture was observed experimentally are shown in figure 5. The nodel point numbers on this diagram are those for which critical values for various fracture criteria are determined and presented in figures 7 and 8.

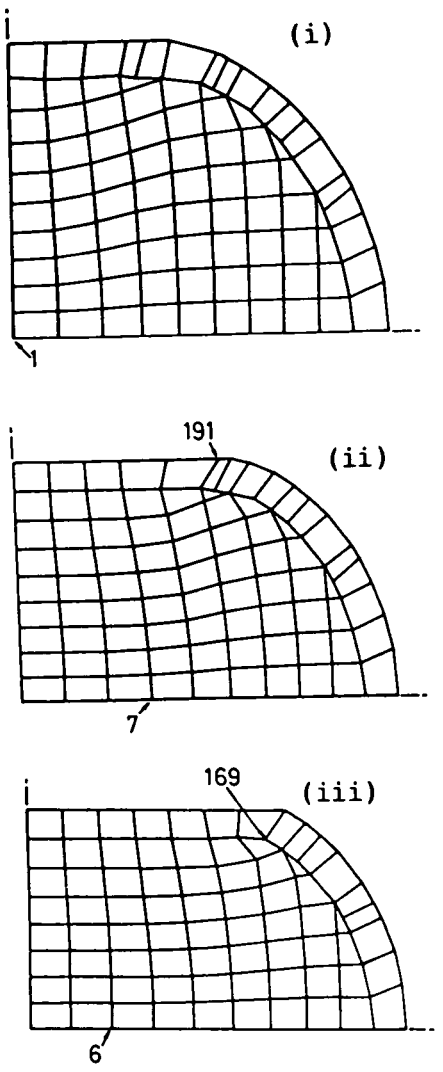

Figure 5.
Distorted finite-element grids at the experimental level of fracture for (i) initially circular section, (ii) initial H/W = 2.03, (iii) initial H/W = 1.33.

Finite-element predicted hardness distributions (Vickers Pyramid Number) are shown in figure 6 for the three different geometries. As the hardness distribution is related directly to the distribution of generalised plastic strain, comparison with experimental hardness values on the three sections is a good test of the accuracy of the predictions. Good correlation is found here as shown in figure 6 with average differences of the order of 6 per cent. The highest values of hardness found in approximately diagonal regions confirm the qualitative experimental observations and also the findings of Jain and Kobayashi (13).

Prediction of fracture initiation site. The deformation pattern alone is not sufficient to show where fracture will occur, though it identifies regions of severe shear. Various criteria for the fracture of ductile materials have been assessed as to their suitability for the prediction of fracture initiation and the following four criteria have been selected for further investigation because of their compatibility with the output of the continuum finite-element analysis.

1. Freudenthal (1) proposed that the absorbed energy per unit volume is the critical parameter at fracture. That is:-

$$\int_0^{\bar{\varepsilon}_f} \bar{\sigma} \, d\bar{\varepsilon} = C1$$

where C1 is the critical, (material dependent), value at fracture; $\bar{\sigma}$ is generalised stress; $\bar{\varepsilon}$ is generalised plastic strain. The subscript f denotes the value at fracture.
This generalised plastic work to fracture criterion was also used in a fracture mechanics context by Gillemot (17).

2. Cockroft and Latham (2,19) proposed that it is the tensile principal stress, rather than the generalised stress, which is important in fracture initiation. They postulated that fracture occurs when the integral of the largest tensile principal stress component over the plastic strain path to fracture equals a critical value characteristic of the material. This is expressed by the following equation, and may be interpreted as a critical tensile plastic work to fracture:

$$\int_0^{\bar{\varepsilon}_f} \sigma_1 \, d\bar{\varepsilon} = C2$$

where C2 is the critical material-dependent value at fracture and σ_1 is the maximum principal tensile stress.

3. Brozzo et al (3) proposed an empirical modification to Cockroft and Latham's fracture criterion as it predicted equivalent fracture strains which were too low when compared with experimental results for sheet forming. They suggested that the state of hydrostatic stress should appear explicitly in the criterion of fracture. The modified equation was presented in the following form:-

$$\int_0^{\bar{\varepsilon}_f} \frac{2\sigma_1}{3(\sigma_1-\sigma_H)} \, d\bar{\varepsilon} = W^*_{tf}$$

where W^*_{tf} is the critical material dependent value at fracture and σ_H is hydrostatic stress.

4. Using a different approach, Ghosh (4) proposed a fracture criterion based on the statistical process of shear joining of voids in the stretch forming of sheet materials. This was given by:-

$$\left(1 + \frac{\sigma_2}{\sigma_1}\right) \sigma_1^2 = K_f$$

where K_f is a material constant, being a modified form of fracture stress parameter containing inputs from the size, volume fraction and growth rate of voids.

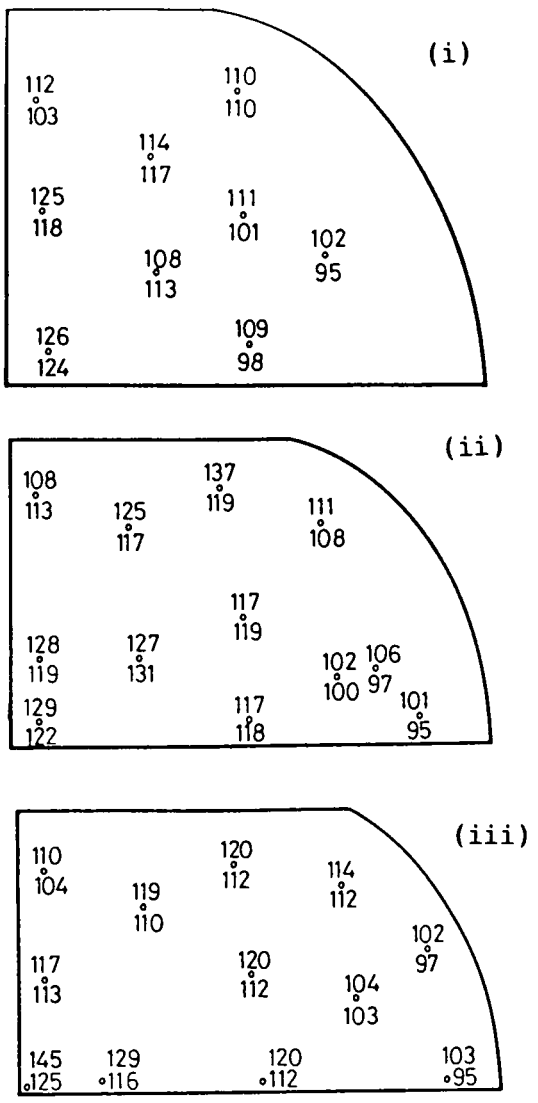

Figure 6.
Hardness distributions (VPN) at the experimental level of fracture for (i) initially circular section, (ii) initial H/W = 2.03, (iii) initial H/W = 1.33. At each location the experimental hardness appears above the finite-element prediction.

Numerical values for all four of these criteria were calculated using results from the finite-element analysis. The element or elements showing the highest value of the calculated parameter will be expected to fail first. The detailed changes as deformation proceeds are shown in figures 7 and 8 for the two plastic work criteria.

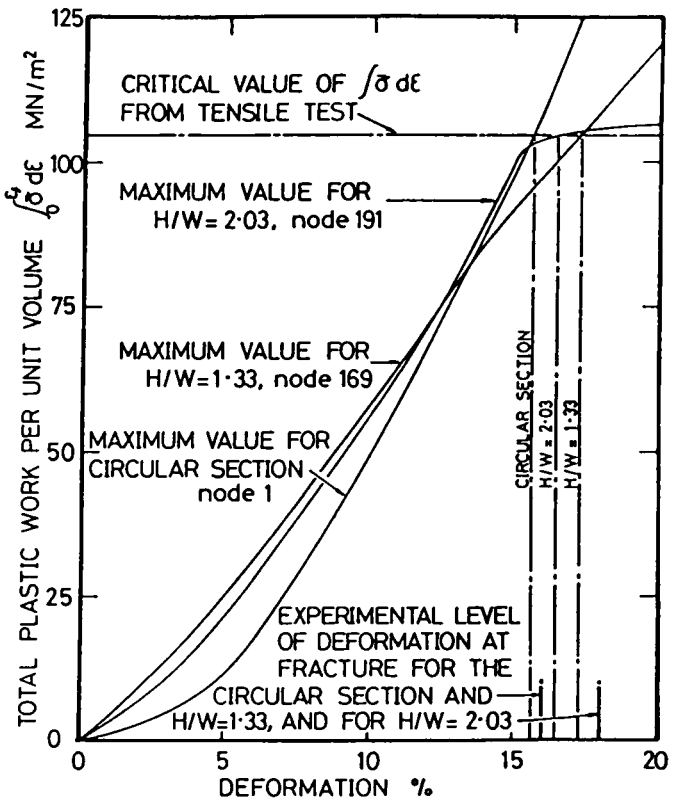

Figure 7.
Variation of the maximum value of total generalised plastic work per unit volume up to the experimental level of deformation at fracture for each of the three geometries. Location of nodal points is given in figure 5.

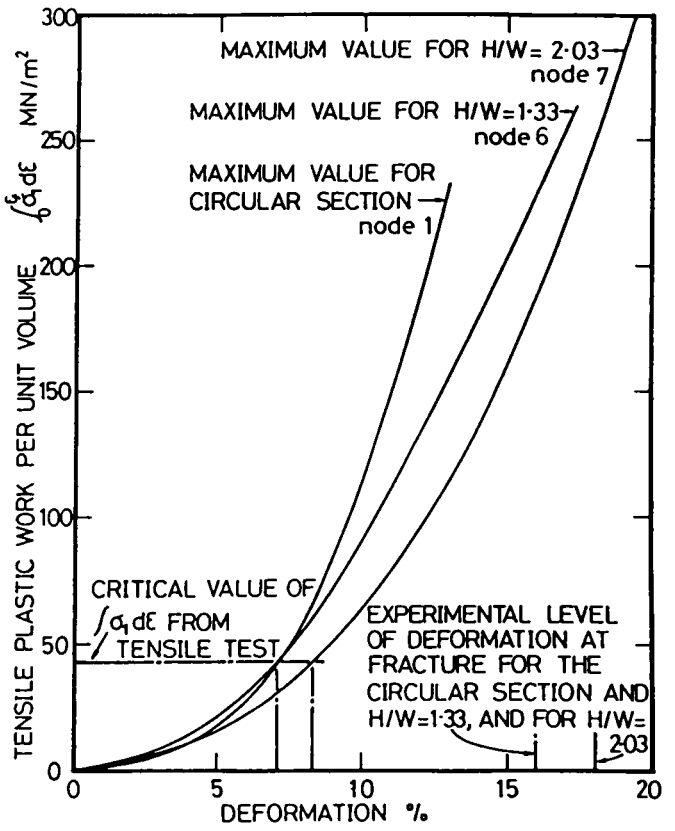

Figure 8.
Variation of the maximum value of tensile plastic work per unit volume up to the experimental level of deformation at fracture for each of the three geometries. Location of nodal points is given in figure 5.

Table 1 contains a summary of the predictions of fracture site. A tic indicates a correct prediction of the experimental fracture site, and a cross an incorrect prediction. Only the generalised plastic work criterion is successful for all three geometries. The Cockroft & Latham and Brozzo criteria predict the correct site for the initially circular section specimen, but not for the specimens with machined flats. The fracture criterion proposed by Ghosh did not predict the fracture sites in any of the three cases examined.

Specimen	Cockroft and Latham	Generalised Work	Brozzo	Ghosh
circular	√	√	√	×
H/W = 1·33	×	√	×	×
H/W = 2·03	×	√	×	×

Table 1.
Summary of the predictions of fracture site.

For the generalised work, and tensile work criteria, where the predictions of site were correct, correlation with the experimental level of deformation at fracture was attempted. The critical values for fracture were determined from an axisymmetric tensile test taking into account the tri-axial stress state in the neck by incorporating the Bridgman correction (18). From figures 7 and 8 it is apparent that only the generalised work criterion gave satisfactory correlation with experiment.
The tensile plastic work fracture criterion was derived for tensile situations and may be expected to give a reasonable prediction of fracture site, but not necessarily of the level of deformation at fracture, in situations where there is a large tensile principal stress component at the fracture initiation site. This is found to be the case for the specimens of initially circular cross section, but for the specimens with machined flats the largest accumulated tensile work is not at the fracture site at all. The finite-element method is clearly extremely valuable in determining the detailed stress and strain distributions developed during forging processes. It is this type of information which will enable a critical assessment of fracture criteria in a wide range of processes to be made in a way that would not be possible experimentally, and has not been possible with previous theories. The four criteria assessed in this paper are those which could be incorporated most easily into a finite-element type of analysis, but this does not preclude assessment of other criteria which could be handled with further work in a similar way. The finite-element results can be used to examine the contribution of individual parameters. The hydrostatic stress for example was not influential in determining the fracture sites in the side-pressing operation but it will be important in other forming operations. The hydrostatic stress will probably need to be combined with the total plastic work in some way to form a criterion of fracture of general application on metalforming processes.

CONCLUSIONS.

The plane-strain side-pressing of 7075 aluminium alloy has been examined experimentally and theoretically using an elastic-plastic finite-element method. Three different cross sections of workpiece were analysed. In each case the good agreement between the experimental and finite-element hardness distributions confirmed the reliability of the finite-element predictions of deformation.
The finite-element results were further used in conjunction with various fracture criteria to predict the site of fractures observed experimentally. These had occurred in the centre of the billet for workpieces of circular section and in the workpiece corner near the platen for those with machined flats.
Fracture criteria based on tensile plastic work predicted the correct site only for the circular section billet. A criterion based on the principal stress ratio was not successful in any of the cases considered here.
It was found that a criterion based on the total plastic work was successful in predicting both the site and level of deformation for all the geometries examined.
The influence of hydrostatic stress was not particularly important in the process considered here but it is probable that it will need to be included for general forming applications.

ACKNOWLEDGEMENTS.

Our thanks are due in no small part to Dr Ian Pillinger who wrote the FE computer program used in this work. We also wish to thank the Science and Engineering Research Council for financial support, and the staff of the Centre for Computing and Computer Science, University of Birmingham, and the University of Manchester Regional Computer Centre for the use of facilities, and Alcan for the supply of material. Valuable discussions with Professor A.G. Atkins and Dr. B. Dodd of the University of Reading are gratefully acknowledged.

REFERENCES.

1. FREUDENTHAL,A.M. (1950) Wiley, New York. 'The inelastic behaviour of engineering materials and structures.'
2. COCKROFT,M.G. & LATHAM,D.J. (1968) 'Ductility and Workability of metals'. J Inst Metals 96, pp33-39
3. BROZZO,P., DELUCA,B. & RENDINA,R (1972) 'A new method for the prediction of the formability limits of metal sheets.' Sheet metal forming and formability. Proceedings 7th biennial congress of the international deep drawing research group.
4. GHOSH,A.K.(1976) 'A criterion for ductile fracture in sheets under biaxial loading.' Met Trans 7A, pp523-533
5. McCLINTOCK,F.A. (1968) 'A criterion for ductile fracture by the growth of holes.' Trans ASME J Appl Mech 35, pp363
6. McCLINTOCK,F.A., KAPLAN,S.M. & BERG,C.A. (1966) 'Ductile fracture by hole growth in shear bands.' Int J Frac Mech 2, pp614
7. RICE,J.R. & TRACEY,D.M. (1969) 'On the ductile enlargement of voids in triaxial stress fields.' J Mech Phys Solids 17, pp201-217

8. MARCINIAK,Z. & KUCZYNSKI,K. (1979) 'The forming limit curve for bending processes.' Int J Mech Sci 21, pp609-621
9. PARMAR,A. & MELLOR,P.B. (1980) 'Growth of voids in biaxial stress fields.' Int J Mech Sci 22, pp133-150
10. OYANE,M., SATO,T., OKIMOTO,K. & SHIMA,S. (1980) 'Criteria for ductile fracture and their applications.' J Mech Work Tech 4, pp65-81
11. OH,S.I.,CHEN,C.C. & KOBAYASHI,S. (1979) 'Ductile fracture in axisymmetric extrusion and drawing. Part 2. Workability in extrusion and drawing.' Trans ASME J Eng Ind 101,pp36-44
12. OSAKADA,K. & MORI,K. (1978) 'Prediction of ductile fracture in cold forging.' Annals CIRP, 27,pp135-139
13. JAIN,S.C. & KOBAYASHI,S. (1970) 'Deformation and fracture of an aluminium alloy in plane-strain side-pressing', Proc 11th Machine tool design and research conference, University of Birmingham, pp 1137-1154, Macmillan Press (1971).
14. LEE,C.H. & KOBAYASHI,S. (1971) 'Analysis of axisymmetric upsetting and plane-strain side-pressing of solid cylinders using the finite-element method'. Trans ASME J Eng Ind 96, pp 445-454
15. PILLINGER,I. (1984) 'The prediction of metal flow and properties in three dimensional forging using the finite-element method'. Ph.D. thesis, University of Birmingham.
16. CLIFT,S.E. (1984) 'Identification of defect locations in forged products using the finite-element method'. MSc thesis, University of Birmingham
17. GILLEMOT,L.F. (1976) 'Criterion of crack initiation and spreading'. Eng Fract Mech 8,pp239-253
18. BRIDGMAN,P.W. (1944) 'The stress distribution at the neck of a tension specimen'. Trans ASM 32,pp553-574
19. COCKROFT,M.G. & LATHAM,D.J. (1966) 'A simple criterion of fracture for ductile materials.' National Engineering Labotatory, Report no 240, Glasgow.